Università degli Studi dell'Aquila

Dipartimento di Scienze Fisiche e Chimiche

Dottorato di Ricerca in Scienze Fisiche e Chimiche
XXXVIII ciclo

A Condensed Matter perspective for Dark Matter detection

Supervisore:

Prof. Gianni Profeta

Dottorando:

Paolo Settembri

Matricola: **289015**
SSD: **PHYS-04/A**

Anno Accademico 2024/2025

Sailors in the ocean of the unknown

Contents

Abstract **v**

List of Publications **vii**

Acknowledgements **ix**

Introduction **1**

1 Dark Matter **5**

1.1 Evidence on the existence of Dark Matter 6

1.1.1 The problem of the missing mass 6

1.1.2 Cosmological evidences 10

1.2 Dark Matter particles 11

1.2.1 DM particle candidates 12

1.2.2 DM production mechanisms 14

1.2.3 Detection strategies 15

1.3 Direct Detection Scattering Rates 18

1.3.1 Scattering Kinematics and Dark Matter Halo 20

1.3.2 Scattering Dynamics 24

1.3.3 Detector Effects and Exclusion limits 26

2 Nuclear Scattering Events and the Defect Formation in NaI Crystals **31**

2.1 DM-Nuclei Elastic Scattering 32

2.1.1 Scattering Kinematics 32

2.1.2 Scattering Rate 34

2.2 The COSINUS experiment 41

2.3 Defect formation in NaI crystals 44

2.3.1 Computational details 45

2.3.2 Molecular dynamics and DFT results 46

2.3.3 Defects effect and DM signal 49

3 Anisotropic DM-e^- scattering **55**
3.1 DM Electron scattering rate . . . 56
3.1.1 Dielectric function definition . . . 57
3.1.2 Scattering rate expressions . . . 58
3.1.3 Energy loss function . . . 61
3.2 Ab-initio calculation of dielectric functions . . . 63
3.2.1 Density Functional Theory . . . 63
3.2.2 Response function within TDDFT . . . 68
3.2.3 Derivation of the Kohn-Sham response . . . 70
3.2.4 Longitudinal dielectric function in crystals . . . 73
3.3 Dielectric Function implementation in the GPAW code . . . 77
3.3.1 Implementing crystal symmetries . . . 78
3.3.2 Spherical average . . . 83

4 Anisotropic Migdal effect **87**
4.1 The Migdal effect rate in semiconductors . . . 88
4.2 New formulation for the anisotropic rate . . . 92
4.2.1 Rewriting the momentum scalar product . . . 92
4.2.2 Wigner-D matrices . . . 93
4.2.3 Simplifying the **q** integral . . . 95
4.2.4 Isotropic and anisotropic term expressions . . . 96
4.2.5 Zernike expansion . . . 98

5 DM detection with superconductors **103**
5.1 Scattering rate in superconductors . . . 104
5.2 Superconducting Density Functional Theory . . . 106
5.2.1 Hohenberg Kohn theorem for SCDFT . . . 107
5.2.2 Auxiliary Kohn-Sham system for SCDFT . . . 109
5.2.3 Kohn-Sham equations in SCDFT . . . 109
5.2.4 Solving the SCDFT gap equation . . . 112
5.3 New implementations for superconductors and low-gap semiconductors . . . 113
5.3.1 Testing and application for low-gap semiconductors . . . 115

Conclusions **117**

Appendix A: Reference frames and Laboratory motion **119**
A.1 Reference frames . . . 119
A.1.1 Crystal and Laboratory frames . . . 119
A.1.2 Geocentric Equatorial frame . . . 120

A.1.3 Galactic frame . . . 121
A.2 Laboratory velocity . . . 121
A.2.1 Computing the scalar product $\hat{\mathbf{q}} \cdot \mathbf{v}_{\rm lab}$ . . . 122

Appendix B: Additional calculations **125**
B.1 SHM Marginal Speed Distribution . . . 125
B.2 SHM Mean Inverse Speed . . . 126
B.3 SHM Radon Transform . . . 127
B.4 Radon Transform to Mean Inverse Speed relation . . . 128
B.5 Expression of J_2 in the anisotropic Migdal effect correction . . . 129
B.6 Rewriting the DM-electron scattering rate using Zernike functions . . . 130

Appendix C: Density Functional Theory **133**
C.1 Functionals for exchange and correlation . . . 133
C.2 Plane wave method calculations . . . 135
C.3 Full-potential linearized augmented-plane-wave method . . . 138
C.4 Projector augmented wave method . . . 140

Bibliography **143**

Abstract

Dark matter remains a central unresolved problem in physics; direct detection via non-gravitational interactions requires pushing detector thresholds and understanding complex material responses. This thesis develops and validates a multiscale theoretical–computational framework that links microscopic electronic structure and lattice dynamics to experimentally measurable signals in next-generation low-threshold detectors. We derive and implement accurate scattering rates for both nuclear and electronic recoils, and introduce numerical tools to compute ab initio dielectric functions, including algorithmic simplifications for anisotropic materials, using time-dependent density-functional theory and electronic-structure methods. Molecular dynamics and atomistic simulations are combined with electronic calculations to model defect creation, lattice response, and their impact on excitations and charge collection. We apply these methods to realistic detector contexts, including scintillating cryogenic calorimeters, semiconducting targets, and superconducting sensors. The results produce concrete, testable predictions for signal rates and spectral features, quantify how microscopic defects can bias or obscure signals, and offer design guidance to optimize sensitivity to light dark matter. By providing a coherent pathway from first principles to observables, this work improves the fidelity of signal modeling and informs the design and interpretation of future direct-detection experiments.

List of Publications

- F. Bisti, P. Settembri, J. Minár, et al. **Evidence of spin and charge density waves in Chromium electronic bands**. Communications Materials 6, 70 (2025). DOI: https://doi.org/10.1038/s43246-025-00789-0.

- P. Settembri, F. Mazzola, I. Vobornik, et al. **Unveiling strain-responsive topological landscapes in the NiTe2 Dirac semimetal**. Physical Review B 110, 20 (2024). DOI: https://doi.org/10.1103/PhysRevB.110.L201401.

- D.L. Helis, A. Melchiorre, A. Puiu, et al. **First measurement of Gallium Arsenide as a low-temperature calorimeter**. European Physical Journal C 84, 749 (2024). DOI: https://doi.org/10.1140/epjc/s10052-024-13123-8.

- P. Settembri, The COSINUS collaboration, M. Di Giambattista, et al. **Defect Formation in NaI Crystals: A Novel Pathway to Dark Matter Detection**. Under Review in Physical Review D.

- A. Melchiorre, D.L. Helis, A. Puiu, et al. **First measurement of GaAs as a scintillating calorimeter: achievements and prospects**. arXiv preprint arXiv:2507.07119v1.

- P. Settembri, A. Al-Adulrazzaq, M. Heikinheimo, et al. **Anisotropic Migdal effect for Dark Matter detection**. In preparation.

- P. Settembri, A. Sanna, G. Profeta, et al. **Dielectric function of Superconductors from first principles**. In preparation.

- V. Minkov, A. Cucciari, P. Settembri, et al. **High Temperature Superconductivity in Lanthanum Superhydrides**. In preparation.

- L. Smith, P. Settembri, A. Cucciari, et al. **Nuclear quantum effects in high-pressure hydrides using NEO-DFT**. In preparation.

Acknowledgements

I would like to use this space to thank all the people who shared this journey with me.

Firstly, I want to thank my supervisor, Prof. Gianni Profeta, for his unwavering support, patience, and invaluable insights. He has been a consistent mentor, having overseen not only this Ph.D. work but also my Master's and Bachelor's theses, and his influence was pivotal in guiding me toward condensed matter physics. From the mechanics courses, through my experience tutoring his computational physics course, to the joint research underlying this thesis, our professional relationship has continuously developed over almost a decade. This work represents the latest milestone in this enduring connection.

I am also grateful to all the collaborators with whom I had the pleasure of working. Your expertise, stimulating discussions, and dedication have significantly enriched me, my scientific research, and this thesis. A special thanks also goes to the professors who taught and mentored me throughout my academic career, providing me with the foundational knowledge necessary for this work.

Ever since I was a kid, I have always shown a desire for the sciences, specifically for physics. I would go around screaming that I wanted to discover something about the Universe and drawing dream-houses with telescopes going through the roof. My family helped me cultivate this passion in my younger years and fully supported me in pursuing it, even when things were not easy. It is all thanks to you if I will now become a Dr. in Physics.

I think it is very hard to find a person who shares your life-goals, motivation, and ideals. A person who is honest and kind, supportive and compassionate. This is the person whom I found in Carolina. Thank you for being by my side during the highs and lows of these years. I can only dream of continuing to be next to each other, supporting one another in reaching our goals.

A huge thank you goes to all the friends I made throughout these years. Thank you for checking my documents before any important submission, hearing my frustration, and, most importantly, having fun together, making life more colorful. Leaving L'Aquila after so long will surely be tough. I can only hope that one day I will be in an environment close to that which I had in L'Aquila with all of you.

Introduction

Dark matter (DM) remains one of the most compelling enigmas in contemporary physics. Its gravitational imprint is manifest across cosmic scales, from galactic rotation curves to cosmic microwave background anisotropies; yet its non-gravitational properties remain elusive. The existence of dark matter is a necessary ingredient in the current theoretical framework: if it does not exist, the entire cosmological paradigm would require profound revision. Direct detection experiments seek to provide the first non-gravitational evidence of DM by observing rare interactions between hypothetical DM particles and ordinary baryonic matter within real detector materials. Achieving this goal is exceptionally challenging, requiring detectors with ultralow energy thresholds, optimal background suppression, and robust control of systematic uncertainties.

Progress on this front increasingly relies on a close interplay between experiments, materials science, and theory. New detection strategies are being developed that explore a wide range of target media, from noble liquids to engineered semiconductors and superconductors, each offering distinct response channels. Condensed matter systems host a complex ensemble of interacting fields and quasiparticle excitations, providing multiple avenues for energy deposition: from high-energy nuclear recoils to lower-energy collective modes such as excitons, magnons, phonons, and other quasiparticles. Understanding how these excitations are triggered by DM interactions is essential for identifying viable detection signatures.

Advances in ab initio and condensed-matter theory now allow a first principles description of how real materials respond to microscopic perturbations, complementing the ongoing technological push toward lower thresholds. Together, these experimental and theoretical efforts form an increasingly interdisciplinary program aimed at uncovering the particle nature of dark matter through direct, non-gravitational observation.

This thesis addresses the theoretical, computational, and materials-specific aspects required to interpret and optimize next-generation low-threshold detectors, with particular attention to electronic response channels that become important for light dark matter and to material effects that can open new experimental possibilities.

The main goal of the presented work is building and validating a framework that connects

microscopic electronic structure and lattice dynamics to observables in direct detection experiments. The thesis pursues the following interconnected goals: deriving and implementing accurate scattering rates for both nuclear and electron recoils, investigating how spurious effects like microscopic defects in detector crystals can modify an experiment signal, and exploring novel accurate strategies for superconductor-based detectors.
To accomplish this, we combined analytic derivations with multiscale numerical modeling. Molecular dynamics and atomistic simulations model defect creation and lattice response and are interfaced with electronic calculations to assess their impact on excitations and charge collection. Time-dependent density-functional theory and electronic-structure calculations supply ab initio dielectric functions with new algorithmic developments that simplify the description of the anisotropic response.
The work is grounded in realistic detector contexts to produce concrete, testable predictions. These contexts include scintillating cryogenic calorimeters, such as the NaI-based detectors used by the COSINUS experiment, and emerging technologies like semiconductor and superconducting sensors. By building a coherent pathway from microscopic theory to experimental observables, these contributions enhance the accuracy of signal predictions and provide guidance for the development of next-generation low-threshold detectors.
In the following, we report how the thesis is structured and summarize the contents of each chapter:

- Chapter 1 provides a general introduction to the main concepts of dark matter direct detection. We begin with the astrophysical and cosmological evidence for dark matter, review the leading particle candidates, and discuss the different detection strategies. We then focus on direct detection experiments, developing a general framework valid for different types of interactions, and introduce the key ingredients required to characterize such experiments.

- Chapter 2 focuses on direct detection through nuclear scattering events. After introducing the basic principles of these experiments, we narrow our attention to thermal detectors and in particular describe the COSINUS project. Building on the framework of the previous chapter, we derive the nuclear scattering rate. The chapter then presents original work in which we investigate the formation of defects in NaI target crystals, combining molecular dynamics with first-principles electronic-structure calculations. We demonstrate how defect formation can affect the response of such detectors and may allow for a complementary electronic detection channel.

- Chapter 3 is devoted to DM–electron scattering. We first derive the corresponding scattering rate and define the central role of the dielectric function. We introduce the

main concepts of density functional theory (DFT) and describe how the dielectric function can be obtained within time-dependent DFT. Original implementations that improve the efficiency of calculating the dielectric function at finite momentum transfer are then discussed.

- Chapter 4 describes the Migdal effect in the context of DM detection, with an overview of the theory and the main approximations. We then present our new reformulation of the Migdal effect rate, which allows for a more efficient calculation, facilitating the computation of the anisotropic rate.

- Chapter 5 explores the use of superconducting detectors, which are emerging as one of the most promising technologies for future dark matter searches. After introducing the fundamentals of superconducting density functional theory, we present original work aimed at computing the full anisotropic dielectric function in the superconducting state.

Chapter 1

Dark Matter

In recent decades, astrophysical observations, such as galaxy rotation curves, gravitational lensing, and measurements of the cosmic microwave background, have demonstrated that visible matter, composed of Standard Model (SM) particles, accounts for only about 15% of the total mass-energy budget of our Universe. The remaining mass is attributed to dark matter (DM), and dark energy, components defined by their absence of interactions with electromagnetic radiation.

Although DM governs gravitational dynamics on an astronomical scale, it remains invisible to direct telescopic observation. DM not only shapes the anisotropies of the cosmic microwave background (CMB), but also drives the formation of cosmic structures. Independent evidence arises from colliding galaxy clusters, where the spatial separation of the hot X-ray emitting gas and the lensing mass demonstrates an invisible, collisionless mass component. A leading hypothesis is that DM consists of one or more particles, potentially forming a "dark" sector analogous to the visible, "light", sector of SM particles. If such DM particles exist, Earth would be continuously traversed by a flux of them. Should they interact weakly with ordinary matter via other forces besides gravity, they could occasionally scatter off nuclei and electrons, depositing a detectable energy in low-background detectors. This method, the direct detection of DM, offers a non-gravitational confirmation of DM's particle nature, and a positive signal would represent one of the most significant discoveries in modern physics. Complementary search strategies include indirect detection, searching for the products of DM annihilation or decay, and collider production of DM candidates, working coherently with direct detection experiments in the search for DM particles.

We will now review the major evidence demonstrating the existence of DM, explore the properties of hypothetical DM particles, and examine the strategies for detecting them using non-gravitational interactions. We then focus on the direct detection approach, providing a formal description of such experiments and the expected DM scattering rate.

1.1 Evidence on the existence of Dark Matter

1.1.1 The problem of the missing mass

Cluster of galaxies Historically, the earliest evidence regarding the existence of dark matter stems from the missing mass problem, a discrepancy between theoretical predictions of various astronomical phenomena and experimental observations. Such discrepancies can be explained by the presence of undetectable matter, hence "dark", which increases the density of matter in galaxies.
Fritz Zwicky in his study of the "Coma" galaxy cluster [1], starting from the idea of describing a galaxy as a thermodynamic gas of gravitating stars, applied the virial theorem to said cluster (bound system of gravitationally interacting galaxies).
The Virial theorem, in the case of gravitational interactions, links the average kinetic energy of the system to its average potential energy according to:

$$\langle T \rangle = -\frac{1}{2}\langle V \rangle \ . \tag{1.1}$$

From an estimate of the total mass of the "Coma" cluster M and its radius R he obtained a theoretical prediction for the velocity dispersion of galaxies:

$$\sqrt{\langle v^2 \rangle} = \left(\frac{3GM}{5R}\right)^{\frac{1}{2}} \approx 82 \text{ km/s} \ ; \tag{1.2}$$

$$\sigma_v = \sqrt{\frac{\langle v^2 \rangle}{3}} \approx 47 \text{ km/s} \ . \tag{1.3}$$

From Doppler effect measurements on spectral lines, he estimated the apparent velocity of the galaxies, finding for several of them a velocity dispersion of about 1100 km/s, much greater than predicted.
To obtain, starting from the virial theorem, a velocity dispersion of the same order, a matter density 400 times greater than the stellar density must be assumed; the "Coma" cluster would otherwise not be a bound system, in fact it would not respect the virial theorem and would disperse in time.
Thus, it is inferred that only a small fraction of the mass is observable, while the remaining fraction is "dark". An early hypothesis, by Zwicky himself, was that such "dark matter" was composed of gas, cold stars and other solid bodies.

Galaxy rotation velocity One of the main evidences in favor of the existence of dark matter and its central role in gravitational phenomena on astronomical scales comes from

the galactic rotation curves, i.e. the velocity v of visible matter orbiting at a distance r from the galactic center [2]. Using Newtonian mechanics, one can have a prediction of the rotation curve. Assuming circular orbits for stars rotating around the galactic center at a distance r from the center, identifying the force of gravity with the centripetal force, we obtain:

$$m_{star}\frac{v_{star}^2}{r} = G\frac{m_{star}M(r)}{r^2} \ , \tag{1.4}$$

Solving with respect to v_{star}:

$$v_{star} = v(r) = \sqrt{\frac{GM(r)}{r}} \ , \tag{1.5}$$

with $v(r)$ the rotation curve, G Newton's gravitational constant, and $M(r)$ the mass contained within the sphere of radius r.
The quantity $M(r)$ can be expressed analytically from the mass density distribution of the galaxy as:

$$M(r) = \iiint d^3\mathbf{r}' \ \rho(\mathbf{r}') \ \Theta(r - r') \ , \tag{1.6}$$

where Θ is the Heaviside step function, selecting $r' < r$ in the integration. Considering that the visible mass within a galaxy is mainly concentrated around its center, $M(r)$ should take on an approximately constant value in the outermost regions, resulting in a predicted rotation velocity trend $v(r) \sim \frac{1}{\sqrt{r}}$. Although the Keplerian trend turns out to be valid for planetary orbits, experimental measurements of galaxy rotational velocities have yielded results clearly discordant with this prediction [3].
Over decades, rotation curves have been measured using different experimental techniques for numerous galaxies; none of these have shown the Keplerian trend, but an approximately constant value of the rotational velocity as they move away from the center of the galaxy. In Fig. 1.1 the galaxy rotation curve for the Messier 33 spiral galaxy is shown, with the different contributions highlighted [4].
Measurements are usually made from starlight for areas where their concentration is sufficiently high, while at great distances a Doppler effect analysis is made on the $\lambda = 21$ cm line of Hydrogen, emitted from gas clouds in the outer areas of the galaxy.
Such a spectral line is caused by the transition of Hydrogen from a parallel spin state between electron and proton to an antiparallel (less energetic) spin state, resulting in the emission of a photon.
Such a result can be explained by a trend of $M(r)$ in the outer regions that is linear with the distance from the galactic center; thus, there would be more total mass in the galaxies than just visible mass, and especially the outermost regions would be much more massive than expected [5].

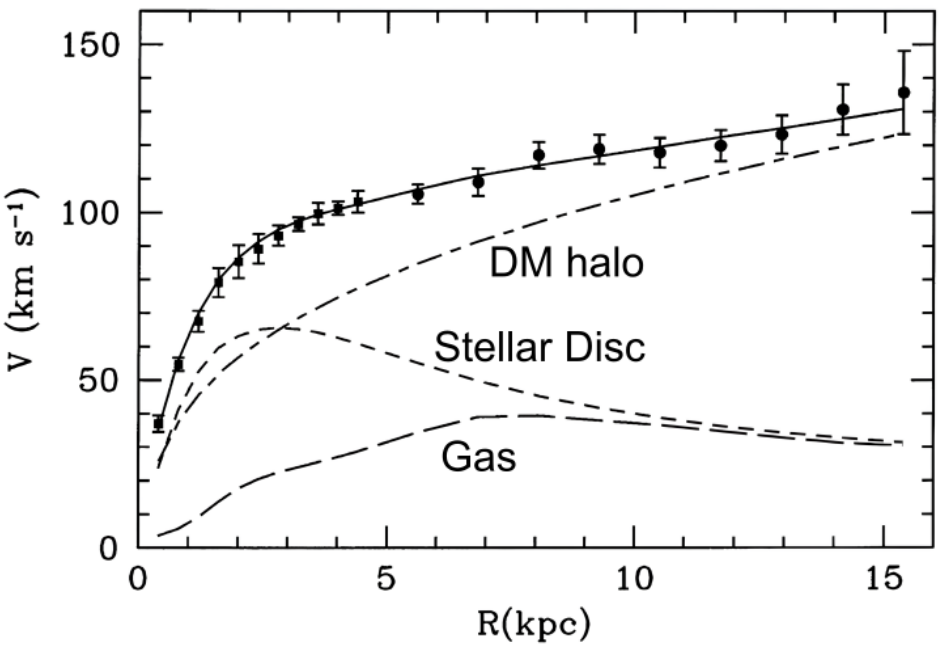

Figure 1.1: Galaxy rotation curve of the spiral galaxy Messier 33, figure from Ref. [4]. The data points show the measured rotation curve and the continuous black line a best-fitting model. The different contributions are also shown: DM halo (dot-dashed line), stellar disc (short-dashed line) and gases (long-dashed line).

These results seem to support the existence of dark matter and especially the presence of a halo of DM in which galaxies are immersed.

Gravitational lensing and the Bullet Cluster When a massive body lies along the line between a distant galaxy and the observer, the light propagating from the former to the latter is deflected, changing the image and/or intensity observed according to the mass of the body; this phenomenon, predicted by Einstein's theory of general relativity, is called gravitational lensing.

In the case of clear image distortions, we speak of "strong lensing", while less obvious distortions fall into the category of "weak lensing"; in this case, the presence of a massive body can be determined by a statistical study of the alignment of different sources (galaxies, clusters) in the background [8, 9]. If, on the other hand, no distortions are present but the amount of light received by the object due to the passage of a massive body along the line of sight varies over time, the phenomenon is called "microlensing".

Weak lensing effects from galaxy clusters have been observed in recent decades, and with object mass being a crucial parameter of the phenomenon, it has been possible to obtain measurements of cluster masses with results compatible with fits of galaxy rotation curves [10, 11].

In addition to supporting the presence of a large amount of unseen mass within galaxies,

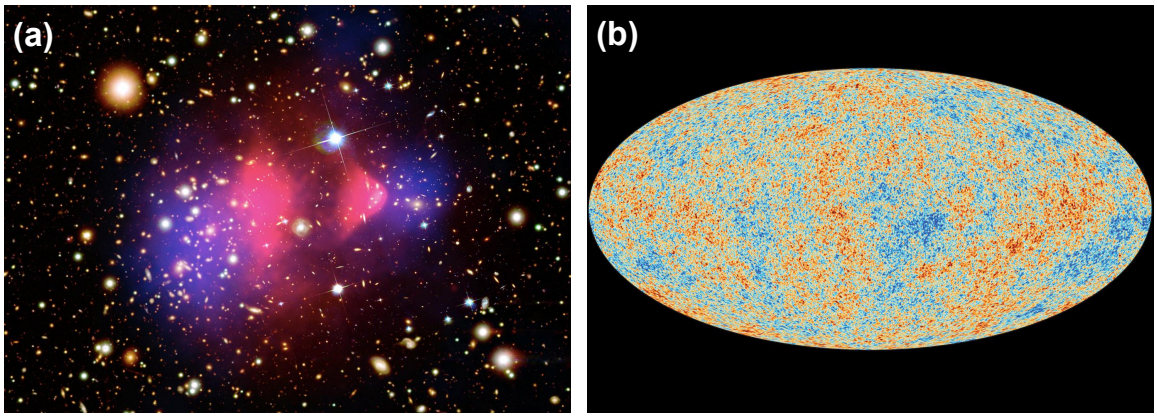

Figure 1.2: (a) Overlap of the optical image, the X-ray image (red) and the gravitational potential obtained from weak lensing (blue) of the Bullet Cluster [6]. (b) Image of the CMB from ESA and the Planck collaboration [7].

weak lensing processes allow the mass distribution within clusters to be mapped. One particular case in which the process of weak lensing has enabled the study of mass distribution is the "Bullet Cluster" (1E 0675-558) [12, 13]. The results obtained from the study of the "Bullet Cluster", composed of two clusters of galaxies moving apart after passing through each other, can be clearly visualized in Fig. 1.2 (a).

The gases in the galaxies are separated from them during the collisions, due to their electromagnetic interactions, and are a source of X-rays. The X-ray image of the cluster is shown in red in Fig. 1.2 (a).

In the absence of DM, the mass distribution obtained from weak lensing, shown in blue in Fig. 1.2 (a), should follow the X-ray observations, since the gases constitute the predominant part of the mass of the system.

Instead, the results obtained were different, with the mass distribution centered on the galaxies; thus, most of the mass is in the form of undetectable, collisionless matter (unaffected by the crossing of the two clusters) [14].

This type of separation, which has been observed on several occasions in recent years, provides further evidence in favor of the existence of DM and also challenges proposals such as that of the MOdified Newtonian Dynamics (MOND) [15]. MOND is a theory proposed as an alternative to dark matter, in which Newton's second law is modified at very low accelerations, and is notably capable of explaining phenomena like galaxies rotation curves, without invoking dark matter. But since in MOND gravity arises solely from visible matter, the lensing signal of the "Bullet Cluster" should coincide with the baryons (gases), in contrast with observations. MOND is thus incapable of explaining mass-light separation phenomena.

1.1.2 Cosmological evidences

Further evidence for the existence of dark matter emerges on a cosmological scale and, especially, from the cosmic background radiation and the mechanisms of structure formation in the Universe.

In its earliest stages, the Universe was composed of an almost homogeneous plasma of baryons, electrons and photons at thermal equilibrium; it was also opaque to photons, which, due to Thompson scattering with electrons, had a short average free path [16].

As the Universe expanded and cooled, neutral atoms began to form; subsequently, the Universe relatively quickly became transparent to electromagnetic radiation and photons began to propagate freely. The photons that carried out their last scattering before that expansion and still propagate in the Universe today form the Cosmic Microwave Background (CMB): a background radiation that respects the Planckian blackbody spectrum corresponding to a temperature of about 2.7 K [17]. In Fig. 1.2 (b) the CMB is shown.

An important feature of the CMB is the presence of temperature fluctuations which are connected to the gravitational fluctuations necessary for the formation of galaxies and cluster structures. These anisotropies can be traced to the presence in the early Universe of two opposing processes, gravitational clustering, which tends to form regions of higher density, and photon radiation pressure, which tends to do the opposite. The peaks in the CMB spectrum depend strongly on the density of both baryonic matter and dark matter, since only baryonic matter undergoes the radiation effect [18].

Within the ΛCDM model, the standard model of cosmology, which describes an isotropic, homogeneous, flat Universe, the total energy density breaks down into ordinary matter, dark matter, and dark energy in the form of the cosmological constant Λ. From the fits of the spectrum obtained from Planck; the following values of the $\Omega_i \equiv \rho_i/\rho_c$ parameter, which is the contribution to the critical density ρ_c (energy density of a flat Universe) of a given constituent, were obtained [19]:

$$\Omega_{\mathrm{b}} = 0.049 \ , \quad \Omega_{\mathrm{M}} = 0.31 \ , \tag{1.7}$$

where Ω_{b} refers to the baryonic mass, and Ω_{M} refers to dark and ordinary matter.

Thus, it is concluded that baryonic matter contributes only 15% of the total matter in the Universe; therefore, there is a form of matter other than ordinary matter that does not interact with photons and that has a predominant contribution to the energy density of the Universe.

Another piece of evidence in favor of the existence of dark matter comes from the formation of galaxy structures and clusters in the Universe. Such processes are studied by numerical N-body simulations of gravitating particles, comparing the formed structures

with observations [20]. Such simulations show that without dark matter, galaxies would have formed too late to explain the current state of the Universe; it is also understood how DM velocity is a critical factor in the formation of minor structures. The high-speed motion of a relativistic "hot" Dark Matter suppresses the formation of minor structures, unlike the non-relativistic "cold" Dark Matter, which reproduces a hierarchical cosmological structure, as in the real Universe [21, 22].

In the following section we will review the possible explanations and candidates for dark matter.

1.2 Dark Matter particles

Starting from the astrophysical and cosmological observations, different possibilities have been considered to explain DM.
An initial hypothesis saw DM as composed by Massive Compact Halo Objects (MACHOs), small, massive, dark objects of baryonic matter, drifting in interstellar space, like: black holes, neutron stars, rogue planets, rocks, dim stellar remnants [23].
Projects like MACHO and EROS-2 searched for dark stellar bodies by using microlensing: the temporary amplification of the brightness of a large number of background stars, due to the gravitational lensing of a massive, transient object. These projects ruled out MACHOs as the primary source of DM in the galaxy, due to a not sufficient excess of microlensing events [24].
A new possible candidate for DM arose in later years in the form of Primordial Black Holes (PBHs), formed by the gravitational collapse of density fluctuations in the early Universe, which were necessary for the formation of structure [25]. These non-stellar black holes could have survived until now, possibly forming the galactic halo; however there are severe constraints on PBHs as DM. In the end, the attempts of explaining the evidences for DM with ordinary matter alone failed and a non-baryonic explanation for the galactic halo became necessary.
The hypothesis that DM is made of a particle, or particles composing a so called dark sector, was then born. We then need to derive the various conditions that the hypothetical DM particle must satisfy:

- it must not reflect, absorb or emit light;
- it must be stable in the time scales of the Universe;
- it must be non-relativistic, in order to allow the formation of structures;
- it must be collision-less and non dissipative, which means that it does not interact, or at most only weak interactions, with ordinary matter apart from gravity;

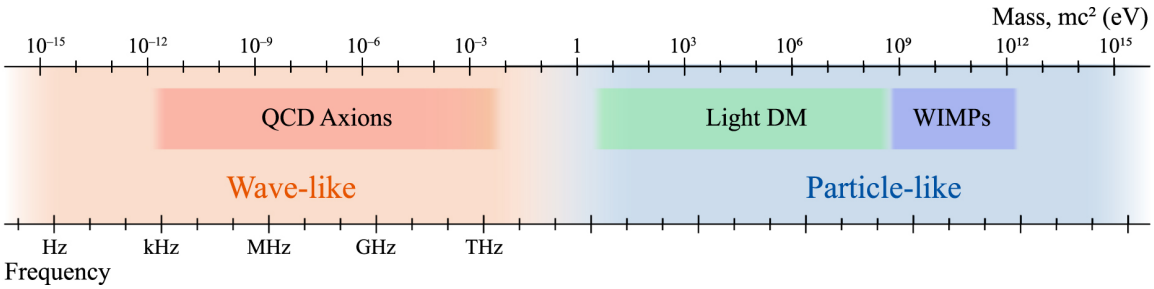

Figure 1.3: Three of the main DM candidates, WIMPs, light DM and axions, in their corresponding expected mass ranges (figure from Ref. [28]).

- it must be produced in the early stages of the Universe in the right amounts.

Before searching for new potential particles, a check on whether any of the known particles satisfy all these requirements must be performed.
In this sense, neutrinos were historically the first dark matter particle candidates, but due to upper limits on the masses of different neutrinos $\sum_i m_i < 0.11\text{eV}$, the relative contribution to the energy density in the Universe is estimated to be [26]:

$$\Omega_\nu < 2.6 \times 10^{-3} \ . \tag{1.8}$$

Neutrinos thus contribute only to a small portion of the non-baryonic matter in the Universe; they would also behave as "hot" dark matter in the early stages of the Universe, preventing the formation of structures [27]. There are currently several theoretical models that predict the existence of particles that could behave like dark matter, in the following subsection we review some of the major candidates: WIMPs, light DM and Axions, which are shown in Fig. 1.3 with the corresponding mass range.

1.2.1 DM particle candidates

WIMPs WIMPs (Weakly Interacting Massive Particles) are a category of particles containing numerous candidates for DM particles. From a cosmological point of view, a particle with a mass of the order of 100 GeV and a cross section at the electroweak scale would explain the cosmological abundance of DM, as described by the freeze-out production mechanism reported in the following section.
A strong evidence for WIMPs comes also from SUSY, a beyond-the-Standard-Model theory called supersymmetry, which postulates the existence of superpartners for all Standard Model particles [29]. Among these particles, some are predicted to be in the WIMP mass range, to be stable enough to be present in today's Universe and to have interactions with normal matter in the electroweak scale [30, 31]. The accidental coincidence in mass and cross section between these two hypotheses is known as the "WIMP miracle".

The category of WIMPs is characterized by a Gev-TeV mass range, a non-gravitational interaction with ordinary matter, which should not be stronger than the SM weak interaction.
Different types of experiments have been performed since the hypotheses of the WIMP particle: in colliders experiments trying to verify the existence of WIMPS have searched for a missing-momentum signal, while underground experiments searched for direct detection signals.
The Dark MAtter/Large sodium Iodide Bulk for RAre processes (DAMA/LIBRA) [32] experiment obtained the only positive claim for WIMP detection at the present time, with an annual modulation of the signal observed for more than 13 annual cycles in their NaI crystal detectors. Since then different experiments have failed to confirm their results, obtaining null results in the same region of the parameter space [33, 34, 35]. Due to the null results of different direct detection and collider experiments that have been performed for this mass range, the WIMP has become highly unlikely, with many experiments now trying to improve their sensitivity to search for WIMPs in a wider mass range.

Light DM Several different theoretical models predict the existence of new possible DM candidates; in particular alternatives to traditional WIMPs that have lighter masses and particle-like characteristics, which fall under the collective name of light DM [36, 37, 38].
One of the candidates for light DM is the sterile neutrino, an hypothetical particle that, opposite to SM neutrinos which have left handed chirality, has a right handed chirality, implying that they do not interact with standard model gauge bosons [39]. The possible existence of sterile neutrinos has been hinted at by experimental results on neutrino oscillations [40]. The existence of sterile neutrinos with a very weak interaction strength with normal matter and mass in the keV scale, would make them a possible DM candidate. Their early Universe production would happen via a non-thermal mechanism like the freeze-in [41].
As it will be clear from the following sections, a DM particle with lower mass will induce lower energy excitations in a target material. Lower thresholds and different mechanisms, like electronic excitations, are then needed to probe such DM particles.

Axions Axions are hypothetical particles proposed to solve the strong CP problem in quantum chromodynamics (QCD). While a priori CP (charge conjugation, C, and parity, P, symmetries) is not a conserved symmetry in QCD, no sign of CP violation has been experimentally observed. The CP symmetry is instead known to be violated in electroweak interactions [42, 43]. This inconsistency would be resolved by the introduction of a new global symmetry and a consequent new type of particle, which was named axion [44].

The standard axion was then excluded by experimental searches, but since then general realizations, like the Invisible Axion (with a much weaker coupling than the standard axion), led to the creation of the large class of Axion-Like Particles (ALPs).
These particles would be produced non-relativistic through a non-thermal mechanism during the early Universe, and would act as a collision-less fluid.
It has been theoretically shown that axions would be converted into detectable photons if in a strong magnetic field, leading to a large number of experiments performed using haloscopes.
As graphically shown in Fig. 1.3, when the DM mass m_χ falls under 0.1 eV, it is expected to behave like waves with a de Broglie frequency f determined by its mass. For this reason, experiments interested in this mass range must be sensitive to signals originating from the wave-like behavior of DM.

1.2.2 DM production mechanisms

One of the requirements for a DM particle candidate is the existence of a production mechanism that happened in the early Universe and predicts the correct amount of DM density in our current Universe. Out of the several production mechanisms, in the following we will focus on the freeze-out and freeze-in scenario, which are two of the main ones.
In the freeze-out scenario we hypothesize that in the early Universe DM was initially in thermal equilibrium with the SM bath [45, 46]. At temperatures much greater than m_χ, DM particles are being continuously created by and annihilating into lighter particles, the rate of annihilation processes like $\chi\bar{\chi} \to e^+e^-$ is equal to the rate of the reverse reaction $e^+e^- \to \chi\bar{\chi}$. However, as the Universe temperature T decreases, the reverse reaction that produces new DM particles becomes suppressed, since the lighter particles will lose the energy necessary for the reaction. The number density of DM starts then to drop exponentially, since the annihilation processes keep happening. As the DM number density decreases so will their annihilation rate $\Gamma_{\chi\bar{\chi}}$, and at some point the annihilation rate will drop below the expansion rate of the Universe. The annihilation process will then shut off, since DM particles and anti-particles no longer come into contact; a constant number of DM particles will then remain in the Universe as thermal relic. This production mechanism is called "thermal freeze-out", and it directly relates the annihilation cross section to the relic abundance; a larger cross section will imply a lower density of DM left in today's Universe. Further more, the existence of an annihilation channel which couples DM to the SM, like $\chi\bar{\chi} \to e^+e^-$, implies that the related scattering process $\chi e^- \to \chi e^-$ must exist, permitting a direct detection of DM particles [47].
The DM particles do not need to be a thermal relic; there can be different production mechanisms that do not rely on DM being in thermal equilibrium, one of these is the

freeze-in mechanism [48]. In this scenario DM is in thermal contact with the SM without being in thermal equilibrium. Initially, the abundance of DM is zero but very weak interactions in the SM plasma create DM via reactions of the type $e^+e^- \to \chi\bar{\chi}$; the abundance of DM will always be small enough that the annihilation process does not occur with an appreciable rate, and the DM never equilibrates. The production process will shut off when the temperature drops below m_χ, or if $m_\chi < m_e$, when the temperature drops below m_e and positrons drop out of equilibrium.
Several constraints on their mass and cross section, can be imposed on the DM particles when different consequences of their production mechanism are taken into account; however, this is not our scope. We now assume that DM particles have been produced and are now present in today's Universe accordingly to a given mechanism, and discuss the different possible detection strategies.

1.2.3 Detection strategies

While there is a lot of evidence of the existence of DM, it is purely gravitational. Nonetheless, DM particles may interact via one of the known forces, like via the Z or the Higgs fields, or with a new field that connects the "light" and "dark" sectors, like the dark photon. In that case, the search for non-gravitational evidence for DM is possible, and it can be divided into three main detection strategies.

Direct production In the case of DM interacting with ordinary matter, it might be possible to produce it in high-energy particle collisions, as in particle accelerators like the Large Hadron Collider (LHC)[49, 50]. The particles, after their creation, would leave the detector and the signal of their creation would be a lack of energy in the final state, called Missing Transverse Energy (MET).
However, colliders alone could not confirm that a newly discovered weakly interacting particle is a good candidate for a DM particle, as they could not, for example, verify the stability of the particle, only determining a lower bound on its lifetime. A complementary detection would still be needed to confirm that the newly discovered particle is indeed the sought dark matter, connecting it to the galactic halo [51].

Indirect Detection The indirect detection strategy is based on the possibility that DM particles can decay, or annihilate, into Standard Model (SM) particles [52]. In such a case, through cosmic ray and neutrino telescopes, it would be possible to observe an excess of the SM particle fluxes from areas of high dark matter density, like the galactic center of the Milky Way, neighboring dwarf galaxies or galaxy clusters. There are several possible detection channels, like DM annihilation into γ-rays [53], anti-protons and positrons [54],

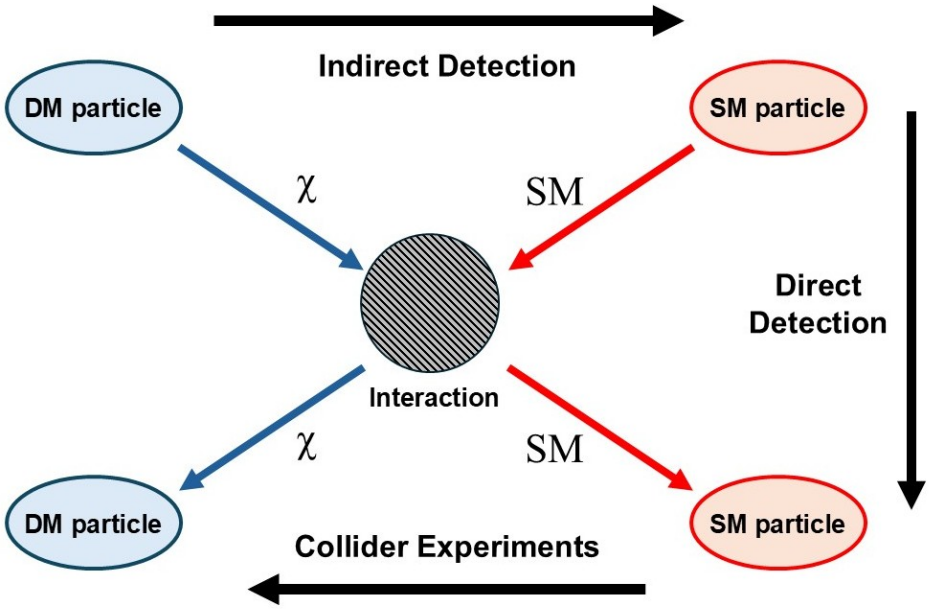

Figure 1.4: Scheme of the three main detection strategies for DM via non-gravitational interactions. In direct production (collider experiments) SM particles collide and create DM particles; in indirect detection DM particles annihilate and produce SM particles; in direct detection DM particles scatter off SM particles.

or neutrinos [55]; in these cases, an evidence for DM would be a monochromatic beam in the cosmic ray spectrum.
Another possible discovery channel is an excess of the neutrino flux from the Sun; with neutrinos produced by the annihilation of DM particles gravitationally captured by the Sun [56].
One of the main challenges of an indirect detection is the distinction between the flux of the DM annihilation products and the background coming from other astrophysical sources. Also, when observing charged particles, assigning the observation to a particular source can be difficult, since such particles can get deflected and diffused by galactic magnetic fields or scatterings [57].

Direct Detection Direct detection is based on the search for interactions between incident DM particles from the DM halo enveloping the Milky Way and SM particles within a target in an Earth-based detector [58, 59, 60].
The idea of detecting dark matter particles directly by observing their scattering with atomic nuclei was born from the proposal of using an analogous approach to spot neutrinos, and was then applied to WIMPs in the GeV mass range, since such particles would induce keV-scale nuclear recoils at observable rates [61, 62]. As the Earth orbits the Sun, the velocity of our detector through the galactic dark matter halo changes slightly over

the year, leading to a small but predictable annual modulation in the event rate; this is a powerful tool to distinguish a true dark matter signal from background events [63].
The DAMA collaboration reported a modulation in their sodium-iodide (NaI) crystals, finding a yearly period and a peak in the days that one would expect from a dark matter wind. DAMA/NaI and its successor DAMA/LIBRA have since confirmed this modulation through over twenty annual cycles, with a statistical significance of 13.7σ [64, 32]. Yet, other NaI-based searches like DM-Ice17 [65], ANAIS-112 [66] and COSINE-100 [67], as well as liquid-xenon and other target experiments, have failed to see a matching effect [68].
Modern direct-detection experiments, which can be divided in two categories, crystal targets and liquid noble targets, employ a "two-channel" readout strategy to reject background events and isolate potential dark matter recoils. In cryogenic solid-state detectors—such as EDELWEISS [33] (using germanium) and CDMS [35] (using silicon and germanium), both the ionization charge and the temperature rise (due to phonons) from a recoil are measured simultaneously. The next-generation SuperCDMS [69] experiment, now at SNOLAB, continues to refine this approach. A related method is used by CRESST [34], where scintillation photons and phonons in calcium-tungstate crystals are recorded simultaneously. Meanwhile, large liquid-noble time-projection chambers like XENON [70], LUX [71], PandaX [72] (xenon) and DarkSide [73] (argon) detect both the prompt scintillation light and a second time-delayed scintillation pulse induced by a ionization charge, allowing three-dimensional event reconstruction and exceptional discrimination between nuclear recoils and electron-recoil backgrounds. Other direct detection searches experiments include Ref.s [74, 75, 76, 77].
As the hunt for ever-weaker dark matter interactions intensified, it became clear that significantly larger detector masses were required, yet scaling solid-state cryogenic detectors beyond the kilogram scale proved prohibitively expensive and exacerbated issues related to background contamination. For liquid noble targets, it is easier to up-scale the detector mass, but despite the rapidly increasing target masses, now reaching the multi-tonne scale, and the steadily improving sensitivity that ruled out progressively smaller WIMP cross sections, no unambiguous evidence for dark matter has been obtained in terrestrial experiments.
Due to the lack of detection, a shift from the traditional GeV-scale WIMP framework toward lighter sub-GeV DM candidates emerged in the scientific community. Conventional nuclear-recoil experiments are ineffective for DM masses below a few GeV due to a combination of factors: the resulting energy depositions often fall below the detector thresholds, and the overall detection efficiency is substantially reduced in this low-energy regime. To extend sensitivity into the sub-GeV regime, novel ideas have been pursued [78]: exploiting

the Migdal effect whereby a nuclear scatter can ionize an atomic electron [79], or directly targeting dark matter–electron scattering, in which MeV-scale particles can impart nearly their full kinetic energy to bound electrons, resulting in ionization [80]. Beyond these, an array of cutting-edge proposals, ranging from scintillators optimized for electron recoils and two-dimensional directional targets like graphene [81] to superfluid helium detectors [82], superconducting sensors [83], and many other possibilities are under active development, broadening the scope of direct detection well beyond the classic nuclear-recoil approach [84]. We will now focus on the formalism of direct detection experiments.

1.3 Direct Detection Scattering Rates

In a typical direct detection experiment for Dark Matter, we look for the energy and momentum that are deposited in the target material via a given interaction mechanism. To build and characterize a similar experiment, an evaluation of the expected number of events in the target must be performed. To this end the scattering rate per unit of target mass and time must be evaluated. In the following we adopt mostly the formalism used in Ref. [85]. Using the Fermi's Golden Rule its expression is [86]:

$$R(t) = \frac{1}{\rho_{\mathrm{T}}} \frac{\rho_\chi}{m_\chi} \int d^3\mathbf{v}\ f_\chi(\mathbf{v};t) \int \frac{V d^3\mathbf{p}'_\chi}{(2\pi)^3} \times \\ \times \sum_f |\langle f, \mathbf{p}'_\chi | \Delta H_{\chi \mathrm{T}} | i, \mathbf{p}_\chi \rangle|^2\ 2\pi\delta(E_f - E_i + E'_\chi - E_\chi)\ . \tag{1.9}$$

Let's describe the different elements in this expression. We are considering an arbitrary detector of volume V and density ρ_{T}; the mass of the DM particle is described by m_χ, while ρ_χ is the DM mass density, which has been inferred from gravitational measurements obtaining $\rho_\chi \simeq 0.3 - 0.5$ GeV/cm^3. The DM velocity distribution in the laboratory frame is described by $f_\chi(\mathbf{v};t)$, which we will discuss in the following subsection. The interaction between the DM particles and the target is described by the non-relativistic interaction Hamiltonian $\Delta H_{\chi \mathrm{T}}$; $|i\rangle$ and $|f\rangle$ are the initial and final detection states, with energy E_i and E_f, respectively. As we will show in the following chapters, depending on the scattering process that is used in a given DM direct detection experiment, these quantities will change accordingly.

Since DM detection experiments generally operate at very low temperatures, to reduce thermal noise, we can consider the system to be in its ground state; a sum over an ensemble of initial states is thus not needed.

For the DM eigenstates we can consider them to be plane waves, eigenstates of the free-particle DM Hamiltonian, in the form $|\mathbf{p}_\chi\rangle = e^{i\mathbf{p}_\chi \cdot \mathbf{r}}/\sqrt{V}$. The DM particle energy is

described by E_χ and E'_χ before and after the scattering, respectively. Assuming no entanglement between the DM and the target we have $|i, \mathbf{p}_\chi\rangle \equiv |i\rangle \otimes |\mathbf{p}_\chi\rangle$, and similarly for $|f, \mathbf{p}'_\chi\rangle$. Notice that we are making no assumptions about the DM spin.
To further simplify our expression, we assume that one operator $\mathcal{O}$ in $\Delta H_{\chi\mathrm{T}}$ is more dominant, which can be factorized in $\mathcal{O}_\chi$ and $\mathcal{O}_\mathrm{T}$ that only act on DM and target systems states respectively. Then the matrix element of the interaction Hamiltonian can be factorized into Fourier components:

$$\langle f, \mathbf{p}'_\chi|\Delta H_{\chi\mathrm{T}}|i, \mathbf{p}_\chi\rangle \equiv \int \frac{d^3\mathbf{q}}{(2\pi)^3}\ \langle \mathbf{p}'_\chi|\mathcal{O}_\chi(\mathbf{q})|\mathbf{p}_\chi\rangle \times \langle f|\mathcal{O}_\mathrm{T}(\mathbf{q})|i\rangle\ . \tag{1.10}$$

By using the plane wave expressions for $|\mathbf{p}_\chi\rangle$ and $|\mathbf{p}'_\chi\rangle$, we will obtain the momentum conservation $\mathbf{q} = \mathbf{p}_\chi - \mathbf{p}'_\chi$, and the matrix element will reduce to:

$$\langle f, \mathbf{p}'_\chi|\Delta H_{\chi\mathrm{T}}|i, \mathbf{p}_\chi\rangle = \frac{1}{V}\sqrt{\frac{\pi\bar{\sigma}(q)}{\mu_\chi^2}}\langle f|\mathcal{O}_\mathrm{T}(\mathbf{q})|i\rangle\ ; \tag{1.11}$$

were $(\pi\bar{\sigma}(q)/\mu_\chi^2)^{1/2}$ is the interaction strength written in terms of a cross section $\bar{\sigma}(q)$ and the reduced mass μ_χ, which will depend on the specific scattering process.
As a final step we want to rewrite the rate expression by introducing an auxiliary variable ω and integrating over ω with the delta function $\delta(\omega + E'_\chi - E_\chi)$:

$$\begin{aligned} R(t) = \frac{1}{\rho_\mathrm{T}}\frac{\rho_\chi}{m_\chi}\int d^3\mathbf{v}\ f_\chi(\mathbf{v};t)\int\frac{V d^3\mathbf{p}'_\chi}{(2\pi)^3}\int d\omega\ \delta(\omega + E'_\chi - E_\chi)\times \\ \times\sum_f \frac{1}{V^2}\frac{\pi\bar{\sigma}(q)}{\mu_\chi^2}|\langle f|\mathcal{O}_\mathrm{T}(\mathbf{q})|i\rangle|^2\ 2\pi\delta(E_f - E_i - \omega)\ . \end{aligned} \tag{1.12}$$

We now swap the integration over $\mathbf{q}$ and $\mathbf{p}'_\chi$ using the momentum conservation for the DM and define the dynamic structure factor $S(\mathbf{q}, \omega)$, which fully contains the information on the target response:

$$S(\mathbf{q},\omega) = \frac{2\pi}{V}\sum_f\ |\langle f|\mathcal{O}_\mathrm{T}(\mathbf{q})|i\rangle|^2\ \delta(E_f - E_i - \omega)\ . \tag{1.13}$$

We then obtain the following final expression for the rate:

$$R(t) = \frac{1}{\rho_\mathrm{T}}\frac{\rho_\chi}{m_\chi}\int d^3\mathbf{v}\ f_\chi(\mathbf{v};t)\int\frac{d^3\mathbf{q}}{(2\pi)^3}\int d\omega\ \delta(\omega + E'_\chi - E_\chi)\frac{\pi\bar{\sigma}(q)}{\mu_\chi^2}\ S(\mathbf{q},\omega)\ . \tag{1.14}$$

To obtain the rate, we weight the target response by the DM potential strength, and integrate over the phase space in terms of the momentum transferred $\mathbf{q}$ and deposited

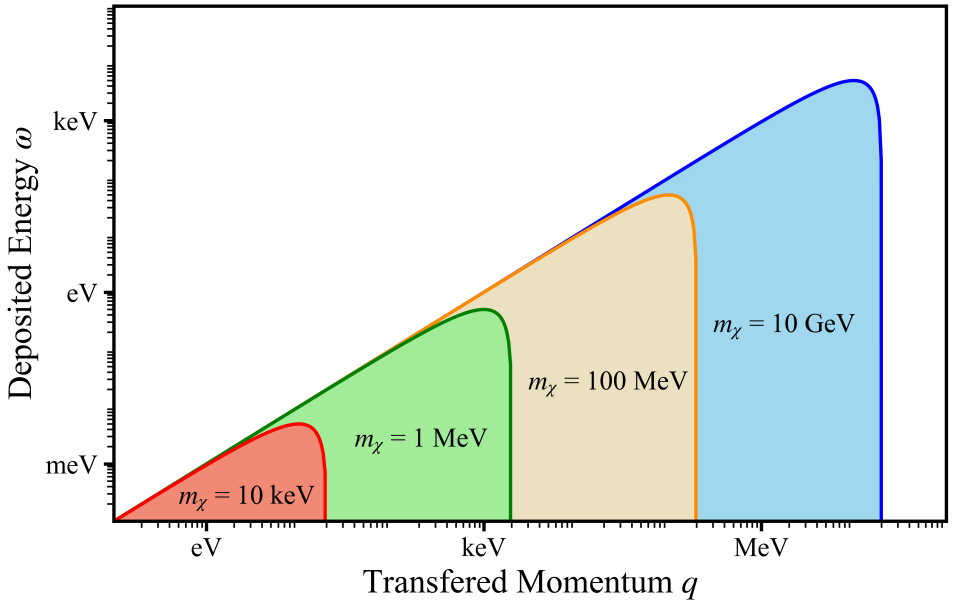

Figure 1.5: Phase-space ω-q that are kinematically allowed, for $v = 10^{-3}$ and different DM masses.

energy ω by the DM, and the DM velocity distribution. Eq. (1.14) will be the starting point for the derivation of the scattering rate for different scattering processes.

1.3.1 Scattering Kinematics and Dark Matter Halo

The DM phase space integration region is dictated by the kinematics of the scattering; we then want to relate the deposited energy with the transferred momentum.
The incoming DM particle with momentum $\mathbf{p}_\chi = m_\chi \mathbf{v}$ scatters off a detector target and exits with momentum $\mathbf{p}'_\chi$, since the DM particle is non-relativistic its energy is $E_\chi = p_\chi^2/2m_\chi$ and $E'_\chi = p_\chi'^2/2m_\chi$ before and after the scattering respectively. We can write the energy deposited in the target $\omega_\mathbf{q}$ in terms of the momentum transfer $\mathbf{q} = \mathbf{p}_\chi - \mathbf{p}'_\chi$:

$$\omega_\mathbf{q} = E_\chi - E'_\chi = \frac{1}{2} m_\chi v^2 - \frac{(m_\chi \mathbf{v} - \mathbf{q})^2}{2m_\chi} = \mathbf{q}\cdot\mathbf{v} - \frac{q^2}{2m_\chi} \,. \tag{1.15}$$

Eq. (1.15) defines the region in ω and $\mathbf{q}$ that is kinematically allowed for DM scattering as a function of the DM mass and velocity. In Fig. 1.5 we report the kinematically allowed region in the ω-q plane for a fixed velocity of $v = 10^{-3}$ and different DM masses. The upper boundary of these regions is described by an inverted parabola which corresponds to forward scattering, $\mathbf{q}\cdot\mathbf{v} = qv$, and gives the largest possible energy deposit ω for a given q.
The apex of the parabola corresponds to scattering events where the target absorbs all of the incoming DM particle kinetic energy: $\mathbf{p}'_\chi = 0$, $q = m_\chi v$ and $\omega = \frac{1}{2} m_\chi v^2$. Finally, the

right boundary of the curve corresponds to the maximum momentum transfer, which is given by the elastic back-scattering for which $\mathbf{p}'_\chi = -\mathbf{p}_\chi$ and $\omega_{\mathbf{q}} \to 0$.
The information we just discussed has been found by fixing the incoming DM particle speed to a fixed value, but the possible speed values for the DM particles are described by the DM velocity distribution $f_\chi(\mathbf{v})$.
We can define an important quantity starting from Eq. (1.15) when considering the case $\mathbf{q} \parallel \mathbf{v}$, which is the minimum DM initial speed needed to produce an event with transferred energy ω and transferred momentum q:

$$v_{\min}(q,\omega) = \frac{\omega}{q} + \frac{q}{2m_\chi} \ . \tag{1.16}$$

Using this quantity we can define the mean inverse DM speed:

$$\eta(v_{\min};t) = \int_{v\geq v_{\min}} d^3\mathbf{v} \ \frac{f_\chi(\mathbf{v};t)}{v} \tag{1.17}$$

which we can use to write the rate from Eq. (1.14) in the isotropic approximation, in which we assume that the dynamic structure factor depends only on q and not on $\mathbf{q}$, $S(\mathbf{q},\omega) = S(q,\omega)$. Then:

$$\begin{aligned} &\int \frac{dq\ q^2}{(2\pi)^3} \int d\phi \int d\theta \sin(\theta) \int d\omega \ \delta\Big(\omega - \big(\mathbf{v}\cdot\mathbf{q} + \frac{q^2}{2m_\chi}\big)\Big)\Big[\dots\Big] \ = \\ &\int \frac{dq\ q^2}{(2\pi)^3} \int d\omega \ (2\pi) \ \int_{-1}^{1} d\cos(\theta) \ \delta\Big(vq\cos(\theta) - \omega - \frac{q^2}{2m_\chi}\Big)\Big[\dots\Big] \ ; \end{aligned} \tag{1.18}$$

if we now substitute $\mu = \cos(\theta)$ and find the root of the function inside the δ, $\mu_0 = \frac{\omega}{qv} + \frac{q}{2m_\chi v}$, we can use the property of the δ function $\delta\big(vq\mu - \omega - \frac{q^2}{2m_\chi}\big) = \frac{1}{qv}\delta(\mu - \mu_0)$. We then reach the result:

$$\int_{-1}^{1} d\mu \ \delta\big(vq\mu - \omega - \frac{q^2}{2m_\chi}\big) = \frac{1}{qv}\Theta\big(1 - |\mu_0|\big) \ ; \tag{1.19}$$

where the Heaviside step function enforces that the root of the δ function must be inside the integration range for it to have a non-zero integral. We can immediately see that the condition $|\mu_0| \leq 1$ corresponds to $v \geq v_{\min}$. Substituting these results in Eq. (1.14) we finally obtain the isotropic rate:

$$R^{\text{iso}}(t) = \frac{1}{\rho_{\text{T}}}\frac{\rho_\chi}{m_\chi}\int \frac{dq\ q}{(2\pi)^2}\int d\omega \ \eta(v_{\min}(q,\omega);t) \ \frac{\pi\bar{\sigma}(q)}{\mu_\chi^2} \ S(q,\omega) \ . \tag{1.20}$$

We have now shown a general expression for the DM scattering rate both in case of an isotropic (Eq. (1.20)) and anisotropic (Eq. (1.14)) target response, but several quantities

are yet to be defined, one of these is the DM velocity distribution.

Standard Halo Model The DM velocity distribution is for itself an active field of research, with different models that are creating comparing astrometry data, simulations of many-body gravitational dynamics and analytical arguments. Nonetheless, it is useful to adopt simple models that can be used when benchmarking different direct detection experiments. To this end, the most commonly used model is the "Standard Halo Model" (SHM), which describes the dark matter halo as a gas of gravitationally interacting particles at equilibrium, and, consequently, as an isotropic and isothermal halo [87, 63].
In this model the DM density distribution behaves like $\rho(r) \propto 1/r^2$, which is called "isothermal sphere" model and the resulting velocity distribution will follow the characteristic trend of the Maxwell-Boltzmann distribution:

$$f_{\mathrm{SHM}}(\mathbf{v}) \propto e^{-\frac{|\mathbf{v}|^2}{2\sigma_v^2}} \ . \tag{1.21}$$

However, a correction is necessary; in the current halo distribution of dark matter, there cannot be any particles with velocities above the escape velocity of the galaxy, or they would have long since left the galaxy.
The distribution is therefore truncated, becoming:

$$f_{\mathrm{SHM}}(\mathbf{v}) = \frac{1}{(2\pi\sigma_v^2)^{\frac{3}{2}} N_{\mathrm{esc}}} e^{-\frac{|\mathbf{v}|^2}{2\sigma_v^2}} \ \Theta(v_{\mathrm{esc}} - |\mathbf{v}|) \ , \tag{1.22}$$

where Θ is the Heaviside step function, and N_{esc} a normalization constant due to truncation of the distribution:

$$N_{\mathrm{esc}} = \mathrm{erf}\left(\frac{v_{\mathrm{esc}}}{\sqrt{2}\sigma_v}\right) - \sqrt{\frac{2}{\pi}} \frac{v_{\mathrm{esc}}}{\sigma_v} e^{-\frac{v_{\mathrm{esc}}^2}{2\sigma_v^2}} \ . \tag{1.23}$$

Commonly used values for the galactic escape velocity v_{esc} and the velocity dispersion σ_v are $v_{\mathrm{esc}} \approx 528$ km/s and $\sigma_v = \frac{v0}{\sqrt{2}} \approx 165$ km/s with $v0 \approx 233$ km/s the mean DM speed.
Now, while the SHM velocity distribution is isotropic in the galactic rest frame, direct detection experiments are performed in terrestrial laboratories. We thus need the velocity distribution in the lab-frame $f_\chi(\mathbf{v})$, which can be obtained by performing a Galilean boost along the laboratory's velocity $\mathbf{v}_{\mathrm{lab}}$ of the galactic rest frame distribution $f_{\mathrm{SHM}}(\mathbf{v})$:

$$f_\chi(\mathbf{v}; t) = f_{\mathrm{SHM}}(\mathbf{v} + \mathbf{v}_{\mathrm{lab}}(t)) = \frac{1}{(2\pi\sigma_v^2)^{\frac{3}{2}} N_{\mathrm{esc}}} e^{-\frac{|\mathbf{v}+\mathbf{v}_{\mathrm{lab}}(t)|^2}{2\sigma_v^2}} \ \Theta(v_{\mathrm{esc}} - |\mathbf{v} + \mathbf{v}_{\mathrm{lab}}(t)|) \ . \tag{1.24}$$

The laboratory's velocity in the galactic frame can be written as: $\mathbf{v}_{\rm lab}(t) = \mathbf{v}_\odot + \mathbf{v}_{\rm orbit}(t) + \mathbf{v}_{\rm rot}(t) = \mathbf{v}_\oplus(t) + \mathbf{v}_{\rm rot}(t)$, which is the composition of the Sun's velocity in the galactic frame $\mathbf{v}_\odot$, Earth's velocity with respect to the Sun $\mathbf{v}_{\rm orbit}(t)$, which describes Earth's revolution, and the laboratory motion with respect to Earth's center $\mathbf{v}_{\rm rot}$(t), which describes Earth's rotation. The main effect of this transformation is the loss of isotropy of the distribution, causing what is referred to as the "Dark Matter Wind"; more and faster particles will hit Earth from its direction of travel. The lab-frame distribution will also acquire a time dependency due to the yearly motion of Earth around the Sun (annual modulation) and due to Earth rotation over the 24 hour (daily modulation).
Since Earth velocity with respect to the Sun is about $v_{\rm orbit} \approx 30$ km/s, the annual modulation induces a $\sim 10\%$ change in both the DM flux and the high-velocity cutoff of the distribution, depending on the time of the year. In particular, a signal peak is expected around early June, when the Earth's velocity is parallel to that of the Sun, $\mathbf{v}_{\rm orbit} \parallel \mathbf{v}_\odot$, and thus the relative velocity with respect to the center of the galaxy is maximal; in December, on the other hand, a signal minimum is expected, since the Earth's velocity will be antiparallel to that of the Sun, $\mathbf{v}_{\rm orbit} \nparallel \mathbf{v}_\odot$, and thus the relative velocity between Earth and the galactic center is minimal.
In contrast, the linear velocity of the Earth's surface is $v_{\rm rot,eq} \approx 0.5$ km/s at the equator, so the daily modulation does not affect the speed or flux, but it does change the direction of the mean DM velocity. This effect will be particularly relevant for experiments that are sensitive to the direction of the DM "wind", since the event rate will also have a daily modulation. More information on the reference frame and the different velocity terms is reported in Appendix A.1.1 and A.2. It can be useful to define the following function, by absorbing the energy-conserving delta function into the velocity distribution:

$$g(\mathbf{q},\omega;t) \equiv \int d^3\mathbf{v}\ f_\chi(\mathbf{v};t)\ \delta(\omega - \omega_{\mathbf{q}}) = \int d^3\mathbf{v}\ f_{\rm SHM}(\mathbf{v} + \mathbf{v}_{\rm lab}(t))\ \delta(\omega - \omega_{\mathbf{q}}); \qquad (1.25)$$

this function represents the anisotropic analogue of $\eta(v_{\rm min};t)$. Using $g(\mathbf{q},\omega;t)$ we can rewrite the rate from Eq. (1.14) as:

$$R(t) = \frac{1}{\rho_{\rm T}}\frac{\rho_\chi}{m_\chi}\int \frac{d^3\mathbf{q}}{(2\pi)^3}\int d\omega\ g(\mathbf{q},\omega;t)\ \frac{\pi\bar{\sigma}(q)}{\mu_\chi^2}\ S(\mathbf{q},\omega)\ . \qquad (1.26)$$

The marginal speed distribution can be another important quantity, particularly when the directional information is not relevant. It can be derived by integrating out the velocity

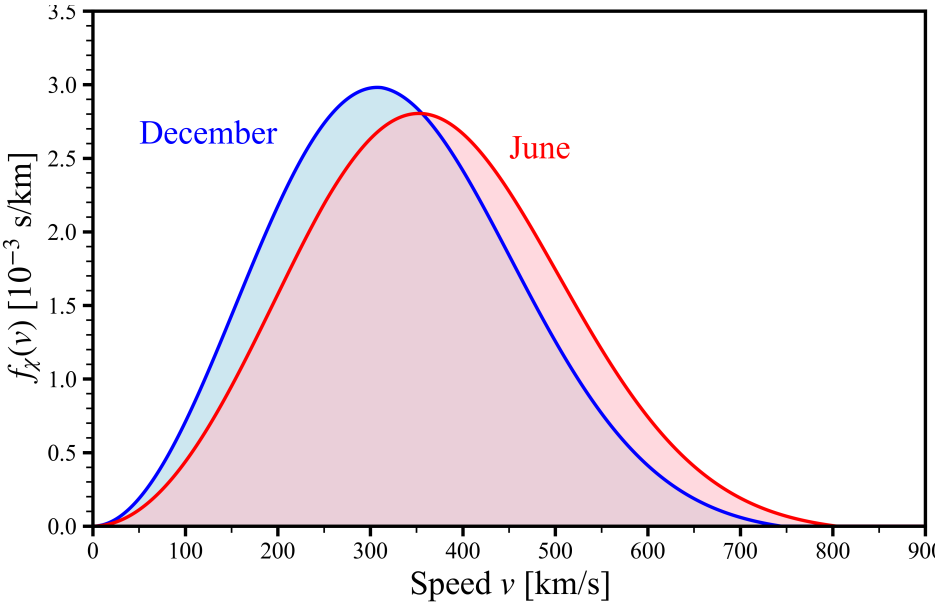

Figure 1.6: SHM marginal speed distribution of DM in the months of December and June.

angles:

$$
\begin{aligned}
f_\chi(v;t) &= \int d\Omega\; v^2 f_\chi(\mathbf{v};t) = \int d\Omega\; v^2 f_{\rm SHM}(\mathbf{v}+\mathbf{v}_{\rm lab}(t)) = \\
&= \frac{1}{N_{\rm esc}} \frac{v}{\sqrt{\pi} v_0 v_{\rm lab}(t)} \Bigg[2 \exp\left(- \frac{v^2 + v_{\rm lab}(t)^2}{v_0^2} \right) \sinh\left(2 \frac{v v_{\rm lab}(t)}{v_0^2} \right) \\
&+ \left(\exp\left(- \frac{(v + v_{\rm lab}(t))^2}{v_0^2} \right) - \exp\left(- \frac{v_{\rm esc}^2}{v_0^2} \right) \right) \Theta(|v + v_{\rm lab}(t)| - v_{\rm esc}) \\
&- \left(\exp\left(- \frac{(v - v_{\rm lab}(t))^2}{v_0^2} \right) - \exp\left(- \frac{v_{\rm esc}^2}{v_0^2} \right) \right) \Theta(|v - v_{\rm lab}(t)| - v_{\rm esc}) \Bigg] \,.
\end{aligned}
\tag{1.27}
$$

To showcase the effect of annual modulation on the velocity distribution, in Fig. 1.6 we report the marginal speed distribution (neglecting the daily modulation due to $\mathbf{v}_{\rm rot}$) for the months of December, $v_\oplus = v_\odot - v_{\rm orbit}$, and June, $v_\oplus = v_\odot + v_{\rm orbit}$, where $v_\odot = 246$ km/s is the Solar speed in the galactic frame and $v_{\rm orbit} = 30$ km/s is Earth's revolution speed. A derivation of Eq. (1.27) and the calculation of $\eta(v_{\rm min};t)$ in the SHM are reported in Appendix B.1 and B.2, respectively.

1.3.2 Scattering Dynamics

In this subsection we want to discuss briefly the dynamics of the DM interactions, which appear in the scattering rate and arise from the term $\langle f, \mathbf{p}'_\chi | \Delta H_{\chi Q} | i, \mathbf{p}_\chi \rangle$ of Eq. (1.9). To do so we are going to consider one of the interaction models frequently used to describe

the DM-SM particles interactions: the dark photon [88, 89].
In the dark photon model, the DM particle has a charge g_D in a "dark" version of electromagnetism, mediated by the so-called dark photon, which is denoted as A' and has a mass $m_{A'}$. The ordinary photon and the dark photon may mix, with the mixing described by the kinetic mixing parameter $\epsilon \ll 1$; this implies that particles with an electromagnetic charge Qe also have a dark photon charge ϵQe. The dark photon couplings with the DM and charged particles allow for thermal contact between DM and SM, which is required to have the correct relic abundance of DM in the modern Universe.
In the non-relativistic limit, the dark photon model presents the following interaction Hamiltonian between DM and charged particles:

$$\Delta H_{\chi Q} = \int \frac{d^3\mathbf{q}}{(2\pi)^3}\, e^{i\mathbf{q}\cdot(\mathbf{r}_Q - \mathbf{r}_\chi)}\, \frac{\epsilon Q e g_D}{q^2 + m_{A'}^2}\ ; \tag{1.28}$$

where $\mathbf{r}_Q$ is the position operator for a particle with electric charge Qe, $\mathbf{r}_\chi$ is the DM position operator and g_D is the dark charge.
Using the fact that the potential is translationally invariant, since it depends only on the relative coordinate $\mathbf{r}_Q - \mathbf{r}_\chi$, we can evaluate the interaction Hamiltonian matrix element between plane-wave DM states:

$$\begin{aligned}\langle \mathbf{p}'_\chi | \Delta H_{\chi Q} | \mathbf{p}_\chi \rangle &= \int \frac{d^3\mathbf{q}}{(2\pi)^3} \int \frac{d^3\mathbf{r}_\chi}{V}\, e^{i(\mathbf{p}_\chi - \mathbf{p}'_\chi)\cdot \mathbf{r}_\chi}\, e^{i\mathbf{q}\cdot(\mathbf{r}_Q - \mathbf{r}_\chi)} \frac{\epsilon Q e g_D}{q^2 + m_{A'}^2} = \\ &= \frac{1}{V} \frac{\epsilon Q e g_D}{q^2 + m_{A'}^2} e^{i\mathbf{q}\cdot\mathbf{r}_Q}\ ;\end{aligned} \tag{1.29}$$

with the integration over the DM coordinates that leads to the momentum conservation $\mathbf{q} = \mathbf{p}_\chi - \mathbf{p}'_\chi$. The matrix element $\langle f, \mathbf{p}'_\chi | \Delta H_{\chi Q} | i, \mathbf{p}_\chi \rangle$ will then have a factorized form:

$$\langle f, \mathbf{p}'_\chi | \Delta H_{\chi Q} | i, \mathbf{p}_\chi \rangle = \frac{1}{V} \frac{\epsilon Q e g_D}{q^2 + m_{A'}^2} \langle f | e^{i\mathbf{q}\cdot\mathbf{r}_Q} | i \rangle = \frac{1}{V} \mathcal{V}(q) \langle f | e^{i\mathbf{q}\cdot\mathbf{r}_Q} | i \rangle\ ; \tag{1.30}$$

where $\mathcal{V}(q)$ is called scattering potential. From Eq. (1.30) we can see that, when compared with Eq. (1.11), $\mathcal{O}_T(\mathbf{q}) = e^{i\mathbf{q}\cdot\mathbf{r}_Q}$ and the cross section $\bar{\sigma}(q)$ is:

$$\bar{\sigma}(q) = \frac{\mu_{T\chi}^2}{\pi} \left(\frac{\epsilon Q e g_D}{q^2 + m_{A'}^2} \right)^2\ ; \tag{1.31}$$

where $\mu_{\chi T} = \frac{m_\chi m_T}{m_\chi + m_T}$ is the DM-target reduced mass, for a proton or electron $m_T = m_p$ or m_e, respectively. It is common to rewrite $\bar{\sigma}(q) = \bar{\sigma}_T \cdot |F_{DM}(q)|^2$, where $\bar{\sigma}_T$ is the fiducial cross section at a fixed momentum q_0 and $F_{DM}(q)$ is the momentum-dependent DM form

factor:

$$F_{DM}(q) = \frac{q_0^2 + m_{A'}^2}{q^2 + m_{A'}^2} \; ; \tag{1.32}$$

which parametrizes the momentum dependence of the scattering potential. The DM form factor presents two limits, one for a heavy mediator (or massive mediator), $m_A \to \infty$, $F_{DM} \to 1$, one for a light mediator (or massless mediator), $m_A \to 0$, $F_{DM} \to (q_0/q)^2$. These two limiting cases span the full range of possibilities for the scattering amplitude. Notice that the heavy mediator limit is equivalent to a contact interaction in the spatial coordinates. Depending on the target, the reference momentum used in $\bar{\sigma}_T$ and $F_{DM}(q)$ is chosen accordingly; for $T = e$, $\bar{\sigma}_e$ represents the cross section of a DM particle scattering off a free electron, with reference momentum q_0, typically chosen as the inverse Bohr radius $q_0 = 1/a_0 = \alpha m_e \simeq 3.7keV$. For $T = p$, $\bar{\sigma}_p$ is the DM-proton cross section at an arbitrary reference momentum q_0, often taken as $q_0 = m_\chi v_0$.
Depending on the specific model, the requirements needed for the production mechanism of dark matter in the early Universe will lead to a restriction of the range of allowed masses for the DM particle and predict a typical cross section; from these values, direct detection experiments can be designed accordingly, to be sensitive in the desired region of the parameter space.
The dark photon model is not the only model that describes a possible interaction between DM and SM particles; however, following the previously shown steps, one can write a complete expression for the scattering rate in terms a fiducial cross section, predict an expected range for the DM mass, and setup a detection experiment accordingly.

1.3.3 Detector Effects and Exclusion limits

In the previous sections we have discussed most of the elements that allow us to calculate the DM scattering rate; but these results are the theoretical rates and in real experiments several factors can intervene, like detector effects.
A real detector, for example, has a finite energy threshold under which it is not capable of detecting any events. To take this effect into account, we can modify the lower bound of the integration in ω and set it to the threshold value ω_{thresh}. In this way we will compute only the number of events with a deposited energy greater than the detector threshold value.
Additionally, one can study the detection efficiency as a function of the deposited energy $\epsilon(\omega)$, which is a real number going from 1 to 0, and represents the fraction of events in the detector with certain deposited energy that will be detected. The rate as seen from

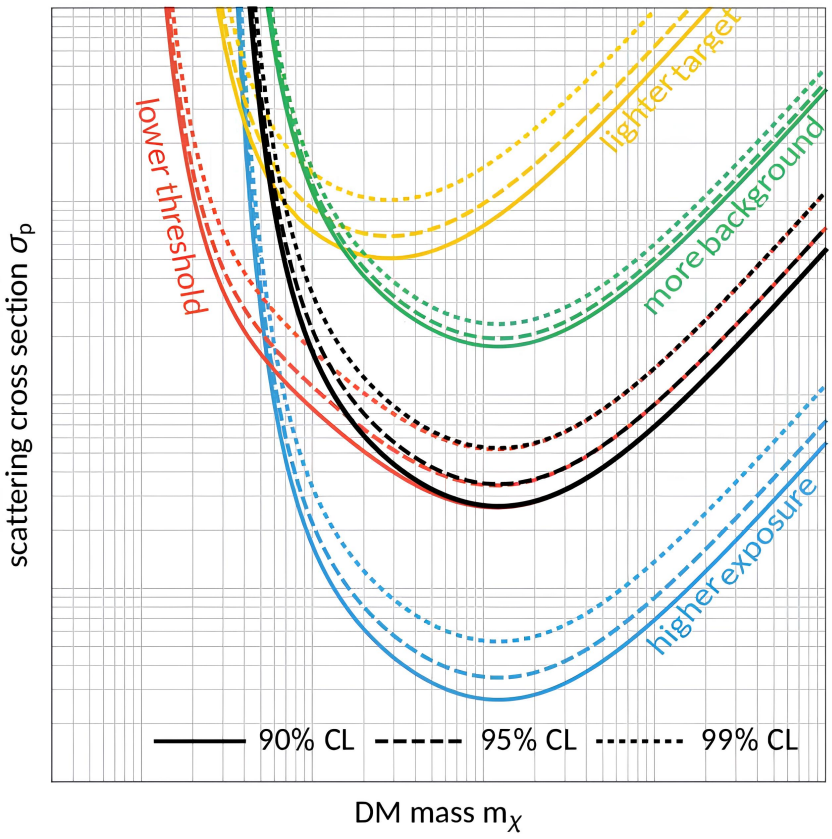

Figure 1.7: Generic exclusion limits in a direct detection experiment. Starting from a reference curve (black) the scaling with respect to different parameters is shown by the different sets of curves (figure from Ref. [90]).

the detector R_{D} can then be written as:

$$R_{\mathrm{D}} = \int_{\omega_{\mathrm{thresh}}}^{\omega_{\mathrm{max}}} d\omega \; \epsilon(\omega) \; \frac{\partial R}{\partial \omega} \; , \tag{1.33}$$

with the differential rate taken from one of the expressions previously seen, e.g. Eq. (1.14). More sophisticated approaches can include a convolution of the differential rate with a kernel describing the detector response function.
Once the signal event rate is computed, the total number of events N expected to happen in an experiment will be given by:

$$N = \mathcal{E} \cdot R \; ; \tag{1.34}$$

where $\mathcal{E}$ is called exposure, and is the product of the target mass and the run-time of the experiment. If the time dependency of the rate is taken into account, to obtain the expected number of events we integrate $R(t)$ over the experiment run-time and multiply the result with the target mass. In the isotropic approximation, for a time independent

rate we can substitute the laboratory's speed in the galactic frame with Sun's speed in the galactic frame, $v_{\rm lab}(t) \to v_{\odot}$, removing the time-dependent orbital and rotational terms.
After a DM direct detection experiment is performed the observed events $N_{\rm obs}$ must be interpreted statistically, comparing them to theoretically predicted number of events N.
No direct detection experiments have yet succeeded in observing a clear DM signal; interpreting these null results becomes, then, fundamental to perform exclusion limits on the DM physical parameters, in particular to exclude regions of the σ-m_{χ} parameter space, for which the experiment was expected to obtain positive results. In Fig. 1.7, the behavior of the exclusion limits as a function of different parameters, like the exposure, the background and the threshold are shown.
One of the main challenges in the analysis of an experiments results is understanding the background: events that can trigger the detector and that must be separated from the desired DM signal. To do so, a reliable background model must be constructed, so that a number of observed signals will be attributed to the background; this is called background subtraction [91].
Let's consider an experiment in which the detector counts events and measures their deposited energies. The Poisson distribution will describe the probability of observing n events for an expected value of μ [92]:

$$P(n|\mu) = \frac{\mu^n}{n!} e^{-\mu} \ . \tag{1.35}$$

We can now define the Confidence Level (CL):

$$\mathrm{CL} = P(n > N_{\rm obs}) = \sum_{n=N_{\rm obs}+1}^{\infty} \frac{\mu^n}{n!} e^{-\mu} = 1 - \mathrm{CDF}(N_{\rm obs}|\mu) \ ; \tag{1.36}$$

where CDF is the Poisson Cumulative Distribution Function.
If a set of parameters predicts that an experiment should have observed more events than it actually did, with a certain CL, then this parameter space point can be excluded by that CL.
To better understand this concept, let's consider an experiment in which no events were observed, $N_{\rm obs} = 0$, and in a background-less condition (the number of expected background events b is null). We want to exclude the regions of the parameters space for which the number of predicted DM events s is so incompatible with the observations that those regions can be excluded with a confidence level of 95%, CL=0.95.

To do so we need to invert Eq. (1.36) and find the solution for μ:

$$\mathrm{CDF}(0|\mu) = P(n \leq 0|\mu) = \sum_{n=0}^{N_{\mathrm{obs}}=0} \frac{\mu^n}{n!} e^{-\mu} = \frac{\mu^0}{0!} e^{-\mu} = e^{-\mu} = 1 - \mathrm{CL} \ ; \tag{1.37}$$

which will result in:

$$\mu = \ln\left(\frac{1}{1-\mathrm{CL}}\right) . \tag{1.38}$$

In the case of CL=0.95, Eq. (1.38) will result in $\mu_{95\%} \approx 3$. We can then state that, in our background-less experiment in which no events were measured, all the regions of the parameter space σ-m_χ that predict an expected number of signal events N greater than $\mu_{95\%}$ are incompatible with the experiment and can be excluded with a 95% confidence level.

To see to which cross section this equates to, we compute the rate R using a reference cross section σ_{ref} for a given DM mass m_χ, then we can define the upper limit cross section σ_{UL} :

$$\sigma_{\mathrm{UL}} = \frac{\mu_{\mathrm{CL}}}{R \cdot \mathcal{E}} \sigma_{\mathrm{ref}} \ . \tag{1.39}$$

All the cross sections $\sigma > \sigma_{\mathrm{UL}}$ can then be excluded with a confidence level of CL.

If we now consider an experiment in which a number of background events b was expected, and no excess above background was measured, $N_{\mathrm{obs}} = b$, to perform the exclusion limit we have to solve the following equation:

$$P(n \leq b|\mu) = \sum_{n=0}^{b} \frac{\mu^n}{n!} e^{-\mu} = 1 - \mathrm{CL} \ . \tag{1.40}$$

In this case, the solution cannot be found through analytical inversion, but can be computed numerically. Let's consider a number of expected background events b=100 and a confidence level of CL=0.9, Eq. (1.40) will result in $\mu_{90\%} \approx 114$. This means that all the regions of the parameter space that predict a number of DM signal events greater than $s = \mu_{90\%} - b \approx 14$ can be excluded with a 90% confidence level.

In the more general case, the number of observed events is different from the expected number of background events; then Eq. (1.36) must be solved for $\mu = b + s$, and the regions that would result in a number of events N greater than s would be excluded.

A variation of this method is the $\mathrm{CL_s}$ method, which is defined by the equation:

$$\frac{P(n \leq N_{\mathrm{obs}}|s+b)}{P(n \leq N_{\mathrm{obs}}|b)} = 1 - \mathrm{CL} \ . \tag{1.41}$$

The denominator suppresses the exclusion power in regions in which the background itself does not explain the data well. This results in larger s values than the standard frequentist exclusion limit, making it more conservative; in our previous example where $N_{\text{obs}} = b = 100$, the method will predict $s \approx 18$, excluding regions that result in a number of predicted events larger than s with a 90% CL.
Both methods that we considered assume no knowledge about the expected spectrum or the background and interpret all observed events as DM signals of equal significance. These counting-only methods are then a more conservative way to obtain exclusion limits than other methods, like the Profile Likelihood Ratio test [93].
We now want to briefly comment on the relation between the upper limit cross section σ_{UL} and the experiment exposure $\mathcal{E}$. From Eq. (1.39) we can understand that in a background-less experiment, where $\mu_{\text{CL}} = s$, the upper limit cross section will be inversely proportional to the exposure, meaning that an experiment with higher exposure can exclude a greater region of the parameter space, so a more powerful result.
But if an irreducible background rate R_b is present, we expect a number of background events $b = R_b \cdot \mathcal{E}$ after an exposure $\mathcal{E}$. Now since the fluctuations in the background will scale as the square root of the number of background events $\sqrt{b}$, and the number of signal events must be larger than the typical background fluctuations to have statistically relevant results, the cross section upper limit will behave like:

$$\sigma \propto \frac{s}{\mathcal{E}} \sim \frac{\sqrt{R_b \cdot \mathcal{E}}}{\mathcal{E}} \propto \frac{1}{\sqrt{\mathcal{E}}} \ . \tag{1.42}$$

The limit cross section in the so called background-dominated regime, will than scale, not with the inverse of the exposure but with the inverse of the square root; this means that while the experiment will keep benefiting from an increase of the experiment exposure, it will do so less than in the background-less regime.
In general, if the background rate is very low, for small exposures you initially start in the background-free regime, and as you integrate longer (or scale up the target mass) you eventually accumulate enough background that the cross section limit transitions to the background-limited behaviour, with the turnover happening around the exposure where $R_b \cdot \mathcal{E}$.

After this section in which we have discussed the key elements of DM direct detection experiments, we will now focus on nuclear scattering events and thermal detectors, and study the specific case of defect formation in NaI crystals.

Chapter 2

Nuclear Scattering events and the Defect Formation in NaI Crystals

Direct detection experiments represent one of the most promising strategies to probe the particle nature of dark matter; and historically, and still today, the majority of such experiments are based on the search for nuclear recoils arising from the elastic scattering of DM particles off nuclei in a suitable target medium. All these experiments differ in the material used as a target, and the output channel used to read the DM event's signal, and see as their main challenges both the extremely low expected interaction rate and the need to distinguish possible DM-induced signals from a variety of backgrounds.
Despite significant efforts by the scientific community, no clear findings have yet been made regarding the direct detection of DM. Among the most discussed and relevant results in the field is the annual modulation signal observed by DAMA/LIBRA, achieved with a statistical significance of 13.7σ, using thallium-doped sodium iodide NaI(Tl) crystals as room temperature scintillating detectors [64, 94]. While the DAMA/LIBRA collaboration claims evidence for dark matter, their results remain highly controversial as numerous other direct detection experiments have set conflicting exclusion limits. However, excluding a DM explanation for the DAMA/LIBRA signal is challenging, as comparisons between experiments depend on assumptions about both the astrophysical distribution and particle physics properties of DM. These conclusions can be highly sensitive to these assumptions. An independent test of the DAMA/LIBRA result using NaI-based detectors would minimize the need for such assumptions [95].
In response to this long-standing tension, the COSINUS experiment [96, 97, 98] was developed. The COSINUS experiment aims to provide a model-independent comparison of the DAMA/LIBRA result by employing a NaI target as a cryogenic scintillating calorimeter. This setup simultaneously measures both scintillation light and phonon signals, enabling particle discrimination on an event-by-event basis. The validity of this model-independent

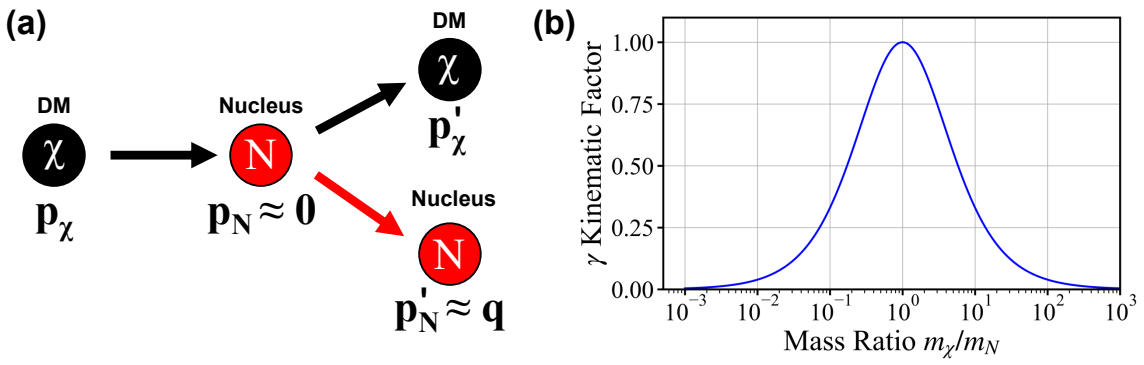

Figure 2.1: (a) Schematics of a DM-Nucleus scattering. (b) Kinematic factor γ as a function of the mass ratio m_χ/m_N.

approach requires achieving both a sufficiently low detection threshold and a large enough exposure [95].

In this chapter we first review the theoretical framework for DM–nucleus scattering, explaining in detail their kinematics and dynamics in the free nucleus approximation. We then describe the operating principles and main concepts of the COSINUS experiment. Finally, an original study on defect formation in NaI crystals is presented, exploring how lattice defects created during nuclear recoil events could influence the detection process, with potential consequences for both existing and future NaI-based direct detection experiments.

2.1 DM-Nuclei Elastic Scattering

2.1.1 Scattering Kinematics

Here we describe the kinematics of the elastic scattering between a dark matter particle of mass m_χ and momentum $\mathbf{p}_\chi$ and target nucleus of mass m_N and momentum $\mathbf{p}_N$. When discussing DM–nucleus scattering, the free-recoil approximation is valid for DM masses in the GeV range and above. At lower DM masses, however, the typical energy and momentum transfers approach those characteristic of ions in a condensed-matter system. Since the typical zero-point momentum in solids is $p_0 \sim$ 30–100 keV [85], the free-ion approximation remains reliable only when the momentum transfer is much larger than p_0. Referring to Fig. 1.5, we can qualitatively distinguish three regimes: for $m_\chi \gtrsim 100$ MeV, DM predominantly induces free elastic nuclear recoils; in the intermediate range of 10 MeV$\lesssim m_\chi \lesssim$100 MeV, the momentum transfer is comparable to the binding scale of the nucleus in the lattice, giving rise to multiphonon excitations; finally, for $m_\chi \lesssim 10$ MeV, DM scattering mainly produces single-phonon excitations [85]. Since this chapter

focuses on the larger DM mass regime, the free nuclei approximation will be used.
A scheme of the DM-nucleus collision is reported in Fig. 2.1 (a). The collision will be described by the conservation of energy and momentum, that, considering that both the DM particle and the nucleus are non-relativistic, will be given by:

$$\begin{cases} \frac{p_\chi^2}{2m_\chi} + \frac{p_N^2}{2m_N} = \frac{p_\chi^{'2}}{2m_\chi} + \frac{p_N^{'2}}{2m_N} \ ; \\ \mathbf{p}_\chi + \mathbf{p}_N = \mathbf{p}_\chi{}' + \mathbf{p}'_N \ ; \end{cases} \tag{2.1}$$

where $\mathbf{p}'_\chi$ and $\mathbf{p}'_N$ are the momenta of the DM particle and the nucleus after the collision. Now considering that the nucleus momentum before the collision will be very small with respect to all the other considered momenta, especially since in direct detection experiments the target is often kept at very low temperatures, we can approximate $\mathbf{p}_N \approx 0$. Then our conservation laws reduce to:

$$\begin{cases} \frac{p_\chi^2}{2m_\chi} = \frac{p_\chi^{'2}}{2m_\chi} + \frac{p_N^{'2}}{2m_N} & ; \quad E_R = \frac{q^2}{2m_N} = \frac{(p_\chi^2 - p_\chi^{'2})}{2m_\chi} \ ; \\ \mathbf{p}_\chi = \mathbf{p}_\chi{}' + \mathbf{p}'_N & ; \quad \mathbf{q} = \mathbf{p}_\chi - \mathbf{p}'_\chi = \mathbf{p}'_N \ ; \end{cases} \tag{2.2}$$

where we introduced the transferred momentum $\mathbf{q} = \mathbf{p}_\chi - \mathbf{p}'_\chi$ and the recoil energy $E_R = \frac{q^2}{2m_N}$, which is the energy transferred to the nucleus through the collision.
To proceed we rewrite the final DM momentum using scalar products and insert the conservation laws:

$$p_\chi^{'2} = p_\chi^2 + q^2 - 2\mathbf{p}_\chi \cdot \mathbf{q} = p_\chi^2 - \frac{m_\chi}{m_N} q^2 \ , \tag{2.3}$$

$$\mathbf{p}_\chi \cdot \mathbf{q} = m_\chi v \ q \cos\theta = \frac{q^2}{2} \frac{m_\chi}{\mu_{\chi N}} \ , \tag{2.4}$$

where $\mu_{\chi N} = \frac{m_\chi m_N}{m_\chi + m_N}$ is the reduced mass of the DM-nucleus system, v is the incoming DM particle speed, and θ is the scattering angle between the incoming DM particle momentum $\mathbf{p}_\chi$ and the recoiling nucleus momentum $\mathbf{q}$.
From this, the magnitude of the momentum transfer and the recoil energy are found to be:

$$q = 2 \ \mu_{\chi N} \ v \ \cos\theta \ , \tag{2.5}$$

$$E_R = \frac{2\mu_{\chi N}^2 v^2 \cos^2\theta}{m_N} = \gamma E_\chi \cos^2\theta \ , \tag{2.6}$$

where $E_\chi = \frac{1}{2} m_\chi v^2$ is the incoming DM particle energy, and $\gamma = \frac{4\mu_{\chi N}^2}{m_\chi m_N}$ is the maximum fraction of energy the DM particle can possibly transfer to the nucleus; this kinematic

factor is shown as a function of the mass ratio in Fig. 2.1 (b). We can see how the γ factor is close to 1 when the $m_\chi \sim m_N$, which is the condition for optimal energy transfer. For light DM, $m_\chi \ll m_N$, only a fraction of energy is transferred to the nucleus, making the scattering process less efficient.

From Eq. (2.6) we can see how the recoil energy E_R depends quadratically on $\cos\theta$, reaching a maximum for $\theta = 0$. In that case the DM particle is back-scattered and transfers the maximum possible momentum transfer and recoil energy for its given speed v: $q_{\theta=0} = 2\mu_{\chi N} v$ and $E_{R,\theta=0} = \frac{2\mu_{\chi N}^2 v^2}{m_N} = \gamma E_\chi$. Since the DM speed is bounded by the galactic escape speed and Earth's motion, there is a kinematic upper limit to the recoil energy E_R:

$$E_{R,\max} = \frac{2\mu_{\chi N}^2 v_{\max}^2}{m_N} = \frac{2\mu_{\chi N}^2 (v_{\rm esc} + v_\odot + v_{\rm orbit})^2}{m_N} \tag{2.7}$$

where $v_{\max} = v_{\rm esc} + v_\odot + v_{\rm orbit}$ is the maximum speed of DM in the local neighborhood when assuming the Standard Halo Model (the rotational speed $v_{\rm rot}$ can also be added but it's contribution is negligible).

An important quantity that can be defined is the minimum velocity required for a DM particle to impart a recoil with energy E_R, found by inverting $E_{R,\theta=0}$:

$$v_{\min}(E_R) = \sqrt{\frac{m_N E_R}{2\mu_{\chi N}^2}} = \sqrt{\frac{2E_R}{m_\chi \gamma}} \ . \tag{2.8}$$

The same quantity can be obtained using Eq. (1.16) and imposing $\omega = E_R = \frac{q^2}{2m_N}$, obtaining: $v_{\min}(E_R) = \frac{q}{2\mu_{\chi N}} = \sqrt{\frac{m_N E_R}{2\mu_{\chi N}^2}}$.

Lastly, the angular distribution of the recoils depends on the interaction model, and in isotropic scattering, the distribution is flat.

In the following subsection we use this information and evaluate the DM-nucleus scattering rate.

2.1.2 Scattering Rate

In the previous chapter we have shown how the scattering rate of DM with condensed matter systems can be written in terms of the dynamic structure factor $S(\mathbf{q}, \omega)$ which describes the response of the system to an energy transfer and momentum transfer ω and $\mathbf{q}$, respectively. Starting from Eq. 1.13, we can write the dynamic structure factor in a condensed matter system as:

$$S(\mathbf{q},\omega) = \frac{2\pi}{V} \sum_f |\langle f| \Big(\sum_k^{N_{\rm ele}} f_e \ e^{i\mathbf{q}\cdot\mathbf{r}_k} + \sum_J^{N_{\rm type}} \sum_I^{N_{\rm nuc}^J} \sum_\alpha^{A_J} f_\alpha \ e^{i\mathbf{q}\cdot\mathbf{r}_{I,\alpha}^J} \Big) |i\rangle|^2 \ \delta(E_f - E_i - \omega) \ , \tag{2.9}$$

where $\mathbf{r}_k$ is position of the k-index electron and $\mathbf{r}^J_{I,\alpha}$ is the position of the α-index nucleon of the I-nucleus of type J. and f_e and f_α are the normalized DM coupling with electrons and nucleons (which can be protons f_p or neutrons f_n) respectively. The couplings are taken as $\mathbf{q}$-independent constants, with the q dependence included in the DM cross section $\bar{\sigma}(q)$, as shown in Eq. (1.31). It is useful to define also the normalized coupling of a ion of type J, $f_J = f_p Z_J + f_n(A_J - Z_J)$, which reduces to $f_J = f_n A_J$ when the interaction does not depend on the nucleon type, $f_p = f_n$. The normalized interaction strengths with the ions f_J will depend on the type of ion and do not factorize out of the structure factor for a system composed of different types of ions. Also, in case of spin-dependent DM interactions, an average over all possible spin states of the ions must be performed; in this work we will not consider this type of interactions.

Dynamic structure factor Let's focus back on elastic nuclear recoils, through a spin-independent interaction with the neutron/proton symmetry $f_n = f_p$; as it is often done, we absorb the coupling strength f_n in the definition of $\bar{\sigma}$. Let's also consider a monoatomic target, $N_{\text{type}} = 1$, which means that only one ion type is present (in the following we drop J from our notation). The dynamic structure factor will reduce to:

$$\begin{aligned} S(\mathbf{q},\omega) &= \frac{2\pi}{V}\sum_f |\langle f|\sum_I^{N_{\text{nuc}}}\sum_\alpha^A\ e^{i\mathbf{q}\cdot\mathbf{r}_{I,\alpha}}|i\rangle|^2\ \delta(E_f - E_i - \omega) = \\ &= \frac{2\pi}{V}\sum_f |\langle f|\mathcal{O}_{\text{T}}|i\rangle|^2\ \delta(E_f - E_i - \omega)\ . \end{aligned} \tag{2.10}$$

We now focus on the calculation of $\sum_f |\langle f|\mathcal{O}_{\text{T}}|i\rangle|^2$. We write the nucleons positions as the sum of the ion positions and its relative coordinate: $\mathbf{r}_{I,\alpha} = \mathbf{R}_I + \mathbf{u}_{I,\alpha}$. We can then write:

$$\mathcal{O}_{\text{T}} = \sum_I^{N_{\text{nuc}}}\sum_\alpha^A\ e^{i\mathbf{q}\cdot(\mathbf{R}_I+\mathbf{u}_{I,\alpha})} = \sum_I^{N_{\text{nuc}}} e^{i\mathbf{q}\cdot\mathbf{R}_I}\sum_\alpha^A\ e^{i\mathbf{q}\cdot\mathbf{u}_{I,\alpha}} = \sum_I^{N_{\text{nuc}}} e^{i\mathbf{q}\cdot\mathbf{R}_I}\ \mathcal{O}_I\ . \tag{2.11}$$

Now the squared matrix elements can be rewritten as:

$$|\langle f|\mathcal{O}_{\text{T}}|i\rangle|^2 = \langle i|\mathcal{O}^\dagger_{\text{T}}|f\rangle\langle f|\mathcal{O}_{\text{T}}|i\rangle = \langle i|\sum_K^{N_{\text{nuc}}}\ e^{-i\mathbf{q}\cdot\mathbf{R}_K}\ \mathcal{O}^\dagger_K|f\rangle\langle f|\sum_I^{N_{\text{nuc}}} e^{i\mathbf{q}\cdot\mathbf{R}_I}\ \mathcal{O}_I|i\rangle \tag{2.12}$$

from this expression we can see how it is possible to split the different terms in diagonal terms where $I = K$ and off-diagonal terms where $I \neq K$. In the case of a scattering off independent nuclei, the scattering is incoherent, which means that different nuclei are scattered with random phases; in this regime, named random phase approximation, the

off-diagonal terms will cancel out.
Using the completeness relation $\sum_f |f\rangle\langle f| = \mathcal{I}$, we can simplify the two exponentials with the ionic coordinate $\mathbf{R}_I$, and re-insert the same sum. We then obtain:

$$\sum_{I}^{N_{\rm nuc}} \sum_{f} \langle i| \sum_{\beta}^{A} \; e^{-i\mathbf{q}\cdot\mathbf{u}_{I,\beta}} |f\rangle\langle f| \sum_{\alpha}^{A} \; e^{i\mathbf{q}\cdot\mathbf{u}_{I,\alpha}} |i\rangle \; . \tag{2.13}$$

We now write $|i\rangle = |N\rangle^{\otimes N_{\rm nuc}} = |N\rangle|N\rangle^{\otimes N_{\rm nuc}-1}$, where $|N\rangle$ represents the nuclear ground state. Since we are focusing on elastic scatterings, in which a momentum is transferred to a nucleus, but the nucleus stays in its ground state, projecting our rate in the elastic channel corresponds in taking $|f\rangle = |i\rangle = |N\rangle^{\otimes N_{\rm nuc}}$. Substituting these expressions in Eq. 2.13, we obtain:

$$\begin{aligned} &\sum_{I}^{N_{\rm nuc}} \langle N| \sum_{\beta}^{A} e^{-i\mathbf{q}\cdot\mathbf{u}_{I,\beta}} |N\rangle \; \langle N| \sum_{\alpha}^{A} e^{i\mathbf{q}\cdot\mathbf{u}_{I,\alpha}} |N\rangle \; ({}^{N_{\rm nuc}-1\otimes}\langle N|N\rangle^{\otimes N_{\rm nuc}-1})^2 = \\ &= \sum_{I}^{N_{\rm nuc}} |\langle N| \sum_{\alpha}^{A} e^{i\mathbf{q}\cdot\mathbf{u}_{I,\alpha}} |N\rangle|^2 = \sum_{I}^{N_{\rm nuc}} A^2 |F_N(\mathbf{q})|^2 = N_{\rm nuc} A^2 |F_N(\mathbf{q})|^2 \; ; \end{aligned} \tag{2.14}$$

where we have the orthonormality of the states, and defined the nuclear form factor $F_N(\mathbf{q})$:

$$F_N(\mathbf{q}) = \langle N| \frac{1}{A} \sum_{\alpha}^{A} e^{i\mathbf{q}\cdot\mathbf{u}_{I,\alpha}} |N\rangle \; . \tag{2.15}$$

Finally, using the previously discussed kinematic information, we identify $E_f - E_i = \frac{q^2}{2m_N}$, and combining the previous result we can write the dynamic structure factor for an elastic scattering off a monoatomic target of free nuclei:

$$S(\mathbf{q},\omega) = \frac{2\pi}{V} N_{\rm nuc} A^2 |F_N(\mathbf{q})|^2 \; \delta\left(\omega - \frac{q^2}{2m_N}\right) \; . \tag{2.16}$$

Nuclear form factor In the previous calculations we considered only individual nuclear recoils considering an high enough momentum transfer q. This leads to a total elastic recoil rate proportional to A^2, where A is the mass number, indicative of coherent scattering off all the nucleons in a nucleus, and linear in the number of target nuclei $N_{\rm nuc}$, indicative of incoherent scattering off all the nuclei in the target. However, this coherence over the nucleons is gradually lost as the momentum transfer q increases, typically at high recoil energies. That is because the DM particle will start probing the internal structure of the nucleus, and the scattering will then become sensitive to the distribution of nucleons. This suppression of the A^2 enhancement factor is encoded in the nuclear form factor,

$F_N(\mathbf{q})$. While for more detailed analyses, the nuclear form factor can be computed from nuclear shell models, including information on the nucleon wavefunctions; a common way to compute the nuclear form factor is to identify it with the Fourier transform of the nucleus mass distribution:

$$F_N(\mathbf{q}) = \frac{1}{A} \int d^3\mathbf{r}\ \rho(\mathbf{r})\ e^{i\mathbf{q}\cdot\mathbf{r}}\ ; \tag{2.17}$$

and describe the nuclear density $\rho(\mathbf{r})$ with a model.
A widely used approximation is the nuclear Helm form factor [99], which models the nucleus as a uniform sphere with a soft edge due to the surface thickness, and provides a universal description of the form factor suppression. Its analytic expression is:

$$F_N^{\text{Helm}}(q) = \frac{3}{qR_N}\ j_1(qR_N)\ e^{-\frac{1}{2}(qs)^2}\ , \tag{2.18}$$

where j_1 is the spherical Bessel function of order one, R_N is the effective nuclear radius and s is the skin thickness parameter. Their values and expressions are parametrized as following:

$$\begin{aligned} &R_N = \sqrt{c^2 + \frac{7}{3}\pi^2 a^2 - 5s^2}\ , \\ &c = \left(1.23A^{\frac{1}{3}} - 0.6\right)\ \text{fm}\,, \\ &s \approx 0.9\ \text{fm}\,, \quad a \approx 0.52\ \text{fm}\,. \end{aligned} \tag{2.19}$$

While, as mentioned, the nuclear form factor tends to 1, $F_N \to 1$ for low momentum transfers, which implies that the coherence is preserved, it starts to fall off at larger q-values, which means that the coherence is lost. This happens when the momentum transfer becomes comparable to the nuclear size:

$$q \gtrsim \frac{1}{R_N}\ , \tag{2.20}$$

where $R_N \sim$ 1-5 fm; converting in energies these two radius values will result in $\approx$ 197 MeV and $\approx$ 39 MeV, respectively. By comparing these values with Fig. 1.5 we can see that the nuclear form factor becomes relevant for DM particles with mass in the GeV–TeV range, while for sub-GeV DM particles the nucleus will behave as point-like and the form factor can be neglected.

Scattering rate Combining Eq. 1.26 and Eq. 2.16, we obtain the scattering rate per unit of mass and time in our considered DM-nuclei scattering process [100, 101, 102, 103]:

$$R(t) = \frac{1}{\rho_{\mathrm{T}}}\frac{\rho_\chi}{m_\chi}\int \frac{d^3\mathbf{q}}{(2\pi)^3}\int d\omega\ g(\mathbf{q},\omega;t)\ \frac{\pi\bar{\sigma}_n}{\mu_{\chi n}^2}F_{DM}(q)^2\ \frac{2\pi}{V}N_{\mathrm{nuc}}A^2|F_N(\mathbf{q})|^2\ \delta\Big(\omega-\frac{q^2}{2m_N}\Big)\ ; \tag{2.21}$$

where $\mu_{\chi n}$ is the DM-nucleon reduced mass, and $\bar{\sigma}_n$ is the DM-nucleon reference cross section.
Performing the integration in ω by using the δ-function we obtain:

$$R(t) = \frac{N_{\mathrm{nuc}}}{\rho_{\mathrm{T}}V}\frac{\rho_\chi}{m_\chi}\frac{\bar{\sigma}_n}{\mu_{\chi n}^2}A^2\int\frac{d^3\mathbf{q}}{4\pi}\ g\big(\mathbf{q},\frac{q^2}{2m_N};t\big)\ F_{DM}(q)^2|F_N(\mathbf{q})|^2\ \ . \tag{2.22}$$

It can be useful to rewrite the integration in terms of the recoil solid angle Ω and the recoil energy E_R. To do so, we introduce the Radon transform of the DM velocity distribution $\hat{f}(v_{\mathrm{min}},\hat{\mathbf{q}};t)$, which is defined by:

$$\hat{f}_\chi(v_{\mathrm{min}},\hat{\mathbf{q}};t)\equiv\int d^3\mathbf{v}\ f_\chi(\mathbf{v};t)\ \delta(\mathbf{v}\cdot\hat{\mathbf{q}}-v_{\mathrm{min}}). \tag{2.23}$$

By comparing this expression with the g-function from Eq. (1.25), and using Eq. (1.16) and the following delta-function relation:

$$\begin{aligned}\delta(\omega-\omega_{\mathbf{q}}) &= \delta\Big(\omega-\mathbf{v}\cdot\mathbf{q}+\frac{q^2}{2m_\chi}\Big)=\delta\Big(q\Big[\frac{\omega}{q}-\mathbf{v}\cdot\hat{\mathbf{q}}+\frac{q}{2m_\chi}\Big]\Big)= \\ &= \frac{1}{q}\delta\Big(\mathbf{v}\cdot\hat{\mathbf{q}}-\Big[\frac{\omega}{q}+\frac{q}{2m_\chi}\Big]\Big)=\frac{1}{q}\delta(\mathbf{v}\cdot\hat{\mathbf{q}}-v_{\mathrm{min}})\ ;\end{aligned} \tag{2.24}$$

we can see that $\hat{f}_\chi(v_{\mathrm{min}},\hat{\mathbf{q}};t)=q\cdot g(\mathbf{q},\omega;t)$.
When using the Standard Halo Model velocity distribution, Eq. (1.24), we can compute its Radon transform and obtain:

$$\hat{f}_\chi(v_{\mathrm{min}},\hat{\mathbf{q}};t)=\frac{1}{N_{\mathrm{esc}}\sqrt{2\pi\sigma_v^2}}\Big[e^{-\frac{|v_{\mathrm{min}}+\hat{\mathbf{q}}\cdot\mathbf{v}_{\mathrm{lab}}(t)|^2}{2\sigma_v^2}}-e^{-\frac{v_{\mathrm{esc}}^2}{2\sigma_v^2}}\Big]\ . \tag{2.25}$$

In Appendix B.3 we show the calculations performed to compute Eq. (2.25).
In the rate expression of Eq. (2.22) the function $g\big(\mathbf{q},\frac{q^2}{2m_N};t\big)$ can be substituted with

$\hat{f}_\chi(v_{\min}, \hat{\mathbf{q}}; t)/q$, where $v_{\min} = \frac{q}{2\mu_{\chi N}}$ as seen in the previous subsection, obtaining:

$$\begin{aligned} R(t) &= \frac{N_{\text{nuc}}}{\rho_{\text{T}} V} \frac{\rho_\chi}{m_\chi} \frac{\bar{\sigma}_n}{\mu_{\chi n}^2} A^2 \int_\Omega \frac{d\Omega'}{4\pi} \int dq\ q^2\ \frac{\hat{f}_\chi(v_{\min}, \hat{\mathbf{q}}; t)}{q} F_{DM}(q)^2\ |F_N(q, \Omega')|^2 = \\ &= \frac{N_{\text{nuc}}}{\rho_{\text{T}} V} \frac{\rho_\chi}{m_\chi} \frac{\bar{\sigma}_n}{\mu_{\chi n}^2} A^2 \int_\Omega \frac{d\Omega'}{4\pi} \int_{E_{\text{thresh}}}^{E_{R,\max}} dE_R\ m_N\ \hat{f}_\chi(v_{\min}, \hat{\mathbf{q}}; t)\ F_{DM}(E_R)^2\, |F_N(E_R, \Omega')|^2 = \\ &= \frac{\rho_\chi}{m_\chi} \frac{\bar{\sigma}_n}{\mu_{\chi n}^2} A^2 \int_\Omega \frac{d\Omega'}{4\pi} \int_{E_{\text{thresh}}}^{E_{R,\max}} dE_R\ \hat{f}_\chi(v_{\min}, \hat{\mathbf{q}}; t)\ F_{DM}(E_R)^2\, |F_N(E_R, \Omega')|^2\ ; \end{aligned} \tag{2.26}$$

where we have used the definition of the recoil energy $E_R = \frac{q^2}{2m_N}$, which implies $dq\ q = dE_R\ m_N$, to change the integration variable. We can see how the ratio $N_{\text{nuc}}\ m_N/\rho_T V = 1$.

Isotropic rate In case the nuclear form factor is isotropic, so it does not depend on the angle but only on the recoil energy, the rate will be:

$$R^{\text{iso}}(t) = \frac{\rho_\chi}{m_\chi} \frac{\bar{\sigma}_n}{\mu_{\chi n}^2} A^2 \int_\Omega \frac{d\Omega'}{4\pi} \int_{E_{\text{thresh}}}^{E_{R,\max}} dE_R\ \hat{f}_\chi(v_{\min}, \hat{\mathbf{q}}; t)\, F_{DM}(E_R)^2\ |F_N(E_R)|^2\ . \tag{2.27}$$

Performing the integration over the solid angle will then lead to the following expression for the isotropic rate:

$$R^{\text{iso}}(t) = \frac{1}{2} \frac{\rho_\chi}{m_\chi} \frac{\bar{\sigma}_n}{\mu_{\chi n}^2} A^2 \int_{E_{\text{thresh}}}^{E_{R,\max}} dE_R\ \eta(v_{\min}(E_R); t)\, F_{DM}(E_R)^2\ |F_N(E_R)|^2\ . \tag{2.28}$$

This is demonstrated in Appendix B.4 where it is shown, that the function $\eta(v_{\min}; t)$ is, apart from a constant factor, the angular average of the Radon transform $\hat{f}_\chi(v_{\min}, \hat{\mathbf{q}}; t)$. The same result can be obtained starting from Eq. (1.20) and substituting the dynamic structure factor from (2.16) (with the nuclear form factor taken as isotropic) in the isotropic rate.

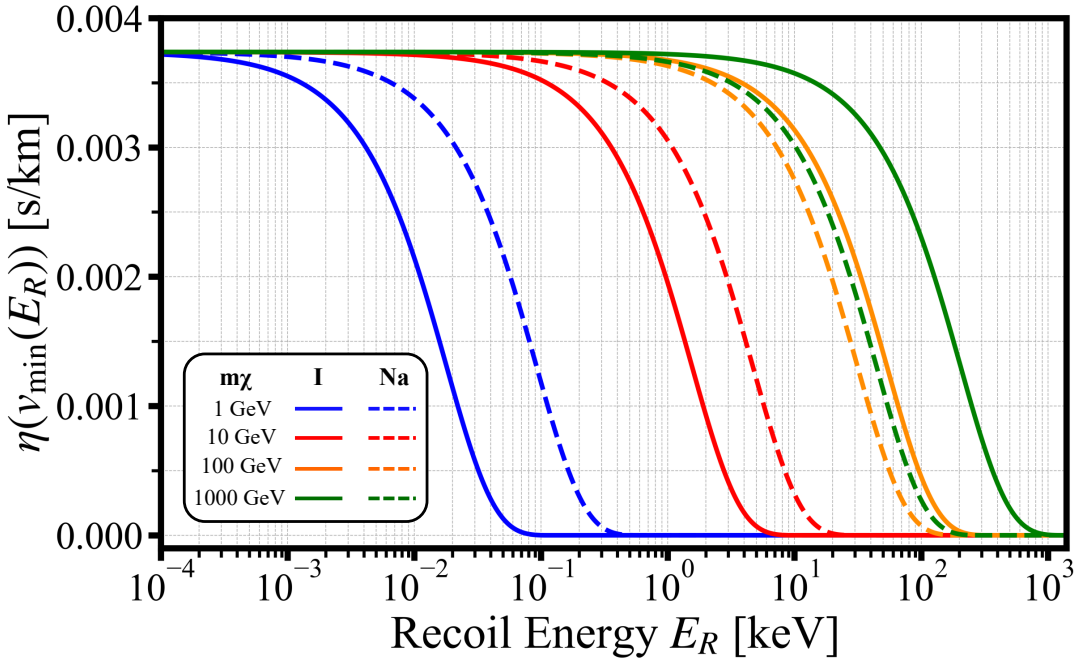

Figure 2.2: Mean inverse speed $\eta(v_{\min}(E_R))$ as a function of the recoil energy E_R for different DM masses m_χ and two targets: ^{127}I Iodine (solid lines) and ^{23}Na Sodium (dashed lines).

Rate for multiatomic targets The generalization of the rate for a target with different types of ions will result in:

$$
\begin{aligned}
R(t) &= \frac{\rho_\chi}{m_\chi}\frac{\bar{\sigma}_n}{\mu_{\chi n}^2}\sum_J^{N_{\text{type}}}\frac{N_{\text{nuc}}^J m_N^J}{\rho_{\text{T}} V}A_J^2\int_\Omega\frac{d\Omega'}{4\pi}\int_{E_{\text{thresh}}}^{E_{R,\max}^J} dE_R\ \ \hat{f}_\chi(v_{\min}^J,\Omega';t)\ \ F_{DM}(E_R)^2\,|F_N^J(E_R,\Omega')|^2\ \ = \\
&= \frac{\rho_\chi}{m_\chi}\frac{\bar{\sigma}_n}{\mu_{\chi n}^2}\sum_J^{N_{\text{type}}} X_J A_J^2\int_\Omega\frac{d\Omega'}{4\pi}\int_{E_{\text{thresh}}}^{E_{R,\max}^J} dE_R\ \ \hat{f}_\chi(v_{\min}^J,\Omega';t)\ \ F_{DM}(E_R)^2\,|F_N^J(E_R,\Omega')|^2\ \ = \\
&= \sum_J^{N_{\text{type}}}\int_\Omega d\Omega'\int_{E_{\text{thresh}}}^{E_{R,\max}^J} dE_R\ \frac{\partial^2 R^J(t)}{\partial\Omega'\partial E_R} = \sum_J^{N_{\text{type}}} R^J(t)\ ;
\end{aligned}
\tag{2.29}
$$

where $X_J = M_J/\sum_J M_J$ represents the mass ratio of the J-th atomic species, A_J is the mass number for a specific type, m_N^J the nuclear mass of a nuclei of type J, N_{nuc}^J the number of ions of type J present in the target, $F_N^J(E_R,\Omega')$ the nuclear form factor for a nuclei of type J and $v_{\min}^J = \sqrt{\frac{m_N^J E_R}{2(\mu_{\chi N}^J)^2}}$, with $\mu_{\chi N}^J = \frac{m_\chi m_N^J}{m_\chi + m_N^J}$, is the minimum DM speed to have a recoil with energy E_R on a nuclei of type J. The maximum recoil energy $E_{R,\max}^J$ is given by Eq. (2.7), substituting m_N with the corresponding nuclei mass m_N^J. We have also defined the rate associated to each ion type $R^J(t)$ and the double-differential rate with respect to the solid angle and recoil energy per ion type $\frac{\partial^2 R^J(t)}{\partial\Omega'\partial E_R}$.These results can be

obtained considering that the dynamical structure factor for a target with different types of ions is given by:

$$S(\mathbf{q},\omega) = \frac{2\pi}{V}\sum_{J}^{N_{\text{type}}} N_{\text{nuc}}^{J} A_J^2 |F_N^J(\mathbf{q})|^2 \, \delta\left(\omega - \frac{q^2}{2m_N^J}\right) , \tag{2.30}$$

where the contribution for a single ion type is summed over all ion types. In Fig. 2.2 the $\eta(v_{\min}(E_R))$ function is showed for different DM masses and two targets: Iodine and Sodium. We can see how for lower values of m_χ Sodium allows for higher recoil energies at fixed η due to better kinematic matching with lighter DM. On the opposite, for larger DM masses Iodine allows higher energy recoils than Sodium. From this example we can see how using a multi-ionic target allows probing different ranges of DM masses.
We will now focus on thermal detectors and specifically the COSINUS project, which uses NaI crystals.

2.2 The COSINUS experiment

Over the past decades, direct-detection experiments made important sensitivity gains across a wide DM-mass range by using different target materials and techniques, with the most discussed and relevant result being the DAMA/LIBRA modulation claim. A model-independent test, which uses the same material, is thus needed, since other target choices would introduce dependencies on such target material and would thus not be model-independent.
Several NaI-based searches exist, like ANAIS [66] and COSINE-100 [67]) or are planned, like SABRE [104]; these room-temperature experiments measure scintillation light emitted by thallium-doped NaI crystals as a single signal and have scaled target masses up to $\mathcal{O}(100\text{ kg})$. However, scintillation-only experiments can typically perform particle identification only statistically via pulse-shape analysis, and not event-by-event, limiting their background rejection [105, 106].

COSINUS (Cryogenic Observation for SIgnature seen in Next-generation Underground Searches) [108] takes a different approach, operating pure NaI crystals at milli-Kelvin temperatures and reading out two signals simultaneously: the scintillation-light signal and the phonon (heat) signal. The phonon channel provides an accurate reconstruction of the total deposited energy with a low threshold for both electron and nuclear recoils, and the light yield, which is the ratio of light to phonon signal, enables powerful event-by-event particle discrimination. With this dual readout, COSINUS can perform a quasi-background-free probe of DM-nucleus scattering as a possible origin of the DAMA/LIBRA modulation. Constructed at the "Laboratori Nazionali del Gran Sasso" (LNGS) underground labo-

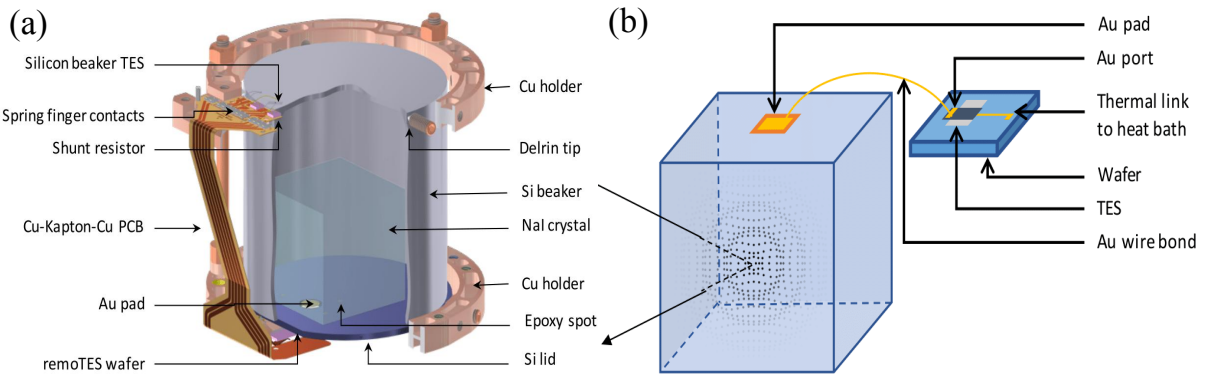

Figure 2.3: (a) Sketch of a detector module for the COSINUS-1π run; different components are highlighted. (b) Schematic drawing of the remoTES detector design. The TES is fabricated onto a carrier wafer and is connected via a Au pad, a Au wire bond, and a Au port to the target crystal. Figures from Ref. [107].

ratories in central Italy during 2021-2024, COSINUS will start the COSINUS-1π run in 2025, with the goal for that run being collecting $\mathcal{E} = 100\,\mathrm{kg}\cdot\mathrm{d}$ of exposure to cross-check elastic DM-nucleus scattering as an explanation for the DAMA modulation signal.

COSINUS detector concept and readout Particle interactions in NaI crystals produce two kinds of measurable excitations: lattice vibrations, so phonons, and scintillation photons. The phonons are read out from the NaI crystal using a Transition Edge Sensor (TES) capable of measuring the induced temperature rise. A TES is operated at its superconducting transition (critical) temperature: upon absorption of energy and the resulting infinitesimal temperature increase, the TES resistance rises sharply, producing a measurable voltage change that constitutes the detector signal. Scintillation photons are simultaneously captured by a beaker-shaped silicon (Si) light detector and read out with a separate TES; this configuration maximizes light collection and vetoes surface backgrounds.

Thanks to the low operational temperatures, cryogenic solid-state detectors enable extremely low energy thresholds and excellent energy resolution for rare-event searches. The TES is composed of thin-film tungsten (W) structures with thicknesses in the order of 0.1-1 μm. In Fig. 2.3 (a) a sketch of the COSINUS detector module is shown. NaI crystals are soft and highly hygroscopic, making direct thin-film fabrication on the crystal problematic, with the risk of degrading surface quality. Due to its high hygroscopicity NaI crystals must also be handled in a controlled atmosphere with very low humidity ($<$ 100 ppm). To address this, COSINUS introduced the remoTES design [109]: the W-TES is fabricated on a separate wafer rather than directly on the NaI crystal. Phonons in the target crystal are collected by a gold (Au) pad evaporated onto the crystal surface; the Au pad is coupled to the TES wafer via an Au wire bond. This remote-coupling scheme

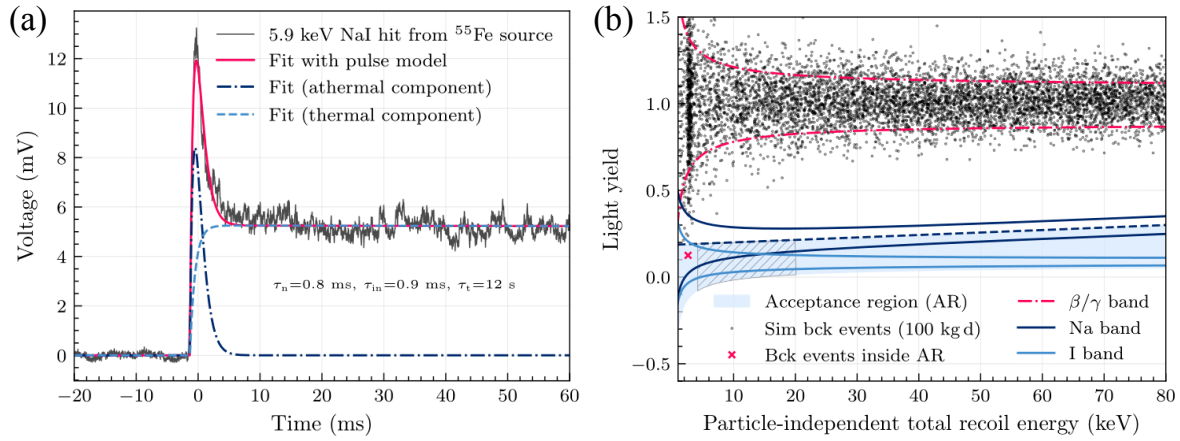

Figure 2.4: (a) Example of a remoTES NaI pulse from an ^{55}Fe calibration source with a pulse shape model fit. (b) Example of particle discrimination on an event-by-event basis, for an exposure of 100 kg·d, allowing for a quasi-background-free experiment, with background events rarely leaking into the acceptance region. Figures from Ref. [107].

has two main advantages: the NaI crystal is physically separated from the TES fabrication process, preserving the crystal's properties; the phonons generated in the target crystal couple efficiently to the electronic system of the Au pad via strong electron-phonon coupling, and the TES provides efficient readout of the phonon signal. In Fig. 2.3 (b) a scheme of the remoTES design is shown.
A typical remoTES pulse is shown in Fig. 2.4 (a). Pulse-shape analysis [110] of remoTES signals shows a decomposition into an athermal and a thermal component used the athermal component, which are associated with phonons thermalizing in the Au pad and the NaI crystal itself, respectively. This same decomposition is applied for TESs directly evaporated on a target crystal. The remoTES concept is therefore beneficial not only for COSINUS but for cryogenic calorimeters broadly when direct TES deposition onto targets is undesirable.

Events discrimination The COSINUS detector module contains a phonon detector, which measures the energy E_p, and a light detector, measuring the energy L. The ratio of these two energies is the so-called light yield, $LY = L/E_p$. Since both E_p and L are measured the event-type-independent total deposited energy E can still be reconstructed [111]. Both channels are calibrated with γ sources so that the β/γ band is normalized to mean light yield 1, since electrons and γ_s interacting with the target's electrons produce the highest light output. For other event types, such as nuclear recoils, the energy partitioning between phonon and light channels results in a quenched light yield. This means they produce significantly less scintillation light than electron recoils of equivalent energy. The spread of each light-yield distribution (called band) is modeled as a Gaussian whose

width is set by light-detector noise and Poisson fluctuations in light production. In Fig. 2.4 (b), simulated data in the LY versus E plane for an assumed exposure of 100 kg·d shows well-separated bands for β/γ, Na recoils and I recoils, with nuclear-recoil bands positioned according to their energy-dependent quenching factors (QFs). For the assumed background level only one event (magenta cross) background event is expected to fall in the so-called acceptance region, showing a strong discrimination power of the COSINUS detector. The acceptance region, which includes events below the mean of the Na band, is chosen to maximize the expected signal in the nuclear-recoil bands while minimizing background leakage.

In summary, COSINUS combines the advantages of cryogenic solid-state calorimetry (very low thresholds, excellent energy resolution) with the target-material fidelity required for a model-independent test of the DAMA result by operating pure NaI at milli-Kelvin temperatures and simultaneously reading out phonon and scintillation signals. The remoTES remote-coupling scheme enables TES-based phonon readout without direct fabrication on hygroscopic NaI crystals, preserving surface quality while maintaining the fidelity of the pulse shape and the discrimination performance required for a quasi-background-free search for DM-nucleus scattering.

2.3 Defect formation in NaI crystals

As discussed in the previous section, sodium iodide (NaI) is a widely used scintillator in direct dark matter searches, with experiments like the COSINUS experiment, using NaI-based cryogenic scintillating calorimeters to test the annually modulating signal reported by DAMA/LIBRA. In this section we report our investigation on defect formation within NaI crystals and its impact on the dark matter detection signal.
In addition to the light and thermal channels, which we previously described in the context of an NaI-based detector, detectors can also be sensitive to a charge signal, which could serve as an additional channel to strengthen experimental results. Recent studies have explored the potential for a charge signal channel arising from defect formation induced by low-mass DM in solid state detectors [112]. These defects, created by the collision of DM particles with the target material, can also alter the phonon measurements by redirecting energy into their formation [113, 114]. The CRESST collaboration recently reported a possible energy-scale shift and discussed defect formation in the target crystal as a potential explanation [115].

We investigate defect formation in NaI crystals induced by DM collisions, focusing on their impact across different detection channels. Combining molecular dynamics (MD) simulations with density functional theory (DFT) calculations, we analyze the electronic

configuration of the system in the presence of defects and characterize their properties. By calculating the DM-nuclei scattering rate, we identify the range of DM masses where defect formation becomes significant. Finally, we discuss the influence of these defects on the detection rate, highlighting the potential for a novel charge signal in NaI-based detectors.

2.3.1 Computational details

The molecular dynamics simulations were performed using the LAMMPS code [116]. In MD one propagates the classical equations of motion for an ensemble of atoms under a specified interaction model; the main ingredients are an initial atomic configuration of positions and velocities, an interatomic potential from which forces are computed, a numerical integrator which solves the trajectories up to a given time, and an ensemble control which allows to impose a desired temperature and/or pressure.
We adopted a 6×6×6 unit cells configuration, with periodic boundary conditions applied on all directions; the NaI unit cell consists in a face-centered cubic (fcc) arrangement of Na^+ and I^- ions, forming the so-called rock-salt structure. Before simulating the collisions, a thermalization of the system was performed by a combination of constant number-volume-energy (NVE) and constant number-volume-temperature (NVT) simulations, keeping the temperature at $\sim$ 1 K, until reaching the equilibrium state (after $\sim$ 2 ps). We modeled the DM particle collision by assigning an energy E and a momentum $\vec{p}$ to an atom, called the PKA (Primary Knock-on Atom). Then to emulate the effect of a thermal bath acting on the system, allowing the relaxation of the released energy, we divided our initial configuration in two regions: an outer region 1 unit cell thick in all directions, that performed an NVT simulation at 1 K, and an inner region that performed an NVE simulation. To correctly describe the dynamic of the atoms after the release of high energies, we used a force field potential [117]. To integrate correctly the equations of motion, we used an adaptive time step (going from 10^{-5} fs to 1 fs) in the initial part of the simulations, when high energies and velocities are involved. Simulations were stopped after the potential energy fluctuations fell below a threshold value of 1 eV, with a typical time of $\sim$ 5 ps. This threshold value is sufficiently smaller than the formation energies of Frenkel pairs in the MD simulations, which, as will be discussed, are $E_{\mathrm{Def,Na}} \sim 4$ eV and $E_{\mathrm{Def,I}} \sim 16$ eV. To analyze the final configuration, and check for the formation of Frenkel pairs, which consist of a vacancy and an interstitial atom pair, we used the Wigner-Seitz defect analysis present in OVITO [118]. This procedure was repeated to create a map of the energy needed to form a defect, for a given direction of the PKA recoil in the solid angle, called Threshold Displacement Energy (TDE). The TDE has been evaluated sampling the full solid angle uniformly for over 180 directions. The possibility of a scat-

tering above the threshold value not producing a defect was not considered. The system's different configuration at the time of the collision may cause these events. But since we considered a very low temperature system, we can effectively treat it as frozen, canceling this possible effect.

To study the electronic properties of the system in the presence and absence of Frenkel pairs, we mapped the system on a smaller 3×3×3 representative subset of the simulation cell. This structure, for the defects case, was derived from the conclusion of the molecular dynamic simulation and included both the interstitial atom and the vacancy. Density functional theory simulations were performed on such reduced system, using the VASP code [119, 120]. For a thorough description of the core mechanics of DFT and its main aspects, see Chapter 3 and Appendix B.
The PBE (Perdew-Burke-Ernzerhof) exchange correlation functional [121] was used, with a kinetic energy cutoff of 350 eV, and a k-point grid of 6×6×6. We relaxed the structure converging the total energy up to a threshold of 10^{-5} eV. For the density of states calculations a 15×15×15 k-point grid was adopted. An electronic gaussian smearing of 0.1 eV was used for all calculations.

2.3.2 Molecular dynamics and DFT results

The performed molecular dynamics simulations allowed the study of the required conditions for the formation of Frenkel pairs, induced by DM collisions on the NaI crystal ions. In Fig. 2.5 we report the electronic density of states (DOS), computed with DFT simulations, for an ideal (black), an Na defect (red) and an I defect (blue) system. To better see the DOS variation due to the defect presence, the DOS of the defected supercells are shifted aligning the valence band maximum (VBM) of atoms far from the defect with the VBM of the ideal system. The major effects appear near the electronic band gap, which is shown in the inset of Fig. 2.5. In the iodine defect case we can see the formation of new occupied electronic states in the band gap at about 1 eV and one empty state at about 3 eV. In Fig. 2.6 (a,b) we report the simulated structures in the proximity of an I interstitial atom and the vacancy left from it, respectively, together with the real space charge densities of the newly formed electronic states. The occupied states are localized around the interstitial atom and extend mainly up to its first nearest neighbors, while the unoccupied state is localized at the vacancy position.
The equivalent case for an Na interstitial atom is reported in Fig. 2.6 (c,d). By analyzing the projected density of states, two energy regions were identified where the electronic states are predominantly localized around the atoms near the interstitial Na atom and the vacancy. In Fig. 2.6 (c,d) the real space charge distributions corresponding to the energy intervals [-3.4,-2.8] eV (panel (c)) and [-0.6,0.0] eV (panel (d)) are shown. These

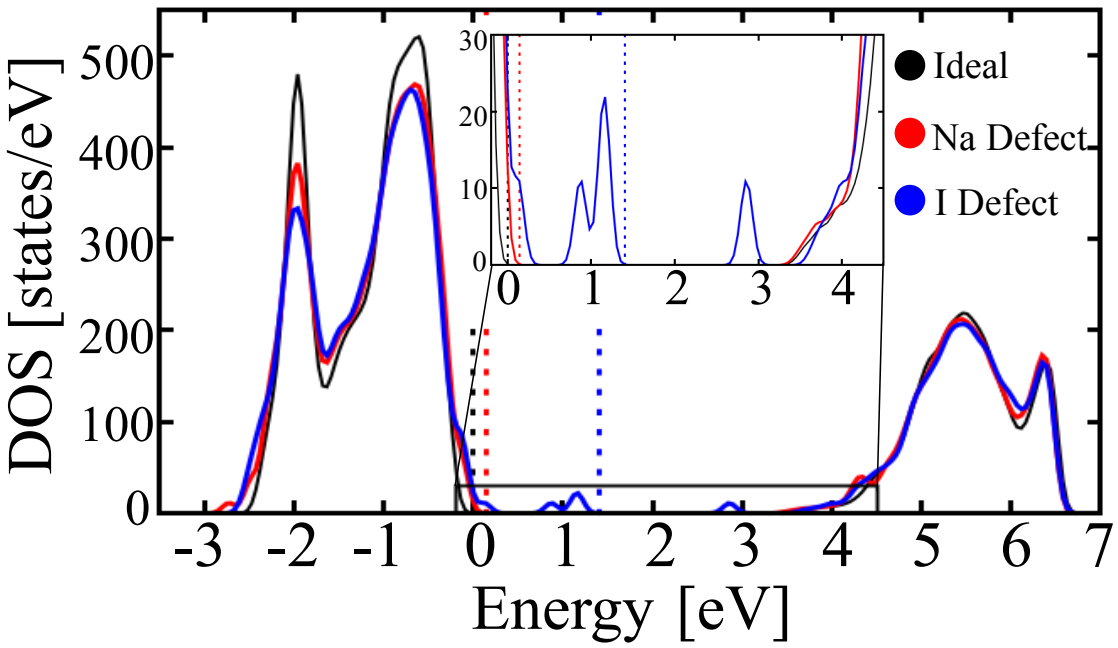

Figure 2.5: Comparison of the electronic density of states between the ideal NaI system in absence of defects (black line), and in the presence of an interstitial Na atom (red line), and I atom (blue line). The highest occupied level relative to the different cases are shown by a vertical dashed line of the corresponding color. An inset of the electronic band gap region is also present, showcasing how in the presence of I interstitial atoms new states emerge in the band gap.

distributions clearly show localization around the interstitial Na atom and the vacancy, respectively. The states around the vacancy are particularly interesting since they influence the DOS near the Fermi energy, potentially altering transport properties and scintillation processes. So while the electronic configuration associated with an Na defect does not introduce new states in the band gap, as shown in Fig. 2.5, we still observe significant changes in the electronic states.

From Fig. 2.6(a-d) we can also note how the interstitial iodine atom, which has a far greater mass with respect to the sodium atom ($m_{\mathrm{I}} = 126.90$ a.m.u.; $m_{\mathrm{Na}} = 22.99$ a.m.u.) causes a more relevant deformation on the neighboring atoms. The two defects also differ in their energetic costs; in fact, by comparing the system's potential energy at the start and end of our MD simulations, we can estimate the formation energy of the Frenkel pairs, obtaining: $E_{\mathrm{Def,Na}} \sim 4$ eV and $E_{\mathrm{Def,I}} \sim 16$ eV.

To further characterize the defect formation in NaI crystals, we studied the lowest energy necessary to form a defect: the threshold displacement energy (TDE). This quantity depends both on the recoil direction, that we identify with the polar angle θ_{rec} and the azimuthal angle ϕ_{rec}, with respect to the [100] crystal direction, and on the atom type the DM collides with, the PKA.

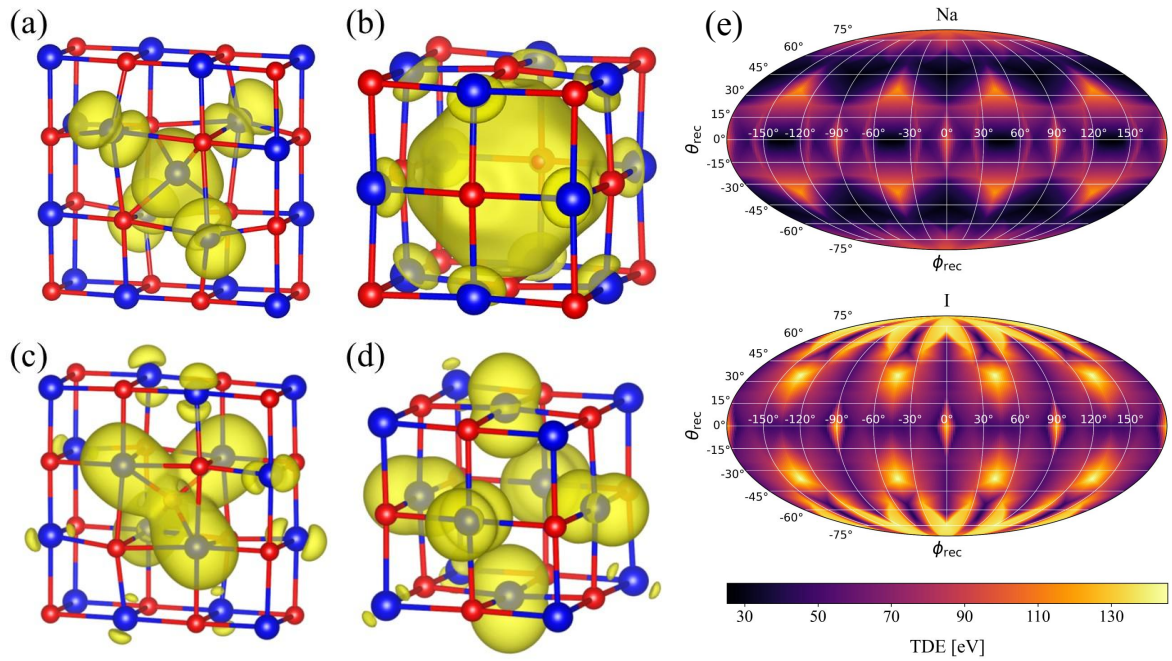

Figure 2.6: (a-b) Iodine interstitial atom and its corresponding vacancy. The yellow surfaces indicate the charge density associated to the states present in the electronic band gap, induced by the I defect. Na atoms are shown in red while I atoms are in blue. (c-d) Sodium interstitial atom and its corresponding vacancy. The yellow surfaces indicate the charge density associated to the states present in the energy range [-3.4,-2.8] eV for panel (c) and [-0.6,0.0] eV for panel (d), relative to the corresponding Fermi energy (red dashed line in Fig. 2.5). (e) Mollweide projection of the TDE, in case of Na atom as the PKA (top), and the I atom (bottom). Lighter regions correspond to high TDE values, while darker ones to lower TDE values.

In Fig. 2.6 (e) a Molleweide projection of the computed TDE is reported. The lowest values of the TDE are in the [110] direction, with $\mathrm{TDE}_{\mathrm{Na}}^{[110]} = 24$ eV and $\mathrm{TDE}_{\mathrm{I}}^{[110]} = 51$ eV, while the highest TDE values are found in the [111] direction, with $\mathrm{TDE}_{\mathrm{Na}}^{[111]} = 119$ eV and $\mathrm{TDE}_{\mathrm{I}}^{[111]} = 147$ eV. We can notice that a I PKA is associated to higher TDE values. Due to the difference in the energy cost between the formation of an Na and an I interstitial atom, the former is more energetically favored. As a consequence, the collisions where the Na atom is the PKA induce an interstitial Na atom as the first defect, for all directions. When the I atoms are the PKA, some of the directions in the solid angle give rise to an interstitial I atom, while others to an Na interstitial atom.

While DFT calculations are needed to obtain information on the electronic states, MD simulations offer a valuable advantage in tracking the system's time evolution, even after the formation of the Frenkel pair. By extending the simulation time range, we observed the presence of localized vibrational modes centered on the interstitial atom. Wavelet analysis of these vibrations revealed an associated frequency above the equilibrium NaI

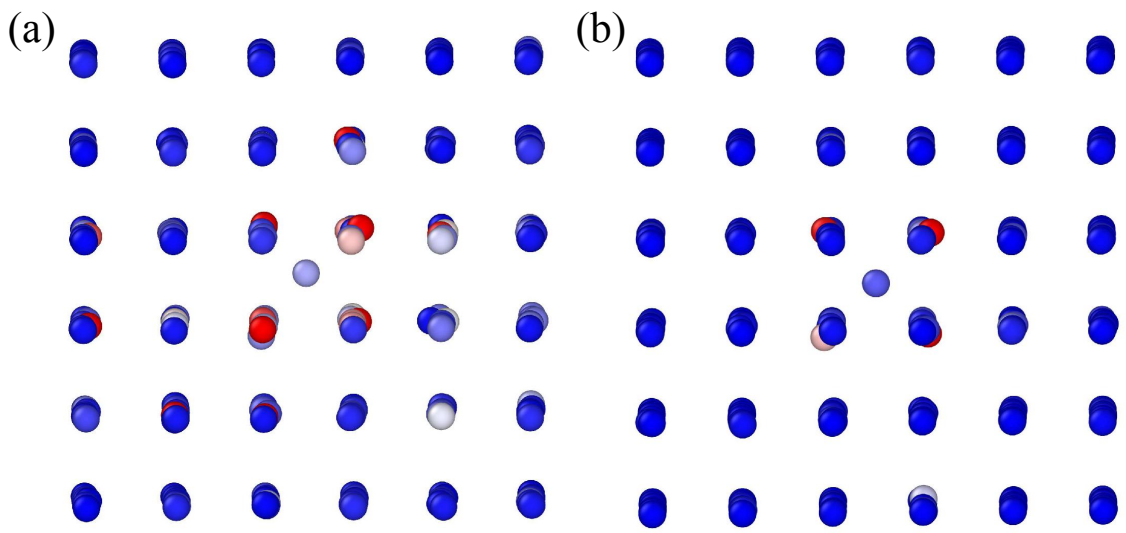

Figure 2.7: Snapshots of the molecular dynamics simulation of a 26 eV DM collision along the [110] direction on an Na PKA. Panel (a) is taken after 1 ps from the collision, while panel (b) after 20 ps. The color coding refers to the atom's kinetic energy, going from blue (lowest energy) to red (highest energy).

phonon energy range. In Fig. 2.7 (a-b) two MD snapshots at different times are shown, with atoms colored according to their kinetic energy. The deposited energy is 26 eV on an Na PKA thus resulting in the formation of an Na Frenkel pair, with the interstitial atom visible in both panels. Panel (a) corresponds to 1 ps after the collision, while panel (b) shows the state after 20 ps. While the majority of atoms lose their kinetic energy through thermalization processes, the atoms near the interstitial Na still keep vibrating after 20 ps. This anomalous behavior persists even after hundreds of ps and can be naturally explained considering the formation of localized vibrational modes with characteristic frequencies lying outside the phonon energy range and weakly coupled with the host phonon modes. All these properties closely resemble the features induced by intrinsic localized modes (ILMs), also called discrete breathers, for which NaI crystals have been identified in the literature as a prime candidate to host them [122, 123, 124, 125, 126]. The possibility of long-lasting intrinsically localized modes in the NaI detector could lead to a slower reset of the experimental signal peak. Additionally, these modes may introduce a thermal component that remains significant on the millisecond timescale, particularly in higher energy events involving the formation of multiple defects.

2.3.3 Defects effect and DM signal

The possible implications of the formation of defects are hereby discussed.
DM events, and in particular higher energy collisions, are expected to produce multiple defects, leading to a loss in the phonon signal, due to the defects formation energy as

pointed out in Refs. [113, 114]. As a consequence, the scintillation light energy and light yield, which quantifies the ratio between the light and phonon signal, can be strongly affected by the formation of defects, see Ref. [127]. In addition, defects' concentration grows up as a function of the operational time, resulting in a degradation of the detector's light output and reduction of the energy resolution [127, 128, 129].
At the same time, the phonon signal is influenced by defect formation, as a part of the energy released during a DM collision is stored as potential energy due to structural deformations. Additionally, we find that defects induce localized vibrational modes in the system, which can also affect the phonon signal's shape with a possible increase of its tail.

Focusing on the electronic channels of detection, the appearance of defect induced in-gap states can have different consequences on the electronic channels of detection. They can enable electronic excitations across the band gap, from valence bands to un-occupied in-gap states or from occupied in-gap states to the conduction bands, through various mechanisms. For example, as the in-gap states energy depends on the interstitial atoms's position, they are modulated by the "local" temperature around the defect possibly inducing a charge transfer from in-gap states towards the conduction band, acting as an "elevator state" as proposed in Refs. [112, 130, 131]. A second possible detection mechanism associated to these states could be the measurement of defect concentration after long exposure to DM flux by means of luminescence and fluorescence techniques [132, 133], in line with what was proposed for the paleo-detection of DM [134]. In addition, as shown in Fig. 2.5, iodine Frenkel pairs can allow previously forbidden transitions at lower energies, which become accessible only after a defect is formed by the collision, which can be exploited as photodetector.
It is thus interesting to investigate the effect of defects on the DM detection rate; to do so we utilize the formalism developed in Section 2.1 to describe the DM-nuclei scattering events, with the assumption of spin-independent interactions and the standard halo model.
The total DM recoil rate R is given by Eq. (2.29), with the contributions from the two nuclei types, Na and I, summed and weighted accordingly. The recoil energy integration range spans from zero (or the cutoff induced by the experimental threshold E_{thresh}) to $E^J_{R,\text{max}}$, which is given by Eq. (2.7). With the assumption of a contact interaction, we have set $F_{DM}(q) = 1$.
To predict the rate of events producing a defect, we must consider that the scattered atom is forced to generate a Frenkel pair when the recoil energy is above the TDE surface. Thus, the so-called defect rate R_{Def} has the same expression as in Eq. (2.7), but a

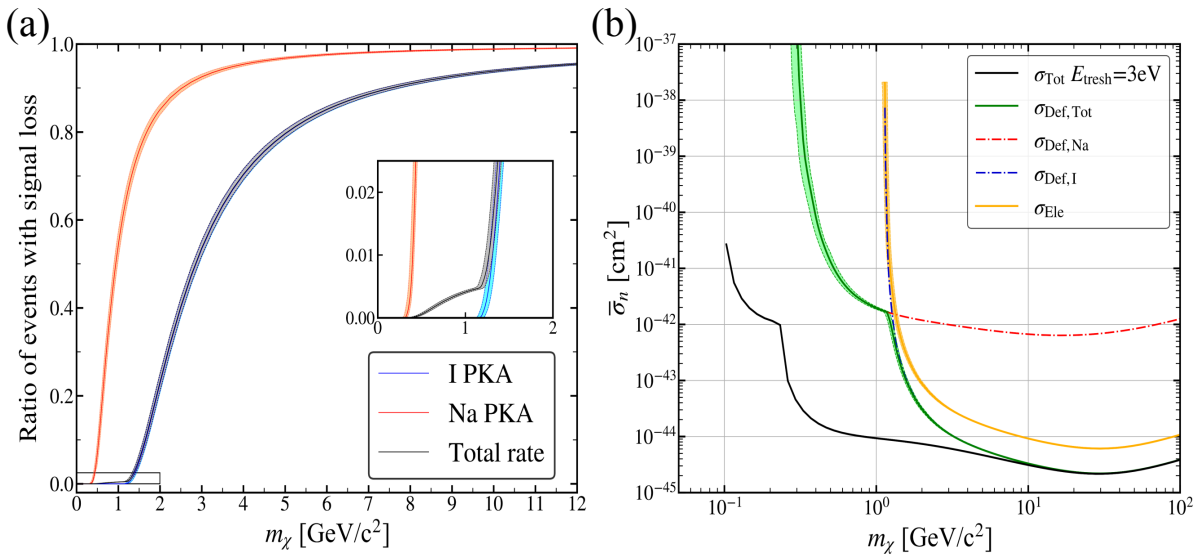

Figure 2.8: (a) Ratio of events with a signal loss due to the formation of Frenkel pairs, as a function of the DM mass and depending on the PKA. The red (blue) line shows the result obtained using the calculated TDE for Na (I), while the dashed lines correspond to a ±5 eV uncertainty on the corresponding TDE. The black line represents the ratio between the total rates $R_{\text{Def.}}/R$. The inset shows a zoom of the plot at lower masses. (b) Experimental reach as a function of the DM particle mass, assuming a 1 kg·yr exposure, and a background-free experiment. In black the total cross section is plotted assuming a threshold of 3 eV; in green the defects cross section for both Na and I is shown, the shaded region corresponds to the uncertainty window on the TDE estimate. In blue and red, dash-dotted lines, the defects cross section for I and Na individually, respectively. In yellow-orange the lower estimate for the electronic channel cross section is reported.

different energy integration range:

$$R_{\text{Def}} = \sum_J^{N_{\text{type}}} \int_\Omega d\Omega' \int_{\text{TDE}^J(\Omega')}^{E^J_{R,\max}} dE_r \frac{\partial^2 R^J}{\partial\Omega' \partial E_r} = \sum_J^{N_{\text{type}}} R^J_{\text{Def}}\,, \tag{2.31}$$

where $\text{TDE}^J(\Omega')$ represents the TDE for the J-th species as the PKA at the solid angle position Ω'. R^J_{Def} represents the single Na and I contributions to the defect rate. All rates are computed using an in-house Python code.

In Fig. 2.8 (a) we report the ratio of DM events forming at least a Frenkel pair, as a function of the DM mass, which is given by the ratio R_{Def}/R. The same ratio evaluated for the two PKA atoms is also shown.
The starting DM mass that enables the defects production is around 0.4 GeV/c^2 for Na-PKA, while for I-PKA it is 1.5 GeV/c^2. The ratio of events generating at least one defect increases for higher DM masses, reaching a value of 90% at around 2.5 GeV/c^2 in the Na

case, and 7.5 GeV/c^2 for I. We can also easily understand the difference in sodium and iodine behavior. Iodine recoil energies are smaller, and its TDE is higher; thus at the same DM masses the relative number of events forming defects will be smaller too. Due to the A_J^2 enhancement factor in the differential rate, the iodine contribution dominates, making the total defect rate closely aligned with the iodine contribution, particularly for larger DM masses. Similarly, the ratio $R_{\rm Def}/R$ largely reflects the iodine contribution, with only a minor deviation at lower masses, as shown in the inset of Fig. 2.8 (a).
Our results are extremely robust against eventual modeling-computational errors, related to the molecular dynamics simulations. In fact, even an overestimated error, as shown in Fig. 2.8 (a), has little to no effect on our quantities of interest.

We now move to the prediction of the experimental reach of an ideal experiment based on such material and the mechanism of nuclear recoils between the DM particles and the system nuclei. The result obtained assuming an exposure $\mathcal{E} = 1$ kg·yr and a background-free experiment is shown in Fig. 2.8 (b). Given the background-free assumption, imposing a confidence level (C.L.) of 95% corresponds to the detection of $N = 3$ events, thus the cross section limits have been set using Eq. (1.39). The black curve in Fig. 2.8 (b) represents the experimental reach for an experiment with a threshold of 3 eV, in which all the DM-nuclei scattering are detectable, and is computed using Eq. (2.29) rate. In green, we report the reach for an experiment based on the detection of DM events that generate at least one defect, of whatever type, using their effects on the different detection channels. The rate from Eq. (2.31) is thus adopted. The reach obtained considering only the Na or I defect rates is shown in red and blue, respectively. The DM masses at which the rate of defect-forming events becomes significant are clearly visible, as is the shift in the main contributor from Na to I atoms.
In yellow-orange we present an estimate of the experimental reach for the electronic channel, which relies on the previously discussed "elevator state" or photodetector mechanisms, enabled by the Iodine defect in-gap states.
This estimate has been performed by considering only the Iodine PKA recoils with direction in the solid angle fraction that leads to interstitial I defects, which we refer to as $\Omega_{\rm I}$. Then we can approximate the rate of events forming in-gap states as:

$$R_{\rm Ele} \sim R^{\rm I}_{\rm Def}\Big(\frac{\Omega_{\rm I}}{4\pi}\Big) \ . \tag{2.32}$$

In Fig. 2.8 (b) the result for $\Omega_{\rm I} = 0.36 \cdot (4\pi)$ is shown. This is a lower estimate for the events rate, since it does not take into account events at higher released energy that generate multiple defects, with at least one being an interstitial I atom, for directions and PKAs that at lower energies only generate an interstitial Na atom. The correct rate would also have to consider these contributions, which cannot be easily estimated, and

would lower the possible detectable cross section, matching for large DM masses the total cross section shown as a black line in Fig. 2.8 (b).

To summarize our results, we investigated the formation of defects in NaI crystals induced by dark matter collisions and their implications for direct detection experiments. By combining molecular dynamics simulations and density functional theory calculations, we characterized the main defects properties, including their formation energies, the anisotropic threshold displacement energy and their effect on the system's electronic states. In particular, we observe a modification of the states close to the valence band maximum of NaI induced by all the analyzed defects; notably, in the case of an iodine Frenkel pair, new electronic states emerge within the band gap. These states allow transitions at energies lower than the band gap, opening potential novel detection channels in NaI-based cryogenic scintillating calorimeters that can enhance their sensitivity to dark matter particles in specific mass ranges.
Furthermore, we have computed the DM-nuclei scattering rates and calculated the ratio of events that will produce a signal loss in the phonon channel due to defect formation, which can also be enhanced by the presence of localized vibrational modes.
We highlight the need for further investigations into defect formation and defect-induced charge signals in NaI-based detectors. Understanding their impact on the phonon and scintillation light channels is crucial, particularly in relation to aging effects during long-term experiments.

Chapter 3

Anisotropic DM-e^- scattering

In the last decade we have witnessed a shift in the direct detection community from the Gev-scale WIMP framework toward lighter sub-GeV DM candidates. For this range of masses, DM becomes kinematically unable to produce detectable nuclear recoils, so a new mechanism becomes necessary.
The combination of new DM models describing possible scattering mechanisms with electrons in condensed matter systems [135, 136, 137], that are accessible for much lighter DM masses, and experimental advances, like the development of ultra–low-threshold detectors, skipper CCDs and other single electrons sensitive technologies, motivated dedicated experimental programs and new analyses targeting the sub-GeV window [33, 138, 69, 139, 140]. The theoretical description of electron scatterings brings new material-dependent physics into the detection problem. In fact, electrons in condensed matter systems live in wavefunctions far from momentum-eigenstates plane waves, and the scattering rate will be described by the many-body electronic response of the target. Screening effects, band structures, local-field effects can all influence both the magnitude and spectral shape of the expected signal. It is then possible and convenient to cast the response of the system in terms of the dielectric response $\varepsilon(\mathbf{q}, \omega)$, which allows for the inclusion of these effects and can be both connected to experimentally accessible data and computed using first-principles calculations based on density functional and time dependent density functional theory (DFT/TDDFT) [141, 142, 143]. In this chapter we will first show how the dynamic structure factor can be recast in terms of the dielectric function for an electronic system, and describe the corresponding scattering rates. After describing analytical model and experimental fits for the energy loss function, we will focus on its first principles calculation, describing DFT and the response function within TDDFT. With this comprehensive overview of the different ingredients necessary to compute the dielectric function of a system, we will describe a set of new implementations that we developed to improve the first principle calculation of the dielectric function, with the goal of making the calculation

of anisotropic scattering rates, like for the DM-e^- scattering and the Migdal effect, more accurate and efficient.

3.1 DM Electron scattering rate

To describe the spin-independent scattering between DM and electrons, we will need the appropriate dynamic structure factor. Starting from Eq. (2.9) we focus only on the electronic term:

$$S(\mathbf{q},\omega) = \frac{2\pi}{V}\sum_f |\langle f|\sum_k^{N_{\rm ele}} f_e\ e^{i\mathbf{q}\cdot\mathbf{r}_k}|i\rangle|^2\ \delta(E_f - E_i - \omega)\ ; \tag{3.1}$$

the coupling constant f_e is equal for all electrons and can be absorbed in the definition of the cross section $\bar{\sigma}_e$. We can rewrite this expression by introducing the electron number density operator, which is the Fourier transform of the electronic density:

$$n_{\mathbf{q}} = \sum_k^{N_{\rm ele}}\ e^{i\mathbf{q}\cdot\mathbf{r}_k} = \int d^3\mathbf{r}\ e^{i\mathbf{q}\cdot\mathbf{r}}\ \sum_k^{N_{\rm ele}}\delta^{(3)}(\mathbf{r}-\mathbf{r_k})\ . \tag{3.2}$$

The dynamic structure factor will thus be rewritten as:

$$S(\mathbf{q},\omega) = \frac{2\pi}{V}\sum_f |\langle f|n_{\mathbf{q}}|i\rangle|^2\ \delta(E_f - E_i - \omega)\ . \tag{3.3}$$

This expression can be recast in terms of the material response function. To show this, we substitute the δ-function by using its definition $\delta(E_f - E_i - \omega) = \frac{1}{2\pi}\int_{-\infty}^{\infty} dt\ e^{i(E_f-E_i-\omega)t}$. Then:

$$\begin{aligned} S(\mathbf{q},\omega) &= \frac{1}{V}\int_{-\infty}^{\infty} dt\ \sum_f \langle i|n_{\mathbf{q}}^\dagger|f\rangle\langle f|n_{\mathbf{q}}|i\rangle\ \ e^{i(E_f-E_i-\omega)t} = \\ &= \frac{1}{V}\int_{-\infty}^{\infty} dt\ e^{-i\omega t}\sum_f \langle i|n_{\mathbf{q}}^\dagger|f\rangle\langle f|e^{iE_f t}n_{\mathbf{q}}\ e^{-iE_i t}|i\rangle = \\ &= \frac{1}{V}\int_{-\infty}^{\infty} dt\ e^{-i\omega t}\langle i|n_{-\mathbf{q}}(0)n_{\mathbf{q}}(t)|i\rangle = \frac{1}{V}\int_{-\infty}^{\infty} dt\ e^{i\omega t}\langle n_{\mathbf{q}}(t)n_{-\mathbf{q}}(0)\rangle\ , \end{aligned} \tag{3.4}$$

where we used the Hermitian property of the density operator $n_{\mathbf{q}}^\dagger = n_{-\mathbf{q}}$, the completeness relation $\sum_f |f\rangle\langle f| = \mathcal{I}$, and the time evolution of states and operators: $e^{-iE_i t}|i\rangle = e^{-iHt}|i\rangle$, $\langle f|e^{iE_f t} = \langle f|e^{-iHt}$, and $n_{\mathbf{q}}(t) = e^{iHt}n_{\mathbf{q}}(0)e^{-iHt}$. Finally, we used the fact that ground-state expectation values satisfy the relation $\langle A(0)B(t)\rangle = \langle B(-t)A(0)\rangle$ for Hermitian operators, and changed integration variable $t \to -t$.

This expression can be rewritten in terms of the retarded density-density response function $\chi(\mathbf{q},\omega)$, which describes the linear response of the system to an external perturbation, and is written as the density-density correlation function [144, 145]:

$$S(\mathbf{q},\omega) = -2\ \mathrm{Im}\bigg(-\frac{i}{V}\int_0^\infty dt\ e^{i\omega t}\langle[n_{\mathbf{q}}(t), n_{-\mathbf{q}}(0)]\rangle\bigg) = -2\ \mathrm{Im}\big(\chi(\mathbf{q},\omega)\big), \tag{3.5}$$

where $[\ldots,\ldots]$ indicates the commutator operator. This identity represents the fluctuation-dissipation theorem at zero temperature, which relates the intrinsic quantum fluctuations of the system, encoded by the density-density correlation function, to its dissipative response to an external field. The quantity $S(\mathbf{q},\omega)$ will describe how the system absorbs energy and momentum from a probe, whether it is a dark matter particle or a SM probe.
The dark matter particles couple to the electron number density, interacting with the target material via perturbations to such density and not to current or spin degrees of freedom. This implies that only the longitudinal response of the material electromagnetic response contributes to the scattering process; while transverse fields which correspond to radiation and current responses are negligible due to the non-relativistic nature of DM particles. We then want to show the relation between the density-density response function $\chi(\mathbf{q},\omega)$ and the longitudinal dielectric function $\varepsilon_L(\mathbf{q},\omega)$ (in the following we will drop the L subscript from our notation for simplicity).

3.1.1 Dielectric function definition

Let's consider a longitudinal electric field $\mathbf{E}$, which is parallel to the wave vector $\mathbf{q}$ and satisfies $\mathrm{rot}\mathbf{E} = 0$. Since the electric field is irrotational an electrostatic potential such that $\mathbf{E} = -\nabla\phi$ exists; the first Maxwell equation $\mathrm{div}\mathbf{E} = \frac{\rho}{\varepsilon_0}$ can then be rewritten as the Poisson equation $-\Delta\phi(\mathbf{q},\omega) = \frac{\rho(\mathbf{q},\omega)}{\varepsilon_0}$. Rewriting this equation in Fourier space and relating the charge density to the number density $\rho = en$ and the electrostatic potential ϕ to the potential energy v, $\phi = v/e$, we obtain:

$$v(\mathbf{q},\omega) = \frac{e^2}{q^2\varepsilon_0} n(\mathbf{q},\omega)\ . \tag{3.6}$$

When an external perturbation v_{ext} is present, there will be an induced charge density in the system $\rho_{\mathrm{ind}} = en_{\mathrm{ind}}$, and the total potential v_{tot} will be given by the sum of the external potential v_{ext} and the induced potential $v_{\mathrm{ind}} = \frac{e^2}{q^2\varepsilon_0} n_{\mathrm{ind}}$.
The relation between the variation of the system's density δn and the external perturbation v_{ext} is described by the density response function χ:

$$n_{\mathrm{ind}}(\mathbf{q},\omega) = \chi(\mathbf{q},\omega) v_{\mathrm{ext}}(\mathbf{q},\omega)\ . \tag{3.7}$$

The dielectric function is instead defined by the relation between the total potential and the external potential:

$$v_{\rm tot} = \frac{v_{\rm ext}}{\varepsilon(\mathbf{q},\omega)} \ . \tag{3.8}$$

Combining these different notions we can write the following relation:

$$v_{\rm tot} = \frac{v_{\rm ext}}{\varepsilon(\mathbf{q},\omega)} = v_{\rm ext} + v_{\rm ind} = v_{\rm ext} + \frac{e^2}{q^2\varepsilon_0}\chi(\mathbf{q},\omega)v_{\rm ext}(\mathbf{q},\omega). \tag{3.9}$$

It is useful to define the Fourier transform of the Coulomb kernel $v(q) = \frac{e^2}{q^2\varepsilon_0}$; expressed in natural units it writes as $v(q) = \frac{4\pi\alpha}{q^2}$ since $\varepsilon_0 = 1$ and $e^2 = 4\pi\alpha$, with $\alpha \simeq 1/137$ the fine structure constant. In cgs-Gaussian units $1/\epsilon_0 = 4\pi$ and $\alpha = e^2$, so $v(q) = \frac{4\pi e^2}{q^2}$; in the following we will continue using natural units. From Eq. (3.9) we obtain the relation between the dielectric function and the response function:

$$\frac{1}{\varepsilon(\mathbf{q},\omega)} = 1 + v(q)\chi(\mathbf{q},\omega) \ , \tag{3.10}$$

then by inverting this relation we obtain:

$$\mathrm{Im}\Big(\chi(\mathbf{q},\omega)\Big) = \frac{q^2}{4\pi\alpha}\mathrm{Im}\Big(\frac{1}{\varepsilon(\mathbf{q},\omega)}\Big) \ . \tag{3.11}$$

An important quantity that is worth introducing is the polarizability P, defined by $n_{\rm ind} = Pv_{\rm tot}$. Then by following analogous steps as in Eq. (3.9), we can find the relation:

$$\varepsilon(\mathbf{q},\omega) = 1 - v(q)P(\mathbf{q},\omega). \tag{3.12}$$

Multiplying Eq. (3.10) and Eq. (3.12) we can obtain a relation between the density-density response function χ (also called reducible polarizability), and the screened response function P (also called irreducible polarizability):

$$\chi(\mathbf{q},\omega) = P(\mathbf{q},\omega) + P(\mathbf{q},\omega)v(q)\chi(\mathbf{q},\omega) \ , \tag{3.13}$$

which has the form of a Dyson equation.

3.1.2 Scattering rate expressions

Substituting Eq. (3.11) in Eq. (3.5) we can relate the dynamic structure factor to the dielectric function:

$$S(\mathbf{q},\omega) = \frac{q^2}{2\pi\alpha}\mathrm{Im}\Big(-\frac{1}{\varepsilon(\mathbf{q},\omega)}\Big) = \frac{q^2}{2\pi\alpha}\mathcal{W}(\mathbf{q},\omega), \tag{3.14}$$

where $\mathcal{W}(\mathbf{q},\omega)$ is the energy loss function (ELF). To better understand its meaning we can rewrite the ELF by expressing the complex dielectric function as $\varepsilon(\mathbf{q},\omega) = \varepsilon_1(\mathbf{q},\omega) + i\varepsilon_2(\mathbf{q},\omega)$

and multiplying and dividing the argument by its complex conjugate:

$$\mathrm{Im}\bigg(-\frac{1}{\varepsilon(\mathbf{q},\omega)}\bigg)=\mathrm{Im}\bigg(\frac{-\varepsilon_1(\mathbf{q},\omega)+i\varepsilon_2(\mathbf{q},\omega)}{|\varepsilon(\mathbf{q},\omega)|^2}\bigg)=\frac{\varepsilon_2(\mathbf{q},\omega)}{|\varepsilon(\mathbf{q},\omega)|^2}\ . \tag{3.15}$$

We can see how the energy loss function is equal to the imaginary part of the dielectric function divided by the so-called screening factor $|\varepsilon(\mathbf{q},\omega)|^2$.

We can substitute the newly found dynamic structure factor in the scattering rate described by Eq. (1.14), obtaining:

$$\begin{aligned}R(t)&=\frac{1}{\rho_{\mathrm{T}}}\frac{\rho_\chi}{m_\chi}\int\frac{d^3\mathbf{q}}{(2\pi)^3}\int d\omega\ g(\mathbf{q},\omega;t)\ \frac{\pi\bar{\sigma}(q)}{\mu_{\chi e}^2}\ \frac{q^2}{2\pi\alpha}\mathcal{W}(\mathbf{q},\omega)=\\&=\frac{1}{\rho_{\mathrm{T}}}\frac{\rho_\chi}{m_\chi}\frac{\bar{\sigma}_e}{\mu_{\chi e}^2}\frac{1}{2\alpha}\int\frac{d^3\mathbf{q}}{(2\pi)^3}\ q^2F_{DM}(q)^2\int d\omega\ g(\mathbf{q},\omega;t)\ \mathcal{W}(\mathbf{q},\omega)=\\&=\frac{1}{\rho_{\mathrm{T}}}\frac{\rho_\chi}{m_\chi}\frac{\bar{\sigma}_e}{\mu_{\chi e}^2}\frac{1}{2\alpha}\int\frac{dq}{(2\pi)^3}\ q^3F_{DM}(q)^2\int d\omega\int_\Omega d\Omega'\hat{f}_\chi(v_{\min},\hat{\mathbf{q}};t)\ \mathcal{W}(\mathbf{q},\omega)\ .\end{aligned} \tag{3.16}$$

Here $\bar{\sigma}_e$ represents the DM-e^- fiducial cross section, $\mu_{\chi e}$ the DM-electron reduced mass and $F_{DM}(q)$ is the DM form factor, $F_{DM}(q)=\frac{\alpha^2m_e^2+m_{A'}^2}{q^2+m_{A'}^2}$ for the dark photon model, with its two limits being $F_{DM}\to 1$ for the massive mediator and $F_{DM}\to\frac{\alpha^2m_e^2}{q^2}$ for the massless mediator. If the angular dependency of the ELF is neglected $\mathcal{W}(\mathbf{q},\omega)\to\mathcal{W}(q,\omega)$, we obtain the isotropic rate:

$$\begin{aligned}R^{\mathrm{iso}}(t)&=\frac{1}{\rho_{\mathrm{T}}}\frac{\rho_\chi}{m_\chi}\frac{\bar{\sigma}_e}{\mu_{\chi e}^2}\frac{1}{2\alpha}\int\frac{dq}{2\pi^2}\ q^3F_{DM}(q)^2\int d\omega\ \mathcal{W}(q,\omega)\int_\Omega\frac{d\Omega'}{4\pi}\hat{f}_\chi(v_{\min},\hat{\mathbf{q}};t)=\\&=\frac{1}{\rho_{\mathrm{T}}}\frac{\rho_\chi}{m_\chi}\frac{\bar{\sigma}_e}{(2\pi)^2\mu_{\chi e}^2}\frac{1}{2\alpha}\int dq\ q^3F_{DM}(q)^2\int d\omega\ \mathcal{W}(q,\omega)\ \eta(v_{\min};t)\ .\end{aligned} \tag{3.17}$$

As usual, the same result can be obtained directly from Eq. (1.20) by substituting the dynamic structure factor. As mentioned in the previous chapters to remove the time dependency of the rate, an average Earth's speed should be used.

Finite temperature effects To introduce the effect of temperature a slight modifications to our formulas is performed by introducing the weights of the initial states in the dynamic structure factor:

$$S(\mathbf{q},\omega)=\frac{2\pi}{V}\sum_{i,f}\frac{e^{-\beta E_i}}{Z}|\langle f|\sum_k^{N_{\mathrm{ele}}}f_e\ e^{i\mathbf{q}\cdot\mathbf{r}_k}|i\rangle|^2\ \delta(E_f-E_i-\omega)\ , \tag{3.18}$$

where $\beta=1/k_BT$ and Z is the system's partition function. Following the previous steps one arrives to the relation:

$$S(\mathbf{q},\omega)=-2\ \frac{1}{(1-e^{-\beta\omega})}\mathrm{Im}\big(\chi(\mathbf{q},\omega)\big)=\frac{q^2}{2\pi\alpha}\frac{1}{(1-e^{-\beta\omega})}\mathrm{Im}\bigg(-\frac{1}{\varepsilon(\mathbf{q},\omega)}\bigg), \tag{3.19}$$

and the rate will thus become:

$$\begin{aligned} R(t) =& \frac{1}{\rho_{\rm T}} \frac{\rho_\chi}{m_\chi} \frac{\bar{\sigma}_e}{\mu_{\chi e}^2} \frac{1}{2\alpha} \int \frac{dq}{(2\pi)^3}\, q^3 F_{DM}(q)^2 \times \\ & \times \int d\omega\, \frac{1}{(1-e^{-\beta\omega})} \int_\Omega d\Omega' \hat{f}_\chi(v_{\rm min}, \hat{\mathbf{q}}; t)\, \mathcal{W}(\mathbf{q}, \omega)\ . \end{aligned} \tag{3.20}$$

Now, since the energy associated to the electronic channel are of the order of the eV, this term can be neglected for experiments performed at low temperatures.

Ionization signal Experiments aiming at detecting DM-e^- scatterings do not measure directly the deposited energy ω, but the ionization signal Q, which is the number of electron-hole pairs produced in a given event. Although modeling the conversion from deposited energy to ionization exactly is extremely challenging, a common approximation is to assume a linear response. In this picture, in addition to the primary electron–hole pair created by the initial scattering, an extra electron–hole pair is produced for every additional energy ϵ deposited above the band-gap energy $E_{\rm gap}$. Here, ϵ is the mean energy required to produce one electron–hole pair and can be measured experimentally; for silicon, ϵ=3.6 eV and $E_{\rm gap}$=1.11 eV. The relation between the deposited energy and the number of electron–hole pairs is therefore [135]:

$$Q(\omega) = 1 + \left\lfloor \frac{\omega - E_{\rm gap}}{\epsilon} \right\rfloor\ . \tag{3.21}$$

Inverting this relation we can define the minimum and maximum deposited energy that will produce Q_i electron-hole pairs: $\omega_{\rm min}(Q_i) = E_{\rm gap} + \epsilon\,(Q_i - 1)$ and $\omega_{\rm max}(Q_i) = E_{\rm gap} + \epsilon\, Q_i$.
The differential rate with respect to the ionization channel Q is obtained by integrating $dR/d\omega$ in the corresponding energy window:

$$\left.\frac{dR(t)}{dQ}\right|_{Q=Q_i} = \int_{\omega_{\rm min}(Q_i)}^{\omega_{\rm max}(Q_i)} d\omega\ \frac{dR(t)}{d\omega}\ . \tag{3.22}$$

A given experiment will have a threshold ionization value $Q_{\rm thr}$, below which it cannot detect electrons excited from the DM event; the optimal threshold is $Q_{\rm thr} = 1$, which corresponds to being sensible to deposited energy of $\omega = E_{\rm gap}$. The minimum DM mass to which an experiment is sensible to is obtained considering a DM particle with velocity $v_{\rm max}$ exciting $Q_{\rm thr}$ electrons:

$$m_\chi^{\rm min} = \frac{2}{(v_{\rm esc} + v_\oplus + v_{\rm orbit})^2} \left[E_{\rm gap} + \epsilon\,(Q_{\rm thr} - 1)\right]\ . \tag{3.23}$$

This equation leads to $m_\chi^{\rm min} \approx 0.3$ MeV and 1.4 MeV when substituting for $Q_{\rm thr} = 1$ and $Q_{\rm thr} = 2$, respectively, for Silicon.
Given a threshold ionization the total rate for an experiment will be given by:

$$R(t; Q_{\rm thr}) = \sum_{Q_i = Q_{\rm thr}}^{Q_{\rm max}} \left.\frac{dR(t)}{dQ}\right|_{Q=Q_i}\ , \tag{3.24}$$

where $Q_{\max}$ indicates the maximum number of ionizations kinematically allowed (or to which the experiment is sensitive).
The last ingredient left to calculate is the energy loss function $\mathcal{W}(\mathbf{q},\omega)$, which we will discuss in the following.

3.1.3 Energy loss function

We will now discuss two widely used models for the energy loss function: the free electron gas and the Mermi

n oscillators. We will then move to a fully ab-initio description based on density functional theory.

Free electron gas The free-electron gas (FEG) dielectric function is a particularly useful analytic model that describes the main scales of the dielectric function. The electrons are described to fill an isotropic Fermi sphere with no lattice structure or band gap; the electrons wavefunctions are thus plane waves. The resulting dielectric function (which is often called Lindhard function) will then be given by [146]:

$$\varepsilon_{\mathrm{FEG}}(q,\omega;\omega_p) = 1 + \frac{3\omega_p^2}{q^2 v_F^2}\left[f_1\left(\frac{\omega}{qv_F},\frac{q}{2m_e v_F}\right) + i f_2\left(\frac{\omega}{qv_F},\frac{q}{2m_e v_F}\right)\right] , \tag{3.25}$$

where

$$\begin{aligned} f_1(u,z) &= \frac{1}{2} + \frac{1}{8z}[g(z-u)+g(z+u)], \\ f_2(u,z) &= \begin{cases} \frac{\pi}{2}u \ , & z+u<1 \ , \\ \frac{\pi}{8z}(1-(z-u)^2) \ , & |z-u|<1<z+u \ , \\ 0 \ , & |z-u|>1 \ , \end{cases} \\ g(x) &= (1-x^2)\log\left|\frac{1+x}{1-x}\right| \ . \end{aligned} \tag{3.26}$$

The parameters that present in these expressions are: the Fermi wave vector $k_F = (3\pi^2 n_e)^{\frac{1}{3}}$, the Fermi velocity $v_F = \frac{k_F}{m_e}$, the plasma frequency $\omega_p = \sqrt{\frac{4\pi\alpha n_e}{m_e}}$. These expressions result in the relation $v_F = \left(\frac{3\pi\omega_p^2}{4\alpha m_e^2}\right)^{\frac{1}{3}}$.
The free electron gas ELF also satisfies an integral constraint, known as the f-sum rule:

$$\int_0^\infty d\omega \ \omega \ \mathcal{W}_{\mathrm{FEG}}(q,\omega) = \frac{\pi}{2}\omega_p^2 \ . \tag{3.27}$$

This analytical model can be very useful to understand the different behaviors of the ELF.

$$\lim_{q\to 0} \mathcal{W}_{\mathrm{FEG}}(q,\omega) = \frac{\pi\omega_p}{2}\delta(\omega-\omega_p) \ . \tag{3.28}$$

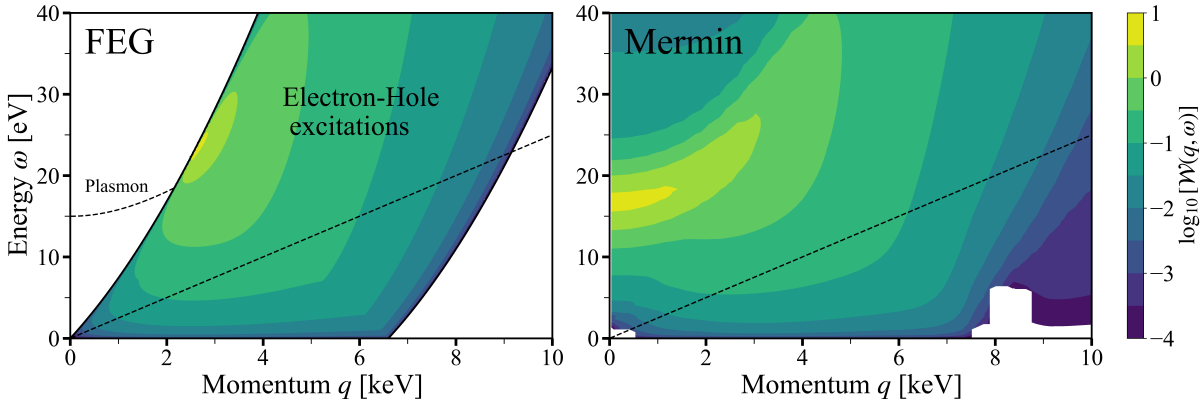

Figure 3.1: Energy loss function as a function of energy and momentum, for the free electron gas (left) and the Mermin model for Si (right), data from Ref. [147]. For the free electron gas we used ω_p =15 eV and $k_F = 3.3$ keV, chosen as representative reference values for Si [148]. The zero-width plasmon for the free electron gas is shown by a dashed line and corresponding text. The kinetically accessible region is bounded by $\omega < q \cdot v$; here this limit, with $v = 2.5 \cdot 10^{-3}$, is shown by a dashed line.

Mermin oscillators In real materials, plasmon peaks acquire a finite width. In dielectrics such as Si and Ge, this broadening is dominated by Landau damping, which arises when the collective oscillation transfers energy into single-particle excitations, and electron–phonon scattering; both of which shorten the plasmon lifetime and smear out the spectral feature [149]. This effect can be included in the Mermin model for the dielectric function, which generalizes the FEG expression in the presence of broadening, using the corresponding parameter Γ [150]:

$$\varepsilon_{\rm Mer}(q,\omega;\omega_p,\Gamma) = 1 + \frac{(1+i\Gamma/\omega)(\varepsilon_{\rm FEG}(q,\omega+i\Gamma)-1)}{1+(i\Gamma/\omega)\frac{\varepsilon_{\rm FEG}(q,\omega+i\Gamma)-1}{\varepsilon_{\rm FEG}(q,0)-1}} \; ; \tag{3.29}$$

we can easily notice how $\varepsilon_{\rm Mer}(q,\omega;\omega_p,0) = \varepsilon_{\rm FEG}(q,\omega;\omega_p)$. The behaviour in the $q \to 0$ limit will be given by:

$$\lim_{q\to 0} \mathcal{W}_{\rm Mer}(q,\omega) = \frac{\omega_p^2 \omega \Gamma}{(\omega^2-\omega_p^2)^2+\omega^2\Gamma^2} \; . \tag{3.30}$$

But although it now includes a finite plasmon width, $\varepsilon_{\rm Mer}$ still describes a homogeneous electron gas, so a further step is to phenomenologically describe a material as a superposition of many electron gas clouds with different densities. Then the ELF will be described by a linear combination of Mermin dielectric functions:

$$\mathrm{Im}\left[\frac{-1}{\varepsilon(q,\omega)}\right] = \sum_i A_i(q)\,\mathrm{Im}\left[\frac{-1}{\varepsilon_{\rm Mer}(q,\omega;\omega_{p,i},\Gamma_i)}\right]\theta(\omega-\omega_{{\rm edge},i}) \; , \tag{3.31}$$

with

$$A_i(q) = A_i(0)\frac{\int_0^\infty d\omega\,\omega\,\mathrm{Im}\left[\frac{-1}{\varepsilon_{\rm Mer}(0,\omega;\omega_{p,i},\Gamma_i)}\right]\theta(\omega-\omega_{{\rm edge},i})}{\int_0^\infty d\omega\,\omega\,\mathrm{Im}\left[\frac{-1}{\varepsilon_{\rm Mer}(q,\omega;\omega_{p,i},\Gamma_i)}\right]\theta(\omega-\omega_{{\rm edge},i})} \; . \tag{3.32}$$

The parameters $\omega_{p,i}$, Γ_i, $\omega_{\text{edge},i}$ and $A_i(0)$ are fitted to experimental data of the electron loss function.
In Fig. 3.1 a plot of the ELF as a function of momentum and energy is showed for the free electron gas and using the Mermin oscillator fit on Si. While this method can greatly improve the ELF description, it still requires sufficient experimental data to be present in the literature, which can be lacking, especially in the high-k regime, since most of the data are taken in the optical limit. Additionally, we do not have directional information to compute the general DM-electron scattering rate.
Calculating the dielectric function of a material using first principles techniques leads to an anisotropic and more accurate result for the material of choice, free from the necessity of previous experiments on such material. In the following section, we introduce the main concepts of density functional theory and derive the expressions for the dielectric constant.

3.2 Ab-initio calculation of dielectric functions

Density-functional theory (DFT) is a computational quantum mechanical modeling method used to investigate the electronic structure of many-body systems.
The fundamental idea is that the properties of a system of many interacting particles can be viewed as a functional of the ground state charge density $n_0(\mathbf{r})$.
DFT is among the most popular and versatile methods available in condensed-matter physics, computational physics, and computational chemistry.
In this section, we will first define the basics of DFT through the Hohenberg-Kohn (HK) theorem [151] and introduce the Kohn-Sham (KS) ansatz [152], which allows an approximated solution of the many-body problem by introducing an auxiliary system of independent particles, the KS electrons. We then focus on defining the Kohn-Sham response function, its relation with the many-body response function and the longitudinal dielectric function in a crystal. Ref.s [153, 154] have been used as main references throughout this section.

3.2.1 Density Functional Theory

Density Functional Theory provides an exact reformulation of the quantum many-body problem in terms of the particle density.

The Hohenberg-Kohn theorems

Consider a system of N electrons in an external potential $V_{\text{ext}}(\mathbf{r})$, governed by the Hamiltonian [151]:

$$\hat{H} = -\frac{1}{2m_e}\sum_i \nabla_i^2 + \sum_i v_{\text{ext}}(\mathbf{r}_i) + \frac{1}{2}\sum_{i\neq j}\frac{4\pi\alpha}{|\mathbf{r}_i - \mathbf{r}_j|}. \tag{3.33}$$

The first Hohenberg and Kohn theorem asserts that the ground-state density $n_0(\mathbf{r})$ uniquely

determines the external potential $V_{\text{ext}}(\mathbf{r})$ up to an additive constant. Consequently, the full many-body Hamiltonian, and thus all many-body wavefunctions and all the system's properties, are determined by $n_0(\mathbf{r})$.

The second Hohenberg and Kohn theorem establishes the existence of a universal energy functional:

$$E_{\text{HK}}[n] = F_{\text{HK}}[n] + \int d\mathbf{r}\, n(\mathbf{r})\, v_{\text{ext}}(\mathbf{r}) \ , \tag{3.34}$$

where $F_{HK}[n] = T[n] + V_{ee}[n]$ contains the kinetic and interaction contributions. More importantly, the theorem states that the energy functional follows a variational principle; this ensures that the exact ground-state density $n_0(\mathbf{r})$ minimizes this functional, yielding the ground-state energy E_0. Its evaluation for any given density $n(\mathbf{r})$ results in energies larger or equal than the ground state one:

$$E_{HK}[n] \geq E_0 \, , \qquad E_{HK}[n_0] = E_0 \ . \tag{3.35}$$

Then if the functional $F_{HK}[n]$ was known, minimizing the total energy of the system $E_{HK}[n]$ with respect to variations in the density function $n(\mathbf{r})$, the exact ground state density and energy would be found.

While Hohenberg and Kohn guarantee the existence of $F_{\text{HK}}[n]$, they do not provide a constructive form. The formulation of Levy and Lieb provides an abstract way to determine the exact functional.

First, for a given density $n(\mathbf{r})$, one considers all antisymmetric wavefunctions Ψ that yield this density. Among these, the one minimizing the expectation value of the kinetic plus interaction energies defines the Levy–Lieb functional [155]:

$$F_{\text{LL}}[n] = \min_{\Psi \to n(\mathbf{r})} \langle \Psi | T + V_{ee} | \Psi \rangle \ . \tag{3.36}$$

We can see the functional F_{LL} as the minimum of the sum of kinetic plus interaction energies for all possible wavefunctions having the given density $n(\mathbf{r})$. Then the minimum over densities of the functional $E_{\text{LL}}[n] = F_{\text{LL}}[n] + \int d^3\mathbf{r}\, n(\mathbf{r})\, v_{\text{ext}}(\mathbf{r})$ leads to the ground state density $n_0(\mathbf{r})$ and energy E_0.

We have seen that a functional can be defined for any density and by minimizing it one would find the exact density and energy of the true interacting many body system; but we still have no method to find the functional other than the original definition. In practice, one adopts an approximated functional and solves the problem using the Kohn-Sham ansatz.

The Kohn-Sham ansatz

The Kohn-Sham approach consists in replacing the many body system with an auxiliary system that can be solved easily. The ansatz of Kohn and Sham assumes that the ground state density of the original interacting system is equal to that of a fictitious non-interacting system; this leads to independent particle equations that can be solved numerically, with all the many body terms

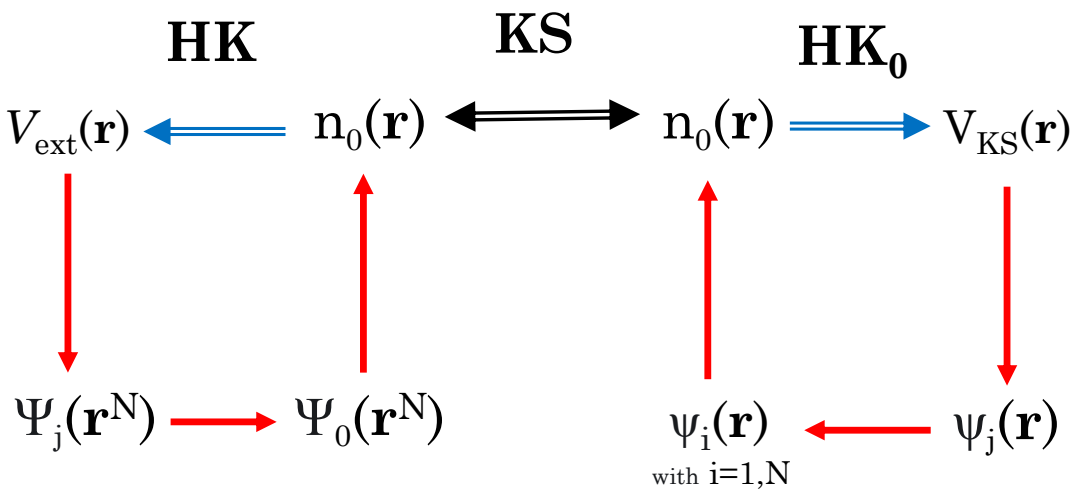

Figure 3.2: Schematic representation of the Kohn-Sham ansatz. The black arrow represents the Kohn-Sham ansatz, connecting the many-body and independent particle systems, through the ground state density. The blu arrows denote the application of the Hohenberg-Kohn theorem, with the potential that is determined from the ground state density, both for the many mody system, "HK", and the auxiliary one, "HK_0". Red arrows denote the solution of the Shröedinger equation obtaining, from the potential, the wavefunctions and from those the ground state density $n_0(\mathbf{r})$.

incorporated into an exchange-correlation functional of the density. From the solutions of these equations one can find the ground state density and energy of the original interacting system, with the accuracy only limited by the approximations in the exchange-correlation functional. In Fig. 3.2 we can see a scheme of the Kohn-Sham ansatz and the relation between the many-body problem and the independent particle auxiliary one.
The Hamiltonian describing the auxiliary independent particle system is in the form [152]:

$$\hat{H}^{\sigma}_{\mathrm{KS}} = -\frac{1}{2m_e}\nabla^2 + v^{\sigma}_{\mathrm{eff}}(\mathbf{r}) \ . \tag{3.37}$$

The ground state of the auxiliary system, which has $N = N^{\uparrow} + N^{\downarrow}$ independent electrons, will have each of the orbitals $\psi^{\sigma}_i(\mathbf{r})$ with the lowest energy eigenvalues ϵ^{σ}_i of the Hamiltonian (3.37) occupied by one electron. Then the density of the auxiliary system will be:

$$n(\mathbf{r}) = \sum_{\sigma} n(\mathbf{r},\sigma) = \sum_{\sigma}\sum_{i}^{N_\sigma} |\psi^{\sigma}_i(\mathbf{r})|^2 \ , \tag{3.38}$$

where N^{σ} is the number of electrons with spin σ. The independent-particle kinetic energy T_s is given by:

$$T_s[n] = -\frac{1}{2m_e}\sum_{\sigma}\sum_{i}^{N_\sigma} \left\langle \psi^{\sigma}_i \middle| \nabla^2 \middle| \psi^{\sigma}_i \right\rangle \ . \tag{3.39}$$

The independent particle kinetic energy T_s is given explicitly as a functional of the orbitals but for each spin σ it must be a unique functional of the density $n(\mathbf{r}, \sigma)$ by application of the Hohenberg-Kohn theorem to the independent particle Hamiltonian.
We also define the classical Coulomb interaction energy of the electron density $n(\mathbf{r})$ interacting with itself, which we refer to as Hartree energy:

$$E_H[n] = \frac{4\pi\alpha}{2} \int d^3\mathbf{r} \int d^3\mathbf{r}' \frac{n(\mathbf{r})n(\mathbf{r}')}{|\mathbf{r} - \mathbf{r}'|} \ . \tag{3.40}$$

Using these quantities, we rewrite the Hohenberg-Kohn expression for the energy functional of Eq. (3.34), in the form:

$$E_{KS}[n] = T_s[n] + E_H[n] + E_{xc}[n] + \int d^3\mathbf{r}\, n(\mathbf{r})\, v_{\text{ext}}(\mathbf{r}) \ . \tag{3.41}$$

Comparing Eq. (3.34) and Eq. (3.41) and considering that the auxiliary density is required to be equal to the true density, we can define the exchange-correlation energy as:

$$E_{xc}[n] = \langle\Psi|T|\Psi\rangle - T_s[n] + \langle\Psi|V_{ee}|\Psi\rangle - E_H[n] \ , \tag{3.42}$$

which contains all the many-body effects of exchange and correlation. So we see that the exchange-correlation energy is the difference of the kinetic energies and internal interaction energies of the true interacting many-body system from those of the auxiliary independent particle system with the electron-electron interactions replaced by the Hartree energy.
If the universal functional $E_{xc}[n]$ was known, then the exact ground state energy and density of the many-body electron problem could be found by solving the Kohn-Sham equations for independent particles. Approximated forms for this functional give us a practical method for calculating the ground state properties of the many-body electron system, with an error that is related to how well we approximated the exchange-correlation functional. In Appendix C.1 the most common approximations for the exchange-correlation functional are described.

Solving the Kohn-Sham equations

Starting from the Kohn-Sham energy functional we now need to construct the Kohn-Sham equations, which describe how the eigenvalues ϵ_i^σ and eigenfunctions ψ_i^σ can be obtained.
Since T_s is explicitly expressed in terms of the orbitals and all other terms are considered to be functionals of the density, we can vary the wavefunctions and use the chain role, obtaining the variational equation:

$$\frac{\delta E_{KS}}{\delta\psi_i^{\sigma*}(\mathbf{r})} = \frac{\delta T_s}{\delta\psi_i^{\sigma*}(\mathbf{r})} + \left[\frac{\delta E_{ext}}{\delta n(\mathbf{r},\sigma)} + \frac{\delta E_{Hartree}}{\delta n(\mathbf{r},\sigma)} + \frac{\delta E_{xc}}{\delta n(\mathbf{r},\sigma)}\right] \frac{\delta n(\mathbf{r},\sigma)}{\delta\psi_i^{\sigma*}(\mathbf{r})} = 0 \ , \tag{3.43}$$

which is subject to the orthonormalization constraints:

$$\langle \psi_i^\sigma | \psi_j^\sigma \rangle = \delta_{i,j}\delta_{\sigma,\sigma'} \ . \tag{3.44}$$

If we now use the expressions (3.38) and (3.39), which give:

$$\frac{\delta T_s}{\delta \psi_i^{\sigma *}(\mathbf{r})} = -\frac{1}{2m_e}\nabla^2 \psi_i^\sigma(\mathbf{r}) \ ; \quad \frac{\delta n^\sigma(\mathbf{r})}{\delta \psi_i^{\sigma *}(\mathbf{r})} = \psi_i^\sigma(\mathbf{r}) \ , \tag{3.45}$$

and use the Lagrange multiplier method for handling the constraints, we obtain the Kohn-Sham Shrödinger-like equations:

$$(\hat{H}_{KS}^\sigma - \epsilon_i^\sigma)\psi_i^\sigma(\mathbf{r}) = 0 \ . \tag{3.46}$$

Where H_{KS} is the Kohn-Sham auxiliary Hamiltonian and has the form of Eq. (3.37), with the effective potential given by:

$$v_{\text{eff}}^\sigma(\mathbf{r}) = v_{\text{ext}}(\mathbf{r}) + \frac{\delta E_H}{\delta n(\mathbf{r},\sigma)} + \frac{\delta E_{xc}}{\delta n(\mathbf{r},\sigma)} = v_{\text{ext}}(\mathbf{r}) + v_H(\mathbf{r}) + v_{xc}^\sigma(\mathbf{r}) \ . \tag{3.47}$$

In this expression we have introduced the Hartree potential:

$$v_H(\mathbf{r}) = 4\pi\alpha \int d^3\mathbf{r}' \frac{n(\mathbf{r}')}{|\mathbf{r}-\mathbf{r}'|} \ , \tag{3.48}$$

and the exchange-correlation potential:

$$v_{xc}^\sigma(\mathbf{r}) = \frac{\delta E_{xc}}{\delta n(\mathbf{r},\sigma)} \ . \tag{3.49}$$

The Kohn-Sham equations, Eq. (3.46), have the form of independent particle equations with the potential that must be found in a self-consistent procedure with the resulting density; they are independent on the form used for the functional $E_{xc}[n]$ and would give the exact ground state density and energy for the interacting system, if the exact functional $E_{xc}[n]$ was used.
The density functional theory calculations based on the Kohn-Sham ansatz are performed adopting the following procedure: an initial guess is chosen for the system density, from which the effective potential is calculated, defining the Kohn-Sham Hamiltonian; then the KS equations are solved, obtaining the auxiliary system eigenvalues and eigenfunctions, and the system electron density is computed.
This completes a cycle of the computation, which restarts a new iteration using the newly calculated density; the progression converges when, within a threshold error, the difference between the input and output densities of an iteration is null. When self-consistency is achieved, the properties of the system can be computed.
Additional information on DFT is reported in Appendix C.2, C.3 and C.4.
We now move to the definition of the density response function and the dielectric function in DFT.

3.2.2 Response function within TDDFT

Since DFT is a ground-state theory, it does not describe electronic excitations. To investigate optical excitations within the linear-response regime, one can instead use Time-Dependent Density Functional Theory (TDDFT). In Ref. [156], Runge and Gross demonstrated that the time dependent density $n(\mathbf{r},t)$ and the time dependent external potential $v_{\text{ext}}(\mathbf{r},t)$ are connected by a one-to-one correspondence.

As for the static version of DFT, time dependent Kohn-Sham equations can be introduced, mapping the many-body problem of interacting electrons subject to a time-dependent external potential $v_{\text{ext}}(\mathbf{r},t)$, onto a system of independent electrons subject to a time-dependent effective potential $v_{\text{eff}}(\mathbf{r},t)$.

As a result Schrödinger-like time-dependent Kohn-Sham equations are defined:

$$i\frac{\partial\psi_n(\mathbf{r},t)}{\partial t} = \left[-\frac{1}{2m_e}\nabla^2 + v_{\text{eff}}(\mathbf{r},t)\right]\psi_n(\mathbf{r},t)\ . \tag{3.50}$$

In the following we will neglect spin for simplicity. The time-dependent density will thus be defined as:

$$n(\mathbf{r},t) = 2\sum_{n\ \text{occ.}} |\psi_n(\mathbf{r},t)|^2\ , \tag{3.51}$$

where the 2 factor comes from spin degeneracy (every spatial wavefunction is occupied by two electrons of opposite spin).

Analogously to Eq. (3.47), the time-dependent effective potential will be defined as:

$$v_{\text{eff}}(\mathbf{r},t) = v_{\text{ext}}(\mathbf{r},t) + v_H(\mathbf{r},t) + v_{xc}(\mathbf{r},t)\ , \tag{3.52}$$

with the Hartree potential being equal to Eq. (3.48) but using $n(\mathbf{r}',t)$ and the time-dependent exchange-correlation potential depending both on the history of the density $n(\mathbf{r},t)$ and the initial interacting many-electron and Kohn-Sham wavefunctions.

If the external perturbation v_{ext} that acts on the system is weak, as compared to the internal electric fields induced by the ions, the induced change in the density can be described as linearly dependent on the applied perturbation.

The response function $\chi(\mathbf{r},\mathbf{r}',t-t')$ will describe the density variation $\delta n(\mathbf{r},t)$ induced by a small variation of the external perturbation $v_{\text{ext}}(\mathbf{r}',t')$:

$$\delta n(\mathbf{r},t) = \int dt' \int d^3\mathbf{r}'\ \chi(\mathbf{r},\mathbf{r}',t-t')\delta v_{\text{ext}}(\mathbf{r}',t')\ , \tag{3.53}$$

$$\chi(\mathbf{r},\mathbf{r}',t-t') = \frac{\delta n(\mathbf{r},t)}{\delta v_{\text{ext}}(\mathbf{r}',t')}\ . \tag{3.54}$$

We can also defined the Kohn-Sham response function $\chi^{KS}(\mathbf{r},\mathbf{r}',t-t')$ describing the reponse of the KS system to a variation of the effective Kohn-Sham potential v_{eff}:

$$\delta n(\mathbf{r},t) = \int dt' \int d^3\mathbf{r}' \; \chi^{KS}(\mathbf{r},\mathbf{r}',t-t')\delta v_{\text{eff}}(\mathbf{r}',t') \; , \tag{3.55}$$

$$\chi^{KS}(\mathbf{r},\mathbf{r}',t-t') = \frac{\delta n(\mathbf{r},t)}{\delta v_{\text{eff}}(\mathbf{r}',t')} \; . \tag{3.56}$$

Now, since we require that the variation of density must be equal both in the original interacting system and the auxiliary Kohn-Sham system, we can connect the interacting system response function $\chi(\mathbf{r},\mathbf{r}',t-t')$ to the KS system response function $\chi^{KS}(\mathbf{r},\mathbf{r}',t-t')$:

$$\begin{aligned} &\int dt' \int d^3\mathbf{r} \; \chi(\mathbf{r},\mathbf{r}',t-t')\delta v_{\text{ext}}(\mathbf{r}',t') = \\ &\quad = \int dt' \int d^3\mathbf{r}' \; \chi^{KS}(\mathbf{r},\mathbf{r}',t-t') \left[\delta v_{\text{ext}}(\mathbf{r}',t') + \delta v_H(\mathbf{r}',t') + \delta v_{xc}(\mathbf{r}',t')\right] \; . \end{aligned} \tag{3.57}$$

To find a more explicit form for Eq. (3.57), we rewrite δv_H and δv_{xc}. Applying the chain rule for δv_H we have:

$$\begin{aligned} \delta v_H(\mathbf{r}',t') &= \int dt_1 \int dt_2 \int d^3\mathbf{r}_1 \int d^3\mathbf{r}_2 \frac{\delta v_H(\mathbf{r}',t')}{\delta n(\mathbf{r}_1,t_1)} \frac{\delta n(\mathbf{r}_1,t_1)}{\delta v_{\text{ext}}(\mathbf{r}_2,t_2)} \delta v_{\text{ext}}(\mathbf{r}_2,t_2) = \\ &= \int dt_1 \int dt_2 \int d^3\mathbf{r}_1 \int d^3\mathbf{r}_2 \frac{4\pi\alpha}{|\mathbf{r_1}-\mathbf{r}'|} \chi(\mathbf{r}_1,\mathbf{r}_2,t_1-t_2)\delta v_{\text{ext}}(\mathbf{r}_2,t_2) \; , \end{aligned} \tag{3.58}$$

where for the second line we used Eq. (3.48) and Eq. (3.54). To rewrite the exchange-correlation term we define the exchange-correlation kernel f^{xc} as the derivative of the time-dependent exchange correlation potential $v_{xc}(\mathbf{r},t)$ with respect to the time-dependent density $n(\mathbf{r}',t')$ evaluated at the ground state density n_0:

$$v_{xc}[n_0+\delta n](\mathbf{r},t) = v_{xc}[n_0](\mathbf{r}) + \int dt' \int d^3\mathbf{r}' \; f^{xc}[n_0](\mathbf{r},\mathbf{r}',t-t')\delta n(\mathbf{r}',t') \; , \tag{3.59}$$

$$f^{xc}[n_0](\mathbf{r},\mathbf{r}',t-t') = \left.\frac{\delta v_{xc}[n](\mathbf{r},t)}{\delta n(\mathbf{r}',t')}\right|_{n=n_0} \; . \tag{3.60}$$

Then, applying the chain rule on δv_{xc} we obtain:

$$\begin{aligned} \delta v_{xc}(\mathbf{r}',t') &= \int dt_1 \int dt_2 \int d^3\mathbf{r}_1 \int d^3\mathbf{r}_2 \frac{\delta v_{xc}(\mathbf{r}',t')}{\delta n(\mathbf{r}_1,t_1)} \frac{\delta n(\mathbf{r}_1,t_1)}{\delta v_{\text{ext}}(\mathbf{r}_2,t_2)} \delta v_{\text{ext}}(\mathbf{r}_2,t_2) = \\ &= \int dt_1 \int dt_2 \int d^3\mathbf{r}_1 \int d^3\mathbf{r}_2 \, f^{xc}(\mathbf{r}',\mathbf{r}_1,t'-t_1)\chi(\mathbf{r}_1,\mathbf{r}_2,t_1-t_2)\delta v_{\text{ext}}(\mathbf{r}_2,t_2) \; . \end{aligned} \tag{3.61}$$

Substituting these expressions into Eq. (3.57), renaming the integration variables and passing to frequency space, we find the relation:

$$\begin{aligned}\chi(\mathbf{r},\mathbf{r}',\omega) =& \chi^{KS}(\mathbf{r},\mathbf{r}',\omega) + \\ &+ \int d^3\mathbf{r}_1 \int d^3\mathbf{r}_2 \; \chi^{KS}(\mathbf{r},\mathbf{r}_1,\omega)\left(\frac{4\pi\alpha}{|\mathbf{r}_1-\mathbf{r}_2|} + f^{xc}(\mathbf{r}_1,\mathbf{r}_2,\omega)\right)\chi(\mathbf{r}_2,\mathbf{r}',\omega) \; ,\end{aligned} \tag{3.62}$$

which is referred to as Dyson equation. Using the Dyson equation it is possible to evaluate the response function of the interacting electron system starting from the response function of the corresponding Kohn-Sham system, using an approximated exchange-correlation kernel. In the following, we derive the Kohn-Sham response function.

3.2.3 Derivation of the Kohn-Sham response

To derive the Kohn-Sham response function, we start by considering a time-dependent perturbation Hamiltonian:

$$\delta H(t) = e^{\eta t}\sum_{i=1}^{N}\delta v(\mathbf{r}_i,t) \; , \tag{3.63}$$

where $\delta v(\mathbf{r},t)$ is an external time-dependent potential and the factor $e^{\eta t}$, with $0<\eta\ll 1$ allows for an adiabatic switching of the perturbation, from $t\to-\infty$ where $e^{\eta t}=0$ to $t=0$ where $e^{\eta t}=1$. Using the density operator $\hat{n}(\mathbf{r})=\sum_{i=1}^{N}\delta(\mathbf{r}-\mathbf{r}_i)$ we can rewrite the perturbation Hamiltonian in frequency space as:

$$\delta H(t) = \int d^3\mathbf{r}\int\frac{d\omega}{2\pi}e^{-i(\omega+i\eta)t}\,\delta v(\mathbf{r},\omega)\hat{n}(\mathbf{r}) \; . \tag{3.64}$$

The unperturbed system, with Hamiltonian $H^{(0)}$, has a set of many-body eigenstates $|\Psi_j^{(0)}\rangle$ and eigenvalues E_j, obtained from the stationary Schrödinger equation $\hat{H}^{(0)}|\Psi_j^{(0)}\rangle = E_j|\Psi_j^{(0)}\rangle$. The time evolution of the unperturbed system is given by: $|\Psi^{(0)}(t)\rangle = e^{-iE_0t}|\Psi_0^{(0)}\rangle$, where $|\Psi_0^{(0)}\rangle$ is the unperturbed ground state and E_0 the unperturbed ground state energy. The time evolution of the perturbed system eigenstate is instead described by the time-dependent Schrödinger equation:

$$i\frac{\partial|\Psi(t)\rangle}{\partial t} = \left(\hat{H}^{(0)}+\delta\hat{H}(t)\right)|\Psi(t)\rangle \; . \tag{3.65}$$

Since we are considering small perturbations, first-order perturbation theory allows us to express $|\Psi(t)\rangle$ as the unperturbed time-dependent solution $|\Psi^{(0)}(t)\rangle$ plus a time-dependent combination of excited states of the unperturbed Schrödinger equation $e^{-iE_jt}|\Psi_j^{(0)}\rangle$:

$$|\Psi(t)\rangle = e^{-iE_0t}|\Psi_0^{(0)}\rangle + \sum_{j\neq0}a_j(t)e^{-iE_jt}|\Psi_j^{(0)}\rangle = |\Psi^{(0)}(t)\rangle + |\delta\Psi(t)\rangle \; , \tag{3.66}$$

where the time-dependent coefficient $a_j(t)$ are given by:

$$\begin{aligned} a_j(t) &= -i \int_{-\infty}^{t} dt' e^{i(E_j - E_0)t'} \langle \Psi_j^{(0)} | \delta \hat{H}(t') | \Psi_0^{(0)} \rangle = \\ &= -i \int d^3\mathbf{r}' \int \frac{d\omega}{2\pi} e^{i((E_j - E_0) - \omega - i\eta)t'} \delta v(\mathbf{r}', \omega) \langle \Psi_j^{(0)} | \hat{n}(\mathbf{r}') | \Psi_0^{(0)} \rangle = \\ &= \int d^3\mathbf{r}' \int \frac{d\omega}{2\pi} \delta v(\mathbf{r}', \omega) \langle \Psi_j^{(0)} | \hat{n}(\mathbf{r}') | \Psi_0^{(0)} \rangle \frac{e^{i((E_j - E_0) - \omega - i\eta)t'}}{\omega - (E_j - E_0) + i\eta} \, . \end{aligned} \tag{3.67}$$

The density variation induced by the time-dependent perturbation can be written as the difference between the density operator expected value using the perturbed $|\Psi(t)\rangle$ and unperturbed $|\Psi^{(0)}(t)\rangle$ wavefunctions:

$$n_{\text{ind}}(\mathbf{r}, t) = \delta n(\mathbf{r}, t) = \langle \Psi(t) | \hat{n}(\mathbf{r}) | \Psi(t) \rangle - = \langle \Psi^{(0)}(t) | \hat{n}(\mathbf{r}) | \Psi^{(0)}(t) \rangle \tag{3.68}$$

Substituting the expression for $|\Psi(t)\rangle$, Eq. (3.66), and for the coefficients $a_j(t)$, Eq. (3.67), we obtain:

$$\begin{aligned} n_{\text{ind}}(\mathbf{r}, t) &= \sum_{j \neq 0} \left[a_j(t) \langle \Psi_0^{(0)} | \hat{n}(\mathbf{r}) | \Psi_j^{(0)} \rangle e^{-i(E_j - E_0)t} + a_j^*(t) \langle \Psi_j^{(0)} | \hat{n}(\mathbf{r}) | \Psi_0^{(0)} \rangle e^{i(E_j - E_0)t} \right] = \\ &= \int \frac{d\omega}{2\pi} e^{-i(\omega + i\eta)t} \Bigg[\int d^3\mathbf{r}' \delta v(\mathbf{r}', \omega) \times \\ &\times \sum_{j \neq 0} \left(\frac{\langle \Psi_j^{(0)} | \hat{n}(\mathbf{r}') | \Psi_0^{(0)} \rangle \langle \Psi_0^{(0)} | \hat{n}(\mathbf{r}) | \Psi_j^{(0)} \rangle}{\omega - (E_j - E_0) + i\eta} - \frac{\langle \Psi_0^{(0)} | \hat{n}(\mathbf{r}') | \Psi_j^{(0)} \rangle \langle \Psi_j^{(0)} | \hat{n}(\mathbf{r}) | \Psi_0^{(0)} \rangle}{\omega + (E_j - E_0) + i\eta} \right) \Bigg] \, . \end{aligned} \tag{3.69}$$

Identifying the square brackets in the second line of Eq. (3.69) as the induced density in frequency space $n_{\text{ind}}(\mathbf{r}, \omega)$ we can define the response function to the external perturbation in frequency space as:

$$\begin{aligned} \chi(\mathbf{r},\mathbf{r}', \omega) &= \frac{\delta n(\mathbf{r}, \omega)}{\delta v(\mathbf{r}', \omega)} = \\ &= \sum_{j \neq 0} \left(\frac{\langle \Psi_j^{(0)} | \hat{n}(\mathbf{r}') | \Psi_0^{(0)} \rangle \langle \Psi_0^{(0)} | \hat{n}(\mathbf{r}) | \Psi_j^{(0)} \rangle}{\omega - (E_j - E_0) + i\eta} - \frac{\langle \Psi_0^{(0)} | \hat{n}(\mathbf{r}') | \Psi_j^{(0)} \rangle \langle \Psi_j^{(0)} | \hat{n}(\mathbf{r}) | \Psi_0^{(0)} \rangle}{\omega + (E_j - E_0) + i\eta} \right) \, . \end{aligned} \tag{3.70}$$

This result formally allows for the calculation of the response function in the many-body system but requires the knowledge of the many-body wavefunctions Ψ. But if we consider a system of independent electrons, like the KS system, in which independent electrons move in an effective potential, we gain additional knowledge on the many-body wavefunctions, which can be written as a Slater determinant of the Kohn-Sham equation solutions ψ. The ground state $\Psi_0^{(0)}$ is given by the Slater determinant of the $N/2$ lowest solution of the KS equations, while excited states $\Psi_j^{(0)}$ are obtained from the ground state $\Psi_0^{(0)}$ by moving one electron from an occupied state ψ_n to an unoccupied state ψ_m (changing the corresponding row in the Slater determinant). Then

the Slater-Condon rule can be used to evaluate the $\langle\Psi_j^{(0)}|\hat{n}(\mathbf{r})|\Psi_0^{(0)}\rangle$ terms present in Eq. (3.70):

$$\langle\Psi_j^{(0)}|\hat{n}(\mathbf{r})|\Psi_0^{(0)}\rangle = \sum_k \int d^{3\frac{N}{2}}\mathbf{r}\ \left[\Psi_j^{(0)}\left(1,\ldots,\frac{N}{2}\right)\right]^* \delta(\mathbf{r}-\mathbf{r}_k)\ \Psi_0^{(0)}\left(1,\ldots,\frac{N}{2}\right) = \psi_m^*(\mathbf{r})\psi_n(\mathbf{r})\ . \tag{3.71}$$

Substituting this result, we obtain the Kohn-Sham response function:

$$\begin{aligned}\chi^{KS}(\mathbf{r},\mathbf{r}',\omega) &= \sum_{n\ \text{occ.}}\sum_{m\ \text{unocc.}} 2\left(\frac{\psi_m^*(\mathbf{r}')\psi_n(\mathbf{r}')\psi_n^*(\mathbf{r})\psi_m(\mathbf{r})}{\omega-(\epsilon_m-\epsilon_n)+i\eta} - \frac{\psi_n^*(\mathbf{r}')\psi_m(\mathbf{r}')\psi_m^*(\mathbf{r})\psi_n(\mathbf{r})}{\omega+(\epsilon_m-\epsilon_n)+i\eta}\right) = \\ &= \sum_{n\ \text{all}}\sum_{m\ \text{all}} 2\tilde{f}_n(1-\tilde{f}_m)\left(\frac{\psi_m^*(\mathbf{r}')\psi_n(\mathbf{r}')\psi_n^*(\mathbf{r})\psi_m(\mathbf{r})}{\omega-(\epsilon_m-\epsilon_n)+i\eta} - \frac{\psi_n^*(\mathbf{r}')\psi_m(\mathbf{r}')\psi_m^*(\mathbf{r})\psi_n(\mathbf{r})}{\omega+(\epsilon_m-\epsilon_n)+i\eta}\right) = \\ &= \sum_{n\ \text{all}}\sum_{m\ \text{all}} 2(\tilde{f}_n-\tilde{f}_m)\left(\frac{\psi_m^*(\mathbf{r}')\psi_n(\mathbf{r}')\psi_n^*(\mathbf{r})\psi_m(\mathbf{r})}{\omega-(\epsilon_m-\epsilon_n)+i\eta}\right)\ .\end{aligned} \tag{3.72}$$

The factor 2 appearing in the first line comes from spin degeneracy. In the second line the sum over occupied and unoccupied states are substituted with a sum over all states by introducing the occupancy of such states $\tilde{f}_n$, which is equal to 1 if the state is occupied and 0 if empty. Finally, the third line is obtained by replacing $n \leftrightarrow m$ in the second term.

When describing periodic crystals, it is useful to rewrite the Kohn-Sham response function $\chi(\mathbf{r},\mathbf{r}',\omega)$ of Eq. (3.56), in momentum space $\chi(\mathbf{q},\mathbf{q}',\omega)$. In a periodic crystal observables follow the discrete translational symmetry $g(\mathbf{r}+\mathbf{R},\mathbf{r}'+\mathbf{R}) = g(\mathbf{r},\mathbf{r}')$, where $\mathbf{R}$ is a lattice vector. As a consequence, its Fourier transform $g(\mathbf{q},\mathbf{q}',\omega)$ will be non-zero only if the vectors $\mathbf{q}$ and $\mathbf{q}'$ differ by a reciprocal lattice vector $\mathbf{G}$. Then we can write $\mathbf{q}\to\mathbf{q}+\mathbf{G}$ and $\mathbf{q}'\to\mathbf{q}+\mathbf{G}'$, where $\mathbf{q}$ now lies in the first Brillouin zone. The Fourier transforms between real space and wavevector space in a crystal then becomes:

$$g_{\mathbf{G},\mathbf{G}'}(\mathbf{q}) = \frac{1}{V_{\text{uc}}}\int_{\text{uc}} d^3\mathbf{r}\int_{\text{uc}} d^3\mathbf{r}'\, e^{-i(\mathbf{q}+\mathbf{G})\cdot\mathbf{r}} g(\mathbf{r},\mathbf{r}') e^{i(\mathbf{q}+\mathbf{G}')\cdot\mathbf{r}'} \tag{3.73}$$

where "uc" indicates the unit cell, V_{uc} the unit cell volume, and we used the notation $g_{\mathbf{G},\mathbf{G}'}(\mathbf{q}) \equiv g(\mathbf{q}+\mathbf{G},\mathbf{q}+\mathbf{G}')$.

Substituting the real-space expression of $\chi^{KS}(\mathbf{r},\mathbf{r}',\omega)$ from Eq. (3.72) in Eq. (3.73), we obtain the Kohn-Sham response function in reciprocal space:

$$\chi^{KS}_{\mathbf{G},\mathbf{G}'}(\mathbf{q},\omega) = \frac{1}{V_{\text{uc}}\,N_k}\sum_{\mathbf{k}}\sum_{n,m}\frac{(f_{n\mathbf{k}}-f_{m\mathbf{k}+\mathbf{q}})}{\omega-(\epsilon_{m\mathbf{k}+\mathbf{q}}-\epsilon_{n\mathbf{k}})+i\eta}\left[Z_{n\mathbf{k},m\mathbf{k}+\mathbf{q}}(\mathbf{G})\right]^* Z_{n\mathbf{k},m\mathbf{k}+\mathbf{q}}(\mathbf{G}'), \tag{3.74}$$

where the matrix elements Z are defined as:

$$\begin{aligned}Z_{n\mathbf{k},m\mathbf{k}+\mathbf{q}}(\mathbf{G}) \equiv \langle\psi_{m\mathbf{k}+\mathbf{q}}|e^{i(\mathbf{q}+\mathbf{G})\cdot\mathbf{r}}|\psi_{n\mathbf{k}}\rangle &= \int_{V_{\text{uc}}} d^3\mathbf{r}\,\psi^*_{m\mathbf{k}+\mathbf{q}}(\mathbf{r})\,e^{i(\mathbf{q}+\mathbf{G})\cdot\mathbf{r}}\,\psi_{n\mathbf{k}}(\mathbf{r}) = \\ &= \int_{V_{\text{uc}}} d^3\mathbf{r}\ u^*_{m\mathbf{k}+\mathbf{q}}(\mathbf{r})\,e^{i\mathbf{G}\cdot\mathbf{r}}\,u_{n\mathbf{k}}(\mathbf{r})\ .\end{aligned} \tag{3.75}$$

In these expressions, we used Bloch's theorem, for which the single particle eigenstates and eigenfunctions are described by their band index number n and the wavevector $\mathbf{k}$ inside the first Brillouin zone, with the eigenfunctions that can be written as $\psi_{n\mathbf{k}}(\mathbf{r}) = e^{i\mathbf{k}\cdot\mathbf{r}}u_{n\mathbf{k}}(\mathbf{r})$, with $u_{n\mathbf{k}}(\mathbf{r})$ being a function that follows the lattice periodicity.
We can then substitute $n \to n\mathbf{k}$, $m \to m\mathbf{k}'$ and it can be demonstrated that matrix elements $\langle\psi_{m\mathbf{k}'}|e^{i(\mathbf{q}+\mathbf{G})\cdot\mathbf{r}}|\psi_{n\mathbf{k}}\rangle$ are non zero only if $\mathbf{k}' = \mathbf{k} + \mathbf{q}$, leading to our final expression. The factor $1/N_k$ arises because the sum over $\mathbf{k}$ represents the discretized Brillouin-zone integral, $\sum_n \to \sum_n \int_{\mathrm{BZ}} \frac{d^3\mathbf{k}}{V_{\mathrm{BZ}}} \to \frac{1}{N_k}\sum_n \sum_{\mathbf{k}}$. We write the expression in this form because DFT codes discretize the Brillouin zone to solve the Kohn-Sham equations.
The factor 2 due to spin degeneracy has been absorbed into the occupancy, defining $f_{n\mathbf{k}} = 2\tilde{f}_{n\mathbf{k}}$, to match our definition with the formalism adopted in several DFT code. The sum of the occupancy yields the total number of electrons in the crystal N: $\sum_{n\mathbf{k}} f_{n\mathbf{k}} = N_k N_{\mathrm{uc}} = N$, where N_k is the number of $\mathbf{k}$ points and N_{uc} the number of electrons in the unit cell. The product $V_{\mathrm{uc}}N_k$ represents the total crystal volume.
Analogously, the Dyson equation for the response function of Eq. (3.62) can also be rewritten in momentum space, obtaining:

$$\begin{aligned}\chi_{\mathbf{G},\mathbf{G}'}(\mathbf{q},\omega) = \chi^{KS}_{\mathbf{G},\mathbf{G}'}(\mathbf{q},\omega) + \\ + \sum_{\mathbf{G}_1,\mathbf{G}_2} \chi^{KS}_{\mathbf{G},\mathbf{G}_1}(\mathbf{q},\omega)\big(v^s_{\mathbf{G}_1,\mathbf{G}_2}(\mathbf{q}) + f^{xc}_{\mathbf{G}_1,\mathbf{G}_2}(\mathbf{q},\omega)\big)\chi_{\mathbf{G}_2,\mathbf{G}'}(\mathbf{q},\omega)\ ,\end{aligned} \tag{3.76}$$

where v^s is the symmetrized version of the Coulomb kernel $v_{\mathbf{G}_1,\mathbf{G}_2}(\mathbf{q}) = \frac{4\pi\alpha}{(\mathbf{q}+\mathbf{G}_1)^2}\delta_{\mathbf{G}_1,\mathbf{G}_2}$:

$$v^s_{\mathbf{G}_1,\mathbf{G}_2}(\mathbf{q}) = \frac{4\pi\alpha}{|\mathbf{q}+\mathbf{G}_1||\mathbf{q}+\mathbf{G}_2|}, \tag{3.77}$$

and $f^{xc}_{\mathbf{G}_1,\mathbf{G}_2}(\mathbf{q},\omega)$ is the Fourier transform of the exchange-correlation kernel of Eq. (3.60).
We now want to define the longitudinal dielectric function in crystals, connecting it to the response function.

3.2.4 Longitudinal dielectric function in crystals

Following analogous steps as those showed in subsection 3.1.1, we can define the longitudinal dielectric function in a crystal. The density response function χ and the polarizability P, which connect the induced density variation to the external potential and the total potential, respectively, will be given by:

$$\chi_{\mathbf{G},\mathbf{G}'}(\mathbf{q},\omega) = \frac{\partial n_{\mathrm{ind}}(\mathbf{q}+\mathbf{G},\omega)}{\partial v_{\mathrm{ext}}(\mathbf{q}+\mathbf{G}',\omega)}\ , \tag{3.78}$$

$$P_{\mathbf{G},\mathbf{G}'}(\mathbf{q},\omega) = \frac{\partial n_{\mathrm{ind}}(\mathbf{q}+\mathbf{G},\omega)}{\partial v_{\mathrm{tot}}(\mathbf{q}+\mathbf{G}',\omega)}\ . \tag{3.79}$$

The generalization of Eq. (3.10) will then become:

$$\begin{aligned}\varepsilon^{-1}_{\mathbf{G},\mathbf{G}'}(\mathbf{q},\omega) =& \delta_{\mathbf{G},\mathbf{G}'} + \frac{4\pi\alpha}{|\mathbf{q}+\mathbf{G}||\mathbf{q}+\mathbf{G}'|}\frac{\partial n_{\text{ind}}(\mathbf{q}+\mathbf{G},\omega)}{\partial v_{\text{ext}}(\mathbf{q}+\mathbf{G}',\omega)} = \\ =& \delta_{\mathbf{G},\mathbf{G}'} + v^s_{\mathbf{G},\mathbf{G}'}(\mathbf{q})\chi_{\mathbf{G},\mathbf{G}'}(\mathbf{q},\omega)\ ,\end{aligned} \tag{3.80}$$

where $\delta_{\mathbf{G},\mathbf{G}'}$ is the Kronecker-delta function, which is equal to 1 if $\mathbf{G} = \mathbf{G}'$ and zero otherwise. We can notice that for a given frequency ω and momentum $\mathbf{q}$, the dielectric function is a symmetric matrix in $\mathbf{G}$ and $\mathbf{G}'$, with the inversion operation performed over this matrix. The relation $\varepsilon = 1 - vP$ in a crystal will be given by:

$$\begin{aligned}\varepsilon_{\mathbf{G},\mathbf{G}'}(\mathbf{q},\omega) =& \delta_{\mathbf{G},\mathbf{G}'} - \frac{4\pi\alpha}{|\mathbf{q}+\mathbf{G}||\mathbf{q}+\mathbf{G}'|}\frac{\partial n_{\text{ind}}(\mathbf{q}+\mathbf{G},\omega)}{\partial v_{\text{tot}}(\mathbf{q}+\mathbf{G}',\omega)} = \\ =& \delta_{\mathbf{G},\mathbf{G}'} - v^s_{\mathbf{G},\mathbf{G}'}(\mathbf{q})P_{\mathbf{G},\mathbf{G}'}(\mathbf{q},\omega)\end{aligned} \tag{3.81}$$

Combining the expressions of $\varepsilon^{-1}_{\mathbf{G},\mathbf{G}'}(\mathbf{q},\omega)$ and $\varepsilon_{\mathbf{G},\mathbf{G}'}(\mathbf{q},\omega)$, we can rewrite the Dyson equation of Eq. (3.13), for a crystal:

$$\begin{aligned}\chi_{\mathbf{G},\mathbf{G}'}(\mathbf{q},\omega) =& P_{\mathbf{G},\mathbf{G}'}(\mathbf{q},\omega) + \\ &+ \sum_{\mathbf{G}_1,\mathbf{G}_2} P_{\mathbf{G},\mathbf{G}_1}(\mathbf{q},\omega)v^s_{\mathbf{G}_1,\mathbf{G}_2}(\mathbf{q})\chi_{\mathbf{G}_2,\mathbf{G}'}(\mathbf{q},\omega)\,.\end{aligned} \tag{3.82}$$

Approximations

Different approximations can be chosen to calculate the longitudinal dielectric function in a first-principle calculation. The quantity that is directly accessible in a DFT computation is χ^{KS}, which describes the response of a system of independent electrons due to a change in the effective potential they are subject to.

The most basic approximation would be $\chi = \chi^{KS}$, which implies that the system responds to the variation of external potential like an independent particles system.

The following approximation would be to substitute the polarizability P with χ^{KS}, then, using Eq. (3.81), we have:

$$\varepsilon^{\text{RPA}}_{\mathbf{G},\mathbf{G}'}(\mathbf{q},\omega) = \delta_{\mathbf{G},\mathbf{G}'} - v^s_{\mathbf{G},\mathbf{G}'}(\mathbf{q})\chi^{KS}_{\mathbf{G},\mathbf{G}'}(\mathbf{q},\omega)\ , \tag{3.83}$$

which is referred to as random phase approximation (RPA). By comparing the Dyson equation between the response function and the polarizability of Eq. (3.82), and the one between the response of the true and of the KS system of Eq. (3.76), we see that for $f^{xc} \to 0$, we regain our approximation $P_{\mathbf{G},\mathbf{G}'}(\mathbf{q},\omega) = \chi^{KS}_{\mathbf{G},\mathbf{G}'}(\mathbf{q},\omega)$, motivating it. In RPA only the classical Hartree (electrostatic) field responds to the external perturbation. Physically, this corresponds to electrons screening the perturbation through their collective Coulomb response, while all finer many-body correlation effects are neglected.

Another common approach is to consider Eq. (3.76) including the exchange-correlation kernel. In particular, the adiabatic local density approximation (ALDA) considers a frequency-independent

and local expression for the kernel:

$$f^{xc,\mathrm{ALDA}}(\mathbf{r}_1,\mathbf{r}_2) = \delta(\mathbf{r}_1-\mathbf{r}_2)\frac{\partial v_{xc}^{\mathrm{LDA}}[n]}{\partial n(\mathbf{r}_1)}\ , \tag{3.84}$$

where $v_{xc}^{\mathrm{LDA}}[n]$ is the local density approximation for the exchange-correlation potential (further described in Appendix C.1). While ALDA captures some short-range exchange–correlation effects, it still neglects memory effects and long-range excitonic interactions [157].

Macroscopic dielectric function

When considering the dielectric function for a periodic system, like a crystal, the total macroscopic electric electric field follows the periodicity of the external perturbation, while the microscopic total electric field exhibits additional rapid oscillations on the scale of the primitive cell. The distinction between the macroscopic and microscopic dielectric function is thus important. Calling $\mathbf{E}$ and $\mathbf{E}_{\mathrm{ext}}$ the total and the external macroscopic electric fields respectively, their relation is defined by:

$$\mathbf{E}(\mathbf{r},\omega) = \int d^3\mathbf{r}'\ \varepsilon^{-1}_{\mathrm{mac}}(\mathbf{r}-\mathbf{r}',\omega)\mathbf{E}_{\mathrm{ext}}(\mathbf{r}',\omega)\,, \tag{3.85}$$

where $\varepsilon_{\mathrm{mac}}$ is the macroscopic dielectric function. Since from a macroscopic prospective the system is homogeneous, the macroscopic dielectric function depends only on the position difference. As a result in momentum space, this relation translates to:

$$\mathbf{E}(\mathbf{q},\omega) = \varepsilon^{-1}_{\mathrm{mac}}(\mathbf{q},\omega)\mathbf{E}_{\mathrm{ext}}(\mathbf{q},\omega)\,. \tag{3.86}$$

The microscopic total electric field $\mathbf{e}$, has large oscillations on the atomic scale, and is connected to the external field by:

$$\mathbf{e}(\mathbf{r},\omega) = \int d^3\mathbf{r}'\ \varepsilon^{-1}(\mathbf{r},\mathbf{r}',\omega)\mathbf{E}_{\mathrm{ext}}(\mathbf{r}',\omega) \tag{3.87}$$

where ε is the microscopic dielectric function. Passing to momentum space, we will have two wavevectors $\mathbf{q}$ and $\mathbf{q}'$, but since we are in a crystal the two wavevectors difference must be a reciprocal lattice vector. We can set $\mathbf{q} = \mathbf{q}+\mathbf{G}$ and $\mathbf{q}' = \mathbf{q}+\mathbf{G}'$, and obtain:

$$\mathbf{e}(\mathbf{q}+\mathbf{G},\omega) = \sum_{\mathbf{G}'}\varepsilon^{-1}_{\mathbf{G}\mathbf{G}'}(\mathbf{q},\omega)\mathbf{E}_{\mathrm{ext}}(\mathbf{q}+\mathbf{G}',\omega)\ . \tag{3.88}$$

Now, it can be proven that for external fields varying on a much larger scale than the atomic distances, $\mathbf{q} \ll \mathbf{G}_{\mathrm{min}}$, we have $\mathbf{e}(\mathbf{q},\omega) = \mathbf{E}(\mathbf{q},\omega)$ and $\mathbf{E}_{\mathrm{ext}}(\mathbf{q}+\mathbf{G}',\omega) = \mathbf{E}_{\mathrm{ext}}(\mathbf{q},\omega)\delta_{\mathbf{G}',\mathbf{0}}$. Then comparing Eq. (3.86) and Eq. (3.88), we can find the relation between the macroscopic dielectric function and the microscopic one:

$$\begin{aligned}\varepsilon^{-1}_{\mathrm{mac}}(\mathbf{q},\omega) &= \varepsilon^{-1}_{\mathbf{00}}(\mathbf{q},\omega)\,,\\ \varepsilon_{\mathrm{mac}}(\mathbf{q},\omega) &= \frac{1}{\varepsilon^{-1}_{\mathbf{00}}(\mathbf{q},\omega)}\,.\end{aligned} \tag{3.89}$$

To obtain the macroscopic dielectric function we then have to invert the microscopic dielectric function with respect to $\mathbf{G}, \mathbf{G}'$ and then take the head $\mathbf{G} = \mathbf{G}' = \mathbf{0}$. This requirement implies that rapid oscillations described by the microscopic dielectric function at large wavevector will affect the macroscopic dielectric function; these are called local field effects (LFEs). If we instead perform the approximation $\varepsilon_{\text{mac}}(\mathbf{q}, \omega) \approx \varepsilon_{\mathbf{00}}(\mathbf{q}, \omega)$, we neglect the local field effects. LFEs matter when the electron density varies strongly within the unit cell, because the microscopic field felt by electrons differs from the averaged macroscopic field. They are thus important in materials with pronounced inhomogeneities (ionic or covalent crystals, layered systems) but are typically small in nearly homogeneous systems, such as simple metals.

Dielectric function at Γ

To study the response of a material to a perturbation with slow spatial variations, we have to consider the $\mathbf{q} \to 0$, $\mathbf{G} = \mathbf{0}$ limit.
Starting from the RPA expression, we set $\mathbf{G} = \mathbf{G}' = \mathbf{0}$ and study the limit $q \to 0$, which will depend on the direction $\hat{\mathbf{q}} = \mathbf{q}/|\mathbf{q}|$ from which we approach the limit:

$$\varepsilon_{\infty}^{\text{RPA}}(\hat{\mathbf{q}}, \omega) = \lim_{q \to 0} \varepsilon_{\mathbf{00}}^{\text{RPA}}(\mathbf{q}, \omega) = 1 - \lim_{q \to 0} \frac{4\pi\alpha}{q^2} \chi_{\mathbf{00}}^{KS}(\mathbf{q}, \omega) \ . \tag{3.90}$$

For simplicity, we will not include local fields effects in our derivation. LFEs would be included by taking $\varepsilon_{\infty}(\hat{\mathbf{q}}, \omega) = 1/[\lim_{q \to 0} \varepsilon_{\mathbf{00}}^{-1}(\mathbf{q}, \omega)]$. From Eq. (3.90) we can see that the Coulomb kernel leads to a divergence of the dielectric response, which must be compensated from the response function. It is convenient to introduce the dielectric tensor $\varepsilon_{\alpha,\beta}(\omega)$ through the relation:

$$\varepsilon_{\infty}^{\text{RPA}}(\hat{\mathbf{q}}, \omega) = \sum_{\alpha,\beta} \hat{\mathbf{q}}_{\alpha} \ \varepsilon_{\alpha\beta}(\omega) \ \hat{\mathbf{q}}_{\beta} \ . \tag{3.91}$$

To evaluate the response function in this limit we have to understand the behavior of the matrix elements $\langle \psi_{m,\mathbf{k}+\mathbf{q}_\alpha} | e^{i\mathbf{q}_\alpha \cdot \mathbf{r}} | \psi_{n\mathbf{k}} \rangle$, in the considered limit. By writing $\mathbf{q}_\alpha = \hat{\mathbf{e}}_\alpha q$, we have:

$$\lim_{q \to 0} \langle \psi_{m,\mathbf{k}+\hat{\mathbf{e}}_\alpha q} | e^{iq\hat{\mathbf{e}}_\alpha \cdot \mathbf{r}} | \psi_{n\mathbf{k}} \rangle = \lim_{q \to 0} iq \langle \psi_{m\mathbf{k}} | \hat{\mathbf{e}}_\alpha \cdot \mathbf{r} | \psi_{n\mathbf{k}} \rangle = iq \frac{\hbar}{m} \frac{\langle \psi_{m\mathbf{k}} | \mathbf{p}_\alpha | \psi_{n\mathbf{k}} \rangle}{\epsilon_{m\mathbf{k}} - \epsilon_{n\mathbf{k}}} \ , \tag{3.92}$$

where we first expanded the exponential up to first order, then used the orthogonality of the wavefunctions, and finally we substituted the matrix elements of $\mathbf{r}$ with the matrix elements of $\mathbf{p}$ by exploiting the commutation rule $[H, \mathbf{r}] = -i\frac{\hbar}{m}\mathbf{p}$. Substituting this result in the Kohn-Sham response function of Eq. (3.74), we obtain:

$$\begin{aligned} \varepsilon_{\alpha\beta}(\omega) = 1 - \lim_{q \to 0} \frac{4\pi\alpha}{q^2} \frac{1}{V_{\text{uc}} N_k} \sum_{\mathbf{k}} \sum_{n,m} \frac{(f_{n\mathbf{k}} - f_{m\mathbf{k}})}{\omega - (\epsilon_{m\mathbf{k}} - \epsilon_{n\mathbf{k}}) + i\eta} \times \\ \times \frac{q^2\hbar^2}{m_e^2} \frac{\left[\langle \psi_{m\mathbf{k}} | \mathbf{p}_\alpha | \psi_{n\mathbf{k}} \rangle\right]^* \langle \psi_{m\mathbf{k}} | \mathbf{p}_\beta | \psi_{n\mathbf{k}} \rangle}{(\epsilon_{m\mathbf{k}} - \epsilon_{n\mathbf{k}})^2} \ . \end{aligned} \tag{3.93}$$

We can see that the $1/q^2$ factor from the Coulomb kernel is perfectly compensated. When taking the limit for $q \to 0$ we have $f_{m\mathbf{k}+\mathbf{q}} \to f_{m\mathbf{k}}$ and $\epsilon_{m\mathbf{k}+\mathbf{q}} \to \epsilon_{m\mathbf{k}}$. We have thus reached the expression for the dielectric tensor:

$$\varepsilon_{\alpha\beta}(\omega) = 1 - \frac{4\pi\alpha}{V_{\mathrm{uc}}\, N_k\, m_e^2} \sum_{\mathbf{k}} \sum_{n,m} \frac{(f_{n\mathbf{k}} - f_{m\mathbf{k}}) \left[\langle \psi_{m\mathbf{k}} | \mathbf{p}_\alpha | \psi_{n\mathbf{k}} \rangle\right]^* \langle \psi_{m\mathbf{k}} | \mathbf{p}_\beta | \psi_{n\mathbf{k}} \rangle}{[\omega - (\epsilon_{m\mathbf{k}} - \epsilon_{n\mathbf{k}}) + i\eta](\epsilon_{m\mathbf{k}} - \epsilon_{n\mathbf{k}})^2} \,, \tag{3.94}$$

where we have set back $\hbar = 1$. This expression can then be used in Eq. (3.91) to compute the response for a generic direction. In a cubic crystal $\varepsilon_{\alpha\beta}(\omega)$ is diagonal, with all equal components $\varepsilon_{xx}(\omega) = \varepsilon_{yy}(\omega) = \varepsilon_{zz}(\omega)$.

3.3 Dielectric Function implementation in the GPAW code

In this section we will discuss the implementations that we introduced in the GPAW (Generalized Projected Augmented Wave) code [158, 159], which is a DFT code that implements the PAW method (see Appendix C.4 for further details), and has been often used for the calculation of the finite momentum dielectric function, in particular by the Dark Matter direct detection community.

The current version of GPAW outputs the macroscopic dielectric $\varepsilon_{\mathbf{00}}(\mathbf{q}, \omega)$, with or without the inclusion of local field effects, for a desired list of frequencies and for a given $\mathbf{q}$ vector which has to lie on the grid on which a precedent ground state calculation has been performed.

In the current version of GPAW, to compute the dielectric function outside of the first Brillouin zone, the point $\mathbf{q} + \mathbf{G}$ must be explicitly requested and $\varepsilon_{00}(\mathbf{q} + \mathbf{G})$ is computed. There are two problems in the current implementation. The first is that when $\mathbf{q} = \mathbf{\Gamma} = (0, 0, 0)$, the calculation of the macroscopic dielectric function $\varepsilon_{\mathbf{00}}(\mathbf{\Gamma} + \mathbf{G})$ results in an error because the code mismatches the request $\mathbf{q} = \mathbf{\Gamma}$, which implies the use of Eq. (3.94), and the request of a finite momentum. The second is that while it is a feasible approach to compute the dielectric function over a line in reciprocal space, it is not efficient when the sampling must cover uniformly the reciprocal space. Since we are interested in computing the integral of Eq. (3.16), the dielectric function on the full grid and over multiple Brillouin zones is required. In Fig. 3.3 we show the energy loss function obtained for Si along the [100] direction obtained using a $10 \times 10 \times 10$ $\mathbf{k}$-point grid. Since the calculation of $\varepsilon_{\mathbf{GG}}(\mathbf{\Gamma})$ in the current GPAW implementation results in a "NaN" error, we can observe that data is missing each time we cross into the subsequent Brillouin zone. We also report an incorrect behavior for longer wavevectors, which is partially corrected when the cutoff energy E_{cut}, which determines the number of used $\mathbf{G}$ vectors, is increased.

To solve these issues we first modified specific subroutines of GPAW to output the microscopic dielectric function $\varepsilon_{\mathbf{G},\mathbf{G}}(\mathbf{q}, \omega)$, which was already computed by the code, before its macroscopic component was taken. By doing this, it is sufficient to compute the dielectric function for

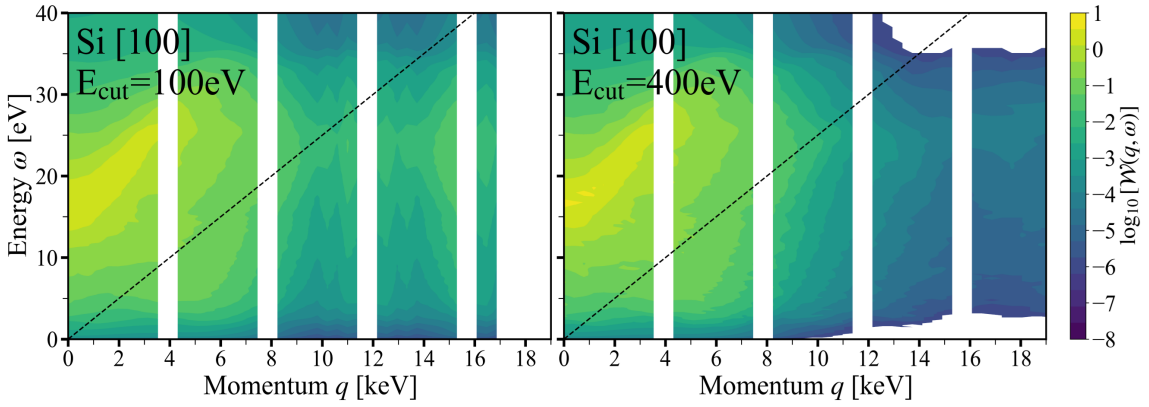

Figure 3.3: Energy loss function in logarithmic scale for Si along the [100] direction. The vertical white gaps point out how the GPAW code fails when computing the dielectric function at a reciprocal lattice vector $\mathbf{G}$. On the left panel a cutoff for the $\mathbf{G}$ wavectors of 100 eV is used, while on the right panel E_{cut}=400 eV. The dashed lines indicate the kinematically allowed region for DM-e^- scattering.

$\mathbf{q} \in 1^{\text{st}}$BZ and the mismatch causing the error when taking the macroscopic component for $\mathbf{q} = \mathbf{\Gamma} + \mathbf{G}$ is no longer present. This implementation also solves the problem observed for large wavevectors. We also output the dielectric function with the inclusion of the local field effects:

$$\varepsilon^{\text{LFE}}_{\mathbf{G},\mathbf{G}}(\mathbf{q},\omega) = \frac{1}{[\varepsilon^{-1}(\mathbf{q},\omega)]_{\mathbf{G},\mathbf{G}}} \ . \tag{3.95}$$

In the following, the superscript "LFE" will be neglected for clarity, as we will always refer to the dielectric function with local field effects included.

Properly converged calculations of the dielectric function require a dense grid of $\mathbf{k}$-points over which the wavefunction and eigenvalues are computed, becoming very computationally demanding if a high number of calculations over $\mathbf{q}$-points are also needed. Thus, to make calculations more efficient, we implemented the use of crystal symmetries for the $\mathbf{q}$-grid over which the dielectric function is computed.

3.3.1 Implementing crystal symmetries

In crystals the translational symmetry allows us to describe the system more easily defining the unit cell, with all physical properties being invariant under translation of a lattice vector $\mathbf{R} = i_0\mathbf{a_0} + i_1\mathbf{a}_1 + i_2\mathbf{a}_2$, where a_j are the primitive lattice vectors and the components are integers.

A crystal can possess also further symmetries, like rotations, reflections, and inversions, forming a group of symmetry operations, which is called space group. Calling $\hat{M}$ a symmetry operation of the crystal, then observables will be invariant under its action, for example the density follows $n(\hat{M}\mathbf{r}) = n(\mathbf{r})$, while for the dielectric function we have $\varepsilon(\hat{M}\mathbf{r}, \hat{M}\mathbf{r}') = \varepsilon(\mathbf{r}, \mathbf{r}')$. Note that if $\hat{M}$ belongs to the space group so does its inverse $\hat{M}^{-1}$; also $\hat{M}$ are orthogonal matrices, keeping the

norm invariant, thus $\hat{M}^{-1} = \hat{M}^T$ and $|\det(\hat{M})| = 1$.
We now want to study how the dielectric function's symmetry relations translate in momentum space. Using Eq. (3.73) for the Fourier transform in a crystal, we can write:

$$\begin{aligned}
\varepsilon_{\mathbf{G},\mathbf{G}'}(\mathbf{k},\omega) &= \frac{1}{V_{\text{uc}}}\int_{\text{uc}} d^3\mathbf{r}\int_{\text{uc}} d^3\mathbf{r}'\, e^{-i(\mathbf{k}+\mathbf{G})\cdot\mathbf{r}}\,\varepsilon(\mathbf{r},\mathbf{r}',\omega)\, e^{i(\mathbf{k}+\mathbf{G}')\cdot\mathbf{r}'} = \\
&= \frac{1}{V_{\text{uc}}}\int_{\text{uc}} d^3\mathbf{x}\int_{\text{uc}} d^3\mathbf{x}'\; e^{-i(\mathbf{k}+\mathbf{G})\cdot\hat{M}\mathbf{x}}\,\varepsilon(\hat{M}\mathbf{x},\hat{M}\mathbf{x}',\omega)\, e^{i(\mathbf{k}+\mathbf{G}')\cdot\hat{M}\mathbf{x}'} = \\
&= \frac{1}{V_{\text{uc}}}\int_{\text{uc}} d^3\mathbf{x}\int_{\text{uc}} d^3\mathbf{x}'\; e^{-i\hat{M}^T(\mathbf{k}+\mathbf{G})\cdot\mathbf{x}}\,\varepsilon(\mathbf{x},\mathbf{x}',\omega)\, e^{i\hat{M}^T(\mathbf{k}+\mathbf{G}')\cdot\mathbf{x}'} = \\
&= \varepsilon_{\hat{M}^T\mathbf{G},\hat{M}^T\mathbf{G}'}(\hat{M}^T\mathbf{k},\omega)\ ,
\end{aligned} \tag{3.96}$$

where we introduced $\mathbf{r} = \hat{M}\mathbf{x}$, $\mathbf{r}' = \hat{M}\mathbf{x}'$.
Non-symmorphic symmetries, which induce interesting phenomena like enforced degeneracies in the system's electronic band structure, are composed by a rotation/reflection/inversion operation and an additional fractional lattice translation:

$$\mathbf{r} \to \mathbf{r}' = \hat{M}\mathbf{r} + \mathbf{t}\ . \tag{3.97}$$

Repeating the same steps of Eq. (3.96), we will obtain:

$$\begin{aligned}
\varepsilon_{\mathbf{G},\mathbf{G}'}(\mathbf{k},\omega) &= \frac{1}{V_{\text{uc}}}\int_{\text{uc}} d^3\mathbf{x}\int_{\text{uc}} d^3\mathbf{x}'\; e^{-i(\mathbf{k}+\mathbf{G})\cdot(\hat{M}\mathbf{x}+\mathbf{t})}\,\varepsilon(\hat{M}\mathbf{x}+\mathbf{t},\hat{M}\mathbf{x}'+\mathbf{t},\omega)\, e^{i(\mathbf{k}+\mathbf{G}')\cdot(\hat{M}\mathbf{x}'+\mathbf{t})} = \\
&= e^{-i(\mathbf{G}-\mathbf{G}')\cdot\mathbf{t}}\frac{1}{V_{\text{uc}}}\int_{\text{uc}} d^3\mathbf{x}\int_{\text{uc}} d^3\mathbf{x}'\; e^{-i\hat{M}^T(\mathbf{k}+\mathbf{G})\cdot\mathbf{x}}\,\varepsilon(\mathbf{x},\mathbf{x}',\omega)\, e^{i\hat{M}^T(\mathbf{k}+\mathbf{G}')\cdot\mathbf{x}'} = \\
&= e^{-i(\mathbf{G}-\mathbf{G}')\cdot\mathbf{t}}\ \varepsilon_{\hat{M}^T\mathbf{G},\hat{M}^T\mathbf{G}'}(\hat{M}^T\mathbf{k},\omega)\ .
\end{aligned} \tag{3.98}$$

We can note how an additional phase factor, related to the translational lattice vector $\mathbf{t}$, appears for non-diagonal components.

Fractional units Before considering how these relations can be used to speed up calculations, we have to define how the symmetry operations act on fractional coordinates, which are used in the internal processing of DFT codes.
Defining $\hat{A}^T = (\mathbf{a}_0, \mathbf{a}_1, \mathbf{a}_2)$ as the matrix containing the crystal's primitive lattice vectors as columns, the Cartesian position $\mathbf{r}$ and its fractional coordinates $\mathbf{s}$, are related by: $\mathbf{r} = \hat{A}^T\mathbf{s}$, and $\mathbf{s} = \hat{A}^{-T}\mathbf{r}$.
When a symmetry operation is applied, the lattice vectors are transformed as $\hat{A}' = \hat{U}\hat{A}$, and the real space vector $\mathbf{r}$ is transformed as:

$$\mathbf{r} \to \mathbf{r}' = \hat{A}'^T\mathbf{s} = (\hat{U}\hat{A})^T\mathbf{s} = \hat{A}^T\hat{U}^T\mathbf{s} = \hat{A}^T\hat{U}^T\hat{A}^{-T}\mathbf{r} = \hat{M}\mathbf{r}\ . \tag{3.99}$$

Now, since the new vector can also be expressed in terms of the original lattice vectors, $\mathbf{r}' = \hat{A}^T\mathbf{s}'$, we can express how the fractional coordinates are transformed: $\mathbf{s} \to \mathbf{s}' = \hat{A}^{-T}\hat{A}^T\hat{U}^T\mathbf{s} = \hat{U}^T\mathbf{s}$. We have also derived the connection between the orthogonal matrix $\hat{M}$, which describes the symmetry operation in Cartesian coordinates, and the $\hat{U}$ matrix, which describes them in fractional coordinates: $\hat{M} = \hat{A}^T\hat{U}^T\hat{A}^{-T}$.
The $\hat{U}$ matrices are not orthogonal, so they do not preserve length, and contain only the integers -1, 0 and 1, in their components. If $\hat{U}$ is a symmetry operation then also $\hat{U}^{-1}$ is.
In the same way, we can write the points in the reciprocal space in Cartesian units, $\mathbf{k}$, or in fractional coordinates, $\mathbf{q}$. The two are related by the reciprocal lattice vectors: $\mathbf{k} = \hat{B}^T\mathbf{q}$, with $\hat{B}^T = (\mathbf{b}_0, \mathbf{b}_1, \mathbf{b}_2) = 2\pi\hat{A}^{-1}$.
Then since the wavevectors in Cartisian units transform as $\mathbf{k}' = \hat{M}^{-1}\mathbf{k} = \hat{M}^T\mathbf{k}$, as can be grasped from Eq. (3.96), we can derive the relation between the wavevectors in fractional units; $2\pi\hat{A}^{-1}\mathbf{q}' = \mathbf{k}' = \hat{M}^T\mathbf{k} = (\hat{A}^{-1}\hat{U}\hat{A})\mathbf{k} = 2\pi\hat{A}^{-1}\hat{U}\mathbf{q}$, then:

$$\mathbf{q}' = \hat{U}\mathbf{q} \ . \tag{3.100}$$

We have thus showed that the rotation of wavevectors in fractional units is described by the integer $\hat{U}$ matrices. We now introduce the scaled reciprocal lattice vectors $\mathbf{g}$ and $\mathbf{g}'$, through the relations $\mathbf{G} = 2\pi\hat{A}^{-1}\mathbf{g}$ and $\mathbf{G}' = 2\pi\hat{A}^{-1}\mathbf{g}'$, and for non-symmorphic transformations, the scaled translational vector $\boldsymbol{\tau}$, with $\mathbf{t} = \hat{A}^T\boldsymbol{\tau}$. By using the following relations, $(\mathbf{G} - \mathbf{G}') \cdot \mathbf{t} = 2\pi\hat{A}^{-1}(\mathbf{g} - \mathbf{g}') \cdot \hat{A}^T\boldsymbol{\tau} = 2\pi\hat{A}\hat{A}^{-1}(\mathbf{g} - \mathbf{g}') \cdot \boldsymbol{\tau} = 2\pi(\mathbf{g} - \mathbf{g}') \cdot \boldsymbol{\tau}$, we can then rewrite Eq. (3.96) and (3.98) as:

$$\varepsilon_{\mathbf{g},\mathbf{g}'}(\mathbf{q}, \omega) = e^{-i2\pi(\mathbf{g}-\mathbf{g}')\cdot\boldsymbol{\tau}}\, \varepsilon_{\hat{U}\mathbf{g},\hat{U}\mathbf{g}'}(\hat{U}\mathbf{q}, \omega) \ . \tag{3.101}$$

Notice that for $\boldsymbol{\tau}$ equal to $\mathbf{0}$ (or to a vector of integers), the prefactor disappears, recovering the symmorphic case.

From the irreducible to the reducible zone Now that we have described the behaviour of the dielectric function under the system's symmetries, we can use this information to compute the dielectric function only for the irreducible $\mathbf{q}_{\text{irr}}$-points, and rotate it to obtain the dielectric function on the full reducible $\mathbf{q}$-points grid.
The relations between the reducible point $\mathbf{q}$ and the corresponding irreducible point $\mathbf{q}_{\text{irr}}$ are given by:

$$\begin{cases} \hat{U}_s\mathbf{q} = \mathbf{q}_{\text{irr}} + \mathbf{N} \ ; \\ \mathbf{q} = \hat{U}_r\mathbf{q}_{\text{irr}} + \hat{U}_r\mathbf{N} = \hat{U}_r\mathbf{q}_{\text{irr}} + \mathbf{N}' \ ; \end{cases} \tag{3.102}$$

where $\hat{U}_s$ indicates the s-th symmetry operation matrix of the system, while $U_r = U_s^{-1}$ is its inverse, and it is the r-th symmetry operation. In case $\hat{U}_s\mathbf{q}$ falls outside of the first Brillouin zone, a reciprocal lattice vector $\mathbf{N}$, which in fractional units is a vector of integers, shifts it back inside it. We also define $\mathbf{N}' = \hat{U}_r\mathbf{N}$.

Now using Eq. (3.101) and the relation between the irreducible and reducible points, we obtain:

$$\begin{aligned}\varepsilon_{\mathbf{g},\mathbf{g}'}(\mathbf{q},\omega) &= e^{-i2\pi(\mathbf{g}-\mathbf{g}')\cdot\boldsymbol{\tau}_s}\varepsilon_{\hat{U}_s\mathbf{g},\hat{U}_s\mathbf{g}'}(\hat{U}_s\mathbf{q},\omega) = e^{-i2\pi(\mathbf{g}-\mathbf{g}')\cdot\boldsymbol{\tau}_s}\varepsilon_{\hat{U}_s\mathbf{g},\hat{U}_s\mathbf{g}'}(\mathbf{q}_{\text{irr}}+\mathbf{N},\omega) = \\ &= e^{-i2\pi(\mathbf{g}-\mathbf{g}')\cdot\boldsymbol{\tau}_s}\varepsilon_{\hat{U}_s\mathbf{g}+\mathbf{N},\hat{U}_s\mathbf{g}'+\mathbf{N}}(\mathbf{q}_{\text{irr}},\omega) = e^{i2\pi\hat{U}_s(\mathbf{g}-\mathbf{g}')\cdot\boldsymbol{\tau}_r}\varepsilon_{\hat{U}_s\mathbf{g}+\mathbf{N},\hat{U}_s\mathbf{g}'+\mathbf{N}}(\mathbf{q}_{\text{irr}},\omega)\ ,\end{aligned} \tag{3.103}$$

and for the opposite relation we get:

$$\begin{aligned}\varepsilon_{\mathbf{g},\mathbf{g}'}(\mathbf{q}_{\text{irr}},\omega) &= e^{-i2\pi(\mathbf{g}-\mathbf{g}')\cdot\boldsymbol{\tau}_r}\ \varepsilon_{\hat{U}_r\mathbf{g},\hat{U}_r\mathbf{g}'}(\hat{U}_r\mathbf{q}_{\text{irr}},\omega) = e^{-i2\pi(\mathbf{g}-\mathbf{g}')\cdot\boldsymbol{\tau}_r}\ \varepsilon_{\hat{U}_r\mathbf{g},\hat{U}_r\mathbf{g}'}(\mathbf{q}-\mathbf{N}') = \\ &= e^{-i2\pi(\mathbf{g}-\mathbf{g}')\cdot\boldsymbol{\tau}_r}\varepsilon_{\hat{U}_r\mathbf{g}-\mathbf{N}',\hat{U}_r\mathbf{g}'-\mathbf{N}'}(\mathbf{q},\omega) = e^{i2\pi\hat{U}_r(\mathbf{g}-\mathbf{g}')\cdot\boldsymbol{\tau}_s}\varepsilon_{\hat{U}_r\mathbf{g}-\mathbf{N}',\hat{U}_r\mathbf{g}'-\mathbf{N}'}(\mathbf{q},\omega)\ .\end{aligned} \tag{3.104}$$

In the last expression of both results we used the relation $\boldsymbol{\tau}_s = -\hat{U}_r^{-T}\boldsymbol{\tau}_r = -\hat{U}_s^T\boldsymbol{\tau}_r$, and the vice-versa, which are obtained from the group multiplication rule. We can use Eq. (3.103) and (3.104) to compute the dielectric function in the irreducible Brillouin zone and obtain it in the full BZ without any approximation.

Procedure description and validation Here we describe an idea of the algorithm structure and show its validity and results. Initially a self consistent calculation (SCF) must be performed to obtain the ground state of the system, then a non-self consistent calculation (NSCF) is performed over a given Monkhorst Pack grid and for a given number of unoccupied bands. Larger grids yield more accurate results, while an increased number of unoccupied bands allows for an improved description at larger frequencies.

Starting from the nscf output we define the symmetry matrices of the system, the irreducible points $\mathbf{q}_{\text{irr}}$ of the grid, and reconstruct the relations of Eq. (3.102), defining the specific $\hat{U}_s$, $\hat{U}_r$, $\mathbf{N}$ and $\mathbf{N}'$ that connect a given $\mathbf{q}$ point to its irreducible counterpart. Then the calculation of the dielectric function $\varepsilon_{\mathbf{G},\mathbf{G}}(\mathbf{q}_{\text{irr}},\omega)$ is performed for all irreducible points of the grid, for the specified frequencies and for a set of $\mathbf{G}$ vector which is defined by imposing $\frac{1}{2}|\mathbf{q}+\mathbf{G}|^2 < E_{\text{cut}}$. The cutoff energy E_{cut} will determine the maximum momentum over which the dielectric function will be obtained, and through the number of $\mathbf{G}$ vectors the inclusion of the full local field effects.

Then a loop over the reducible grid points $\mathbf{q}$ is performed, checking which have $\mathbf{q}_{\text{irr}}$ as their irreducible counterpart, and we assign $\varepsilon_{\mathbf{g}',\mathbf{g}'}(\mathbf{q},\omega) = \varepsilon_{\mathbf{g},\mathbf{g}}(\mathbf{q}_{\text{irr}},\omega)$, with $\mathbf{g}' = \hat{U}_r\mathbf{g} - \mathbf{N}'$. We have thus obtained the microscopic dielectric function over the full grid without any approximation, but at the cost of the calculation over only the irreducible BZ. Notice that since the rotation is performed after the matrix inversion for the inclusion of the local field effects on the irreducible points dielectric function, we only rotate the diagonal components; thus, the prefactor present in Eq. (3.103) and Eq. (3.104) is never present.

Let's consider some explicit results to validate our method. In Fig. 3.4 (a) we show two examples for Si. Let's consider the following $\mathbf{q}$ and $\mathbf{q}_{\text{irr}}$ points from a $20\times20\times20$ grid, which are

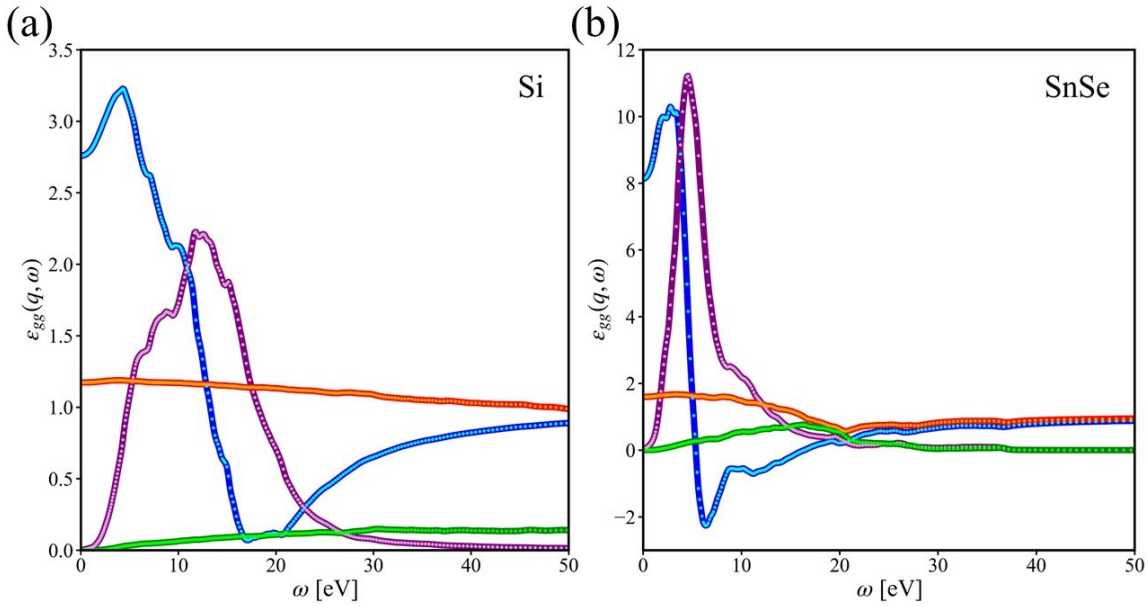

Figure 3.4: (a) Dielectric functions of Si at $\mathbf{q}$ and $\mathbf{q}_{\text{irr}}$ points from Eq. (3.105): $\varepsilon_{(-1,-1,0)}(\mathbf{q}_{\text{irr}},\omega)$ (blue and violet line for real and imaginary part respectively), $\varepsilon_{(-2,-2,0)}(\mathbf{q}_{\text{irr}},\omega)$ (red and green lines), $\varepsilon_{(0,0,0)}(\mathbf{q},\omega)$ (cyan and plum dots) and $\varepsilon_{(0,1,1)}(\mathbf{q},\omega)$ (orange and lime dots). (b) Dielectric functions of SnSe at $\mathbf{q}$ and $\mathbf{q}_{\text{irr}}$ points from Eq. (3.106): $\varepsilon_{(0,0,0)}(\mathbf{q}_{\text{irr}},\omega)$ (blue and violet lines), $\varepsilon_{(0,1,0)}(\mathbf{q}_{\text{irr}},\omega)$ (red and green lines), $\varepsilon_{(0,0,0)}(\mathbf{q},\omega)$ (cyan and plum dots) and $\varepsilon_{(0,-1,0)}(\mathbf{q},\omega)$ (orange and lime dots).

connected by the matrix $\hat{U}_s$ and the vector $\mathbf{N}$:

$$\mathbf{q} = \begin{pmatrix} -0.4 \\ 0.3 \\ 0.2 \end{pmatrix} \quad \mathbf{q}_{\text{irr}} = \begin{pmatrix} 0.4 \\ 0.3 \\ -0.4 \end{pmatrix} \quad \hat{U}_s = \begin{bmatrix} 1 & 0 & -1 \\ 1 & -1 & 0 \\ 1 & 0 & 0 \end{bmatrix} \quad \mathbf{N} = \begin{pmatrix} -1 \\ -1 \\ 0 \end{pmatrix} . \tag{3.105}$$

We then compute the microscopic dielectric function at $\mathbf{q}$ and $\mathbf{q}_{\text{irr}}$ points; from Fig. 3.4 (a) we can see the following equivalences: $\varepsilon_{(0,0,0)}(\mathbf{q},\omega) = \varepsilon_{(-1,-1,0)}(\mathbf{q}_{\text{irr}},\omega)$ and $\varepsilon_{(0,1,1)}(\mathbf{q},\omega) = \varepsilon_{(-2,-2,0)}(\mathbf{q}_{\text{irr}},\omega)$. Because of their equivalence, our algorithm instead of computing $\varepsilon_{\mathbf{g},\mathbf{g}}(\mathbf{q})$ obtains the same result by rotating $\varepsilon_{\mathbf{g},\mathbf{g}}(\mathbf{q}_{\text{irr}})$ following Eq. (3.103) and (3.104).

To show that our results work also for non-symmorphic symmetries, let's consider SnSe (tin selenide), which in its orthorhombic Pnma structure has 6 non-symmorphic symmetries in addition to the identity and the inversion. In Fig. 3.4 (b) we show the following equivalences: $\varepsilon_{(0,0,0)}(\mathbf{q},\omega) = \varepsilon_{(0,0,0)}(\mathbf{q}_{\text{irr}},\omega)$ and $\varepsilon_{(0,-1,0)}(\mathbf{q},\omega) = \varepsilon_{(0,1,0)}(\mathbf{q}_{\text{irr}},\omega)$, with:

$$\mathbf{q} = \begin{pmatrix} -0.125 \\ -0.25 \\ 0.25 \end{pmatrix} \quad \mathbf{q}_{\text{irr}} = \begin{pmatrix} 0.125 \\ 0.25 \\ 0.25 \end{pmatrix} \quad \hat{U}_s = \begin{bmatrix} -1 & 0 & 0 \\ 0 & -1 & 0 \\ 0 & 0 & 1 \end{bmatrix} \quad \boldsymbol{\tau}_s = \begin{pmatrix} 0.5 \\ -0.5 \\ -0.5 \end{pmatrix} \quad \mathbf{N} = \mathbf{0} . \tag{3.106}$$

Since the calculation time of the dielectric function at different $\mathbf{q}$ is approximately the same (except for $\mathbf{\Gamma}$), we can easily estimate our gain in efficiency just from the size of the reducible points grid and the associated irreducible points for a given space group. In Table 3.1 we report some of these values, showing how even for asymmetric systems, like MgB_2, we can still have an important gain.

System	# of Sym.	q-point grid	q-points	$\mathbf{q}_{\mathbf{irr}}$-points	Gain
Si	48	$10 \times 10 \times 10$	1000	47	≈ 21
		$30 \times 30 \times 30$	27000	752	≈ 36
SnSe	8	$10 \times 9 \times 4$	360	90	≈ 4
		$30 \times 27 \times 12$	9720	1568	≈ 6
MgB_2	4	$10 \times 10 \times 8$	800	155	≈ 5
		$30 \times 30 \times 24$	21600	3133	≈ 7

Table 3.1: Table showing the computational gain when performing a dielectric function calculation over the irreducible grid instead of the full grid, for some example systems and grid sizes.

3.3.2 Spherical average

Since the DM-electron scattering rates require either an averaged loss function for the isotropic rate, Eq. (3.17), or the calculation of an integral over solid angles for the anisotropic rate, Eq. (3.16), we implemented an interpolation scheme which starts from the dataset of dielectric functions obtained on the full $\mathbf{q}$ grid, and performs a linear interpolation over a set of homogeneously sampled spheres with different radii q.

The dielectric function at Γ, is not interpolated, but the value calculated for that specific $\mathbf{q}$-point is used. As described in a previous section the dielectric function at Γ is described by a tensor, whose value depends on the the direction over which the limit $\mathbf{q} \to \mathbf{0}$ is performed, as expressed by Eq. (3.91). If the system is not cubic we then use an averaged dielectric function $\bar{\varepsilon}_{\mathbf{00}}(\mathbf{\Gamma}, \omega) = \frac{1}{3}\mathrm{Tr}[\varepsilon_{\alpha\beta}(\omega)]$ for the spherical interpolation starting dataset. If an interpolation over a specific line is performed then Eq. (3.91) is used.

To sample uniformly the points over the different spheres we adopt the Fibonacci sphere method. Unlike a simple sampling in spherical coordinates, in which the polar θ and azimuthal ϕ angles are chosen uniformly, the Fibonacci construction avoids clustering near the poles and gives an almost uniform point distribution, by projecting the golden ratio spiral onto the sphere.

Once the total number of points N_{ang} is set a list of polar and azimuthal angles are generated as:

$$\begin{aligned} \theta_i &= \arccos\left(1 - 2(i + 0.5)/N_{\mathrm{ang}}\right), \\ \phi_i &= (2\pi/\varphi) \cdot i\,, \end{aligned} \tag{3.107}$$

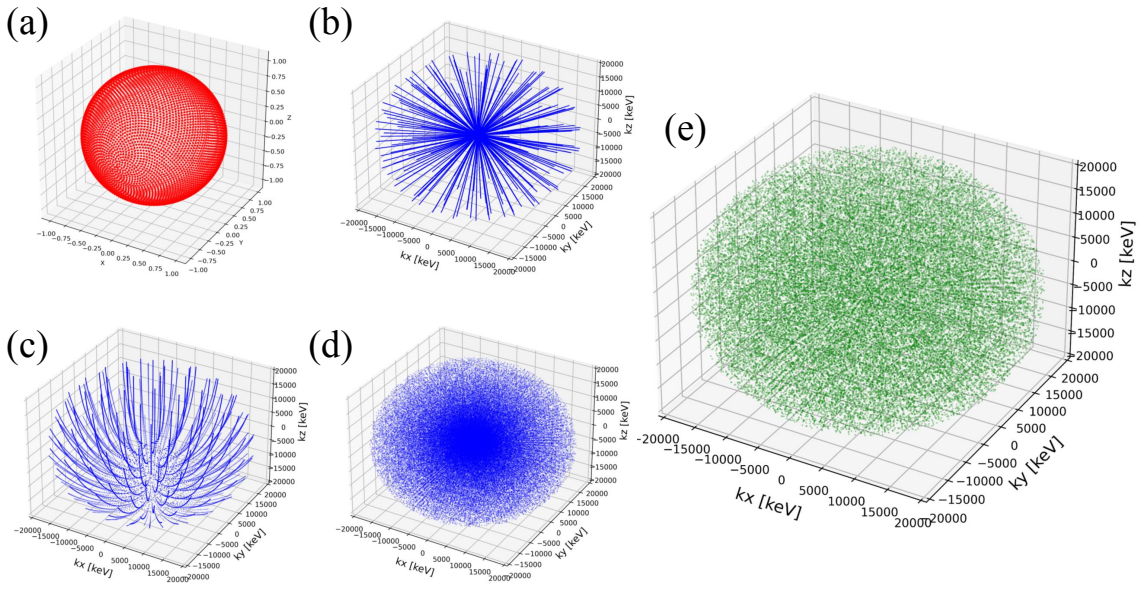

Figure 3.5: (a) Example of a Fibonacci sphere with $N_{\rm ang} = 800$ points, shown as red dots. (b)-(c)-(d) Different erroneous samplings of reciprocal space with points shown as blue dots. In (b) a constant number of $N_{\rm ang} = 200$ points without random sampling is used. In (c) the number of points grows quadratically up to 200 points, with no random sampling. In (d) a random sampling is performed but the number of points for each sphere is set constant. (e) Correct sampling method, for which the number of points grows quadratically with the sphere radius and the points, shown here as green dots, are randomly sample.

where $\varphi = (1 + \sqrt{5})/2$ is the golden ratio, and determines the azimuthal angle increase, and $i = 0, 1, \ldots, N_{\rm ang} - 1$ is an integer index. The polar angle is computed from a linear spacing in $\cos\theta$. The wavevectors over which the dielectric function is then interpolated are given by: $q_x^i = q \sin\theta_i \cos\phi_i$, $q_y^i = q \sin\theta_i \sin\phi_i$ and $q_x^i = q \cos\theta_i$. In Fig. 3.5 (a) an example of a Fibonacci sphere for $N_{\rm ang} = 800$ is shown.

While using this scheme the points are distributed homogeneously over a given sphere, using the same value of $N_{\rm ang}$ for different spheres would result in the points in $\mathbf{q}$ space accumulating on specific lines (see Fig. 3.5 (b)); the space closer to the origin would also be more densely sampled if $N_{\rm ang}$ is constant. To solve the first problem a Fibonacci sphere with a number of points much higher than $N_{\rm ang}$ is selected, then for each sampled sphere $N_{\rm ang}$ points are selected randomly from such Fibonacci sphere. To fix the second problem the number of points for a sphere is not set as constant but grows quadratically with the sphere radius, $N_{\rm ang}(q) \propto q^2$, matching the spherical coordinates Jacobian behaviour, up to a maximum value $N_{\rm ang}^{\rm max}$ which is set for the maximum radius considered $q^{\rm max}$. An example set of points obtained by combining a random sampling of a very dense Fibonacci sphere and a quadratically increasing number of angles per sphere, is shown in Fig. 3.5 (e); in Fig. 3.5 (b)-(c)-(d) the other erroneous sampling methods are shown.

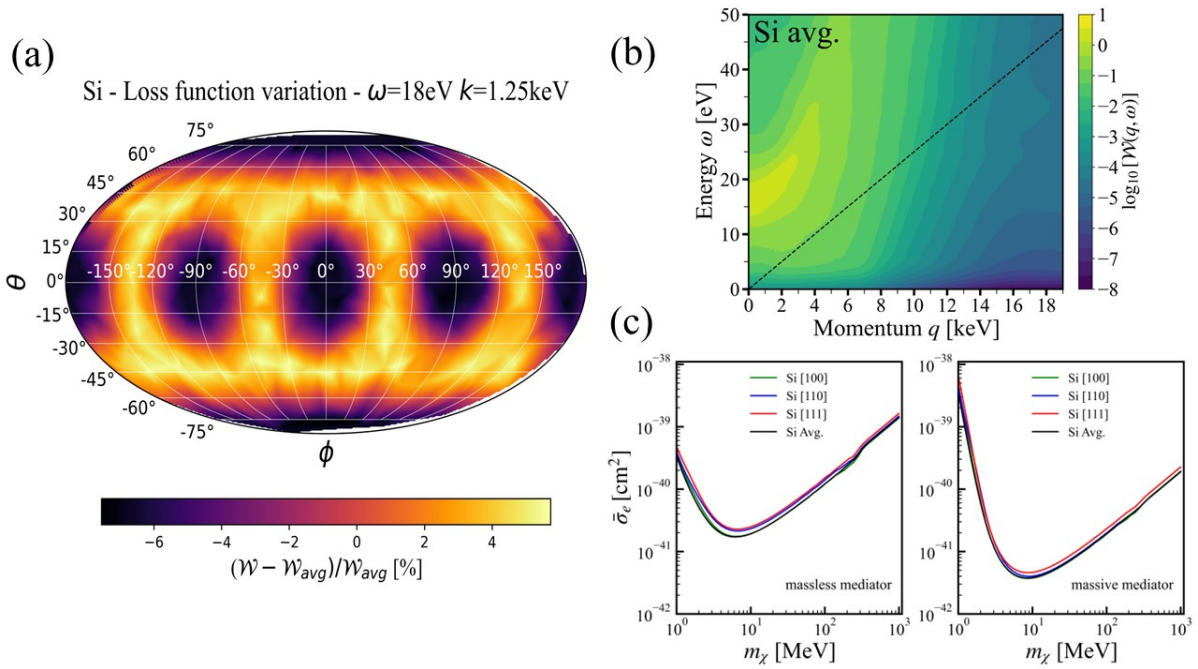

Figure 3.6: (a) Mollweide projection of Si electronic loss function variation with respect to its spherical average for ω=18 eV and k=1.25 keV. (b) Averaged electronic loss function of Si. (c) DM-e^- scattering exclusion plot obtained using the averaged dielectric function and the dielectric function interpolated along different crystal directions, for a massless and a massive mediator.

Once this sampling is performed, we use the "LinearNDInterpolator" function from SciPy [160] to interpolate our dielectric function from the initial Monkhorst-Pack grid to the set of homogeneously sampled spheres. Then, a spherical average can be performed over these spheres, obtaining the averaged dielectric function:

$$\bar{\varepsilon}(q,\omega) = \frac{1}{N_{\text{ang}}(q)} \sum_{i=0}^{N_{\text{ang}}(q)-1} \varepsilon(q,\theta_i,\phi_i,\omega) \ , \tag{3.108}$$

where $q = |\mathbf{q}+\mathbf{G}|$. This quantity can be used to define an averaged loss function:

$$\overline{\mathcal{W}}(q,\omega) = \text{Im}\left(-\frac{1}{\bar{\varepsilon}(q,\omega)}\right), \tag{3.109}$$

which is used to compute the isotropic DM-electron scattering rate of Eq. (3.17).
The number of points over each sphere can also be increased by using the crystal symmetries, by rotating all the points using the orthogonal symmetry matrices $\hat{M}$, without the need to perform additional interpolations.
In Fig. 3.6 (b) we show the averaged loss function for Si obtained using the PBE functional, the RPA approximation, a $\mathbf{G}$ vector cutoff $E_{\text{cut}} = 400$ eV, 70 empty bands, and a $10\times10\times10$ $\mathbf{q}$-grid, with the NSCF calculation performed on a $20\times20\times20$ $\mathbf{k}$-grid; the two grids can be

different but need to be commensurate so that the entire **q**-grid is contained in the **k**-grid. After calculation on the grid, the spherical interpolation and averaging have been performed setting $N_{\rm ang}^{\rm max}$=200. To showcase an example of the electronic loss function modulation, in Fig. 3.6 (a) we report a Mollweide projection of the electronic loss function difference with respect to its average value, for a specific frequency and momentum modulus. The plot has been constructed setting $N_{\rm ang}$=500.

In Fig. 3.6 (c) we show the DM-e^- scattering exclusion plot obtained using the averaged dielectric function, and the dielectric function interpolated along specific crystal directions. The rate calculation has been performed using the DarkELF package [148]. From this comparison, we can establish that the isotropic approximation is valid for Si, since a strong dependency on the considered direction is absent. Finally, we notice that the plasmonic peak of the ELF does not contribute towards the scattering rate since it is outside the kinematically accessible region for the DM-e^- scattering. Since the scattering kinematic is not ideally matched with the electronic response for most semiconductors, an interest in the community has grown towards materials with low band gaps like the ones proposed in Ref.s [161, 162, 163] or doped semiconductors [164]. The datasets that we generate can also be used to compute the anisotropic DM-electron scattering rate of Eq. (3.16) (and for the Migdal effect), directly summing over the **q** vectors of the grid, or by expanding $\varepsilon(\mathbf{q},\omega)$ in terms of spherical harmonics, like the Zernike expansion, simplifying the integration analytically. This second approach will be presented in the following chapter.

Chapter 4

Anisotropic Migdal effect

The Migdal effect is a quantum-mechanical inelastic process that can accompany an otherwise elastic collision of a neutral particle (for example a dark-matter particle or a neutron) with an atomic nucleus: because the nucleus is impulsively displaced, the electronic cloud does not follow the nucleus instantaneously, and there is a finite probability to excite one or more atomic electrons.

The effect was first recognized in the nuclear-decay literature by A. B. Migdal in the late 1930s–early 1940s, who calculated ionization probabilities associated with rapid changes in the nuclear motion and charge during α- and β-decays [165, 166]. Migdal's original physical picture is that of an electron "shake-off" caused by a sudden perturbation of the nuclear potential; over the decades, the same basic mechanism has been invoked to explain a variety of ionization and excitation phenomena in nuclear processes. Interest in the Migdal effect in the context of particle astrophysics and dark-matter (DM) detection began more recently because it offers a route to extend the reach of traditional nuclear-recoil searches to sub-GeV DM masses [167, 168]. For a DM particle whose dominant interaction is with nuclei, the kinetic energy transferred to a recoiling nucleus may be too small to produce an observable nuclear-recoil signal in many detectors. But if a Migdal ionization accompanies that nuclear recoil, the induced electronic excitations can be observed, and since experimental thresholds for electronic excitations are currently much lower than for nuclear recoils, the Migdal effect allows the indirect observation of nuclear recoils of much lower DM masses. However, DM scattering kinematics are quite different from where the Migdal effect was originally studied, and so far there are no direct measurements in the desired regimes.

The majority of theoretical studies have treated the target material as consisting of individual atomic targets [168, 169, 170, 171], similar to the original derivation by Migdal, while recently the effect has also been generalized to condensed matter targets [172, 173, 174, 175, 176]. In atomic targets, the calculation can be performed most conveniently by boosting to the rest frame of the recoiling atom and writing the matrix element in terms of the transition dipole moments for the atom. Ibe et al. [168] comprehensively review this formalism in the context of DM scattering and numerically computed the relevant matrix elements with the Flexible Atomic Code [177].

The Migdal effect in semiconductors is more subtle, due to the delocalized nature of the electron clouds. This prevents one from simply using the boosting method, as the rest frame of the lattice is now a preferential frame. In a condensed target the Migdal-like ionization probabilities are written in terms of the material's energy loss function or dielectric response. Knapen, Kozaczuk and Lin [172] showed that in semiconductors the Migdal rate is closely related to the material's energy loss function and can be calculated ab initio using density-functional-theory methods, permitting realistic projections for SENSEI [178], SuperCDMS [179] and other solid-state experiments.
The boosted detectability is particularly important for DM masses in the ∼10 MeV - 1 GeV range and has lead several direct-detection collaborations to use or reinterpret data with Migdal-model assumptions [180, 181, 182]. Because the Migdal effect (as relevant for scattering) had not been observed unambiguously in a controlled scattering experiment, several efforts aim to measure it with tagged neutron beams. The MIGDAL collaboration [183] aims to produce and detect Migdal electrons from known neutron-induced nuclear recoils, providing calibration and testing of the theoretical predictions. Recent dedicated searches in liquid xenon with tagged neutrons report the first direct investigations of M- and L-shell Migdal transitions [180].
The Migdal effect thus extends the kinematic reach of many existing detector technologies without requiring new direct DM–electron couplings, thereby providing a path to probe lighter DM particles, which requires continued progress in both theoretical predictions and experimental validation.
In this chapter, we will review the Migdal effect rate in semiconductors, along with the main approximations that allow for its calculation, such as the assumption of an isotropic response from the medium. Motivated by the numerical complexity of the anisotropic rate calculation, which is due to the presence of coupled multidimensional integrals, we present a novel reformulation of such rate. This reformulation allows us to decouple the nuclear and electronic contributions, significantly reducing the computational burden, while maintaining the anisotropic information in the electronic loss function.

4.1 The Migdal effect rate in semiconductors

In this section we will describe the rate expression and the main approximations that are relevant for the Migdal effect in semiconductors.
We start by defining the interaction Hamiltonian between a valence electron and its nucleus [172]:

$$H_{Ne} = \int d^3\mathbf{r}' \frac{Z_{\text{ion}}\alpha}{\varepsilon(\mathbf{r}, \mathbf{r}', \omega)|\mathbf{r}' - \mathbf{r}_N|}, \tag{4.1}$$

where $\varepsilon(\mathbf{r}, \mathbf{r}', \omega)$ is the microscopic dielectric function, encoding the screening by the spectator valence electrons, and Z_{ion} is the effective charge seen by the valence electrons, thus treating the nuclei and tightly bound core electrons together as a particle with that charge. We can rewrite the interaction Hamiltonian in momentum space by performing a Fourier transform and

including the momentum-dependent ion charge $Z_{\rm ion}(k)$:

$$H_{Ne} = -4\pi\alpha \sum_{\mathbf{K}} \int_{\rm BZ} \frac{d^3\mathbf{k}}{(2\pi)^3} \frac{Z_{\rm ion}(|\mathbf{k}+\mathbf{K}|) e^{i(\mathbf{r}-\mathbf{r}_N)\cdot(\mathbf{k}+\mathbf{K})}}{\varepsilon_{\mathbf{K}\mathbf{K}}(\mathbf{k},\omega)|\mathbf{k}+\mathbf{K}|^2}, \tag{4.2}$$

where we indicate with $\mathbf{K}$ the reciprocal lattice vector and with $\mathbf{k}$ the electronic momentum in the first Brillouin zone. The momentum dependence of the ion charge, $Z_{\rm ion}(k)$, accounts for the effective ionic charge probed at different length scales. At $k = 0$, one recovers the valence charge; for instance, in Silicon $Z_{\rm ion}(0) = 4$. In the opposite limit, $k \to \infty$, corresponding to probing shorter distances, the electrons experience the full nuclear charge, such that $Z_{\rm ion}(k) \to Z$, where Z is the atomic number. The function $Z_{\rm ion}(k)$ can be obtained from tabulated ionic form factors [184].

Applying Fermi's golden rule with second order-perturbation theory, we can compute the rate associated with the DM-nucleus inelastic scattering:

$$\begin{aligned}\frac{dR(t)}{d\omega} = &\frac{1}{\rho_{\rm T}}\frac{\rho_\chi}{m_\chi}\int d^3\mathbf{v}\, f_\chi(\mathbf{v};t)\int \frac{d^3\mathbf{q}_N}{(2\,\pi)^3}\int \frac{d^3\mathbf{p}_f}{(2\,\pi)^3}\frac{\pi\bar{\sigma}_n}{\mu_{\chi n}^2}\frac{2\pi N_{\rm T} A^2}{V}\times \\ &\times 4\alpha \sum_{\mathbf{K}} \int_{\rm BZ} \frac{d^3\mathbf{k}}{(2\,\pi)^3}\,\frac{Z_{\rm ion}(|\mathbf{k}+\mathbf{K}|)^2}{|\mathbf{k}+\mathbf{K}|^2}\,{\rm Im}\left[-\frac{1}{\varepsilon_{\mathbf{K}\mathbf{K}}(\mathbf{k},\omega)}\right]\left[\frac{1}{\omega - \frac{\mathbf{q}_N\cdot\mathbf{k}}{m_N}} - \frac{1}{\omega}\right]^2 \times \\ &\times |F_{\rm crys}(\mathbf{p}_i - \mathbf{p}_f - \mathbf{q}_N - (\mathbf{k}+\mathbf{K}))|^2\, |F_{\rm DM}(\mathbf{p}_i - \mathbf{p}_f)|^2 \delta(E_i - E_f - E_N - \omega)\ ,\end{aligned} \tag{4.3}$$

where m_N, A, $\mu_{\chi n}$ and ρ_χ are the the nucleus mass, the nucleus mass number, the DM-nucleon reduced mass and the local DM density, respectively, while $\bar{\sigma}_n$ is the DM-nucleon reference cross section that is used to parametrize the experimental reach. In Fig. 4.1 (a) we can see the definition of the different kinematics variables: E_i, $\mathbf{p}_i$ and E_f, $\mathbf{p}_f$ are the initial and final DM energy and momentum; E_N and $\mathbf{q}_N$ are the nucleus energy and recoiling momentum and finally ω and $\mathbf{k}+\mathbf{K}$ are the excited electron transferred energy and momentum. We can notice the presence of two form factors: the DM-mediator form factor $F_{\rm DM}(q) = \frac{q_0^2+m_\phi^2}{q^2+m_\phi^2}$, with q_0 the reference momentum, which is taken to be $q_0 = m_\chi\, v_0$ with v_0 DM velocity dispersion; and the crystal form factor $F_{\rm crys}(\mathbf{p}_i - \mathbf{p}_f - \mathbf{q})$ which encodes the details of the ion ground state. The nuclear form factor of (2.18), is set to 1, since the DM mass range we are considering leads to recoiling nuclear momenta too small for such effects.

For a complete derivation of Eq. (4.3) see Ref. [172].

To simplify Eq. (4.3), which is hard to compute in its current form, we apply the soft limit, which is true as long as $|\mathbf{q}_N \cdot (\mathbf{k}+\mathbf{K})| \ll m_N\,\omega$ and $|\mathbf{k}+\mathbf{K}| \ll q_N$; the range of validity is 10 MeV $\lesssim m_\chi \lesssim$ 10 GeV and $\omega \gtrsim$ a few eV, which is the range of interest for the Migdal effect [172]. This approximation allows us to expand the expressions in Eq. (4.3), and separate the

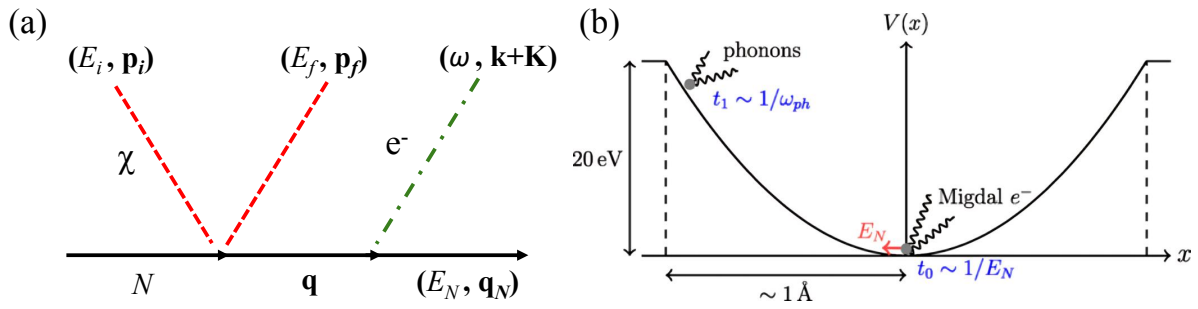

Figure 4.1: (a) Scheme of the Migdal effect's kinematic. (b) Scattering of a nucleus in a harmonic crystal. The impulse approximation is valid if the timescale of the initial collision t_0 is short when compared to the timescale to traverse its potential well t_1, which is set by the phonon frequency $t_1 = 1/\bar{\omega}$. Figure from Ref. [172].

quasi-elastic cross section and the shake-off probability:

$$\frac{dR(t)}{d\omega} = \frac{1}{m_{\rm N}}\frac{\rho_\chi}{m_\chi}\frac{2\pi^2 A^2 \bar{\sigma}_n}{\mu_{\chi n}^2}\int d^3\mathbf{v}\, f_\chi(\mathbf{v};t)\int \frac{d^3\mathbf{q}_N}{(2\pi)^3}\int \frac{d^3\mathbf{p}_f}{(2\pi)^3}\,|F_{\rm crys}(\mathbf{p}_i-\mathbf{p}_f-\mathbf{q}_N)|^2\times \\ \times\,|F_{\rm DM}(\mathbf{p}_i-\mathbf{p}_f)|^2\delta\left(E_i-E_f-\frac{q^2}{2m_N}-\omega\right)\frac{dP(\mathbf{q}_N,\omega)}{d\omega}\,, \tag{4.4}$$

where we have introduced the shake-off probability:

$$\frac{dP(\mathbf{q}_N,\omega)}{d\omega} = 4\alpha\sum_{\mathbf{K}}\int_{\rm BZ}\frac{d^3\mathbf{k}}{(2\pi)^3}\,\frac{Z_{\rm ion}(|\mathbf{k}+\mathbf{K}|)^2}{|\mathbf{k}+\mathbf{K}|^2}\,\frac{|\mathbf{q}_N\cdot(\mathbf{k}+\mathbf{K})|^2}{\omega^4 m_N^2}\mathcal{W}(\mathbf{k}+\mathbf{K},\omega)\,, \tag{4.5}$$

which represents the probability density for an event in which an energy ω is deposited in electronic excitations.

Notice that we have used $\frac{N_T}{\rho_T V} = \frac{1}{m_N}$, like for the elastic nuclear scattering. In a multi-component target we will have $\frac{N_T^J}{\rho_T V} = \frac{X_J}{m_N^J}$, and the total rate will be given by weighting the singular contributions with $X_J = \frac{m_N^J}{\sum_J m_N^J}$; this is true independently from the used approximation.

The strong $1/\omega^4$ behavior of the rate makes crystal targets with low charge threshold particularly attractive when searching for DM-nuclei interactions, and makes the Migdal effect in semiconductors more advantageous when compared to atomic targets, in which the possible excitations are only ionizations.

We can see that while this approximation greatly helps by isolating the dependency over $\mathbf{k}$ to the shake-off probability, there is still a dependency over $\mathbf{q}_N$ inside the shake-off probability, complicating the evaluation of the rate.

Consequently, the isotropic approximation is often applied in the shake-off probability by substituting the ELF $\mathcal{W}(\mathbf{k},\omega)$ with its averaged value $\overline{\mathcal{W}}(k,\omega)$, with the sum over the reciprocal lattice vector being absorbed in the momentum integration $\mathbf{k}+\mathbf{K}\to\mathbf{k}$.

The resulting expression is:

$$\begin{aligned}\frac{dP^{\rm iso}}{d\omega} &= 4\alpha \int \frac{dk}{(2\,\pi)^3}\, k^2 \int_{-1}^{1} d\cos\theta \int_0^{2\pi} d\phi\ \frac{Z_{\rm ion}(k)^2}{k^2}\, \frac{q_N^2\, k^2 \cos^2(\theta)}{\omega^4 m_N^2} \overline{\mathcal{W}}(k,\omega) = \\ &= \frac{4\alpha E_N}{3\pi^2 \omega^4 m_N} \int dk\, k^2 Z_{\rm ion}(k)^2\, \overline{\mathcal{W}}(k,\omega)\ .\end{aligned} \tag{4.6}$$

We can immediately see how the isotropic approximation leads to a decoupling of the integration over the electronic and nuclear momentum.
Codes like DarkELF [148], will thus compute the integral $I(\omega) = \frac{1}{E_N}\frac{dP}{d\omega}$, which is independent from E_N, and perform the integration of the quasi-elastic cross section, weighted with the recoiling energy. The remaining integrations will depend on the approximation chosen for the crystal form factor $F_{\rm crys}(\mathbf{p}_i - \mathbf{p}_f - \mathbf{q}_N)$.
The impulse approximation treats the recoiling ion wavefunctions as plane waves, accounting for the binding potential through the initial state wavefunctions. This holds as long as the recoiling energy is much larger than the average acoustic phonon frequency in the crystal, $E_N \gg \bar{\omega}_{\rm ph}$, with $\bar{\omega}_{\rm ph}$ is of the order of several meV. This validity condition is equivalent to asking for the collision to happen in a timescale $t_0 \sim 1/E_N$ which is relatively quick with respect to the timescale set by the potential well $t_1 \sim \bar{\omega}_{\rm ph}$. Then the DM-nucleus collision and the emission of the Migdal electrons will happen while the nucleus remains near the minimum of the potential well, and only later the nuclei will lose its residual energy to phonons. In Fig. 4.1 (b) a schematic description of the process is shown. In this approximation the crystal form factor will have a Gaussian shape:

$$F_{\rm crys}(\mathbf{p}_i - \mathbf{p}_f - \mathbf{q}_N) = \left(\frac{4\pi}{m_N \bar{\omega}_{\rm ph}}\right)^{\frac{3}{4}} e^{-\frac{|\mathbf{p}_i - \mathbf{p}_f - \mathbf{q}_N|^2}{2 m_N \bar{\omega}_{\rm ph}}}\ , \tag{4.7}$$

with the averaged phonon frequency given by $\bar{\omega}_{\rm ph} = \int_0^\infty d\omega\ \omega D(\omega) \frac{1}{e^{\beta\omega}-1}$, where $D(\omega)$ is the phonon density of state and $\beta = 1/K_B T$. To avoid extrapolating the calculation beyond the regime of validity of the impulse approximation, a threshold value $E_N^{\rm th}$ can be set for the nuclear recoil energy; for example in DarkELF [148] its default value is $E_N^{\rm th} = 4\,\bar{\omega}_{\rm ph}$.
The other common approximation for the crystal form factor is the free ion approximation which treats the nuclei as a free particles. This corresponds to the limit $\omega_{\rm ph} \to 0$ for which the crystal form factor squared asymptotes to a delta function, making the computation significantly faster with respect to the impulse approximation. The rates calculated using the impulse and the free ion approximation mainly disagree for lower DM masses, while they agree for larger values.

In the following section, we will show how the differential rate in the soft limit of Eq. (4.4), can be rewritten, allowing for a de-coupling of the two momentum integrations, without the need for the isotropic approximation. This results paves the way for the calculation of the Migdal effect in anisotropic materials, aiming for an enhanced time modulation of the rate.

4.2 New formulation for the anisotropic rate

In the following, we will show our reformulation of the Migdal effect rate, allowing a reduction in the number of numerical integrals that must be performed and the separation the isotropic and anisotropic contributions.
Let's start by considering the free ion approximation, which implies $|F_{\rm crys}(\mathbf{p}_i - \mathbf{p}_f - \mathbf{q}_N)|^2 \to (2\pi)^3\delta(\mathbf{p}_i - \mathbf{p}_f - \mathbf{q}_N)$ in Eq. (4.4), with the integration over $\mathbf{p}_f$ consequently going to 1. We will use $\mathbf{q}$ instead of $\mathbf{q}_N$ in our notation for simplicity. Our starting expression for the Migdal effect differential rate will thus be:

$$\begin{aligned}\frac{dR(t)}{d\omega} &= \frac{M}{\omega^4}\int d^3\mathbf{v}\, f_\chi(\mathbf{v};t)\int d^3\mathbf{q}\, q^2 F_{DM}(q)^2 \int d^3\mathbf{k}\, Z_{\rm ion}(k)^2(\hat{\mathbf{q}}\cdot\hat{\mathbf{k}})^2\mathcal{W}(\mathbf{k},\omega)\times \\ &\times \delta(E_i - E_f - E_N - \omega) = \frac{M}{\omega^4}\int d^3\mathbf{q}\, q^2 F_{DM}(q)^2 \frac{\hat{f}_\chi(w,\hat{\mathbf{q}};t)}{q}\int d^3\mathbf{k}\, Z_{\rm ion}(k)^2(\hat{\mathbf{q}}\cdot\hat{\mathbf{k}})^2\mathcal{W}(\mathbf{k},\omega)\ ,\end{aligned} \tag{4.8}$$

where $M = \frac{1}{m_N^3}\frac{\rho_\chi}{m_\chi}\frac{2\pi^2 A^2\bar{\sigma}_n}{\mu_{\chi n}^2}\frac{4\alpha}{(2\pi)^6}$ and we performed the integration over the DM incoming velocities by introducing the Radon transform $\hat{f}_\chi(w,\hat{\mathbf{q}};t)$, as shown in Eq. (2.24). Here $w = \frac{\omega}{q} + \frac{q}{2\mu_{N\chi}}$ takes the role of the minimum incoming velocity that is necessary to induce a nuclear recoil q and an electronic excitation of energy ω, and is obtained by inverting the delta function condition $E_i - E_f = \mathbf{q}\cdot\mathbf{v} - \frac{q^2}{2m_\chi} = E_{\mathbf{N}} + \omega = \frac{q^2}{2m_{\rm N}} + \omega$ for $\mathbf{q} \parallel \mathbf{v}$.

4.2.1 Rewriting the momentum scalar product

The shake-off probability of Eq. (4.5) exhibits a coupling of the nuclear and electronic recoil momentum through the term $(\mathbf{q}\cdot\mathbf{k})$. While performing the isotropic approximation on the electronic loss function allows for a decoupling of the two momenta, as seen in Eq. (4.6), in the following, we will obtain the same result while maintaining the anisotropic information.
By defining γ as the angle between the directions $\hat{\mathbf{q}}$ and $\hat{\mathbf{k}}$, we have $(\hat{\mathbf{q}}\cdot\hat{\mathbf{k}})^2 = \cos^2(\gamma)$, which can be rewritten using the Legendre polynomial $P_2(x) = \frac{3x^2-1}{2}$ as $\cos^2(\gamma) = \frac{2P_2(\cos\gamma)+1}{3}$. The Legendre polynomials are defined using the Rodrigues' formula: $P_l(x) = \frac{1}{2^l\, l!}\frac{d^l}{dx^l}(x^2-1)^l$. A very important property of the Legendre polynomials is their connection to the spherical harmonics which are defined, using the Condon-Shortley convention, as:

$$Y_l^m(\theta,\phi) = (-1)^m\sqrt{\frac{2l+1}{4\pi}\frac{(l-m)!}{(l+m)!}}P_l^m(\cos(\theta))e^{im\phi}\ , \tag{4.9}$$

where we introduced the associated Legendre polynomials: $P_l^m(x) = (-1)^m(1-x^2)^{\frac{m}{2}}\frac{d^m}{dx^m}P_l(x)$. In addition, the spherical harmonics addition theorem states:

$$P_l(\cos\gamma) = \frac{4\pi}{2l+1}\sum_{m=-l}^{l} Y_l^m(\hat{\mathbf{n}})\left(Y_l^m(\hat{\mathbf{n}}')\right)^*\ , \tag{4.10}$$

if γ represents the angle between the two directions $\hat{\mathbf{n}}$ and $\hat{\mathbf{n}}'$. By using Eq. (4.10) we can then write:

$$(\hat{q}\cdot\hat{k})^2 = \frac{2}{3}\frac{4\pi}{5}\sum_{m=-l}^{l} Y_2^m(\hat{\mathbf{q}})\left(Y_2^m(\hat{\mathbf{k}})\right)^* + \frac{1}{3}4\pi\, Y_0^0(\hat{\mathbf{q}})Y_0^0(\hat{\mathbf{k}})\ , \tag{4.11}$$

where we used that $P_0(x) = 1$.
The following spherical harmonics properties will come in handy in the next steps:

$$\int d\Omega\ \left(Y_l^m(\hat{\mathbf{k}})\right)^*\ Y_{l'}^{m'}(\hat{\mathbf{k}}) = \delta_{l,l'}\delta_{m,m'} \tag{4.12}$$

$$\int d\Omega\ Y_l^m(\hat{\mathbf{k}}) = \sqrt{4\pi}\delta_{l,0}\delta_{m,0} \tag{4.13}$$

$$\int d\phi\ Y_l^m(\theta,\phi) = 2\pi\delta_{m,0}\sqrt{\frac{2l+1}{4\pi}}P_l(\cos\theta) \tag{4.14}$$

where θ and ϕ are the polar and azimuthal angle, respectively. Substituting Eq. (4.11) We can thus rewrite the differential rate as:

$$\frac{dR}{d\omega} = \frac{M}{\omega^4}\sum_{l=0,2}A_l\sum_{m=-l}^{l}\int d^3\mathbf{q}\ Y_{lm}(\hat{\mathbf{q}})\ q\,F_{DM}(q)^2\hat{f}_\chi(w,\hat{\mathbf{q}};t)\int d^3\mathbf{k}\,Y_{2m}^*(\hat{\mathbf{k}})\ Z_{\rm ion}(k)^2\,\mathcal{W}(\mathbf{k},\omega) \tag{4.15}$$

where $A_0 = \frac{4\pi}{3}$ and $A_2 = \frac{8\pi}{15}$.

4.2.2 Wigner-D matrices

The expression of the Radon transform $\hat{f}_\chi(w,\hat{\mathbf{q}};t)$, see Eq. (2.25), depends on $\hat{\mathbf{q}}$ through the scalar product $\hat{\mathbf{q}}\cdot\mathbf{v}_{\rm lab}$; while we can always set the angle between their respective direction to θ, it will not match the polar angle associated to the spherical harmonics $Y_l^m(\hat{\mathbf{q}})$. To simplify the integration we thus have to rotate the spherical harmonics so that $\mathbf{v}_{\rm lab}$ is aligned to the $\hat{\mathbf{z}}$ direction. We can do so by using the Wigner-D matrices:

$$Y_l^m(\hat{q}) = \sum_{m'=-l}^{l}(D^l_{mm'}(\mathcal{R}))^* Y_l^{m'}(\hat{q}')\ , \tag{4.16}$$

where $\mathcal{R}$ represents the rotation that connects the rest frame of $\mathbf{q}$ and $\mathbf{q}'$.
The rotation is described by the Euler angles α,β,γ which are defined depending on the specific convention. Choosing the ZYZ convention a rotation described by the Euler angles consists of: first a rotation about the z-axis by α, then about the new y'-axis by β, and finally about the z''-axis by γ. In Fig. 4.2 a representation of the YZY convention for the Euler angles is shown. The operator of the rotation will then be given by:

$$D(\mathcal{R}) = D(\alpha,\beta,\gamma) = e^{-i\gamma J_z''}e^{-i\beta J_y'}e^{-i\alpha J_z} = \cdots = e^{-i\gamma J_z}e^{-i\beta J_y}e^{-i\alpha J_z}. \tag{4.17}$$

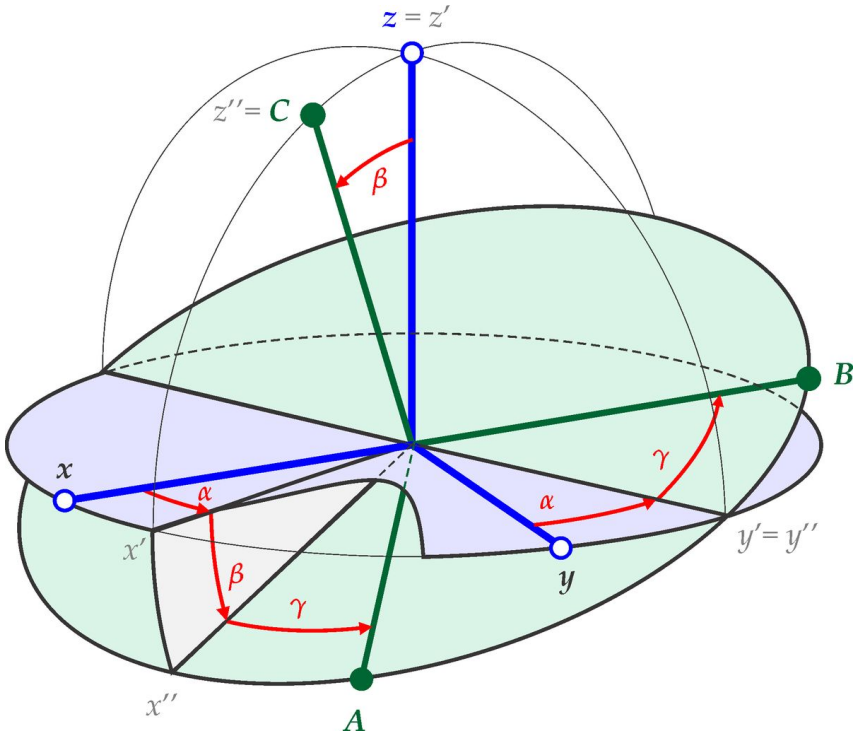

Figure 4.2: ZYZ convention for the Euler angles. ABC indicate the axes of the final coordinate system. Figure from Ref. [185].

The final expression is obtained using conjugation identity $e^{UBU^{-1}} = Ue^{B}U^{-1}$, along with several algebraic manipulations that are beyond the scope of this work [186]. The elements of the Wigner-D matrix will be then defined as:

$$D^{l}_{mm'}(\alpha,\beta,\gamma) = \langle lm|D|lm'\rangle = e^{-im\alpha}\,\langle lm|e^{-i\beta J_y}|lm'\rangle\,e^{-im'\gamma} = e^{-im\alpha}d^{l}_{mm'}(\beta)e^{-im'\gamma}\ , \quad (4.18)$$

where d are the so called Wigner little-d matrices:

$$d^{l}_{mm'}(\beta) = \sqrt{(l+m')(l-m')(l+m)(l-m)}\sum_{k=k_{\min}}^{k_{\max}}\frac{(-1)^k(\cos\frac{\beta}{2})^{2l-2k-m+m'}(\sin\frac{\beta}{2})^{2k-m+m'}}{k!(m'-m+k)!(l+m-k)!(l-m'-k)!}\ , \quad (4.19)$$

where k takes all the integer values for which the arguments of the factorials are nonnegative, which means $k_{\min} = \max(0, m-m')$ and $k_{\max} = \min(l+m, l-m')$.
If the direction C is originally described in the xyz reference frame through the angles θ and ϕ, as conventionally defined in spherical coordinates, we can identify $\alpha = \phi$ and $\beta = \theta$. In our case of interest these two angles will be the ones that define the direction of $\mathbf{v}_{\text{lab}}(t)$ in the crystal reference frame. Since the specific choice of x and y in the xy plane is not relevant, we can ignore the third rotation and set $\gamma = 0$. The velocity $\mathbf{v}_{\text{lab}}(t)$ and its components in the crystal reference frame are well described in Appendix A.2 and in Ref.s [187, 102, 188].
A final property of the Wigner-D matrices that we will find very useful is the following relation

with the spherical harmonics:

$$D^l_{m0}(\phi,\theta,0) = \sqrt{\frac{4\pi}{2l+1}} Y^m_l(\theta,\phi)^* \ . \tag{4.20}$$

Applying the rotation of Eq. (4.16) to the differential rate expression of Eq. (4.15) we find the expression:

$$\begin{aligned}\frac{dR}{d\omega} = \frac{M}{\omega^4}\sum_{l=0,2} A_l \sum_{m,m'=-l}^{l} \left(D^l_{mm'}(\mathcal{R}(t))\right)^* \int d^3\mathbf{k}\, \left(Y^m_2(\hat{\mathbf{k}})\right)^*\, Z_{\rm ion}(k)^2\, \mathcal{W}(\mathbf{k},\omega)\times \\ \times \int d^3\mathbf{q}\; q\; Y^{m'}_l(\hat{\mathbf{q}}) \frac{1}{\sqrt{\pi} v_0 N_{\rm esc}} \left(e^{-\frac{(w+v_{\rm lab}(t)\cos\theta)^2}{v_0^2}} - e^{-\frac{v_{esc}^2}{v_0^2}} \right)\end{aligned} \tag{4.21}$$

where we renamed $\mathbf{q}' \to \mathbf{q}$ for clarity. The next step will then be performing the integration over the solid angle of the integration over $\mathbf{q}$.

4.2.3 Simplifying the q integral

In the $\mathbf{q}$ integral of Eq. (4.21), the dependency on the azimuthal angle ϕ is present only in the spherical harmonics; thus, by using the spherical harmonics property of Eq. (4.14) the integration over $\mathbf{q}$ reduces to:

$$\delta_{m'0}\, \frac{2\pi}{\sqrt{\pi} v_0 N_{\rm esc}} \int dq\, q^3 F_{DM}(q)^2 \int dx \left(e^{-\frac{(w+v_{\rm lab}(t)x)^2}{v_0^2}} - e^{-\frac{v_{\rm esc}^2}{v_0^2}} \right) \sqrt{\frac{2l+1}{4\pi}} P_l(x) \ , \tag{4.22}$$

where $x = \cos(\theta)$. The integration over x is constrained by the condition $v_{\rm esc} - |w + \mathbf{v}_{\rm lab}(t)\cdot\hat{\mathbf{q}}| = v_{\rm esc} - |w + v_{\rm lab}(t)\cos\theta| > 0$ which implies:

$$-\frac{1}{v_{\rm lab}(t)}\left(v_{\rm esc} + w\right) < \cos\theta < \frac{1}{v_{\rm lab}(t)}\left(v_{\rm esc} - w\right) \ . \tag{4.23}$$

Now, since $v_{\rm esc} > v_{\rm lab}(t)$ we have that $-\frac{1}{v_{\rm lab}(t)}\left(v_{\rm esc} + w\right) < -1$, thus setting the lower boundary of the integration over x. Now since $\cos\theta \leq 1$ the upper boundary will be given by:

$$\max \equiv \min\left\{ \frac{1}{v_{\rm lab}(t)}\left(v_{\rm esc} - w\right), 1 \right\} \ . \tag{4.24}$$

Finally, the integration will be non zero only if $\frac{1}{v_{\rm lab}(t)}\left(v_{\rm esc} - w\right) > -1$; by substituting the expression $w = \frac{q}{2\mu_{N\chi}} + \frac{\omega}{q}$, this condition converts to $q^2 - 2\mu_{N\chi}(v_{\rm lab}(t) + v_{\rm esc})q + 2\mu_{N\chi}\omega < 0$. For more clarity we will use $\mu = \mu_{N\chi}$ in the following. The integration over q will then be performed

in the integration region:

$$(q_{\min}(t); q_{\max}(t)) = \left(\mu(v_{\rm lab}(t) + v_{\rm esc}) - \sqrt{\mu^2 (v_{\rm lab}(t) + v_{\rm esc})^2 - 2\mu\omega} \; ; \right. \\ \left. \mu(v_{\rm lab}(t) + v_{\rm esc}) + \sqrt{\mu^2 (v_{\rm lab}(t) + v_{\rm esc})^2 - 2\mu\omega} \right), \tag{4.25}$$

with the condition of real square root which implies $\omega \leq \frac{\mu}{2}(v_{\rm lab}(t) + v_{\rm esc})^2$. We can notice that if $\omega = 0$, which means that there is no electronic excitation induced from the recoiling nucleus, $q_{\min} = 0$ and $q_{\max} = 2\mu(v_{\rm lab}(t) + v_{\rm esc})$, which is exactly what we would obtain from Eq. (2.7) in an elastic nuclear scattering.
Combining this information, we are left with the task of computing the integrals:

$$J_l(q, \omega; t) = \frac{1}{\sqrt{\pi} v_0 N_{\rm esc}} \int_{-1}^{\max} dx \left(e^{-\frac{(w + v_{\rm lab}(t) x)^2}{v_0^2}} - e^{-\frac{v_{\rm esc}^2}{v_0^2}} \right) P_l(x) \tag{4.26}$$

for $l = 0, 2$. By comparing J_0 with the integration of the Radon transform over the solid angle presented in Appendix B.4, we can see that $J_0(q, \omega; t) = \eta(w; t)$, where $\eta(w; t)$ is the mean inverse DM speed of Eq. (B.11). The integration of J_2 can also be performed analytically, with the results shown in Appendix B.5. Thus, only the radial part of the $\mathbf{q}$ integral from Eq. (4.21) remains to be evaluated numerically.

4.2.4 Isotropic and anisotropic term expressions

The differential rate is split into two terms, one for $l = 0$ which is the isotropic term and one for $l = 2$ which is the anisotropic correction. Using our previous results we obtain the isotropic term:

$$\begin{aligned} \frac{dR^{\rm iso}(t)}{d\omega} &= \frac{M}{\omega^4} A_0 \left(D^0_{00'} \right)^* \; I_0^0 \frac{1}{\sqrt{4\pi}} \int_{q_{\min}}^{q_{\max}} dq \; q^3 F_{DM}(q)^2 2\pi \eta(w; t) \\ &= \frac{\rho_\chi}{m_\chi} \frac{A^2 \bar{\sigma}_n}{\mu_{\chi n}^2} \frac{\alpha}{3\pi^2} \frac{1}{m_N^3 \omega^4} \int dk \; k^2 Z^2(k) \; \overline{\mathcal{W}}(k, \omega) \int_{q_{min}}^{q_{\max}} dq \, q^3 F_{DM}(q) \eta(w; t) \; , \end{aligned} \tag{4.27}$$

where we used $D^0_{00'} = 1$ and denoted the $\mathbf{k}$ integrals with I_l^m:

$$I_l^m = \int d^3\mathbf{k} \left(Y_2^m(\hat{\mathbf{k}}) \right)^* \; Z_{\rm ion}(k)^2 \, \mathcal{W}(\mathbf{k}, \omega), \tag{4.28}$$

which for $l = 0$ leads to:

$$I_0^0 = \int d^3\mathbf{k} \; Y_0^0(\hat{\mathbf{k}}) Z^2(k) \mathcal{W}(\mathbf{k}, \omega) = \sqrt{4\pi} \int dk \; k^2 Z^2(k) \; \overline{\mathcal{W}}(k, \omega) \; . \tag{4.29}$$

Eq. (4.27) matches exactly the Migdal rate in the free nucleus approximation if the isotropic approximation in the shake-off probability, Eq. (4.6), is performed. The integration over q can also be rewritten in terms of the nuclear recoil energy $E_N = \frac{q^2}{2m_\mathrm{N}}$.
Performing the same substitutions, we obtain the anisotropic correction term:

$$\frac{d\Delta R(t)}{d\omega} = \frac{M}{\omega^4}\frac{8\pi}{15}\frac{\sqrt{5}}{\sqrt{4\pi}}\left(\sum_{m=-2}^{2} I_2^m (D^2_{m0}(t))^*\right)\int_{q_{min}}^{q_{\max}} dq\, q^3 F_{DM}(q)^2 J_2(q,\omega;t)\ . \tag{4.30}$$

As we can see from the Eq. (4.28) and Eq. (4.20), both I_2^m and D^2_{m0} are complex objects, but the scattering rate is a real object. It is thus convenient to rewrite these quantities in terms of the real spherical harmonics Y_{lm}, which are related to the complex spherical harmonics Y_l^m via:

$$Y_l^m = \begin{cases} \frac{1}{\sqrt{2}}(Y_{l,-m} - iY_{l,m}) & \text{for } m < 0\,; \\ Y_{l0} & \text{for } m = 0\,; \\ \frac{(-1)^m}{\sqrt{2}}(Y_{l,m} + iY_{l,-m}) & \text{for } m > 0\,. \end{cases} \tag{4.31}$$

If we introduce the real version of the I_l^m integrals:

$$I_{lm} = \int d^3\mathbf{k}\ Y_{lm}(\hat{\mathbf{k}})\, Z(k)^2\ \mathcal{W}(\mathbf{k},\omega)\ , \tag{4.32}$$

and consider Eq. (4.28), we see that:

$$I_l^m = \begin{cases} \frac{1}{\sqrt{2}}(I_{l,-m} + iI_{lm}) & \text{for } m < 0\,; \\ I_{l0} & \text{for } m = 0\,; \\ \frac{(-1)^m}{\sqrt{2}}(I_{l,m} - iI_{l,-m}) & \text{for } m > 0\,. \end{cases} \tag{4.33}$$

Using Eq. (4.31) and Eq. (4.33), and performing some immediate algebraic steps, we obtain;

$$\sum_{m=-2}^{2} I_2^m (D^2_{m0})^* = \sqrt{\frac{4\pi}{5}}\sum_{m=-2}^{2} I_{2m} Y_{2m}\ . \tag{4.34}$$

The expressions for the $l = 2$ real spherical harmonics are the following: $Y_{2,-2} = d_{xy} = \frac{1}{4}\sqrt{\frac{15}{\pi}}\sin^2(\theta)\sin(2\phi)$, $Y_{2,-1} = d_{yz} = \frac{1}{4}\sqrt{\frac{15}{\pi}}\sin(2\theta)\sin(\phi)$, $Y_{2,0} = d_{z^2} = \frac{1}{4}\sqrt{\frac{5}{\pi}}\left(3\cos^2(\theta) - 1\right)$, $Y_{2,1} = d_{xz} = \frac{1}{4}\sqrt{\frac{15}{\pi}}\sin(2\theta)\cos(\phi)$, $Y_{2,2} = d_{x^2-y^2} = \frac{1}{4}\sqrt{\frac{15}{\pi}}\sin^2(\theta)\cos(2\phi)$; where we reported also the corresponding atomic orbitals.
Putting everything together, we arrive at the final expression for the anisotropic correction of

the Migdal effect rate in the soft limit and free ion approximation:

$$\frac{d\Delta R(t)}{d\omega} = \frac{\rho_\chi}{m_\chi}\frac{A^2\bar{\sigma}_n}{\mu_{\chi n}^2}\frac{\alpha}{15\pi^3}\frac{1}{m_N^3\omega^4}\left(\sum_{m=-2}^{2} I_{2m}Y_{2m}\left(\theta_{\rm lab}(t),\phi_{\rm lab}(t)\right)\right)\int_{q_{min}}^{q_{\rm max}} dq\, q^3 F_{DM}(q)J_2(q,\omega;t)\,. \tag{4.35}$$

To compute Eq. (4.35), the numerical integration in q and the integrals I_{lm} must be computed. Comparing Eq. (4.35) with our starting expression, Eq. (4.8), we see that our derivation allows us to rewrite the original two coupled three-dimensional integrals over $\mathbf{q}$ and $\mathbf{k}$ into a decoupled one-dimensional numerical integral over q and the three dimensional integrals I_{lm} over $\mathbf{k}$. As we will show in the following subsection, I_{lm} can be further simplified using the properties of spherical harmonics.

Through our calculations, we have moved the dependence from $\mathbf{v}_{\rm lab}(t)$ direction from inside the $\mathbf{q}$ integral into the spherical harmonics Y_{2m}. The integral over q still depends on the norm $v_{\rm lab}(t)$, through the integral J_2 and the limits of integration. If we focus on a time frame, such as a day to study the rate daily modulation, the variation of the speed $v_{\rm lab}(t)$ can be neglected, then the integral over q will not depend on t and can be computed only once, and all the time dependency will be described by the linear combination of $Y_{2m}(\theta_{\rm lab}(t),\phi_{\rm lab}(t))$.

4.2.5 Zernike expansion

The integration over $\mathbf{k}$ necessary to compute I_{lm} can be numerically intensive and can be performed either through a direct Riemann sum or by fitting an expansion for the energy loss function $\mathcal{W}$.

We choose to utilize the Zernike functions [189, 190], which allow us to take advantage of the properties of spherical harmonics. The expansion to the order L of a quantity $\mathcal{F}(\mathbf{k},\omega)$ is defined, for a given energy ω, by:

$$\mathcal{F}(\mathbf{k},\omega) \simeq \sum_{n=0}^{L}\sum_{l=0}^{n}\sum_{m=-l}^{l} a_{nlm}(\omega)Z_{nlm}(\mathbf{k}) = \sum_{n=0}^{L}\sum_{l=0}^{n}\sum_{m=-l}^{l} a_{nlm}(\omega)R_{nl}(k)Y_{lm}(\theta,\varphi)\,, \tag{4.36}$$

where $Z_{nlm}(\mathbf{k})$ are the Zernike functions and R_{nl} are the Zernike polynomials. In our case, for each energy, we want to expand the electron loss function $\mathcal{W}(\mathbf{k},\omega)$, or, in the case where the momentum dependence of the ion effecting charge $Z(k)$ is considered, we expand $Z^2(k)\mathcal{W}(\mathbf{k},\omega)$. Note that since the argument k of the polynomials R_{nl} has to be $k \in (0,1)$,we will introduce a maximum value $k_{\rm max}$ and use $k/k_{\rm max}$ as our variable.

Coefficients of the expansion are found through a linear least squares problem:

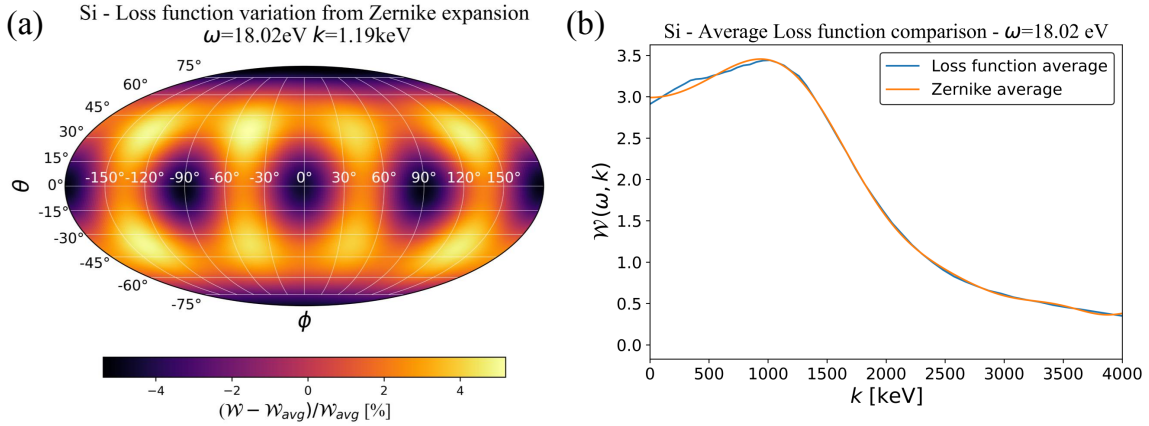

Figure 4.3: (a) Mollweide projection of Si ELF variation with respect to its spherical average, reconstructed from its Zernike expansion, for $\omega = 18.02$ eV and $k = 1.19$ keV. (b) Spherically averaged loss function of Si at $\omega = 18.02$ eV as a function of momentum; DFT data in blue, reconstruction from Zernike expansion in orange.

$$\chi^2(\omega) = \sum_i \left(\sum_{nlm} a_{nlm}(\omega) R_{nl}(k_i/k_{\max}) Y_{lm}(\theta_i, \phi_i) - Z(k_i/k_{\max}) \mathcal{W}(k_i/k_{\max}, \theta_i, \phi_i, \omega) \right)^2 \equiv$$
$$\equiv ||Ax(\omega) - b(\omega)||^2 \ . \tag{4.37}$$

Here, the vector b has length M, which is given by the number of $\mathbf{k}$ points for which the energy loss function has been calculated, x is the vector of the coefficients a_{nlm}, which has length $N \ll M$ and $A_{ij} = R_j(k_i)Y_j(\theta_i, \phi_i)$ is a $M \times N$ matrix with the values of the Zernike functions, where the j index stands for nlm. The indices take values $0 \leq |m| \leq l \leq n \leq L$, where L is the order of the expansion, and also $(n-l)/2 \in \mathbb{N}$. This means that for an even n, $l = 0, 2, \ldots, n$, so $n/2+1$ values, while for odd n, $l = 1, 3, \ldots, n-2, n$, so $(n+1)/2$ values. Considering that for each value of l we have $2l+1$ possible values of m, one can find that for each value of n, independently from its parity, we have $(n+2)(n+1)/2$ terms. Summing this value over n up to the expansion order L, we find the order of the expansion: $N = \frac{(L+1)(L+2)(L+3)}{6}$.
Once the $A(\omega)$ matrix and the $b(\omega)$ vectors are defined, finding the coefficients of the expansion is a linear least squares problem: $\min_{a_{\{nlm\}}(\omega)} \chi(\omega)^2$. The linear regression was performed using a code developed in-house. Fig. 4.3 (a) shows a Mollweide projection of Si energy loss function reconstructed from its Zernike expansion, which can be compared with Fig. 3.6 (a). Fig. 4.3 (b) shows a comparison between the average loss function obtained from the interpolated DFT data and reconstructed from the Zernike coefficients.
Once the Zernike expansion has been performed, we can use it to compute the integrals I_{lm} and write them in terms of combinations of the $a_{nlm}(\omega)$ coefficients.

Let's start by considering the isotropic term for $l = 0$:

$$\begin{aligned} I_{00} &= k_{\rm max}^3 \int_0^1 dk\ k^2 \sum_{n=0}^{L} \sum_{l=0/1}^{n} \sum_{m=-l}^{l} a_{nlm}(\omega) R_{nl}(k) \int d\Omega\ Y_{00}(\hat{\mathbf{k}}) Y_{lm}(\theta,\varphi) = \\ &= k_{\rm max}^3 \sum_{n=0}^{L} a_{n00}(\omega) \int_0^1 dk\ k^2 R_{n0}(k) = k_{\rm max}^3 \frac{a_{000}(\omega)}{3}\ , \end{aligned} \tag{4.38}$$

where we used the orthogonality of the real spherical harmonics, which are analogous to Eq. (4.12), and that $R_{00} = 1$ and $\int_0^1 dk\ k^2 R_{nl}(k) R_{n'l}(k) = \frac{\delta_{nn'}}{2n+3}$ [190]. By comparing Eq. (4.38) and Eq.(4.29), we can see that $Z(k)^2 \overline{\mathcal{W}}(k,\omega) = \frac{1}{\sqrt{4\pi}} \sum_{n=0}^{L} a_{n00}(\omega) R_{n0}(k)$, where in the left side we have sent $k \to k/k_{\rm max}$ so that $k \in (0,1)$.

Analogously to Eq. (4.38), we can rewrite the I_{2m} integrals:

$$\begin{aligned} I_{2m} &= \int d^3\mathbf{k}\ Y_{lm}(\hat{\mathbf{k}})\, Z^2(k) \mathcal{W}(\mathbf{k},\omega) = \sum_{n=0}^{L} \sum_{l'=0/1}^{n} \sum_{m'=-l}^{l} a_{nlm}(\omega)\, k_{\rm max}^3 \int_0^1 dk\ k^2 R_{nl}(k) \times \\ &\times \int d\Omega\ Y_{2m}(\hat{\mathbf{k}})\, Y_{l'm'}(\hat{\mathbf{k}}) = k_{\rm max}^3 \sum_{n=2\ \text{even}}^{L} a_{n2m}(\omega) \int_0^1 dk\ k^2 R_{n2}(k)\ , \end{aligned} \tag{4.39}$$

where possible values of n are the even numbers from 2 to L, since $l = 2$. To solve the integral with the radial Zernike functions we use their relation to the Jacobi polynomials $P_s^{(\alpha,\beta)}(x)$, $R_{nl}(k) = k^l\, P_{(n-l)/2}^{(0,l+\frac{1}{2})}(2k^2 - 1)$, and the integration properties of the Jacobi polynomials [190, 191], obtaining :

$$\int_0^1 dk\ k^2 R_{n2}(k) = \frac{(-1)^{\frac{n}{2}-1}}{2} \frac{\Gamma(n/2)\Gamma(5/2)}{\Gamma((n+5)/2)}\ , \tag{4.40}$$

where $\Gamma(n)$ is the Gamma function, and its values are well known and tabulated. We thus obtain:

$$I_{2m} = k_{\rm max}^3 \sum_{n=2\ \text{even}}^{L} a_{n2m}(\omega) \frac{(-1)^{\frac{n}{2}-1}}{2} \frac{\Gamma(n/2)\Gamma(5/2)}{\Gamma((n+5)/2)}\ . \tag{4.41}$$

Using Eq. (4.38) and Eq. (4.41), we trade-off the evaluation of the $\mathbf{k}$ integrals in I_{lm}, with an expansion of the energy loss function in terms of Zernike functions, with the final result for I_{lm} given by a linear combination of the expansion coefficients.

In Appendix B.6, we show how the Zernike expansion, in combination with the use of the Wigner-D matrices, can be used to rewrite the DM-electron scattering rate. Although this procedure allows us to split the isotropic term and its anisotropic correction, the absence of a scalar product term like $(\hat{\mathbf{q}} \cdot \hat{\mathbf{k}})$, will imply that the full sum over l is performed, instead of a selection of only the $l = 0$ and $l = 2$ terms like for the Migdal effect, making this approach less advantageous.

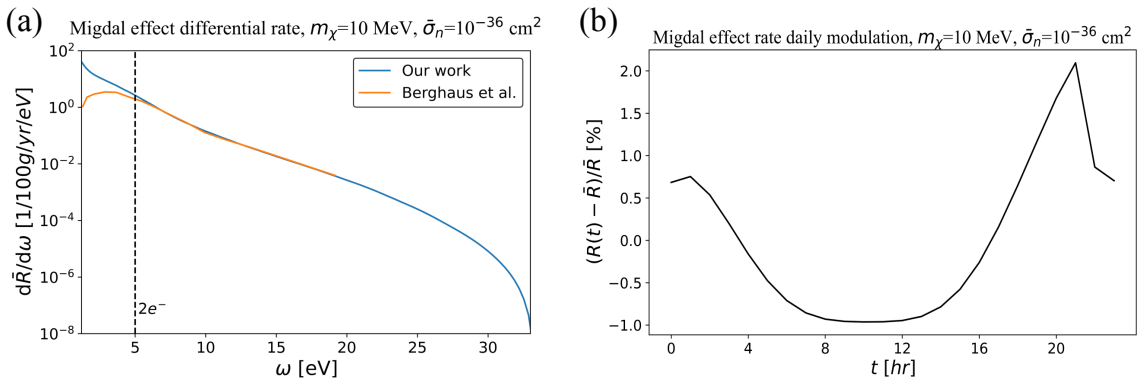

Figure 4.4: Preliminary work on Si. (a) Daily averaged Migdal effect differential rate for m_χ =10 MeV, compared with the isotropic differential rate from Ref. [175]. The vertical dashed line indicates the lowest energy necessary to excite 2 electrons. (b) Daily modulation of the Migdal rate for m_χ =10 MeV.

We are currently working on developing a code that, starting from the first principle calculation of the anisotropic energy loss function of a material, computes the anisotropic correction to the Migdal effect we derived in Eq. (4.35), both with and without the use of the Zernike expansion. In Fig. 4.4 preliminary results for Si are shown. In panel (a) the daily averaged Migdal effect differential rate for m_χ =10 MeV, computed using Eq. (4.27) and Eq. (4.35), is compared with the isotropic differential rate from Ref. [175]. Panel (b) shows the daily modulation of the Migdal rate in Si for the same DM mass. While Si is too isotropic for a visible effect on the overall rate, we can still observe a predicted daily modulation of about 2%.

Chapter 5

DM detection with superconductors

Many new ideas have recently been proposed to search for light DM in the laboratory [192, 193, 194]; among the new ideas, superconducting targets stand out with the lowest possible thresholds, giving them sensitivity to the lowest DM masses through DM–electron interactions [195, 196, 197]. With superconducting energy gaps of order meV, such detectors may eventually probe DM with mass as low as the keV scale.

Superconductivity offers a uniquely advantageous platform for low-threshold particle detection because of two closely related features: a sharply defined energy gap in the electronic excitation spectrum and the existence of long-lived, collective electronic states. In a conventional (BCS) superconductor [198], electrons near the Fermi surface form Cooper pairs via an attractive interaction, producing a condensate that carries current without dissipation. Breaking a Cooper pair requires a minimum energy, equal to the superconducting gap Δ, so the quasiparticle excitations above the ground state appear only for energies $\geq \Delta$. Since for typical metallic superconductors Δ lies in the meV range, many orders of magnitude smaller than the eV-scale gaps relevant in semiconductor detectors, even minute energy depositions, such as those produced by scattering with very light DM, can produce measurable excitations, like Bogoliubov quasiparticles, that serve as detection channels. Direct breaking of a Cooper pair converts an otherwise invisible sub-eV energy deposition into two quasiparticles carrying kinetic energy above the gap that can also down-convert into detectable phonons [197]. State-of-the-art readout technologies, including transition-edge sensors [199], kinetic inductance detectors [200], and superconducting tunnel junctions [201], can register the resulting quasiparticles or small changes in the superconductor's electromagnetic response with extremely low noise, enabling thresholds down to Δ.

In this chapter, we will first review how the scattering rate in superconductors has been described in the literature. We will then introduce the main aspects of superconducting density functional theory and showcase our novel developments on the description of response functions in superconductors.

5.1 Scattering rate in superconductors

In the seminal work by Hochberg et al. [197], the scattering of a DM particle in a superconductor is described not as a scattering with individual electrons, but as the excitation of the BCS vacuum [198]. The elementary excitations of the superconducting ground state are described by the Bogoliubov quasiparticles, which are coherent superpositions of electrons and holes.
The process can be described as a pair production of Bogoliubov quasiparticles (QPs), which corresponds to the breaking of a Cooper pair, in the form: $|\chi\rangle\,|0_{\rm BCS}\rangle \to |\chi'\rangle\,|{\rm QP}_1, {\rm QP}_2\rangle$, with the transferred momentum $\mathbf{q}$ being shared by the two QPs for the momentum conservation.
This description is suitable for studying collisions where the deposited energy ω is of the order of the superconducting gap, with the smallest detectable deposit being set by the superconducting gap. Consequently, these processes enable the study of sub-MeV DM particles.
The scattering rate can be described by an expression that is equivalent to the DM-electron scattering, as in Eq. (3.16), but with a corrected expression for the energy loss function. The key aspects introduced by Ref. [197] to achieve this goal, are the introduction of the Bogoliubov quasiparticles energies and the rewriting of the effective interaction between the DM and the superconducting state.
For the QPs dispersion relation $E(\mathbf{p}) = \sqrt{\xi_{\mathbf{p}}^2 + \Delta^2}$ is used, where Δ is half the superconducting gap and $\xi_{\mathbf{p}} = \frac{\mathbf{p}^2}{2m^*} - E_F$ the normal state eigenvalues, which are described as parabolic bands with an effective mass, relative to the Fermi energy.
To rewrite the DM interaction, we start by considering that the DM particles will couple to the electronic density of the system, which in Fourier space can be written as:

$$\rho_e(\mathbf{q}) = \sum_s \int \frac{d^3\mathbf{p}}{(2\pi)^3} c^\dagger_{\mathbf{p}-\mathbf{q},s} c_{\mathbf{p},s} \ , \tag{5.1}$$

where $c^\dagger_{\mathbf{p},s}$ and $c_{\mathbf{p},s}$ are the creation and annihilation operators for an electron with momentum $\mathbf{p}$ and spin s. To study the superconducting system the Bogoliubov QPs are introduced through the homonymous transformation:

$$c_{\mathbf{p},\uparrow} = u_{\mathbf{p}}\gamma_{\mathbf{p}\uparrow} + v_{\mathbf{p}}\gamma^\dagger_{-\mathbf{p}\downarrow} \ , \quad c^\dagger_{-\mathbf{p},\downarrow} = -v_{\mathbf{p}}\gamma_{\mathbf{p}\uparrow} + u_{\mathbf{p}}\gamma^\dagger_{-\mathbf{p}\downarrow} \ , \tag{5.2}$$

where $\gamma^\dagger$ and γ are the creation and annihilation operators of the Bogoliubov QPs. Using the transformations of Eq. (5.2), we can rewrite the density operator in (5.1), which will be composed of different $\gamma\gamma$, $\gamma^\dagger\gamma$ and $\gamma^\dagger\gamma^\dagger$ terms. Since we are searching for interactions that create two quasiparticles, we can isolate the $\gamma^\dagger\gamma^\dagger$ term, obtaining after some manipulation:

$$\rho_e(\mathbf{q}) \supset \int \frac{d^3\mathbf{p}}{(2\pi)^3} (u^*_{\mathbf{p}+\mathbf{q}} v_{\mathbf{p}} + u_{\mathbf{p}} v^*_{\mathbf{p}+\mathbf{q}}) \gamma^\dagger_{-\mathbf{p}-\mathbf{q}\uparrow} \gamma^\dagger_{\mathbf{p}\downarrow} \ . \tag{5.3}$$

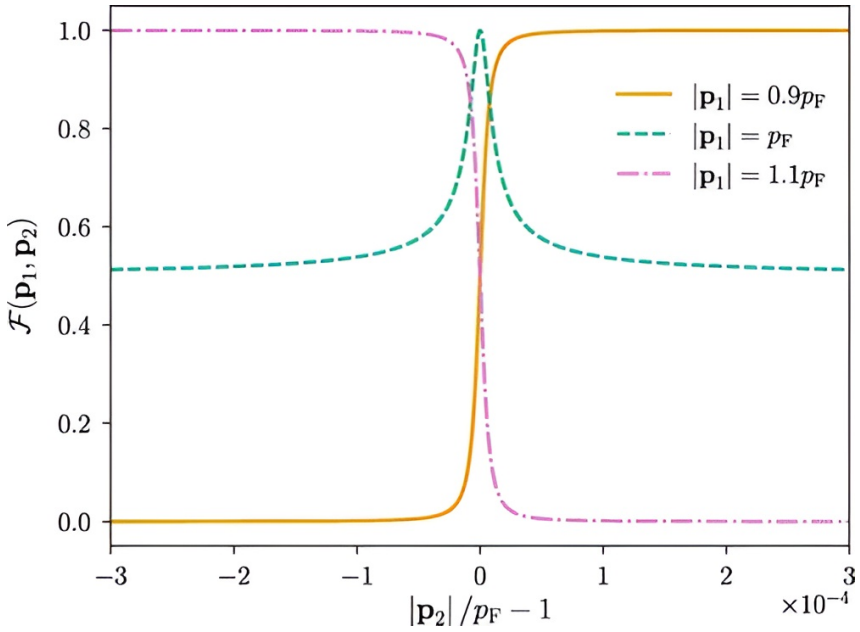

Figure 5.1: BCS coherence factor for several fixed values of $|\mathbf{p}_1|$ as a function of $|\mathbf{p}_2|$. Figure from Ref. [197].

Continuing with the definition of the rate, Ref. [197] then defines the BCS coherence factor, which is related to the modulus square of $\rho_e(\mathbf{q})$:

$$\mathcal{F}_{\mathrm{BCS}}(\mathbf{p}_1, \mathbf{p}_2) = |u^*_{\mathbf{p}_1} v_{\mathbf{p}_2} + u_{\mathbf{p}_2} v^*_{\mathbf{p}_1}|^2 = \frac{1}{2}\left(1 - \frac{\xi_{\mathbf{p}_1}\xi_{\mathbf{p}_2} - \Delta^2}{E_{\mathbf{p}_1} E_{\mathbf{p}_2}}\right) \; ; \tag{5.4}$$

where for the final expression we used $|u_{\mathbf{p}}|^2 = \frac{1}{2}\left(1 + \frac{\xi_{\mathbf{p}}}{E(\mathbf{p})}\right)$ and $|v_{\mathbf{p}}|^2 = \frac{1}{2}\left(1 - \frac{\xi_{\mathbf{p}}}{E(\mathbf{p})}\right)$. From Fig. 5.1 we can understand the behavior of the BCS structure factor. Pauli blocking only permits the creation of an electron-hole pair if the electron is above the Fermi surface and the hole is below; thus if both $\mathbf{p}_1$ and $\mathbf{p}_2$ are on the same side of the Fermi surface, the coherence factor will vanish rapidly. Otherwise, it quickly approaches 1. In the limit of $p_1 \ll \sqrt{2m^* E_F}$ and $p_1 \gg \sqrt{2m^* E_F}$, the coherence factor will be 1, and two QPs will become an electron-hole pair: $E(\mathbf{p}_1) \simeq E_F - \mathbf{p}_1^2/2m^*$ and $E(\mathbf{p}_1) \simeq \mathbf{p}_2^2/2m^* - E_F$, restoring the electron scattering behavior. The coherence factor is then linked, via the dynamical structure factor, to the imaginary part of the dielectric function in the superconducting phase:

$$\mathrm{Im}\left(\varepsilon_{\mathrm{BCS}}(\mathbf{q}, \omega)\right) = \frac{2\pi\alpha}{q^2} \int \frac{d^3\mathbf{p}_1}{(2\pi)^3} \int \frac{d^3\mathbf{p}_2}{(2\pi)^3} \mathcal{F}_{\mathrm{BCS}}(\mathbf{p}_1, \mathbf{p}_2)(2\pi)^4 \delta(\mathbf{q} - \mathbf{p}_1 - \mathbf{p}_2)\delta(\omega - E(\mathbf{p}_1) - E(\mathbf{p}_2)) \; . \tag{5.5}$$

Finally, in Ref. [197] screening effect are included using the free electron gas dielectric function of Eq. (3.25), approximating the energy loss function for the system with:

$$\mathcal{W}(\mathbf{q}, \omega) = \mathrm{Im}\left[-\frac{1}{\varepsilon_{\mathrm{BCS}}(\mathbf{q}, \omega)}\right] \simeq \frac{\mathrm{Im}\left(\varepsilon_{\mathrm{BCS}}(\mathbf{q}, \omega)\right)}{|\varepsilon_{\mathrm{FEG}}(\mathbf{q}, \omega)|^2} \; . \tag{5.6}$$

The formalism we just described was used to study the angular distribution of excitations produced in isotropic superconducting targets. An anisotropic distribution for the initial excitations produced by the dark matter scattering was found.
These results opened the way for the study of superconducting targets for a directional detection of very low mass DM particles, but we can notice several approximations and constraints that is worth investigating. The main points are the use of a parabolic dispersion with an effective mass for the normal state band structure; the use of the superconducting gap as an empirical parameter that is set to match the specific superconductor of interest, for example $\Delta_{\mathrm{Al}} \simeq 0.3$ meV. Finally, this approach is limited to isotropic superconductors and cannot treat more complex systems, like anisotropic gaps [202] and multi-gap superconductors [203], for which the interplay between the DM wind and gap anisotropy could be studied.

With the objective of introduce all these corrections in the description of the DM scattering in superconductors, in the next section we will discuss Superconducting Density Functional Theory, which is a powerful tool, that allows for the study of superconductivity in complex system, and that we will use for our purposes.

5.2 Superconducting Density Functional Theory

Superconducting density functional theory (SCDFT) is an extension of DFT to account for the symmetry breaking, associated with particle-number conservation, that occurs in a superconductor [198, 204]. SCDFT was initially proposed in 1988 [205] by Oliveira, Gross and Kohn, and was later revisited [206, 207] to include the multi-component DFT of Kreibich and Gross [208], adding in this way the effect of nuclear motion. In this section, we briefly review the key aspects of SCDFT.
The foundation of SCDFT lies in the non-relativistic Hamiltonian for interacting electrons and nuclei, expressed as:

$$H = H_e + H_{Ne} + H_N + H_{\mathrm{ext}} \ , \tag{5.7}$$

where e denotes electrons, N represents nuclei, and "ext" refers to external fields.
The electronic Hamiltonian H_e is defined as:

$$H_e = \int d\mathbf{r}\, \psi_\sigma^\dagger(\mathbf{r}) \left(-\frac{\nabla^2}{2} - \mu \right) \psi_\sigma(\mathbf{r}) + \frac{1}{2} \int d\mathbf{r}\, d\mathbf{r}'\, \psi_\sigma^\dagger(\mathbf{r}) \psi_{\sigma'}^\dagger(\mathbf{r}') \frac{1}{|\mathbf{r} - \mathbf{r}'|} \psi_{\sigma'}(\mathbf{r}') \psi_\sigma(\mathbf{r}) \ , \tag{5.8}$$

where $\psi_\sigma^\dagger(\mathbf{r})$ and $\psi_\sigma(\mathbf{r})$ are the electronic creation and annihilation field operators, and μ is the chemical potential.
In SCDFT, nuclei are explicitly included, since their dynamics contribute significantly to the

superconducting coupling mechanism. The nuclear Hamiltonian H_N is given by:

$$H_N = -\int d\mathbf{R}\, \Phi^\dagger(\mathbf{R}) \frac{\nabla^2}{2m_N} \Phi(\mathbf{R}) + \frac{1}{2} \int d\mathbf{R}\, d\mathbf{R}'\, \Phi^\dagger(\mathbf{R}) \Phi^\dagger(\mathbf{R}') \frac{Z^2}{|\mathbf{R} - \mathbf{R}'|} \Phi(\mathbf{R}') \Phi(\mathbf{R}) \ , \tag{5.9}$$

where $\Phi^\dagger(\mathbf{R})$ and $\Phi(\mathbf{R})$ are the ionic creation and annihilation field operators, m_N is the nuclear mass, and Z the atomic number.
The electron-nucleus interaction is described by:

$$H_{Ne} = -\int d\mathbf{R}\, d\mathbf{r}\, \psi_\sigma^\dagger(\mathbf{r}) \Phi^\dagger(\mathbf{R}) \frac{Z}{|\mathbf{R} - \mathbf{r}|} \Phi(\mathbf{R}) \psi_\sigma(\mathbf{r}) \ . \tag{5.10}$$

An external field is included in the Hamiltonian to induce phase symmetry breaking, facilitating superconducting condensation, since without such symmetry breaking, a perturbative approach based on the Hamiltonian would not yield a superconducting state.
Guided by BCS theory [198] and Eliashberg theory [209, 210], the symmetry breaking is introduced via coupling to an external superconductor, allowing Cooper pairs to tunnel in and out. This external field is represented as:

$$H_{\Delta_{\text{ext}}} = \int d\mathbf{r}\, d\mathbf{r}'\, \Delta_{\text{ext}}^*(\mathbf{r}, \mathbf{r}') \psi_\uparrow(\mathbf{r}) \psi_\downarrow(\mathbf{r}') + \text{h.c.} \ , \tag{5.11}$$

where $\Delta_{\text{ext}}(\mathbf{r}, \mathbf{r}')$ acts as the symmetry-breaking field.
This form simplifies theoretical considerations by involving only two field operators, though it introduces a Cooper pair source and sink, thereby relaxing the fixed particle number constraint. Additional external fields include one that couples to the electronic density:

$$H_{v_{\text{ext}}} = \int d\mathbf{r}\, v_{\text{ext}}(\mathbf{r}) \psi_\sigma^\dagger(\mathbf{r}) \psi_\sigma(\mathbf{r}) \ , \tag{5.12}$$

and another that couples to the nuclei:

$$H_{W_{\text{ext}}} = W_{\text{ext}}(\{\mathbf{R}_i\}) \int d\mathbf{R}_j\, \Phi^\dagger(\mathbf{R}_j) \Phi(\mathbf{R}_j) \ . \tag{5.13}$$

Unlike the electronic external potential, the ionic potential couples all nuclei, facilitating the construction of a non-interacting ionic system that behaves like phonons under an external potential.

5.2.1 Hohenberg Kohn theorem for SCDFT

SCDFT, in its modern formulation [206, 207], relies on three densities: the electronic density $\rho(\mathbf{r})$; the anomalous density $\chi(\mathbf{r}, \mathbf{r}')$, which represents the spatial correlations between electrons forming Cooper pairs; and the diagonal part of the nuclear N-particle density matrix $\Gamma(\{\mathbf{R}_i\})$.

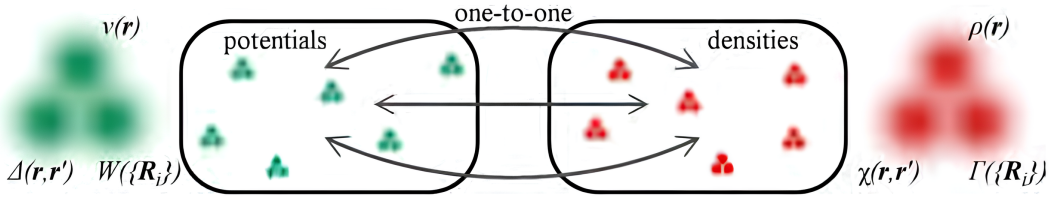

Figure 5.2: Scheme of the correspondence between potentials (v,Δ,W) and densities (ρ,χ,Γ) in SCDFT. Figure from Ref. [211].

The three densities are defined as follows:

$$\begin{cases} \rho(\mathbf{r}) = \mathrm{Tr}\left[\varrho_0 \sum_\sigma \psi^\dagger_\sigma(\mathbf{r})\psi_\sigma(\mathbf{r})\right], \\ \chi(\mathbf{r},\mathbf{r}') = \mathrm{Tr}\left[\varrho_0 \psi_\uparrow(\mathbf{r})\psi_\downarrow(\mathbf{r}')\right], \\ \Gamma(\{\mathbf{R}_i\}) = \mathrm{Tr}\left[\varrho_0 \prod_j \Phi^\dagger(\mathbf{R}_j)\Phi(\mathbf{R}_j)\right], \end{cases} \tag{5.14}$$

where ϱ_0 is the grand canonical density matrix:

$$\varrho_0 = \frac{e^{-\beta(H-\mu N)}}{\mathrm{Tr}\, e^{-\beta(H-\mu N)}}\,. \tag{5.15}$$

SCDFT is founded on a generalized Hohenberg-Kohn theorem at finite temperature, asserting that there exists a one-to-one correspondence between the densities $\rho(\mathbf{r})$, $\chi(\mathbf{r},\mathbf{r}')$, $\Gamma(\{\mathbf{R}_i\})$ and the external potentials $v_{\mathrm{ext}}(\mathbf{r})$, $\Delta_{\mathrm{ext}}(\mathbf{r},\mathbf{r}')$, $W_{\mathrm{ext}}(\{\mathbf{R}_i\})$. A variational principle then ensures the existence of a functional Ω such that:

$$\begin{cases} \Omega[\rho_0,\chi_0,\Gamma_0] = \Omega_0\ , \\ \Omega[\rho,\chi,\Gamma] > \Omega_0 \quad \text{for } \rho,\chi,\Gamma \neq \rho_0,\chi_0,\Gamma_0\ , \end{cases} \tag{5.16}$$

where Ω_0 is the grand canonical potential for the ground state densities ρ_0, χ_0, and Γ_0.
The relationship between observables and densities, coupled with the decomposition of the Hamiltonian into internal interactions, Eq.s (5.8), (5.9), (5.10), and external couplings, Eq.s (5.11), (5.12), and (5.13), allows the thermodynamic potential $\Omega[\rho,\chi,\Gamma]$ to be expressed as:

$$\begin{aligned} \Omega[\rho,\chi,\Gamma] =& F[\rho,\chi,\Gamma] + \int d\mathbf{r}\, v_{\mathrm{ext}}(\mathbf{r})\rho(\mathbf{r}) + \int d\mathbf{R}_i\, \Gamma(\{\mathbf{R}_i\})W_{\mathrm{ext}}(\{\mathbf{R}_i\}) + \\ &+ \int d\mathbf{r}\, d\mathbf{r}'\, \Delta^*_{\mathrm{ext}}(\mathbf{r},\mathbf{r}')\chi(\mathbf{r},\mathbf{r}') + \mathrm{h.c.}\ ; \end{aligned} \tag{5.17}$$

where $F[\rho,\chi,\Gamma]$ is a universal functional. This functional is termed universal because it is independent of the external potentials and is uniquely defined by the choice of the Hamiltonian and the selected set of densities. However, explicit dependence on external potentials remains, as these are necessary to anchor the minimization process to a specific physical problem.

5.2.2 Auxiliary Kohn-Sham system for SCDFT

We now want to move from the exact one-to-one mapping we just established to a practical computational framework; to do so, an auxiliary Kohn-Sham system is introduced, like we have seen in Section 3.2.1 for standard DFT.
The Kohn-Sham system is a non-interacting system with external potentials such that its minimization yields the same densities as the physical interacting system.
The thermodynamic potential of the Kohn-Sham system is defined as:

$$\begin{aligned}\Omega_s[\rho,\chi,\Gamma] = T_{s,e}[\rho,\chi,\Gamma] + T_{s,N}[\rho,\chi,\Gamma] - \frac{1}{\beta}S[\rho,\chi,\Gamma] + \int d\mathbf{r}\, v_s(\mathbf{r})\rho(\mathbf{r}) + \\ + \int d\mathbf{R}_i\, \Gamma(\{\mathbf{R}_i\})W_s(\{\mathbf{R}_i\}) + \int d\mathbf{r}\, d\mathbf{r}'\, \Delta_s^*(\mathbf{r},\mathbf{r}')\chi(\mathbf{r},\mathbf{r}') + \text{h.c.}\,,\end{aligned} \tag{5.18}$$

where T represents the kinetic energy functionals and $S = -\mathrm{Tr}\left[\varrho_0 \ln(\varrho_0)\right]$ the entropy functional.
The Kohn-Sham external potentials are chosen as:

$$\begin{cases} v_s(\mathbf{r}) = v_{\text{ext}}(\mathbf{r}) + v_H(\mathbf{r}) + v_{xc}(\mathbf{r})\,, \\ \Delta_s(\mathbf{r},\mathbf{r}') = \Delta_{\text{ext}}(\mathbf{r},\mathbf{r}') + \Delta_{xc}(\mathbf{r},\mathbf{r}')\,, \\ W_s(\{\mathbf{R}_i\}) = W_{\text{ext}}(\{\mathbf{R}_i\}) + W_H(\{\mathbf{R}_i\}) + W_{xc}(\{\mathbf{R}_i\})\,, \end{cases} \tag{5.19}$$

where the subscript H denotes Hartree terms, and xc corresponds to exchange-correlation potentials, which are defined as:

$$\begin{cases} v_{xc}[\rho,\chi,\Gamma] = \frac{\delta F_{xc}[\rho,\chi,\Gamma]}{\delta\rho}\,, \\ \Delta_{xc}[\rho,\chi,\Gamma] = \frac{\delta F_{xc}[\rho,\chi,\Gamma]}{\delta\chi}\,, \\ W_{xc}[\rho,\chi,\Gamma] = \frac{\delta F_{xc}[\rho,\chi,\Gamma]}{\delta\Gamma}\,. \end{cases} \tag{5.20}$$

Finally, the exchange-correlation functional $F_{xc}[\rho,\chi,\Gamma]$ is defined as:

$$F_{xc}[\rho,\chi,\Gamma] = F[\rho,\chi,\Gamma] - T_{s,e}[\rho,\chi,\Gamma] - T_{s,N}[\rho,\chi,\Gamma] + \frac{1}{\beta}S[\rho,\chi,\Gamma]\,. \tag{5.21}$$

Through functional differentiation of Eq.s (5.17) and (5.18), it is evident that both systems are minimized by the same densities, ρ, χ, and Γ.

5.2.3 Kohn-Sham equations in SCDFT

Now that the Kohn-Sham potentials have been defined, the Kohn-Sham equations for SCDFT can be formulated, providing a computationally tractable framework to describe superconducting systems accurately.

Ionic equations

The ionic equation retains the familiar form:

$$\left[-\sum_j \frac{\nabla_j^2}{2m_N^j} + W_s(\{\mathbf{R}_i\})\right] \Phi_n(\{\mathbf{R}_i\}) = \mathcal{E}_n \Phi_n(\{\mathbf{R}_i\}) \ , \tag{5.22}$$

where m_N^j is the mass of the atom labeled by the j index, $\mathcal{E}_n$ are the eigenvalues, and $\Phi_n(\{\mathbf{R}_i\})$ are the ionic eigenstates. Eq. (5.22) has the same structure of the nuclear Born-Oppenheimer equation.

Considering that we are interested in solids at low temperature, nuclei will perform small-amplitude oscillations around the equilibrium positions; we can then expand the potential $W_s(\{\mathbf{R}_i\})$ around the equilibrium positions, transforming the ionic degrees in phonon coordinates. The ionic Kohn-Sham hamiltonian will then reduce to:

$$H_s^{\rm ph} = \sum_{\nu,\mathbf{q}} \omega_{\nu\mathbf{q}} \left[b_{\nu\mathbf{q}}^\dagger b_{\nu\mathbf{q}} + \frac{1}{2}\right] \tag{5.23}$$

where $b_{\nu\mathbf{q}}^\dagger$ and $b_{\nu\mathbf{q}}$ are the creation and annihilation operators of phonons the branch ν and wavevector $\mathbf{q}$, with $\omega_{\nu\mathbf{q}}$ being the corresponding phonon frequency. The ionic density matrix in the harmonic approximation will be given by:

$$\Gamma(\{\mathbf{R}_i\}) = \sum_{\nu,\mathbf{q}} n_\beta(\omega_{\nu\mathbf{q}}) |h_{\nu\mathbf{q}}(\mathbf{Q})|^2 \ , \tag{5.24}$$

where $n_\beta(\omega_{\nu\mathbf{q}})$ are the Bose occupation numbers and $h_{\nu\mathbf{q}}(\mathbf{Q})$ the harmonic oscillator wavefunctions referring to the collective coordinates $\mathbf{Q}$. Note that the phonon eigenfrequencies $\omega_{\nu,\mathbf{q}}$ are functionals of the set of densities $[\rho,\chi,\Gamma]$, and will be affected by the superconducting order parameter.

Electronic equations

The electronic Kohn-Sham equations are derived from the electronic Hamiltonian:

$$H_s^e = \sum_\sigma \int d\mathbf{r}\, \psi_\sigma^\dagger(\mathbf{r}) \left[-\frac{\nabla^2}{2} + v_s(\mathbf{r}) - \mu\right] \psi_\sigma(\mathbf{r}) + \int d\mathbf{r}\, d\mathbf{r}' \ \left[\Delta_s^*(\mathbf{r},\mathbf{r}')\psi_\uparrow(\mathbf{r})\psi_\downarrow(\mathbf{r}') + \text{h.c.}\right] \ . \tag{5.25}$$

Due to the coupling introduced by $\Delta_s(\mathbf{r},\mathbf{r}')$, the Hamiltonian is non-diagonal in the field operators, complicating its solution. To solve the electronic equations, the Bogoliubov-Valatin transformation [204] is then used:

$$\psi_\sigma(\mathbf{r}) = \sum_i \left[u_i(\mathbf{r})\gamma_{i\sigma} - \text{sgn}(\sigma) v_i(\mathbf{r}) \gamma_{i\sigma}^\dagger\right] \ , \tag{5.26}$$

where $u_i(\mathbf{r})$ and $v_i(\mathbf{r})$ are the Bogoliubov quasi-particle amplitudes, and $\gamma^\dagger_{i\sigma}$ and $\gamma_{i\sigma}$ are the quasi-particle annihilation and creation operators.
The diagonalization conditions will then lead to the Bogoliubov-deGennes (BdG) equations [204]:

$$\left[-\frac{\nabla^2}{2} + v_s(\mathbf{r}) - \mu\right] u_i(\mathbf{r}) + \int dr'\, \Delta_s(\mathbf{r},\mathbf{r}')v_i(\mathbf{r}') = E_i u_i(\mathbf{r}) \ , \tag{5.27}$$

$$\left[-\frac{\nabla^2}{2} + v_s(\mathbf{r}) - \mu\right] v_i(\mathbf{r}) - \int d\mathbf{r}'\, \Delta_s^*(\mathbf{r},\mathbf{r}')u_i(\mathbf{r}') = -E_i v_i(\mathbf{r}) \ . \tag{5.28}$$

These are the electronic Kohn-Sham equations for SCDFT. The quasi-particle amplitudes $u_i(\mathbf{r})$ and $v_i(\mathbf{r})$ are then used to calculate the particle density $\rho(\mathbf{r})$ and the anomalous density $\chi(\mathbf{r},\mathbf{r}')$:

$$\rho(\mathbf{r}) = 2\sum_i \left[|u_i(\mathbf{r})|^2 f(E_i) + |v_i(\mathbf{r})|^2 f(-E_i)\right] \ , \tag{5.29}$$

$$\chi(\mathbf{r},\mathbf{r}') = \sum_i \left[u_i(\mathbf{r})v_i^*(\mathbf{r}')f(-E_i) - v_i^*(\mathbf{r})u_i(\mathbf{r}')f(E_i)\right] \ , \tag{5.30}$$

where $f(E)$ is the Fermi-Dirac distribution function.
In the absence of superconductivity, both χ and Δ vanish, and the BdG equation (5.27) reduces to the conventional Kohn-Sham equation of standard DFT:

$$\left[-\frac{\nabla^2}{2} + v_s(\mathbf{r}) - \mu\right] \varphi_i(\mathbf{r}) = \xi_i \varphi_i(\mathbf{r}), \tag{5.31}$$

where $\varphi_i(\mathbf{r})$ and $\xi_i = \epsilon_i - \mu$ are the eigenfunctions and eigenvalues, respectively. Eq. (5.28) would instead lead to an equivalent equation but with inverted eigenvalues, which can be seen as an equation for holes instead of electrons. We can then see the non particle-conserving superconducting coupling Δ_s as connecting the two equations in SCDFT.

Band decoupling approximation

The primary approximation that helps us solve Eq.s (5.27) and (5.28), simplifies the problem by decoupling its degrees of freedom. In fact, a decoupling of high and low energy scales, separating the high-energy chemical interactions responsible for bonding from the low-energy pairing interactions that drive superconductivity, allows for an independent treatment of bonding and pairing mechanisms.
The particle and hole amplitudes $u_i(\mathbf{r})$ and $v_i(\mathbf{r})$ can be expanded in the complete set of wavefunctions $\{\varphi_i\}$ of the normal-state Kohn Sham equation, Eq. (5.31). By neglecting possible structural transitions induced by the superconducting transition, and hybridization between different bands, which in general is extremely small apart from bands that are degenerate (or close to degeneracy), we can apply the band decoupling approximation, writing the Bogoliubov quasi-particle amplitudes as [206]: $u_i(\mathbf{r}) \approx \tilde{u}_i\, \varphi_i(\mathbf{r})$, $v_i(\mathbf{r}) \approx \tilde{v}_i\, \varphi_i(\mathbf{r})$. For a more compact notation we will use $\tilde{u}_i \to u_i$ and $\tilde{v}_i \to v_i$. In momentum space the electronic state i will be expressed by

the band index n and the wavevector $\mathbf{k}$, we will thus have $u_i \to u_{n\mathbf{k}}$. Using these expressions in Eq.s (5.27) and (5.28) will result in:

$$u_{n\mathbf{k}} = \frac{1}{\sqrt{2}}\mathrm{sgn}(E_{n\mathbf{k}})e^{\phi_{n\mathbf{k}}}\sqrt{1+\frac{\xi_{n\mathbf{k}}}{|E_{n\mathbf{k}}|}} \tag{5.32}$$

$$v_{n\mathbf{k}} = \frac{1}{\sqrt{2}}\sqrt{1-\frac{\xi_{n\mathbf{k}}}{|E_{n\mathbf{k}}|}} \tag{5.33}$$

where $\phi_{n\mathbf{k}} = \Delta_s(n\mathbf{k})/|\Delta_s(n\mathbf{k})|$ is the phase of the superconducting gap, the energy $E_{n\mathbf{k}}$ is defined as $E_{n\mathbf{k}} = \pm\sqrt{\xi_{n\mathbf{k}}^2 + |\Delta_s(n\mathbf{k})|^2}$ and $\xi_{n\mathbf{k}} = \varepsilon_{n\mathbf{k}} - \mu$ is the one-electron energy measured from the chemical potential μ, where $\varepsilon_{n\mathbf{k}}$ is obtained by solving the normal Kohn-Sham equation. Using these results for the densities of Eq.s (5.29) and (5.30) leads to:

$$\rho(\mathbf{r}) = \sum_{n\mathbf{k}}\left[1-\frac{\xi_{n\mathbf{k}}^2}{|E_{n\mathbf{k}}|}\tanh\left(\frac{\beta|E_{n\mathbf{k}}|}{2}\right)\right]|\varphi_{n\mathbf{k}}(\mathbf{r})|^2 \ , \tag{5.34}$$

$$\chi(\mathbf{r},\mathbf{r}') = \frac{1}{2}\sum_{n\mathbf{k}}\frac{\Delta_s(n\mathbf{k})}{|E_{n\mathbf{k}}|}\tanh\left(\frac{\beta|E_{n\mathbf{k}}|}{2}\right)\varphi_{n\mathbf{k}}(\mathbf{r})\varphi^*_{n\mathbf{k}}(\mathbf{r}') \ . \tag{5.35}$$

With these approximations, the superconducting problem is reduced to constructing the Kohn-Sham anomalous potential $\Delta_s(nk)$, which is defined by solving Eq. (5.20). Substituting in Eq. (5.20) the explicit dependence on the anomalous density χ with a dependence on Δ_s, by performing:

$$\frac{\delta F_{xc}[\rho,\chi,\Gamma]}{\delta\chi} \to \frac{\delta F_{xc}[\rho,\Delta_s,\Gamma]}{\delta\Delta_s} \ , \tag{5.36}$$

we obtain a closed, self-consistent equation for the Kohn-Sham anomalous potential Δ_s, known as the SCDFT gap equation.

5.2.4 Solving the SCDFT gap equation

The choice of approximation for $F_{xc}[\rho,\chi,\Gamma]$ will determine the expression for the SCDFT gap equation, with different possible models and parameterizations depending on the material system and the desired level of accuracy.
Let's consider as an example the LM2005 functional from Ref.s [206, 207], for which the gap equation explicit form reads:

$$\Delta_{xc}(n\mathbf{k}) = \mathcal{Z}(n\mathbf{k})\Delta_{xc}(n\mathbf{k}) + \frac{1}{2}\sum_{n'\mathbf{k}'}\mathcal{K}(n\mathbf{k},n'\mathbf{k}')\frac{\tanh\left(\frac{\beta}{2}E_{n'\mathbf{k}'}\right)}{E_{n'\mathbf{k}'}}\Delta_{xc}(n'\mathbf{k}') \ , \tag{5.37}$$

where $\mathbf{k}' \equiv \mathbf{k}+\mathbf{q}$ and the two kernels $\mathcal{K}$ and $\mathcal{Z}$ are defined as:

$$\mathcal{Z}(n\mathbf{k}) = \sum_{n'\mathbf{k}'}\sum_{\nu}\left|g^{\nu}_{n'\mathbf{k}',n\mathbf{k}}\right|^2\left[I'(\xi_{n\mathbf{k}},\xi_{n'\mathbf{k}'},\omega_{\nu\mathbf{q}}) + I'(\xi_{n\mathbf{k}},-\xi_{n'\mathbf{k}'},\omega_{\nu\mathbf{q}})\right] \ , \tag{5.38}$$

$$\mathcal{K}(n\mathbf{k}, n'\mathbf{k}') = W(n\mathbf{k}, n'\mathbf{k}') - \frac{\sum_\nu \left| g^\nu_{n'\mathbf{k}', n\mathbf{k}} \right|^2 \left[I(\xi_{n\mathbf{k}}, \xi_{n'\mathbf{k}'}, \omega_{\nu\mathbf{q}}) - I(\xi_{n\mathbf{k}}, -\xi_{n'\mathbf{k}'}, \omega_{\nu\mathbf{q}}) \right]}{\tanh(\frac{\beta}{2}\xi_{n\mathbf{k}}) \tanh(\frac{\beta}{2}\xi_{n'\mathbf{k}'})}. \quad (5.39)$$

Here W is the screened Coulomb interaction, assumed to be static, and $g^\nu_{n'\mathbf{k}+\mathbf{q},n\mathbf{k}} = \sqrt{\frac{\hbar}{2\omega_{\nu\mathbf{q}}}} \langle \varphi_{n'\mathbf{k}+\mathbf{q}} | \Delta V^{\nu\mathbf{q}}_{\text{scf}} | \varphi_{n\mathbf{k}} \rangle$ are the electron-phonon coupling constants, with $\Delta V^{\nu\mathbf{q}}_{\text{scf}}$ the variation in the Kohn-Sham potential due to the ionic displacement corresponding to the phonon mode of frequency $\omega_{\nu\mathbf{q}}$. Finally we introduced the functions:

$$I'(\xi, \xi', \omega) = \frac{\partial I(\xi, \xi', \omega)}{\partial \xi} \ , \quad (5.40)$$

$$I(\xi, \xi', \omega) = J(\xi, \xi', \omega) - J(\xi, \xi', -\omega) \ , \quad (5.41)$$

$$J(\xi, \xi', \omega) = \left[f_\beta(\xi) + n_\beta(\omega) \right] \frac{f_\beta(\xi') - f_\beta(\xi - \omega)}{\xi - \xi' - \omega} \ , \quad (5.42)$$

where f_β and n_β are the Fermi and Bose distribution functions, respectively.

Once the SCDFT gap equation has been defined, we are ready to solve the SCDFT Kohn-Sham equations self-consistently. We start by approximating the Kohn-Sham potentials of Eq. (5.19) to initiate the cycle: for v_s we can use the Kohn-Sham potential stemming from a standard DFT calculation for the non-superconducting ground state; from the Born-Oppenheimer potential of such ground state the potential W^0_s is defined; finally, the starting pair potential Δ^0_s can be approximated by a square well centered at the Fermi energy with width of the order of the Debye frequency and height computed from a BCS model.
The self-consistency cycle then starts; for the electronic problem Eq. (5.31) is solved and the densities ρ and χ are computed through Eq.s (5.34) and (5.35), using Eq.s (5.32) and (5.33). For the ionic problem, Eq. (5.22) is solved expanding the ionic potential to harmonic order, obtaining the phonon eigenfrequencies and eigenmodes, then Eq. (5.24) is used to compute the ionic density Γ. Now that the three densities $[\rho, \chi, \Gamma]$ have been obtained, we use them to evaluate the new Kohn-Sham potentials $[v_s, \Delta_s, W_s]$. If self-consistency is reached, the cycle is stops, otherwise, the new potentials are used to restart the cycle.

In the following section, we will show how SCDFT can be used to improve our description of the DM scattering in superconductors, and how some of its aspects can also be used to describe scattering with narrow gap semiconductors.

5.3 New implementations for superconductors and low-gap semiconductors

An important aspect of solving the SCDFT equations, which will be particularly relevant for the following section, is the need to describe the energy bands over a large energy window while requiring a very good resolution in a small energy window around the Fermi energy.
In Ref [207] this problem is tackled using an algorithm that performs a spline fit over a Fourier

series of the bands eigenvalues calculated over a hundreds of **k** points, according to scheme by Koelling and Wood [212]. Using this fit, the energies ξ are generated over a very large set of random **k** points, distributed according to a Metropolis algorithm that accumulates a large number of **k** points in the first few meV's around the Fermi surface. Convergence is usually reached using 15000–20000 independent points for each band crossing the Fermi surface, and about 1000 independent points per band to describe the remaining bands [207].
Consequently, new algorithms that aim at using SCDFT as a starting point to compute a superconductor response function, need to take this aspect into account.
Here we will first introduce two strategies for using SCDFT to improve the description of DM scattering, and then describe our new developments for that scope.

Generalizing the structure factor

A first approach to generalizing the description of DM scattering events in superconductors is using the SCDFT QPs energies to rewrite the coherence factor of Eq. (5.4):

$$\mathcal{F}_{\text{SCDFT}}(n\mathbf{k}_1, m\mathbf{k}_2) = |u^*_{n\mathbf{k}_1} v_{m\mathbf{k}_2} + u_{m\mathbf{k}_2} v^*_{n\mathbf{k}_1}|^2 = \frac{1}{2}\left(1 - \frac{\xi_{n\mathbf{k}_1}\xi_{m\mathbf{k}_2} - \Delta_{n\mathbf{k}_1}\Delta_{m\mathbf{k}_2}}{|E_{n\mathbf{k}_1}||E_{m\mathbf{k}_2}|}\right) , \tag{5.43}$$

where $\xi_{n\mathbf{k}} = \epsilon_{n\mathbf{k}} - \mu$ and $|E_{n\mathbf{k}}| = \sqrt{\xi^2_{n\mathbf{k}} + \Delta^2_{n\mathbf{k}}}$, while $\Delta_{n\mathbf{k}}$ is obtained by solving the SCDFT gap equation.

RPA Response function of a superconductor

A more complete approach is to properly construct the dielectric function in the superconducting state. Starting from the density response function of Eq. (3.74), and using the Bogoliubov transformation, we can find the response function for the superconducting system, which is composed of 4 terms:

$$\chi_1(\mathbf{q},\omega) = \sum_i \sum_j \frac{f(E_i) - f(E_j)}{\omega + (E_i - E_j) + i\eta} |Z_{i,j}|^2 \; w_i w_j \left(|u_i|^2|u_j|^2 + u_i v_i u_j v_j\right) \; ; \tag{5.44}$$

$$\chi_2(\mathbf{q},\omega) = \sum_i \sum_j \frac{f(-E_i) - f(-E_j)}{\omega + (-E_i + E_j) + i\eta} |Z_{i,j}|^2 \; w_i w_j \left(|v_i|^2|v_j|^2 + u_i v_i u_j v_j\right) \; ; \tag{5.45}$$

$$\chi_3(\mathbf{q},\omega) = \sum_i \sum_j \frac{f(-E_i) - f(E_j)}{\omega + (-E_i - E_j) + i\eta} |Z_{i,j}|^2 \; w_i w_j \left(|v_i|^2|u_j|^2 - u_i v_i u_j v_j\right) \; ; \tag{5.46}$$

$$\chi_4(\mathbf{q},\omega) = \sum_i \sum_j \frac{f(E_i) - f(-E_j)}{\omega + (E_i + E_j) + i\eta} |Z_{i,j}|^2 \; w_i w_j \left(|u_i|^2|v_j|^2 - u_i v_i u_j v_j\right) \; . \tag{5.47}$$

Here $f(x) = \frac{1}{e^{\beta x}+1}$ with $\beta = \frac{1}{K_B T}$, and w_i and w_j are the random **k** points weights. We indicate with Z_{ij} the matrix element:

$$Z_{ij} = \langle \varphi_j | e^{i\mathbf{q}\cdot\mathbf{r}} | \varphi_i \rangle \; , \tag{5.48}$$

where φ_i are the normal state Kohn Sham eigenfunctions. Since in SCDFT the Bogoliubov amplitudes are given on random $\mathbf{k}$ points, each with a corresponding band index, we introduce the indexes $n\mathbf{k} \to i$ and $m\mathbf{k}' \to j$, which run over all random $\mathbf{k}$ points. Consequently, also $\mathbf{q} = \mathbf{k}' - \mathbf{k}$ will be a random vector.

5.3.1 Testing and application for low-gap semiconductors

The main idea at the base of our algorithm to compute the response function in a superconducting material is to split the problem, using the different scales that characterize the superconducting coupling and the electronic band structure.
We define an energy window around the Fermi level; transitions inside the region will be treated using the superconductor version of the response function, while transitions outside the region will use the standard expression of Eq. (3.74).
The superconducting term will read from the output of SCDFT calculations the random $\mathbf{k}$ points with their weights w; the Bogoliubov energies E and the one particle energies ξ.
Computing the matrix elements Z_{ij} for all the random $\mathbf{k}$ points would be too demanding, we compute them on a regular grid, over which the normal state Kohn Sham equations are solved; then for a given random $\mathbf{q}$ vector, the closest matrix element $Z_{ij}(\bar{\mathbf{q}})$ is used as an approximation. The higher energy transitions are directly computed over the regular grid, including both the matrix elements and the eigenvalues.
We used the ELK code [213], which is a DFT code that uses the full-potential linearized augmented-plane-wave method (see Appendix C.3 for more information). In ELK we compute the higher energy contributions in the response function and the matrix elements on the regular grid. We then developed a fortran code, which combines the matrix elements from ELK and the output from SCDFT.

To first test our approach, we decided to calculate the dielectric function for a simple semiconductor, with the expression of the response function given by Eq. (3.74), and replicate the random $\mathbf{k}$ points generation scheme used in SCDFT.
This approach, aside from testing, can also be useful for studying narrow-gap semiconductors, for which the band gap can be on the order of $\mathcal{O}(10\text{ meV})$, allowing for an improved convergence with respect to the used grid size. Using Fast Fourier transforms, a denser grid than the original one is generated; then random $\mathbf{k}$ points are generated (along with their band index), and their eigenvalues are interpolated from the nearest values on the dense grid. These points are then accepted or rejected using a rejection sampling of a Saxon-Wood distribution:

$$P(E) = P_{\min} + (1 - P_{\min}) \frac{1 + e^{-\frac{w}{s}}}{1 + e^{\frac{|E - E_F| - w}{s}}} \ . \tag{5.49}$$

This distribution is equal to 1 for $E = E_F$, and drops after a width described by w, with a smearing of s, $P_{\min}$ ensures the presence of eigenvalues further away from the Fermi level. The result is a set of random points distributed more densely at energies closer to the Fermi energy.

Using the newly generated eigenvalues and the matrix elements on the regular grid, we then compute the response function and thus the dielectric function.

We are currently working on implementing the calculation of the dielectric function from random points in semiconductors, to then implement the expression for superconductors.

Conclusions

The persistent enigma of dark matter requires an intensely interdisciplinary effort. This thesis positions itself at the vital intersection of fundamental theory, advanced computational physics, and materials science, aiming to provide the rigorous theoretical and computational framework essential for the interpretation and optimization of next-generation direct detection experiments. The core goal of this work was to build and validate a pathway connecting microscopic electronic structure and lattice dynamics to macroscopic experimental observables.

We investigated the formation of defects in NaI crystals induced by DM collisions, employing combined molecular dynamics and density functional theory. Our analysis characterized key defect properties, including formation energies and anisotropic threshold displacement energies, and their effect on the system's electronic structure. Critically, we discovered that defects modify the electronic states near the valence band maximum, with the iodine Frenkel pair notably creating new states within the band gap. These defect-induced electronic states enable transitions at sub-band-gap energies, suggesting a novel detection channel in NaI-based cryogenic scintillating calorimeters that could enhance sensitivity to specific DM mass ranges. This work underscores the crucial need for ongoing investigations into defect-induced charge signals and their impact on both phonon and scintillation channels, particularly concerning detector aging in long-term experiments.

We focused on enhancing the theoretical tools for calculating DM scattering rates. We implemented novel functions in existing DFT codes to optimize the calculation of the anisotropic dielectric response in semiconductors. By exploiting crystal symmetry, we significantly accelerated calculations that are otherwise prohibitively time-consuming when anisotropic information at large wavevectors is required. This anisotropic information is crucial for accurately modeling both DM–electron scattering and the Migdal effect.
Furthermore, we developed an efficient reformulation of the Migdal effect rate, drastically simplifying the computation of its anisotropic component. This provides a more robust means of accounting for this secondary ionization channel, essential for light DM detection, and now grants fast, efficient access to the daily modulation and directional information of the Migdal effect, making screening for optimal anisotropic target materials feasible.

We started paving the way towards a first-principles description of DM scattering in superconductors. Building on the fundamentals of Superconducting Density Functional Theory, our original contribution aims at computing the anisotropic dielectric function in the superconduct-

ing state. This crucial step enhances our ability to accurately model superconducting sensors, a technology highly promising for achieving the ultra-low energy thresholds required for future DM searches.

Future efforts aim at completing and expanding our work to fully realize the potential of these new detection strategies, contributing toward the long-awaited non-gravitational discovery of dark matter.

Appendix A: Reference frames and Laboratory motion

When describing the velocity distribution of incoming Dark Matter particles, as seen in Section 1.3.1, including the motion of Earth (and of the laboratory) with respect to the DM halo is fundamental for the scattering rate estimate. In this Appendix, we introduce all the relevant quantities, mainly following Ref. [187], with the objective of making this thesis self-contained.

A.1 Reference frames

In this first section we introduce all the reference frames which will allow us to rewrite the motion of the laboratory with respect to the DM halo in the laboratory reference frame, and ultimately in the crystal frame.

A.1.1 Crystal and Laboratory frames

For condensed matter targets, a set of Cartesian axes $\hat{\mathbf{X}}$, $\hat{\mathbf{Y}}$, and $\hat{\mathbf{Z}}$, identifies the crystal frame. The momentum deposited in the crystal by a scattering event will be given by $\hat{\mathbf{q}} = q_X\hat{\mathbf{X}} + q_Y\hat{\mathbf{Y}} + q_Z\hat{\mathbf{Z}}$.
The reference frame of the laboratory, is defined as follows: its origin is in the laboratory, the x-axis points North, $\hat{\mathcal{N}}$, the y-axis West, $\hat{\mathcal{W}}$, and the z-axis to the zenith, $\hat{\mathcal{Z}}$.
The standard configuration corresponds to aligning the crystal frame and the laboratory frame, which implies $\hat{\mathbf{X}} = \hat{\mathcal{N}}$, $\hat{\mathbf{Y}} = \hat{\mathcal{W}}$ and $\hat{\mathbf{Z}} = \hat{\mathcal{Z}}$.
In general, the relation between the two frames can be written as:

$$\begin{cases} \hat{\mathbf{X}} = \alpha_X\hat{\mathcal{N}} + \beta_X\hat{\mathcal{W}} + \gamma_X\hat{\mathcal{Z}} \ ; \\ \hat{\mathbf{Y}} = \alpha_Y\hat{\mathcal{N}} + \beta_Y\hat{\mathcal{W}} + \gamma_Y\hat{\mathcal{Z}} \ ; \\ \hat{\mathbf{Z}} = \alpha_Z\hat{\mathcal{N}} + \beta_Z\hat{\mathcal{W}} + \gamma_Z\hat{\mathcal{Z}} \ ; \end{cases} \qquad \begin{cases} \hat{\mathcal{N}} = \alpha_X\hat{\mathbf{X}} + \alpha_Y\hat{\mathbf{Y}} + \alpha_Z\hat{\mathbf{Z}} \ ; \\ \hat{\mathcal{W}} = \beta_X\hat{\mathbf{X}} + \beta_Y\hat{\mathbf{Y}} + \beta_Z\hat{\mathbf{Z}} \ ; \\ \hat{\mathcal{Z}} = \gamma_X\hat{\mathbf{X}} + \gamma_Y\hat{\mathbf{Y}} + \gamma_Z\hat{\mathbf{Z}} \ ; \end{cases} \tag{A.1}$$

where the α_i, β_i and γ_i coefficients are the "direction cosines" between the axes of the two reference frames. In particular $\alpha_X = \hat{\mathbf{X}} \cdot \hat{\mathcal{N}}$, $\beta_X = \hat{\mathbf{X}} \cdot \hat{\mathcal{W}}$, $\gamma_X = \hat{\mathbf{X}} \cdot \hat{\mathcal{N}}$, and, analogously, all the other coefficients can be defined. Experimentally, one would have to measure the angles between

the two sets of axes to correctly describe the transformation between these two reference frames. If the crystal and laboratory axes are aligned, which is the case we considered, then $\alpha_X = \beta_Y = \gamma_Z = 1$ while all other parameters will be equal to zero.

A.1.2 Geocentric Equatorial frame

The geocentric-equatorial inertial frame is defined as follows: the origin is at the center of the Earth, the $\hat{\mathbf{x}}_e$ axis points in the vernal equinox direction (Υ), the $\hat{\mathbf{y}}_e$ axis points to the celestial equator with right ascension 90° (moving 90° eastwards from Υ along the equatorial line), and the $\hat{\mathbf{z}}_e$ axis points to the north celestial pole.
The transformation from the laboratory frame to the geocentric equatorial frame is obtained combining two rotations: a rotation of (90°-$\lambda_{\rm lab}$) degrees counterclockwise around the laboratory y-axis, so that z' aligns to the north celestial pole, and a rotation of ($15t_{\rm lab}$+180) degrees clockwise around the new z' axis to align x'' ti the direction of the vernal equinox. Here $\lambda_{\rm lab}$ is the latitude of the laboratory in degrees, $t_{\rm lab}$ is the local apparent sidereal time (LAST) in hours, indicating the hour angle of the vernal equinox at the laboratory location. The LAST time can be written as [214]:

$$t_{\rm lab} = t_{\rm GAST} + l_{\rm lab}/15 = (101.0308 + 36000.770\,T_0 + 15.04107\,{\rm UT})/15 + l_{\rm lab}/15\ , \tag{A.2}$$

where $l_{\rm lab}$ is the longitude in degrees of the laboratory and $t_{\rm GAST}$ is the Greenwich apparent sidereal time (GAST) in hours. Finally, UT is the universal time expressed in hours, $\lfloor\cdot\rfloor$ is the floor function, and MJD is the modified Julian date, which is the time measured in days from 00:00 UT on 17 November 1858. Considering the particular arbitrary day of 25 September 2010 we have $T_0 = 0.00729637$. The LAST can also be computed online using apposite online tools, like Ref. [215].
Performing the two rotations previously described we construct the transformation between the laboratory rest frame and the geocentric equatorial frame:

$$\begin{cases} \hat{\mathbf{x}}_e = -\cos(t^\circ_{\rm lab})\left[\sin(\lambda_{\rm lab})\hat{\mathcal{N}} - \cos(\lambda_{\rm lab})\hat{\mathcal{Z}}\right] + \sin(t^\circ_{\rm lab})\hat{\mathcal{W}}\ ; \\ \hat{\mathbf{y}}_e = -\sin(t^\circ_{\rm lab})\left[\sin(\lambda_{\rm lab})\hat{\mathcal{N}} - \cos(\lambda_{\rm lab})\hat{\mathcal{Z}}\right] - \cos(t^\circ_{\rm lab})\hat{\mathcal{W}}\ ; \\ \hat{\mathbf{z}}_e = \cos(\lambda_{\rm lab})\hat{\mathcal{N}} + \sin(\lambda_{\rm lab})\hat{\mathcal{Z}}\ ; \end{cases} \tag{A.3}$$

with $t^\circ_{\rm lab} = 15\,t_{\rm lab}$ the laboratory LAST converted to degrees. Inverting these relations we find:

$$\begin{cases} \hat{\mathcal{N}} = -\sin(\lambda_{\rm lab})\left[\cos(t^\circ_{\rm lab})\hat{\mathbf{x}}_e + \sin(t^\circ_{\rm lab})\hat{\mathbf{y}}_e\right] + \cos(\lambda_{\rm lab})\hat{\mathbf{z}}_e\ ; \\ \hat{\mathcal{W}} = \sin(t^\circ_{\rm lab})\hat{\mathbf{x}}_e - \cos(t^\circ_{\rm lab})\hat{\mathbf{y}}_e\ ; \\ \hat{\mathcal{Z}} = \cos(\lambda_{\rm lab})\left[\cos(t^\circ_{\rm lab})\hat{\mathbf{x}}_e + \sin(t^\circ_{\rm lab})\hat{\mathbf{y}}_e\right] + \sin(\lambda_{\rm lab})\hat{\mathbf{z}}_e\ . \end{cases} \tag{A.4}$$

In our work, we used the "Laboratori Nazionali del Gran Sasso" coordinates for the laboratory coordinates: $\lambda_{\rm lab} = 42.45°$ and $l_{\rm lab} = 13.7°$.

A.1.3 Galactic frame

Finally, we need to introduce the galactic coordinate frame: its origin is at the Sun position, $\hat{\mathbf{x}}_g$ points towards the Galactic center, $\hat{\mathbf{y}}_g$ points in the galactic rotation direction, and $\hat{\mathbf{z}}_g$ points to the north Galactic pole.
The transformation from the geocentric equatorial frame to the galactic frame is described by the orthogonal matrix $\mathcal{P}$:

$$\begin{cases} \hat{\mathbf{x}}_g = \mathcal{P}_{11}\,\hat{\mathbf{x}}_e + \mathcal{P}_{12}\,\hat{\mathbf{y}}_e + \mathcal{P}_{13}\,\hat{\mathbf{z}}_e\,; \\ \hat{\mathbf{y}}_g = \mathcal{P}_{21}\,\hat{\mathbf{x}}_e + \mathcal{P}_{22}\,\hat{\mathbf{y}}_e + \mathcal{P}_{23}\,\hat{\mathbf{z}}_e\,; \\ \hat{\mathbf{z}}_g = \mathcal{P}_{31}\,\hat{\mathbf{x}}_e + \mathcal{P}_{32}\,\hat{\mathbf{y}}_e + \mathcal{P}_{33}\,\hat{\mathbf{z}}_e\,; \end{cases} \tag{A.5}$$

where $\mathcal{P}_{11} = -0.06699$, $\mathcal{P}_{12} = -0.8728$, $\mathcal{P}_{13} = -0.4835$, $\mathcal{P}_{21} = 0.4927$, $\mathcal{P}_{22} = -0.4503$, $\mathcal{P}_{23} = 0.7446$, $\mathcal{P}_{31} = -0.8676$, $\mathcal{P}_{32} = -0.1883$ and $\mathcal{P}_{33} = 0.4602$.
These values are set for the epoch of January 1950.0 [216], and their variation with respect to current times can be neglected for our purposes. The inverse transformation will be described by the transposed matrix $\mathcal{P}^T$:

$$\begin{bmatrix} \hat{\mathbf{x}}_e \\ \hat{\mathbf{y}}_e \\ \hat{\mathbf{z}}_e \end{bmatrix} = \mathcal{P}^T \begin{bmatrix} \hat{\mathbf{x}}_g \\ \hat{\mathbf{y}}_g \\ \hat{\mathbf{z}}_g \end{bmatrix} . \tag{A.6}$$

A.2 Laboratory velocity

We can now identify the different components of the laboratory velocity with respect to the center of the Galaxy $\mathbf{v}_{\rm lab}$, and use the relation between the different reference frames to compute the scalar product $\hat{\mathbf{q}} \cdot \mathbf{v}_{\rm lab}$ present in the Radon transform of the DM velocity distribution, Eq. (2.25).
The laboratory velocity can be written as the sum of the Solar motion, Earth's revolution, and Earth's rotation: $\mathbf{v}_{\rm lab} = \mathbf{v}_\odot + \mathbf{v}_{\rm orbit} + \mathbf{v}_{\rm rot}$.

Solar motion The solar motion in the galactic rest frame has two components: the galactic rotation of the Sun and the peculiar motion of the Sun:

$$\mathbf{v}_\odot = \mathbf{v}_{\odot,\rm rot} + \mathbf{v}_{\odot,\rm pec} = v_{\odot,\rm rot}\,\hat{\mathbf{y}}_g + \left[U\hat{\mathbf{x}}_g + V\hat{\mathbf{y}}_g + W\hat{\mathbf{z}}_g\right] , \tag{A.7}$$

where $v_{\odot,\rm rot} = 220$ km/s [217] and $(U, V, W) = (11.1, 12.2, 7.3)$ km/s [218].

Earth's revolution The velocity of the Earth's revolution around the Sun can be written as:

$$\mathbf{v}_{\rm orbit} = v_{\rm orbit}(\lambda(t))[\cos(\delta_x)\sin(\lambda(t)-\lambda_x)\,\hat{\mathbf{x}}_g + \cos(\delta_y)\sin(\lambda(t)-\lambda_y)\,\hat{\mathbf{y}}_g + \cos(\delta_z)\sin(\lambda(t)-\lambda_z)\,\hat{\mathbf{z}}_g]\ , \tag{A.8}$$

where $\lambda(t)$ is the Sun's ecliptic longitude. Earth's orbital speed is $v_{\rm orbit}(\lambda(t)) = \langle v_{\rm orbit}\rangle\,[1 - e\sin(\lambda(t)-\lambda_0)]$, with $\langle v_{\rm orbit}\rangle = 29.8$ km/s; $\lambda_0 = 13^\circ$ and $e = 0.016722$ are the ecliptic longitude of the orbit's minor axis and the ellipticity of the Earth's orbit, respectively. In Eq. (A.8), $\delta_i = (-5^\circ.5303, 59^\circ.575, 29^\circ.812)$ and $\lambda_i = (266^\circ.141, -13^\circ.3485, 179^\circ.3212)$ are the ecliptic latitudes and longitudes of the galactic frame axes $(\hat{\mathbf{x}}_g, \hat{\mathbf{y}}_g, \hat{\mathbf{z}}_g)$, respectively.
The Sun's ecliptic longitude $\lambda(t)$ can be expressed as [219]:

$$\lambda(t) = L + (1^\circ.915 - 0^\circ.0048\,T_0)\sin(g) + 0^\circ.020\sin(2g)\ , \tag{A.9}$$

where $L = 281^\circ.0298 + 36000^\circ.77\,T_0 + 0^\circ.04107$ UT is the mean longitude of the Sun corrected for aberration, $g = 357^\circ.9258 + 35999^\circ.05\,T_0 + 0^\circ.04107$ UT is the mean anomaly (polar angle of orbit).

Earth's rotation The velocity of Earth's rotation around itself is given by:

$$\mathbf{v}_{\rm rot} = -v_{\rm rot,eq}\cos\lambda_{\rm lab}\hat{\mathcal{W}}\ , \tag{A.10}$$

where $v_{\rm rot,eq} = \frac{2\pi R_{\rm lab}}{(1\text{ sideral day})} = 0.4651$ km/s is the rotation speed at the Equator, with $R_{\rm lab} = 6378.137$ km Earth's equatorial radius and one sidereal day being 23.934 hr.

A.2.1 Computing the scalar product $\hat{\mathbf{q}}\cdot\mathbf{v}_{\rm lab}$

To compute the Radon transform of the DM velocity distribution, the calculation of the scalar product $\hat{\mathbf{q}}\cdot\mathbf{v}_{\rm lab}$ is necessary. To obtain this result, the different components of $\mathbf{v}_{\rm lab}$, given by Eqs (A.7), (A.8), and (A.10), must be rewritten in the crystal reference frame, with axes $(\hat{\mathbf{X}}, \hat{\mathbf{Y}}, \hat{\mathbf{Z}})$, using the transformations described by Eqs (A.1), (A.3), and (A.5). The most important contribution will come from $\hat{\mathbf{q}}\cdot\mathbf{v}_\odot$ and will be time dependent due to the time dependency in the transformation of the rest frames. The time dependency of $\hat{\mathbf{q}}\cdot\mathbf{v}_{\rm orbit}$ will come from $\lambda(t)$ and the coordinates transformation. Finally, the term $\hat{\mathbf{q}}\cdot\mathbf{v}_{\rm rot}$ will given the smallest contribution and will be time-independent since both the lab and the crystal are rotating with the Earth.
The expressions of the single contributions can be found in Ref. [187]; here we provide the final

expression, which is found combining the different terms:

$$\begin{aligned}\hat{\mathbf{q}}\cdot\mathbf{v}_{\rm lab} = (\alpha_X q_X + \alpha_Y q_Y + \alpha_Z q_Z)\{&[-\cos(t^\circ_{\rm lab})A(t) + \sin(t^\circ_{\rm lab})B(t)]\sin\lambda_{\rm lab} + C(t)\cos\lambda_{\rm lab}\}+\\ &+(\beta_X q_X + \beta_Y q_Y + \beta_Z q_Z)\{\sin(t^\circ_{\rm lab})A(t) + \cos(t^\circ_{\rm lab})B(t) - v_{\rm rot,eq}\cos\lambda_{\rm lab}\}+\\ &+(\gamma_X q_X + \gamma_Y q_Y + \gamma_Z q_Z)\{[\cos(t^\circ_{\rm lab})A(t) - \sin(t^\circ_{\rm lab})B(t)]\cos\lambda_{\rm lab} + C(t)\sin\lambda_{\rm lab}\}\ ;\end{aligned} \tag{A.11}$$

where:

$$\begin{cases} A(t) = 0.4927\, v_{\odot,\rm rot} - 1.066\ \text{km/s}\ + v_{\rm orbit}(t)\mathcal{A}(t)\,; \\ B(t) = 0.4503\, v_{\odot,\rm rot} + 16.56\ \text{km/s}\ + v_{\rm orbit}(t)\mathcal{B}(t)\,; \\ C(t) = 0.7445\, v_{\odot,\rm rot} + 7.077\ \text{km/s}\ + v_{\rm orbit}(t)\mathcal{C}(t)\,; \end{cases} \tag{A.12}$$

and:

$$\begin{cases} \mathcal{A}(t) = \mathcal{P}_{11}\cos\delta_x\sin(\lambda(t)-\lambda_x) + \mathcal{P}_{21}\cos\delta_y\sin(\lambda(t)-\lambda_y) + \mathcal{P}_{31}\cos\delta_z\sin(\lambda(t)-\lambda_z)\,; \\ \mathcal{B}(t) = \mathcal{P}_{12}\cos\delta_x\sin(\lambda(t)-\lambda_x) + \mathcal{P}_{22}\cos\delta_y\sin(\lambda(t)-\lambda_y) + \mathcal{P}_{32}\cos\delta_z\sin(\lambda(t)-\lambda_z)\,; \\ \mathcal{C}(t) = \mathcal{P}_{13}\cos\delta_x\sin(\lambda(t)-\lambda_x) + \mathcal{P}_{23}\cos\delta_y\sin(\lambda(t)-\lambda_y) + \mathcal{P}_{33}\cos\delta_z\sin(\lambda(t)-\lambda_z)\,. \end{cases} \tag{A.13}$$

Plugging everything together the scalar product and thus the Radon transform can be evaluated as a function of time, for the specific laboratory position.

The laboratory velocity direction By writing $\hat{\mathbf{q}}\cdot\mathbf{v}_{\rm lab} = \varrho\ (\alpha_X q_X + \alpha_Y q_Y + \alpha_Z q_Z) + \xi(\beta_X q_X + \beta_Y q_Y + \beta_Z q_Z) + \zeta\ (\gamma_X q_X + \gamma_Y q_Y + \gamma_Z q_Z)$, we can immediately see that in the crystal frame the laboratory velocity is given by:

$$\begin{aligned}\mathbf{v}_{\rm lab} &= (\varrho\,\alpha_X + \xi\,\beta_X + \zeta\ \gamma_X)\,\hat{\mathbf{X}} + (\varrho\,\alpha_Y + \xi\,\beta_Y + \zeta\ \gamma_Y)\,\hat{\mathbf{Y}} + (\varrho\,\alpha_Z + \xi\,\beta_Z + \zeta\ \gamma_Z)\,\hat{\mathbf{Z}} = \\ &= v_{\rm lab,X}\,\hat{\mathbf{X}} + v_{\rm lab,Y}\,\hat{\mathbf{Y}} + v_{\rm lab,Z}\,\hat{\mathbf{Z}}\ .\end{aligned} \tag{A.14}$$

If the crystal frame is oriented as the laboratory frame, Eq. (A.14) reduces to: $\mathbf{v}_{\rm lab} = \varrho\,\hat{\mathbf{X}} + \xi\,\hat{\mathbf{Y}} + \zeta\,\hat{\mathbf{Z}}$.
Using spherical coordinates, the laboratory velocity will be defined by: $v_{{\rm lab},X} = v_{\rm lab}\sin\theta_{\rm lab}\cos\phi_{\rm lab}$, $v_{{\rm lab},Y} = v_{\rm lab}\sin\theta_{\rm lab}\sin\phi_{\rm lab}$, $v_{{\rm lab},Z} = v_{\rm lab}\cos\theta_{\rm lab}$. Using these relations, one can find the angles $(\theta_{\rm lab}, \phi_{\rm lab})$ defining the laboratory speed in the crystal reference frame, which we have used in Chapter 4 when rewriting the Migdal effect expression.

The laboratory speed When the detector response is approximated to be isotropic, the scattering rate will no longer depend on the direction of $\mathbf{v}_{\rm lab}$, like through the Radon transform, but will only depend on the speed of the laboratory in the galactic rest frame $v_{\rm lab}$, in particular through the inverse mean speed $\eta(v_{\rm min}; t)$.
In this case, it is much more convenient to write all the velocity terms in the galactic rest

frame, before calculating the laboratory speed. Given the different magnitude of the typical solar speed $v_{\odot,\mathrm{rot}}$, Earth's orbital speed $\langle v_{\mathrm{orbit}} \rangle$ and rotational speed $v_{\mathrm{rot,eq}}$, different truncations can be performed. The first approximation is to neglect Earth's motion, then $v_{\mathrm{lab}} \simeq v_{\odot}$, with $v_{\odot} = |\mathbf{v}_{\odot,\mathrm{rot}} + \mathbf{v}_{\odot,\mathrm{pec}}| = \sqrt{U^2 + (v_{\odot,\mathrm{rot}} + V)^2 + W^2}$; we can see that in this case there will be no time dependency in the laboratory speed.
To include the contribution of the Earth's orbit we add the velocity term of Eq. (A.8), we will then have $v_{\mathrm{lab}} \simeq v_{\mathrm{lab}}(t)$, with $v_{\mathrm{lab}}(t) = |\mathbf{v}_{\odot} + \mathbf{v}_{\mathrm{orbit}}(t)|$, which will have a time-dependency due to Earth's motion. Finally, if no approximation is performed, the contribution from Earth's rotation must be included, then $\mathbf{v}_{\mathrm{lab}} = |\mathbf{v}_{\odot} + \mathbf{v}_{\mathrm{orbit}} + \mathbf{v}_{\mathrm{rot}}|$. It is convenient to rewrite Eq. (A.10) in the galactic rest frame, we obtain:

$$\begin{aligned} \mathbf{v}_{\mathrm{rot}} = &- v_{\mathrm{rot,eq}} \cos\lambda_{\mathrm{lab}} ([\mathcal{P}_{11} \sin(t^{\circ}_{\mathrm{lab}}) - \mathcal{P}_{12} \cos(t^{\circ}_{\mathrm{lab}})]\hat{\mathbf{x}}_g + \\ &+ [\mathcal{P}_{21} \sin(t^{\circ}_{\mathrm{lab}}) - \mathcal{P}_{22} \cos(t^{\circ}_{\mathrm{lab}})]\hat{\mathbf{y}}_g + [\mathcal{P}_{31} \sin(t^{\circ}_{\mathrm{lab}}) - \mathcal{P}_{32} \cos(t^{\circ}_{\mathrm{lab}})]\hat{\mathbf{z}}_g), \end{aligned} \tag{A.15}$$

which will also be time dependent. By summing all the velocity terms written in the galactic frame, we can calculate $v_{\mathrm{lab}}(t)$.
Eq. (A.14) could also be used to obtain the same result for v_{lab}, but in case of isotropic approximation this is a much faster and cleaner approach.

Appendix B: Additional calculations

B.1 SHM Marginal Speed Distribution

Here we derive the marginal speed distribution $f_\chi(v;t)$ in the Standard Halo Model, by integrating the velocity distribution in the laboratory frame over the solid angle.
Let θ be the angle between the DM velocity $\mathbf{v}$ and the laboratory's velocity $\mathbf{v}_{\rm lab}(t)$, and define $\mu = \cos(\theta)$. The integration over ϕ is trivial, yielding:

$$\begin{aligned} f_\chi(v;t) &= \int d\Omega\ v^2 f_\chi(\mathbf{v};t) = \int d\Omega\ v^2 \frac{1}{(2\pi\sigma_v^2)^{\frac{3}{2}} N_{\rm esc}} e^{-\frac{|\mathbf{v}+\mathbf{v}_{\rm lab}(t)|^2}{2\sigma_v^2}} \Theta(v_{\rm esc} - |\mathbf{v}+\mathbf{v}_{\rm lab}(t)|) = \\ &= \frac{2\pi v^2}{(2\pi\sigma_v^2)^{\frac{3}{2}} N_{\rm esc}} \int_{-1}^{+1} d\mu\ e^{-\frac{\left(v^2+v_{\rm lab}^2(t)+2vv_{\rm lab}(t)\mu\right)}{2\sigma_v^2}} \Theta\big(v_{\rm esc}^2 - (v^2+v_{\rm lab}^2(t)+2vv_{\rm lab}(t)\mu)\big)\ . \end{aligned} \tag{B.1}$$

The argument of the Heaviside function defines a maximum allowed value of μ:

$$\mu \leq \mu_{\rm max} = \frac{v_{\rm esc}^2 - v^2 - v_{\rm lab}^2(t)}{2vv_{\rm lab}(t)}\ . \tag{B.2}$$

When $\mu_{\rm max} \geq 1$, the full integration range is allowed, and the integration will result in:

$$\int_{-1}^{1} d\mu\ e^{-A-B\mu} = e^{-A}\frac{2}{B}\sinh(B)\ ; \tag{B.3}$$

with $A = \frac{v^2+v_{\rm lab}(t)^2}{2\sigma_v^2}$ and $B = \frac{vv_{\rm lab}(t)}{\sigma_v^2}$.
When $\mu < 1$, the integration range is truncated:

$$\int_{-1}^{\mu_{\rm max}} d\mu\ e^{-A-B\mu} = \frac{e^{-A+B}}{B} - \frac{e^{-A-B\mu_{\rm max}}}{B} = e^{-A}\frac{2}{B}\sinh(B) + \frac{1}{B}(e^{-A-B} - e^{-A-B\mu_{\rm max}})\ . \tag{B.4}$$

The second term represents the upper tail correction and contributes only when $\mu_{\rm max} \leq 1$, which corresponds to $v_{\rm esc}^2 \leq v^2 + v_{\rm lab}^2(t) + 2vv_{\rm lab}(t) = (v + v_{\rm lab}(t))^2$, and can be represented by the Heaviside function $\Theta(|v + v_{\rm lab}(t)| - v_{\rm esc})$.
In addition, when $\mu_{\rm max} < 1$, the entire integration domain will be excluded. This occurs when $v_{\rm esc}^2 \leq v^2 + v_{\rm lab}^2(t) - 2vv_{\rm lab}(t) = (v - v_{\rm lab}(t))^2$ and corresponds to the Heaviside function $\Theta(|v -$

$v_{\rm lab}(t)| - v_{\rm esc})$. In this case, the lower tail is overcounted, and must be subtracted:

$$\int_{-1}^{\mu_{\rm max}} d\mu\ e^{-A-B\mu} = \frac{1}{B}(e^{-A+B} - e^{-A-B\mu_{\rm max}})\ . \tag{B.5}$$

Inserting both corrections we obtain the full integral result:

$$\begin{aligned} f_\chi(v;t) = \frac{2\pi v^2}{(2\pi\sigma_v^2)^{\frac{3}{2}} N_{\rm esc}} \Big[& e^{-A}\frac{2}{B}\sinh(B) \\ & + \frac{1}{B}(e^{-A-B} - e^{-A-B\mu_{\rm max}})\Theta(|v + v_{\rm lab}(t)| - v_{\rm esc}) \\ & - \frac{1}{B}(e^{-A+B} - e^{-A-B\mu_{\rm max}})\Theta(|v - v_{\rm lab}(t)| - v_{\rm esc})\Big]\ . \end{aligned} \tag{B.6}$$

Substituting the expressions of A and B we can see how:

$$\begin{aligned} e^{-A-B} &= e^{-\frac{(v+v_{\rm lab}(t))^2}{2\sigma_v^2}}\ , \\ e^{-A+B} &= e^{-\frac{(v-v_{\rm lab}(t))^2}{2\sigma_v^2}}\ , \\ e^{-A-B\mu_{\rm max}} &= e^{-\frac{v_{\rm esc}^2}{2\sigma_v^2}}\ . \end{aligned} \tag{B.7}$$

Then we can immediately obtain the final result, shown in Eq. (1.27), for the SHM marginal speed distribution;

$$\begin{aligned} f_\chi(v;t) = \frac{1}{N_{\rm esc}}\frac{v}{\sqrt{\pi}v_0 v_{\rm lab}(t)} \Bigg[& 2\exp\left(-\frac{v^2 + v_{\rm lab}(t)^2}{v_0^2}\right)\sinh\left(2\frac{v v_{\rm lab}(t)}{v_0^2}\right) \\ & + \left(\exp\left(-\frac{(v + v_{\rm lab}(t))^2}{v_0^2}\right) - \exp\left(-\frac{v_{\rm esc}^2}{v_0^2}\right)\right)\Theta(|v + v_{\rm lab}(t)| - v_{\rm esc}) \\ & - \left(\exp\left(-\frac{(v - v_{\rm lab}(t))^2}{v_0^2}\right) - \exp\left(-\frac{v_{\rm esc}^2}{v_0^2}\right)\right)\Theta(|v - v_{\rm lab}(t)| - v_{\rm esc})\Bigg]\ ; \end{aligned} \tag{B.8}$$

where $v_0^2 = 2\sigma_v^2$. The time dependency that is inherited from $v_{\rm lab}(t)$ leads to a daily and a yearly modulation; the daily modulation can be neglected by substituting the laboratory's speed $v_{\rm lab}(t)$ with Earth's speed in the galactic frame $v_\oplus(t)$, while the yearly modulation can be neglected using the speed of the Sun in the galactic frame $v_\odot$, leading to a time independent speed distribution.

B.2 SHM Mean Inverse Speed

Here we report the expression of the mean inverse speed function $\eta(v_{\rm min};t)$ in the Standard Halo Model [220].

A direct way to perform the calculation is to write $\eta(v_{\rm min};t)$ as the integration of the marginal

speed distribution:

$$\eta(v_{\min};t) = \int_{v\geq v_{\min}} d^3\mathbf{v}\ \frac{f_\chi(\mathbf{v};t)}{v} = \int_{v_{\min}}^{\infty} dv\ \frac{1}{v}\int d\Omega\ v^2 f_\chi(\mathbf{v};t) = \int_{v_{\min}}^{\infty} dv\ \frac{f_\chi(v;t)}{v}\ . \tag{B.9}$$

We can then use the expression from Eq. (B.8), and only the speed integration will be left. Notice that the inverse speed $\frac{1}{v}$ cancels out with a factor v present in front of $f_\chi(v;t)$. The integration of the first term will result in:

$$\begin{aligned}&\int dv\ 2e^{\left(-\frac{v^2+v_{\rm lab}(t)^2}{v_0^2}\right)}\sinh\left(2\frac{vv_{\rm lab}(t)}{v_0^2}\right) = v_0\int_{x_{\min}}^{\infty} dx\ 2e^{-x^2-y^2}\sinh(2xy) = \\ &= v_0\int_{x_{\min}}^{\infty} dx\ e^{-(x-y)^2} - e^{-(x+y)^2} = v_0\frac{\sqrt{\pi}}{2}\Big[\mathrm{erf}(x_{\min}+y) - \mathrm{erf}(x_{\min}-y)\Big]\ ;\end{aligned} \tag{B.10}$$

where $x = \frac{v}{v_0}$, $x_{\min} = \frac{v_{\min}}{v_0}$, $y = \frac{v_{\rm lab}(t)}{v_0}$ and $\mathrm{erf(z)} = \frac{2}{\sqrt{\pi}}\int_0^z e^{-t^2}dt$. Then with a similar approach the tail correction terms can be computed, with the end result depending on the relations between $v_{\min}$, $v_{\rm esc}$ and $v_{\rm lab}(t)$:

$$\eta(v_{\min};t) = \begin{cases} 0 \qquad \text{for } v_{\min} \geq v_{\rm esc} + v_{\rm lab}(t)\ ; \\ \frac{1}{2v_{\rm lab}(t)N_{\rm esc}}\left[\mathrm{erf}(\frac{v_{\rm esc}}{v_0}) - \mathrm{erf}(\frac{v_{\min}-v_{\rm lab}(t)}{v_0}) - \frac{2}{\sqrt{\pi}}\frac{(v_{\rm esc}+v_{\rm lab}(t)-v_{\min})}{v_0}e^{-\frac{v_{\rm esc}^2}{v_0^2}}\right] \\ \qquad \text{for } |v_{\rm esc} - v_{\rm lab}(t)| \leq v_{\min} < v_{\rm esc} + v_{\rm lab}(t)\ ; \\ \frac{1}{2v_{\rm lab}(t)N_{\rm esc}}\left[\mathrm{erf}(\frac{v_{\min}+v_{\rm lab}(t)}{v_0}) - \mathrm{erf}(\frac{v_{\min}-v_{\rm lab}(t)}{v_0}) - \frac{4}{\sqrt{\pi}}\frac{v_{\rm lab}(t)}{v_0}e^{-\frac{v_{\rm esc}^2}{v_0^2}}\right] \\ \qquad \text{for } v_{\min} < |v_{\rm esc} - v_{\rm lab}(t)|\ . \end{cases} \tag{B.11}$$

As for the marginal speed distribution, time dependency can be removed by substituting the laboratory's speed with the Sun's speed $v_{\rm lab}(t) \to v_\odot$.

B.3 SHM Radon Transform

Here we show the calculation of the Radon transform of the Standard Halo Model velocity distribution function:

$$\hat{f}_\chi(v_{\min}, \hat{\mathbf{q}}; t) = \int d^3\mathbf{v}\ f_{\rm SHM}(\mathbf{v} + \mathbf{v}_{\rm lab}(t))\ \delta(\mathbf{v}\cdot\hat{\mathbf{q}} - v_{\min})\ . \tag{B.12}$$

We define the variables $\mathbf{u} = \mathbf{v} + \mathbf{v}_{\rm lab}(t)$ and $w = v_{\min} + \hat{\mathbf{q}}\cdot\mathbf{v}_{\rm lab}(t)$. We can then rewrite the delta function $\delta(\mathbf{v}\cdot\hat{\mathbf{q}} - v_{\min})$ as:

$$\delta(\mathbf{u}\cdot\hat{\mathbf{q}} - v_{\min} - \mathbf{v}_{\rm lab}(t)\cdot\hat{\mathbf{q}}) = \delta(\mathbf{u}\cdot\hat{\mathbf{q}} - (v_{\min} + \mathbf{v}_{\rm lab}(t)\cdot\hat{\mathbf{q}})) = \delta(\mathbf{u}\cdot\hat{\mathbf{q}} - w)\ . \tag{B.13}$$

Then we can write:

$$\hat{f}_\chi(v_{\rm min},\hat{\mathbf{q}};t) = \int d^3\mathbf{u}\ \delta(\mathbf{u}\cdot\hat{\mathbf{q}}-w)\ \frac{1}{N_{\rm esc}(2\pi\sigma_v^2)^{\frac{3}{2}}}\ e^{-\frac{u^2}{2\sigma_v^2}}\ \Theta(v_{\rm esc}-u)\ . \tag{B.14}$$

We then separate the integration in a part parallel to $\hat{\mathbf{q}}$ and one perpendicular. We define $s=\mathbf{u}\cdot\hat{\mathbf{q}}$ and $\mathbf{u}_\perp$, such that $\mathbf{u}=s\hat{\mathbf{q}}+\mathbf{u}_\perp$. Then the integration over s will lead to $s=w$ using the delta-function, and for the integration over $\mathbf{u}_\perp$ we use the polar coordinates (r,θ), finding the result shown in Eq.(2.25):

$$\begin{aligned}
&\hat{f}_\chi(v_{\rm min},\hat{\mathbf{q}};t) = \frac{1}{N_{\rm esc}(2\pi\sigma_v^2)^{\frac{3}{2}}}\int d^2\mathbf{u}_\perp\ e^{-\frac{w^2+u_\perp^2}{2\sigma_v^2}}\ \Theta(v_{\rm esc}^2-w^2-u_\perp^2) = \\
&= \frac{1}{N_{\rm esc}(2\pi\sigma_v^2)^{\frac{3}{2}}}\int d\theta\int dr\ r\ e^{-\frac{w^2+r^2}{2\sigma_v^2}}\ \Theta(v_{\rm esc}^2-w^2-r^2) = \\
&= \frac{e^{-\frac{w^2}{2\sigma_v^2}}(2\pi)}{N_{\rm esc}(2\pi\sigma_v^2)^{\frac{3}{2}}}\int_0^{\sqrt{v_{\rm esc}^2-w^2}} dr\ r\ e^{-\frac{r^2}{2\sigma_v^2}} = \frac{e^{-\frac{w^2}{2\sigma_v^2}}(2\pi)\sigma_v^2}{N_{\rm esc}(2\pi\sigma_v^2)^{\frac{3}{2}}}\left[1-e^{-\frac{v_{\rm esc}^2-w^2}{2\sigma_v^2}}\right] = \\
&= \frac{1}{N_{\rm esc}\sqrt{2\pi\sigma_v^2}}\left[e^{-\frac{|v_{\rm min}+\hat{\mathbf{q}}\cdot\mathbf{v}_{\rm lab}(t)|^2}{2\sigma_v^2}} - e^{-\frac{v_{\rm esc}^2}{2\sigma_v^2}}\right] .
\end{aligned} \tag{B.15}$$

The expression for the scalar product $\hat{\mathbf{q}}\cdot\mathbf{v}_{\rm lab}$ has been derived in Appendix A.2.

B.4 Radon Transform to Mean Inverse Speed relation

In this section we want to demonstrate the relation between the Radon transform $\hat{f}_\chi(v_{\rm min},\hat{\mathbf{q}};t)$ from Eq. (2.25) and the mean inverse DM speed $\eta(v_{\rm min};t)$ from Eq. (1.17). In particular the mean inverse speed function $\eta(v_{\rm min};t)$ corresponds to the angular average of the Radon transform, apart from a numerical factor. To show this we start from the angular average of the Radon transform:

$$\begin{aligned}
&\frac{1}{4\pi}\int_\Omega d\Omega'\,\hat{f}_\chi(v_{\rm min},\hat{\mathbf{q}};t) = \frac{1}{4\pi}\int_\Omega d\Omega'\int d^3\mathbf{v}\ f_\chi(\mathbf{v};t)\ \delta(\mathbf{v}\cdot\hat{\mathbf{q}}-v_{\rm min}) = \\
&= \int d^3\mathbf{v}\ f_\chi(\mathbf{v};t)\cdot\left[\frac{1}{4\pi}\int_\Omega d\Omega'\ \delta(\mathbf{v}\cdot\hat{\mathbf{q}}-v_{\rm min})\right] .
\end{aligned} \tag{B.16}$$

Then we rewrite the integral in square brackets:

$$\frac{1}{4\pi}\int_\Omega d\Omega'\ \delta(\mathbf{v}\cdot\hat{\mathbf{q}}-v_{\rm min}) = \frac{2\pi}{4\pi}\int_{-1}^{1} d\mu\ \delta(v\mu-v_{\rm min}) = \frac{1}{2v}\Theta(v-v_{\rm min})\ , \tag{B.17}$$

where we used the relation $\int_{-1}^1 d\mu\ \delta(v\mu-v_{\rm min}) = \frac{1}{|v|}\Theta\big(1-|\frac{v_{\rm min}}{v}|\big) = \frac{1}{v}\Theta\big(v-v_{\rm min}\big)$. Combining everything we obtain:

$$\frac{1}{4\pi}\int_\Omega d\Omega'\,\hat{f}_\chi(v_{\rm min},\hat{\mathbf{q}};t) = \frac{1}{2}\int d^3\mathbf{v}\ \frac{f_\chi(\mathbf{v};t)}{v}\Theta(v-v_{\rm min}) = \frac{1}{2}\eta(v_{\rm min};t)\ . \tag{B.18}$$

We have thus demonstrated that $\eta(v_{\min};t)$ is equal to two times the angular average of the Radon transform, explaining the factor 1/2 that appears in Eq. (2.28).

B.5 Expression of J_2 in the anisotropic Migdal effect correction

In this section we will show the result of the J_l integral from Eq. (4.26), in the case $l = 2$:

$$J_2(q,\omega;t) = \frac{1}{2}\frac{1}{\sqrt{\pi}v_0 N_{\rm esc}}\int_{-1}^{\max} dx \left(e^{-\frac{(w+v_{\rm lab}(t)x)^2}{v_0^2}} - e^{-\frac{v_{esc}^2}{v_0^2}} \right)(3x^2-1)\ . \tag{B.19}$$

The integration can be performed easily performed, and after some algebraic manipulation we obtain:

$$\int_{-1}^{\max} dx \left(e^{-\frac{(w+v_{\rm lab}(t)x)^2}{v_0^2}} - e^{-\frac{v_{esc}^2}{v_0^2}} \right)(3x^2-1) = \frac{1}{4(v_{\rm lab}(t)/v_0)^3}\left[\sqrt{\pi}\left(6\frac{w^2}{v_0^2} - 2\frac{v_{\rm lab}(t)^2}{v_0^2} + 3\right)\times \right.$$
$$\left. \times \,\mathrm{erf}\left(\frac{w+v_{\rm lab}(t)x}{v_0}\right) + 4\frac{v_{\rm lab}(t)^3(x-x^3)}{v_0^3}e^{-\frac{v_{\rm esc}^2}{v_0^2}} + 6\frac{w-v_{\rm lab}(t)x}{v_0}e^{-\frac{(w+v_{\rm lab}(t)x)^2}{v_0^2}}\right]_{-1}^{\max}. \tag{B.20}$$

The result will then depend on the value of max from Eq. (4.24), and we can distinguish three different cases. If max<-1, which means $\frac{1}{v_{\rm lab}(t)}(v_{\rm esc}-w) < -1$ so $w > v_{\rm esc} + v_{\rm lab}(t)$, and considering that $-1 < x < 1$ since $x = \cos\theta$, we have $J_2 = 0$. This is what to expect, since the condition on the minimum velocity w requires it to be larger than the sum of the galactic escape velocity and the laboratory's motion.
If max=$\frac{1}{v_{\rm lab}(t)}(v_{\rm esc}-w)$ which means $-1 < \frac{1}{v_{\rm lab}(t)}(v_{\rm esc}-w) < 1$, $v_{\rm esc}-v_{\rm lab}(t) < w < v_{\rm esc}+v_{\rm lab}(t)$, we obtain:

$$J_2(q,\omega;t) = \frac{1}{4(v_{\rm lab}(t)/v_0)^3}\left[\sqrt{\pi}\left(6\frac{w^2}{v_0^2} - 2\frac{v_{\rm lab}(t)^2}{v_0^2} + 3\right)\left[\mathrm{erf}\left(\frac{v_{\rm esc}}{v_0}\right) - \mathrm{erf}\left(\frac{w-v_{\rm lab}(t)}{v_0}\right)\right] + \right.$$
$$\left. + \left(4\frac{v_{\rm lab}(t)^2(v_{\rm esc}-w) - (v_{\rm esc}-w)^3}{v_0^3} + 6\frac{2w-v_{\rm esc}}{v_0}\right)e^{-\frac{v_{\rm esc}^2}{v_0^2}} - 6\frac{w+v_{\rm lab}(t)}{v_0}e^{-\frac{(w-v_{\rm lab}(t))^2}{v_0^2}}\right]. \tag{B.21}$$

If max=1 which means $\frac{1}{v_{\rm lab}(t)}(v_{\rm esc}-w)>1$ so $w<v_{\rm esc}-v_{\rm lab}(t)$, we obtain:

$$J_2(q,\omega;t)=\frac{1}{4(v_{\rm lab}(t)/v_0)^3}\left[\sqrt{\pi}\left(6\frac{w^2}{v_0^2}-2\frac{v_{\rm lab}(t)^2}{v_0^2}+3\right)\left[\mathrm{erf}\left(\frac{w+v_{\rm lab}(t)}{v_0}\right)-\mathrm{erf}\left(\frac{w-v_{\rm lab}(t)}{v_0}\right)\right]+\right.$$
$$\left.+6\frac{w-v_{\rm lab}(t)}{v_0}e^{-\frac{(w+v_{\rm lab}(t))^2}{v_0^2}}+6\frac{w+v_{\rm lab}(t)}{v_0}e^{-\frac{(w-v_{\rm lab}(t))^2}{v_0^2}}\right]. \tag{B.22}$$

Time dependency is removed if the laboratory's speed is substituted with Sun's speed, $v_{\rm lab}(t)\to v_\odot$.

B.6 Rewriting the DM-electron scattering rate using Zernike functions

In this section we rewrite the DM-electron scattering rate using the Zernike expansion and other concepts introduced in section 4.2.
Starting from Eq. (3.16) for the DM-electron scattering rate, we can rewrite the solid angle integration:

$$I(q,\omega)=\int_\Omega d\Omega'\hat{f}_\chi(v_{\rm min},\hat{\mathbf{q}};t)\ \mathcal{W}(\mathbf{q},\omega)=\sum_{n=0}^{L}\sum_{l=0/1}^{n}\sum_{m=-l}^{l}a_{nlm}(\omega)R_{nl}(q)\int_\Omega d\Omega'\hat{f}_\chi(v_{\rm min},\hat{\mathbf{q}};t)Y_{lm}(\theta,\varphi) \tag{B.23}$$

where we have first introduced the Zernike expansion for the ELF $\mathcal{W}(\mathbf{q},\omega)$. To apply the Wigner-D matrices, we need to rewrite the real spherical harmonics Y_{lm} in terms of the complex ones Y_l^m. We know that:

$$Y_{lm}=\begin{cases}\frac{i}{\sqrt{2}}(Y_l^m-(-1)^mY_l^{-m}) & \text{for } m<0\,;\\ Y_l^0 & \text{for } m=0\,;\\ \frac{1}{\sqrt{2}}(Y_l^{-m}+(-1)^mY_l^m) & \text{for } m>0\,.\end{cases} \tag{B.24}$$

If we split the sum over m in three terms, we rewrite the spherical harmonics and apply the Wigner-D matrices. For $m<0$ we will have:

$$\sum_{m'=-l}^{l}\frac{i}{\sqrt{2}}(D^l_{mm'})^*\ Y_l^{m'}(\theta,\varphi)-(-1)^m\sum_{m''=-l}^{l}(D^l_{-m,m''})^*\ Y_l^{m''}(\theta,\varphi)\,. \tag{B.25}$$

Now when performing the integration over ϕ we can use Eq. (4.14) and see that only the terms $m' = 0$ and $m'' = 0$ will be selected. We will thus have:

$$\begin{aligned} &2\pi\sqrt{\frac{2l+1}{4\pi}}P_l(\cos\theta)\left[\frac{i}{\sqrt{2}}(D^l_{m0})^* - (-1)^m(D^l_{-m,0})^*\right] = \\ &= 2\pi P_l(\cos\theta)\left[\frac{i}{\sqrt{2}}Y_l^m - (-1)^m Y_l^{-m}\right] = 2\pi P_l(\cos\theta)Y_{lm} \ , \end{aligned} \tag{B.26}$$

where we used the relation between the Wigner-D matrices and the complex spherical harmonics from Eq. (4.20). The same procedure can be repeated for $m = 0$ and $m > 0$. We thus reach the expression:

$$\begin{aligned} I(q,\omega) = &\sum_{n=0}^{L}\sum_{l=0/1}^{n}\sum_{m=-l}^{l} a_{nlm}(\omega)R_{nl}(q)2\pi Y_{lm}\left(\theta_{\rm lab}(t),\phi_{\rm lab}(t)\right)\times \\ &\times\int_{-1}^{\rm max} dx\ \frac{1}{\sqrt{\pi}v_0 N_{\rm esc}}\left[e^{-\frac{|v_{\rm min}+v_{\rm lab}(t)x|^2}{v_0^2}} - e^{-\frac{v_{\rm esc}^2}{v_0^2}}\right]P_l(x) \ , \end{aligned} \tag{B.27}$$

where $\left(\theta_{\rm lab}(t),\phi_{\rm lab}(t)\right)$ indicates the angles that describe the position of $\mathbf{v}_{\rm lab}(t)$ in the crystal reference frame, which have been defined in Appendix A.2. The value of max leads to the same conditions shown in the previous section. Renaming the integrals over the polar angle as: $J_l(q,\omega;t) = \frac{1}{\sqrt{\pi}v_0 N_{\rm esc}}\int_{-1}^{\rm max} dx\left[e^{-\frac{|v_{\rm min}+v_{\rm lab}(t)x|^2}{v_0^2}} - e^{-\frac{v_{\rm esc}^2}{v_0^2}}\right]P_l(x)$; we see that they are equivalent to those we defined for the Migdal effect and that $J_0(v_{\rm min};t) = \eta(v_{\rm min};t)$.
Recombining everything with the rate expression of Eq. (3.16), we obtain the following expression for the differential rate:

$$\begin{aligned} \frac{dR(t)}{d\omega} = &\frac{\rho_\chi}{\rho_{\rm T} m_\chi}\frac{\bar{\sigma}_e}{2(2\pi)^2\alpha\mu_{\chi e}^2}\sum_{n=0}^{L}\sum_{l=0/1}^{n}\sum_{m=-l}^{l} a_{nlm}(\omega)Y_{lm}\left(\theta_{\rm lab}(t),\phi_{\rm lab}(t)\right)\times \\ &\times q_{\rm max}^4\int_0^1 dq\ q^3 F_{DM}(q)^2 R_{nl}(q)J_l(q,\omega;t) \ . \end{aligned} \tag{B.28}$$

The isotropic rate can be obtained by selecting the $l = 0$ (so also $m = 0$) term:

$$\begin{aligned} \frac{dR^{\rm iso}(t)}{d\omega} &= \frac{\rho_\chi}{\rho_{\rm T} m_\chi}\frac{\bar{\sigma}_e}{2(2\pi)^2\alpha\mu_{\chi e}^2}\sum_{n=0\ \text{even}}^{L}\frac{1}{\sqrt{4\pi}}a_{n00}(\omega)q_{\rm max}^4\int_0^1 dq\ q^3 F_{DM}(q)^2 R_{n0}(q)\eta(q,\omega) = \\ &= \frac{\rho_\chi}{\rho_{\rm T} m_\chi}\frac{\bar{\sigma}_e}{2(2\pi)^2\alpha\mu_{\chi e}^2}\int dq\ q^3 F_{DM}(q)^2\overline{\mathcal{W}}(q,\omega)\eta(q,\omega;t) \ , \end{aligned} \tag{B.29}$$

where $\overline{\mathcal{W}}(q,\omega) = \sum_{n=0\ \text{even}}^{L}\frac{1}{\sqrt{4\pi}}a_{n00}(\omega)R_{n0}(q)$ and the sum over n is performed only over the even integers since only for even n the term $l = 0$ is present. We can see that the expression is the same as Eq. (3.17). The anisotropic correction to the rate can thus be separated, and its

expression is given by:

$$\frac{d\Delta R(t)}{dt} = \frac{\rho_\chi}{\rho_{\mathrm{T}} m_\chi} \frac{\bar{\sigma}_e}{2(2\pi)^2 \alpha \mu_{\chi e}^2} \sum_{n=1}^{L} \sum_{l=2/1}^{n} \sum_{m=-l}^{l} a_{nlm}(\omega) Y_{lm}\left(\theta_{\mathrm{lab}}(t), \phi_{\mathrm{lab}}(t)\right) \times \\ \times q_{\mathrm{max}}^4 \int_0^1 dq\ q^3 F_{DM}(q)^2 R_{nl}(q) J_l(q, \omega; t)\,, \tag{B.30}$$

where the start over n starts from $n = 1$, since $n = 0$ only has the term $l = 0$, and the sum over l starts from $l = 1$ as usual if n is odd, and from $l = 2$ is n is even.

We have thus shown how we can explicitly separate the isotropic term and the anisotropic correction, with the directional information of $\mathbf{v}_{\mathrm{lab}}(t)$ contained in $Y_{lm}\left(\theta_{\mathrm{lab}}(t), \phi_{\mathrm{lab}}(t)\right)$. If the time dependency of the speed $v_{\mathrm{lab}}(t)$ is neglected, like if a time frame of 1 day is considered, the integrals $J_l(q, \omega)$ must be computed only once, with the time dependency coming only from linear combination of spherical harmonics $Y_{lm}\left(\theta_{\mathrm{lab}}(t), \phi_{\mathrm{lab}}(t)\right)$.

Differently from the result obtained for the Migdal effect, in which a selection of the $l = 0$ and $l = 2$ terms derived from the scalar product $(\hat{\mathbf{q}} \cdot \hat{\mathbf{k}})$ between the nuclear and electron momentum, for the DM-electron scattering rate all the integrals $J_l(q, \omega; t)$ up to the expansion order L, must be computed. Although they can all be computed analytically, this can make this approach less inviting with respect to a direct Riemann sum over $\mathbf{q}$.

Appendix C: Density Functional Theory

C.1 Functionals for exchange and correlation

In this section we will briefly review some of the most commonly used approximations for the exchange-correlation functional.

Local density approximation (LDA)

The local density approximation is the earliest approach at approximating the xc-functional and is based on the knowledge that in the homogeneous electron gas the effects of exchange and correlation are local. Then the exchange-correlation energy can be approximated assuming that the xc-energy density is the same as the homogeneous electron gas $\epsilon_{xc}^{\text{hom}}$ at the respective density:

$$E_{xc}^{\text{LDA}}[n] = \int d^3\mathbf{r}\, n(\mathbf{r})\, \epsilon_{xc}^{\text{hom}}(n(\mathbf{r})) = \int d^3\mathbf{r}\, n(\mathbf{r})\, [\epsilon_x^{\text{hom}}(n(\mathbf{r})) + \epsilon_c^{\text{hom}}(n(\mathbf{r}))]\,. \tag{C.1}$$

The only information needed when applying the LDA is the exchange-correlation energy of the homogeneous gas as a function of the density. The exchange energy of the homogeneous gas that is given by:

$$\epsilon_x^{\text{hom}} = \frac{E_x}{N} = -\frac{3}{4\pi}k_F = -\frac{3}{4}\left(\frac{3}{\pi}n\right)^{\frac{1}{3}}\,, \tag{C.2}$$

while the correlation energy can be computed with accuracy using Monte Carlo methods. The reasoning behind the local approximation is that for the typical densities of solids, the range of the exchange and correlation is rather short, but is not justified by a formal expansion and we must consider to which extent the approximation works by actual applications, being best for solids close to the homogeneous gas and worst for very inhomogeneous systems like atoms.
A more general version of LDA is the LSDA (local spin density approximation), in which the xc-energy functional is written in terms of the two spin densities $n^{\uparrow}(\mathbf{r})$ and $n^{\downarrow}(\mathbf{r})$, or the total density $n(\mathbf{r}) = n^{\uparrow}(\mathbf{r}) + n^{\downarrow}(\mathbf{r})$ and the fractional spin polarization:

$$\zeta(\mathbf{r}) = \frac{n^{\uparrow}(\mathbf{r}) - n^{\downarrow}(\mathbf{r})}{n(\mathbf{r})}\,. \tag{C.3}$$

Generalized-gradient approximations (GGAs)

The first step beyond the local density approximation is to use a functional not only of the density n at each point, but also of the magnitude of the density gradient $|\nabla n|$. This approximation falls under the name of Generalized-gradient approximation (GGA), and can be defined as:

$$\begin{aligned} E_{xc}^{\mathrm{GGA}}[n] &= \int d^3\mathbf{r}\ n(\mathbf{r})\ \epsilon_{xc}(n(\mathbf{r}), |\nabla n(\mathbf{r})|) = \\ &= \int d^3\mathbf{r}\ n(\mathbf{r}) \epsilon_x^{\mathrm{hom}}(n(\mathbf{r}))\ F_{xc}(n(\mathbf{r}), s)\ , \end{aligned} \tag{C.4}$$

where $\epsilon_{xc}^{hom}(n)$ is xc-energy density for the homogeneous gas and F_{xc}, which is dimensionless, is the exchange-correlation enhancement factor, and is a function of the reduced density gradient s:

$$s = \frac{|\nabla n|}{2k_F n} \tag{C.5}$$

with $k_F = (3\pi^2 n)^{\frac{1}{3}}$.

Numerous forms for the exchange enhancement factor $F_{xc}(n, s) = F_x(n, s) + F_c(n, s)$ exist; three widely used examples are Becke (B88), Perdew and Wang (PW91) and Perdew,Burke and Enzerhof (PBE) forms.

In the region $0 < s < 3$, which is the most relevant for physical applications, F_x have nearly identical shapes, so different GGAs give similar improvements for many conventional systems with small density gradient contributions. In the region $s > 3$ the enhancement factors have different limiting behaviors due to the choice of different physical conditions for $s \to \infty$, for example $F_x^{\mathrm{PBE}}(s) \sim \text{const}$.

The lowest order gradient expansion at high density for the correlation enhancement factor F_c has been studied:

$$F_c(s) = \frac{\epsilon_c^{\mathrm{hom}}(n)}{\epsilon_x^{\mathrm{hom}}(n)}(1 - 0.21951s^2 + \dots)\,, \tag{C.6}$$

while for large density gradients the magnitude of correlation energy decreases and vanishes for $s \to \infty$; this can be understood from the fact that large gradients are associated with strong confining potentials that increase the level spacings and reduce the effect of interactions compared to the independent electron terms.

Among the GGAs, PBE is widely used due to its balance between accuracy and computational cost, and its derivation based on physical constraints and norm-conservation principles rather than empirical fitting.

Meta-GGAs and Hybrid functionals

Meta-GGAs represent a further step in complexity, incorporating not only the local density and its gradient, but also the kinetic energy density or the Laplacian of the density. We can define

the orbital kinetic energy density as:

$$\tau(\mathbf{r}) = \frac{1}{2}\sum_{n\mathbf{k}} |\nabla\psi_{n\mathbf{k}}(\mathbf{r})|^2 \ . \tag{C.7}$$

The general meta-GGA functional is then:

$$E_{xc}^{\text{meta-GGA}}[n] = \int d^3\mathbf{r}\ n(\mathbf{r})\ \epsilon_{xc}(n(\mathbf{r}), |\nabla n(\mathbf{r})|, \tau(\mathbf{r}))\ . \tag{C.8}$$

Meta-GGAs tend to offer improved accuracy with respect to GGAs. An example is the SCAN (Strongly Constrained and Appropriately Normed) functional, which satisfies all known exact constraints that a meta-GGA can, without empirical fitting.

Hybrid Functionals

Hybrid functionals incorporate a fraction of the exact Hartree-Fock exchange into the XC-functional. One of the motivations in support of hybrid functionals is the systematic underestimate of band gaps by GGAs and meta-GGAs. The general form of a hybrid functional is:

$$E_{xc}^{\text{hybrid}} = aE_x^{\text{HF}} + (1-a)E_x^{\text{DFT}} + E_c^{\text{DFT}} \tag{C.9}$$

where E_x^{DFT} and E_c^{DFT} are a GGA or meta-GGA exchange and correlation energy respectively, and E_x^{HF} is the Hartree-Fock exchange:

$$E_x^{\text{HF}} = -\frac{1}{2}\sum_{n\mathbf{k}}^{\text{occ.}}\sum_{m\mathbf{k}'}^{\text{occ.}} \int d^3\mathbf{r} \int d^3\mathbf{r}'\ \frac{\psi_{n\mathbf{k}}^*(\mathbf{r})\psi_{m\mathbf{k}'}^*(\mathbf{r}')\psi_{m\mathbf{k}'}(\mathbf{r})\psi_{n\mathbf{k}}(\mathbf{r}')}{|\mathbf{r}-\mathbf{r}'|}\ . \tag{C.10}$$

The mixing parameter a is typically determined empirically; for example, in PBE0 a=0.25 is used. Other so-called range-separated hybrid functionals, like HSE06, split the exchange term into short-range and long-range components and mix them differently to improve performance for periodic solids. Hybrid functionals provide improved descriptions of band gaps and charge transfer excitations, but at a significantly higher computational cost due to the non-local nature of the exact exchange.

C.2 Plane wave method calculations

The plane wave method is a general methodology used for solving differential equations; in our case we consider a Shrödinger-like equation, the Kohn-Sham equation, where each electron moves in an effective potential $v_{\text{eff}}(\mathbf{r})$, so the eigenstates must satisfy:

$$\hat{H}_{KS}(\mathbf{r})\psi_i(\mathbf{r}) = \Big[-\frac{1}{2}\nabla^2 + v_{\text{eff}}(\mathbf{r})\Big]\psi_i(\mathbf{r}) = \epsilon_i\psi_i(\mathbf{r})\ , \tag{C.11}$$

where we are considering a unpolarized systems for simplicity, and used Hartree atomic units ($\hbar = 1$, $m_e = 1$). We can expand the eigenfunctions in the complete set of Fourier components, obtaining:

$$\psi_i(\mathbf{r}) = \sum_{\mathbf{q}} c_{i\mathbf{q}}\, e^{i\mathbf{q}\cdot\mathbf{r}} = \sum_{\mathbf{q}} c_{i\mathbf{q}}\, |\mathbf{q}\rangle\,, \tag{C.12}$$

where $c_{i\mathbf{q}}$ are the expansion coefficients of the wavefunction in the basis of orthonormal plane waves $|\mathbf{q}\rangle$. Inserting (C.12) in (C.11) and multiplying from the left by $\langle\mathbf{q}'|$ and summing over $\mathbf{q}$, we obtain our equation in the Fourier space:

$$\sum_{\mathbf{q}} \left\langle \mathbf{q}' \middle| \hat{H}_{KS} \middle| \mathbf{q} \right\rangle c_{i,\mathbf{q}} = \epsilon_i c_{i,\mathbf{q}'}\ , \tag{C.13}$$

where we used the orthonormality relation $\langle\mathbf{q}'|\mathbf{q}\rangle = \delta_{\mathbf{q},\mathbf{q}'}$.
We now have to evaluate the matrix elements of the Hamiltonian, for the kinetic energy operator we have:

$$\left\langle \mathbf{q}' \middle| -\frac{1}{2}\nabla^2 \middle| \mathbf{q} \right\rangle = \frac{1}{2}|q|^2 \delta_{\mathbf{q},\mathbf{q}'}\ . \tag{C.14}$$

Since the potential follows the periodicity of the crystal, $v_{\text{eff}}(\mathbf{r}+\mathbf{R}) = v_{\text{eff}}(\mathbf{r})$, its Fourier transform can be written in the form:

$$v_{\text{eff}}(\mathbf{r}) = \sum_m v_{\text{eff}}(\mathbf{G}_m) e^{i\mathbf{G}_m\cdot\mathbf{r}}, \tag{C.15}$$

where $\mathbf{G}_m$ are the reciprocal lattice vectors; then the matrix elements of the potential will be given by:

$$\left\langle \mathbf{q}' \middle| v_{\text{eff}} \middle| \mathbf{q} \right\rangle = \sum_m v_{\text{eff}}(\mathbf{G}_m) \left\langle \mathbf{q}' \middle| e^{i\mathbf{G}_m\cdot\mathbf{r}} \middle| \mathbf{q} \right\rangle = \sum_m v_{\text{eff}}(\mathbf{G}_m)\delta_{\mathbf{q}'-\mathbf{q},\mathbf{G}_m}\ , \tag{C.16}$$

so they will be non zero only if $\mathbf{q}'$ and $\mathbf{q}$ differ by a reciprocal lattice vector $\mathbf{G}_m$. We can then define $\mathbf{q} = \mathbf{k} + \mathbf{G}_m$ and $\mathbf{q}' = \mathbf{k} + \mathbf{G}'_m$, with $\mathbf{k} \in$ 1BZ, without loss of generality; their difference will be $\mathbf{q} - \mathbf{q}' = \mathbf{G}_m - \mathbf{G}'_m = \mathbf{G}''_m$, which is a reciprocal lattice vector as required. Then $\left\langle \mathbf{q}' \middle| v_{\text{eff}} \middle| \mathbf{q} \right\rangle = v_{\text{eff}}(\mathbf{G}_{m'} - \mathbf{G}_m)$.
Finally we can write the Kohn-Sham equation for any $\mathbf{k}$, in the form of a matrix equation:

$$\sum_m H_{m'm}(\mathbf{k}) c_{im}(\mathbf{k}) = \epsilon_i(\mathbf{k})\, c_{im'}(\mathbf{k})\,, \text{with} \tag{C.17}$$

$$H_{m'm}(\mathbf{k}) = \left\langle \mathbf{k}+\mathbf{G}_{m'} \middle| \hat{H}_{KS} \middle| \mathbf{k}+\mathbf{G}_m \right\rangle = \frac{1}{2}|\mathbf{k}+\mathbf{G}_m|^2\delta_{m,m'} + v_{\text{eff}}(\mathbf{G}_{m'} - \mathbf{G}_m)\,. \tag{C.18}$$

The first Brillouin zone is discritized in a finite grid, usually in a Monkhorst-Pack grid, of N_k $\mathbf{k}$-points, and for each of those the KS equations must be solved.
In case of a non-local potential, $v_{\text{eff}}(\mathbf{G}_{m'} - \mathbf{G}_m)$ has to be generalized to $v_{\text{eff}}(\mathbf{K}_m, \mathbf{K}_{m'})$, where $\mathbf{K}_m = \mathbf{k} + \mathbf{G}_m$.
Solving Eq. (C.17) for each $\mathbf{k}$ we obtain the system eigenvalues $\epsilon_i(\mathbf{k}) \equiv \epsilon_{i\mathbf{k}}$ and the coefficients for the plane-wave expansion of the wavefunctions $c_{im}(\mathbf{k}) \equiv c_{i\mathbf{k}}(\mathbf{G}_m)$. Then the eigenfunctions

can be calculated using:

$$\psi_{i\mathbf{k}}(\mathbf{r}) = \sum_m c_{im}(\mathbf{k})\, e^{i(\mathbf{k}+\mathbf{G}_m)\cdot\mathbf{r}} = e^{i\mathbf{k}\cdot\mathbf{r}}\, u_{i\mathbf{k}}(\mathbf{r})\,, \text{with} \tag{C.19}$$

$$u_{i\mathbf{k}}(\mathbf{r}) = \sum_m c_{im}(\mathbf{k}) e^{i\mathbf{G}_m\cdot\mathbf{r}}\ . \tag{C.20}$$

We now focus on how the electron density is described in a plane wave method. For an independent particle problem, like the Kohn-Sham one, the density can be written as:

$$n(\mathbf{r}) = \frac{1}{N_k}\sum_{\mathbf{k},i} f_{i\mathbf{k}}\, n_{i\mathbf{k}}(\mathbf{r}),\ \text{with}\ n_{i\mathbf{k}}(\mathbf{r}) = |\psi_{i\mathbf{k}}(\mathbf{r})|^2, \tag{C.21}$$

where i is the band index at each **k**-point and $f_{\mathbf{k},i}$ is the state occupancy. Using the plane wave expression of Eq. (C.19) for the wavefunction, we can rewrite the local density $n_{i\mathbf{k}}(\mathbf{r})$:

$$n_{i\mathbf{k}}(\mathbf{r}) = \sum_{m,m'} c^*_{im}(\mathbf{k}) c_{im'}(\mathbf{k}) e^{i(\mathbf{G}_{m'}-\mathbf{G}_m)\cdot\mathbf{r}}\ , \tag{C.22}$$

with its Fourier components being:

$$n_{i\mathbf{k}}(\mathbf{G}) = \sum_m c^*_{i,m}(\mathbf{k}) c_{i,m''}(\mathbf{k}), \tag{C.23}$$

where m'' denotes the index of $\mathbf{G}_{m''} = \mathbf{G}_m + \mathbf{G}$.
Despite its simplicity, Eq. (C.23) is not the most efficient way to compute $n(\mathbf{r})$ or $n(\mathbf{G})$ because we need a double sum to find all the Fourier components, requiring N_G^2 operations, where N_G is the number of **G**-vectors needed to describe the density. If we had instead the Bloch states on a grid of N_R points in real space, the density could be computed just by taking a square, needing N_R operations. A common approach is then to perform Fast Fourier Transforms (FFT), transforming from one space to the other in $NlnN$ operations, with $N = N_R = N_G$: transforming the wavefunction plane-wave coefficients we obtain the real space wavefunction, and taking its square the real space density; then transforming again the reciprocal space density is computed. Note that since $n \propto |\psi|^2$ the Fourier components of the density extend twice as far in each direction as those needed for the wavefunction ψ; FFT requires a parallelepiped grid, while usually for the wavefunction a spherical cutoff:

$$u_{i\mathbf{k}}(\mathbf{r}) = \sum_m^{\frac{1}{2}|\mathbf{k}+\mathbf{G}_m|^2<E_{\text{cut}}} c_{i\mathbf{k}}(\mathbf{G}_m)\ e^{i\mathbf{G}_m\cdot\mathbf{r}}\ , \tag{C.24}$$

with E_{cut} being the plane wave energy cutoff. Then the number of points in the FFT grid $N = N_R = N_G$ for the density must be roughly an order of magnitude larger than the number of **G** vectors used as basis for the wavefunction. Despite all of these complications, the FFT approach is the most efficient for large systems.

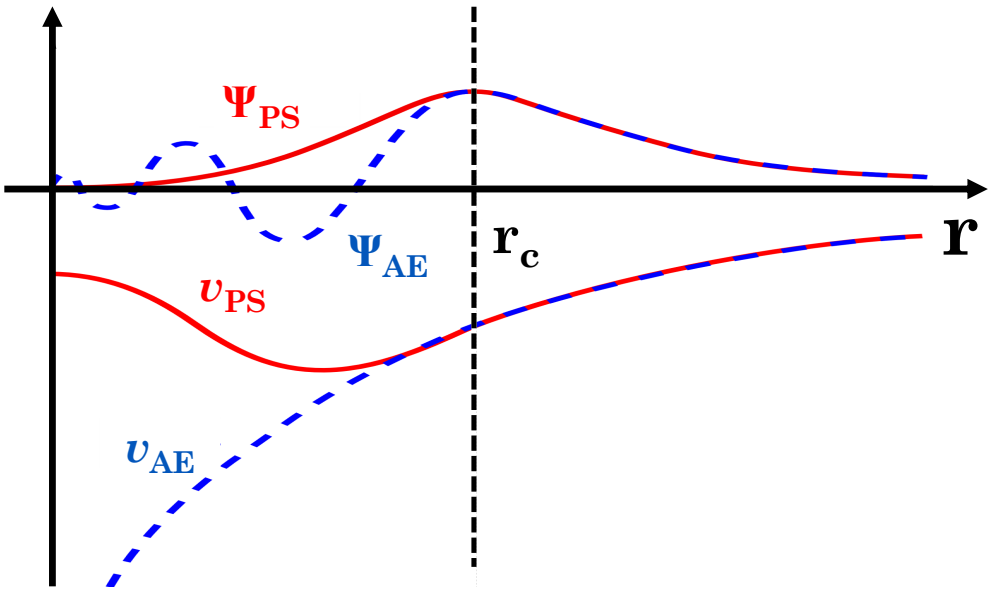

Figure C.1: Sketch of the comparison between the all-electron potential and wavefunction (blue) and the Pseudo potential and wavefunction (red). We note that the all-electron and the pseudo wavefunction and potentials match above the chosen cutoff radius.

Strongly localized electrons require a large number of plane waves in the expansion of the cell periodic function $u_{n\mathbf{k}}(\mathbf{r})$, which means a large value for the energy cutoff E_{cut} in Eq. (C.24) is required for convergence, slowing calculations. To avoid this problem, in some DFT codes core electrons are neglected (frozen core approximations), while valence electrons are treated using a pseudopotential approach.
Pseudopotentials are used to replace the strong Coulomb potential of the nucleus and the effects of the tightly bound core electrons with an effective ionic potential on the valence electrons. A pseudopotential can be generated in an atomic calculation and then used to compute the properties of valence electrons in solids, since the core states remain almost unchanged. Since they are not unique, different types of pseudopotentials exist, like Norm-Conserving Pseudopotentials (NCPP) and Ultrasoft Pseudopotentials (USPP), allowing to choose different forms depending on the desired speed and accuracy. In Fig. C.1 a simple scheme of a generic pseudopotential and pseudowavefunction is shown.

C.3 Full-potential linearized augmented-plane-wave method

The full-potential linearized augmented-plane-wave method (FLAPW) is an all-electron, full-potential approach for solving the Kohn–Sham equations in periodic solids. Since it makes no shape approximation for the effective potential (so no pseudopotential scheme) and treats core and valence electrons on the same footing, FLAPW is among the most precise and efficient methods for solv-

ing the KS equations. One of the main aspects of this method is the partitioning of space into two regions: muffin-tin spheres of radius R_{MT_α} centered on each atom α, where the potential is expanded in spherical harmonics and interstitial regions, where the potential is smooth and expanded in plane waves. In this method the wave function is expanded in the LAPW basis set, $\psi_{n\mathbf{k}}(\mathbf{r}) = \sum_{\mathbf{G}} c_{n\mathbf{k}}(\mathbf{G})\phi_{\mathbf{k},\mathbf{G}}(\mathbf{r})$, with the basis functions represented piecewise as:

$$\phi_{\mathbf{k},\mathbf{G}}(\mathbf{r}) = \begin{cases} \sum_{lm} \left[a_{l,m}^{\mathbf{G},\alpha}(\mathbf{k})\, u_{l,\alpha}(r_\alpha, E_{l,\alpha}) + b_{l,m}^{\mathbf{G},\alpha}(\mathbf{k})\, \dot{u}_{l,\alpha}(r_\alpha, E_{l,\alpha}) \right] Y_{l,m}(\hat{\mathbf{r}}_\alpha) & \text{for } \mathbf{r} \text{ in } \mathrm{MT}_\alpha\,, \\ e^{i(\mathbf{k}+\mathbf{G})\cdot\mathbf{r}} & \text{for } \mathbf{r} \text{ in IR}\,, \end{cases} \tag{C.25}$$

where $Y_{l,m}(\hat{\mathbf{r}}_\alpha)$ are spherical harmonics and $\mathbf{r}_\alpha = \mathbf{r} - \mathbf{R}_\alpha$ is the position relative to the atomic nucleus α. The values coefficients $a_{l,m}^{\mathbf{G},\alpha}(\mathbf{k})$ and $b_{l,m}^{\mathbf{G},\alpha}(\mathbf{k})$ are determined to ensure continuity in value and derivative of the basis function across the muffin-tin boundary. The radial functions $u_{l,\alpha}(r_\alpha, E_{l,\alpha})$ are the radial solution of the Kohn-Sham Hamiltonian for the spherically averaged potential at the linearization energy $E_{l,\alpha}$. Together with the inclusion of its energy-derivative $\dot{u}_{l,\alpha}(r_\alpha, E_{l,\alpha})$, radial functions allow for an accurate description of the energy dependence in a small window around each $E_{l,\alpha}$. This linearization avoids the need for an energy-dependent basis set. The set of LAPW basis functions is defined by specifying a cutoff parameter $K_{\max} = |\mathbf{k} + \mathbf{G}|_{\max}$, then in each MT sphere the expansion into spherical harmonics is limited to a maximum angular momentum number $l_{\max,\alpha} \approx K_{\max} R_{\mathrm{MT}_\alpha}$. The total effective potential $v_{\mathrm{eff}}(\mathbf{r})$ is expanded, without shape approximations, into a product of radial functions $v_{\mathrm{MT}}^{L}(r)$ and spherical harmonics $Y_L(\hat{\mathbf{r}})$ inside the muffin-tin spheres, while it is expanded in plane waves in the interstitial region:

$$v_{\mathrm{eff}}(\mathbf{r}) = \begin{cases} \sum_{L} v_{\mathrm{MT}}^{L,\alpha}(r_\alpha)\, Y_L(\hat{\mathbf{r}_\alpha}) & \text{for } \mathbf{r} \text{ in } \mathrm{MT}_\alpha\,, \\ \sum_{\mathbf{G}} v_{\mathrm{I}}(\mathbf{G})\, e^{i\mathbf{G}\cdot\mathbf{r}} & \text{for } \mathbf{r} \text{ in IR}\,, \end{cases} \tag{C.26}$$

where $L \equiv (l, m)$. The density will also be separated in two regions:

$$n(\mathbf{r}) = \begin{cases} \sum_{L} n_{\mathrm{MT}}^{L,\alpha}(r_\alpha)\, Y_L(\hat{\mathbf{r}}_\alpha) & \text{for } \mathbf{r} \text{ in } \mathrm{MT}_\alpha\,, \\ \sum_{\mathbf{G}} n_{\mathrm{I}}(\mathbf{G})\, e^{i\mathbf{G}\cdot\mathbf{r}} & \text{for } \mathbf{r} \text{ in IR}\,. \end{cases} \tag{C.27}$$

The Kohn–Sham equations reduce to a generalized eigenvalue problem:

$$\sum_{\mathbf{G}} \hat{H}_{\mathbf{G}',\mathbf{G}}(\mathbf{k}) c_{n\mathbf{k}}(\mathbf{G}) = \epsilon_{n\mathbf{k}} \sum_{\mathbf{G}} S_{\mathbf{G}',\mathbf{G}}(\mathbf{k}) c_{n\mathbf{k}}(\mathbf{G})\ , \tag{C.28}$$

where $\hat{H}_{\mathbf{G}',\mathbf{G}}(\mathbf{k}) = \langle \phi_{\mathbf{k},\mathbf{G}'} | \hat{H} | \phi_{\mathbf{k},\mathbf{G}} \rangle$ is the Hamiltonian matrix and $S_{\mathbf{G}',\mathbf{G}}(\mathbf{k}) = \langle \phi_{\mathbf{k},\mathbf{G}'} | \phi_{\mathbf{k},\mathbf{G}} \rangle$ is the overlap matrix of the LAPW basis functions.
Important parameters that need to be set in a LAPW calculation are the muffin-tin radii R_{MT_α}, which must be chosen to maximize atomic coverage but avoid sphere overlap, and the plane-wave cutoff in the interstitial region, which is typically set by $\frac{1}{2}|\mathbf{k}+\mathbf{G}|^2 \leq E_{\mathrm{cut}}$.
FLAPW implementations, like ELK, WIEN2k and FLEUR, deliver high accuracy for systems with localized electrons by combining an all-electron, full-potential treatment, an energy-linearized radial basis and plane waves in the interstitial region. Their main drawback is the computational cost, but for benchmark and high-precision studies FLAPW remains the method of choice.

C.4 Projector augmented wave method

Many DFT codes, like VASP and GPAW, use the projected augmented wave method (PAW) to describe the valence electrons. In the PAW method space is divided into the augmentation region Ω_a, which are atom-centered spheres, and the interstitial region Ω_i between such spheres. Within the augmentation region Ω_a the all-electron (AE) wavefunction $|\tilde{\psi}_{n\mathbf{k}}\rangle$ is expanded in a set of AE partial-waves $|\phi_i\rangle$:

$$|\psi_{n\mathbf{k}}\rangle = \sum_i a_{i,n\mathbf{k}} |\phi_i\rangle \quad \text{in } \Omega_a \,. \tag{C.29}$$

The AE partial-waves are the solutions of an all-electron KS calculation for a spherical atom of type N (indicating its number of electrons), situated at the atomic site $\mathbf{R}$ and for different angular momentum numbers $L = l, m$ and reference energies $\epsilon_{\alpha l}$. The index i compresses $\mathbf{R}, N, L$ and α. Using the spherical harmonics Y_{lm}, the AE partial waves can be written as:

$$\langle \mathbf{r} | \phi_i \rangle = Y_{lm}(\widehat{\mathbf{r}-\mathbf{R}}) \phi_{Nl\alpha}(|\mathbf{r}-\mathbf{R}|) \,. \tag{C.30}$$

The pseudo (PS) partial waves $\tilde{\phi}_i$ are also generated as:

$$\langle \mathbf{r} | \tilde{\phi}_i \rangle = Y_{lm}(\widehat{\mathbf{r}-\mathbf{R}}) \tilde{\phi}_{Nl\alpha}(|\mathbf{r}-\mathbf{R}|) \,, \tag{C.31}$$

and are smooth functions inside the augmentation-spheres and match the AE partial-waves in the interstitial region. This is done expanding $\tilde{\phi}_{Nl\alpha}(r)$ in terms Bessel functions $j_l(qr)$.
Using these definitions we can introduce the pseudo wavefunctions $|\tilde{\psi}_{n\mathbf{k}}\rangle$ as:

$$|\tilde{\psi}_{n\mathbf{k}}\rangle = \begin{cases} \sum_i a_{i,n\mathbf{k}} |\tilde{\phi}_i\rangle & \text{in } \Omega_a \,, \\ \\ |\psi_{n\mathbf{k}}\rangle & \text{in } \Omega_i \,. \end{cases} \tag{C.32}$$

Since the AE partial waves ϕ_i, and their rapid oscillations in Ω_a, are replaced by the PS partial waves $\tilde{\phi}_i$, and their smooth behavior, the PS wavefunction $|\tilde{\psi}_{n\mathbf{k}}\rangle$ will require a decreased number

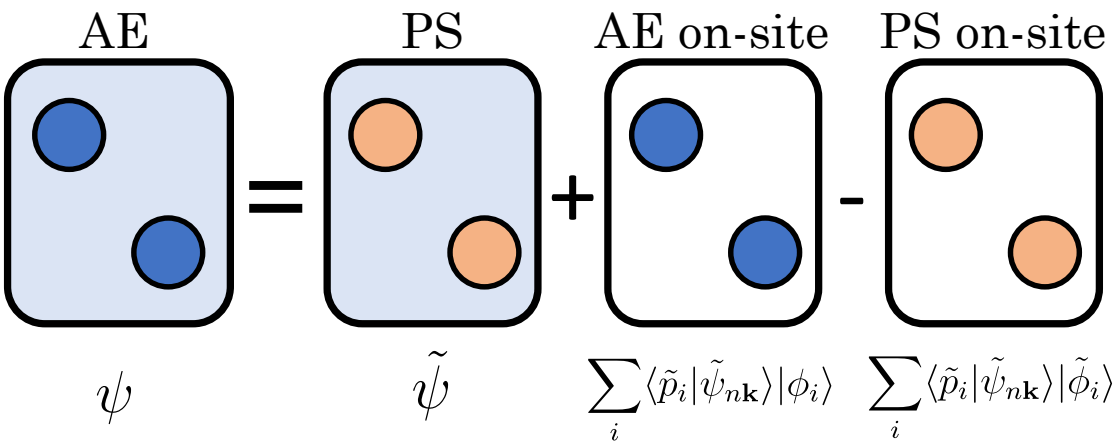

Figure C.2: Wavefunction representation in the Projector Augmented Wave method.

of plane waves.
Finally, the projector functions $|\tilde{p}_i\rangle$, that are dual to the PS partial waves, $\langle \tilde{p}_i | \tilde{\phi}_j \rangle = \delta_{ij}$, are introduced, allowing for writing the coefficients $a_{i,n\mathbf{k}}$ as:

$$\langle \tilde{p}_i | \tilde{\psi}_{n\mathbf{k}} \rangle = \sum_j a_{j,n\mathbf{k}} \langle \tilde{p}_i | \tilde{\phi}_j \rangle = a_{i,n\mathbf{k}} \ . \tag{C.33}$$

Using Eq. (C.29) and Eq. (C.32) we write the AE wavefunction $|\psi_{n\mathbf{k}}\rangle$ as:

$$|\psi_{n\mathbf{k}}\rangle = |\tilde{\psi}_{n\mathbf{k}}\rangle + \sum_i \langle \tilde{p}_i | \tilde{\psi}_{n\mathbf{k}} \rangle |\phi_i\rangle - \sum_i \langle \tilde{p}_i | \tilde{\psi}_{n\mathbf{k}} \rangle |\tilde{\phi}_i\rangle \ . \tag{C.34}$$

We can see that the AE wavefunction is described by the PS wavefunction, which is smooth in the entire space and corresponds to the AE wavefunction in the interstitial region Ω_i. Then the error of the PS wavefunction is corrected by including an AE on-site term inside the augmentation region Ω_a and subtracting the PS on-site contributions. In Fig. C.2 the wavefunction representation is showed graphically.
Using Eq. (C.34) we can rewrite the system's density $n(\mathbf{r})$, separating it in different terms:

$$\begin{aligned} n(\mathbf{r}) &= \frac{1}{N_k} \sum_{n\mathbf{k}} f_{n\mathbf{k}} \langle \psi_{n\mathbf{k}} | \mathbf{r} \rangle \langle \mathbf{r} | \psi_{n\mathbf{k}} \rangle = \\ &= \frac{1}{N_k} \sum_{n\mathbf{k}} f_{n\mathbf{k}} \langle \tilde{\psi}_{n\mathbf{k}} | \mathbf{r} \rangle \langle \mathbf{r} | \tilde{\psi}_{n\mathbf{k}} \rangle + \sum_{ij} \rho_{ij} \langle \phi_i | \mathbf{r} \rangle \langle \mathbf{r} | \phi_j \rangle - \sum_{ij} \rho_{ij} \langle \tilde{\phi}_i | \mathbf{r} \rangle \langle \mathbf{r} | \tilde{\phi}_j \rangle = \\ &= \tilde{n}(\mathbf{r}) + n^1(\mathbf{r}) - \tilde{n}^1(\mathbf{r}) \ , \end{aligned} \tag{C.35}$$

where $\tilde{n}(\mathbf{r})$ is the pseudo density, $\tilde{n}^1(\mathbf{r})$ the on-site PS density, $n^1(\mathbf{r})$ the on-site AE density, and ρ_{ij} is defined as:

$$\rho_{ij} = \frac{1}{N_k} \sum_{n\mathbf{k}} f_{n\mathbf{k}} \langle \tilde{\psi}_{n\mathbf{k}} | \tilde{p}_i \rangle \langle \tilde{p}_j | \tilde{\psi}_{n\mathbf{k}} \rangle = \frac{1}{N_k} \sum_{n\mathbf{k}} f_{n\mathbf{k}} \, a^*_{i,n\mathbf{k}} \, a_{j,n\mathbf{k}} \ . \tag{C.36}$$

In practice, DFT codes that adopt the PAW method create a PAW dataset in which the required information for the different atomic types, like the AE and PS partial waves, is contained.
The dipole transition matrix elements, which are necessary to compute the dielectric function, assume the following form when the PAW method is adopted:

$$\begin{aligned}\langle\psi_{n\mathbf{k}}|e^{i(\mathbf{q}+\mathbf{G})\cdot\mathbf{r}}|\psi_{m\mathbf{k}+\mathbf{q}}\rangle &= \langle\tilde{\psi}_{n\mathbf{k}}|e^{i(\mathbf{q}+\mathbf{G})\cdot\mathbf{r}}|\tilde{\psi}_{m\mathbf{k}+\mathbf{q}}\rangle + \\ &+ \sum_{ij}\langle\tilde{p}_i|\tilde{\psi}_{n\mathbf{k}}\rangle^*\ \langle\tilde{p}_j|\tilde{\psi}_{m\mathbf{k}+\mathbf{q}}\rangle\left[\langle\phi_i|e^{i(\mathbf{q}+\mathbf{G})\cdot\mathbf{r}}|\phi_j\rangle - \langle\tilde{\phi}_i|e^{i(\mathbf{q}+\mathbf{G})\cdot\mathbf{r}}|\tilde{\phi}_j\rangle\right]\ .\end{aligned} \tag{C.37}$$

The second term of the expression, which is related to the correction of the pseudo wavefunctions, is particularly relevant when describing the dielectric function for larger wavevectors and for DM scattering rates, as discussed by Ref. [137], where this correction is referenced as "AE reconstruction".
While this section serves as an essential introduction to the PAW method, for a more complete description, we recommend Ref. [221].

Bibliography

[1] F. Zwicky. "Die Rotverschiebung von extragalaktischen Nebeln". In: *Helvetica Physica Acta* 6 (Jan. 1933), pp. 110–127.

[2] Yoshiaki Sofue and Vera Rubin. "Rotation Curves of Spiral Galaxies". In: *Annual Review of Astronomy and Astrophysics* 39.Volume 39, 2001 (2001), pp. 137–174. ISSN: 1545-4282. DOI: https://doi.org/10.1146/annurev.astro.39.1.137. URL: https://www.annualreviews.org/content/journals/10.1146/annurev.astro.39.1.137.

[3] Horace W. Babcock. "The rotation of the Andromeda Nebula". In: *Lick Observatory Bulletins* 19 (Jan. 1939), pp. 41–51. DOI: 10.5479/ads/bib/1939licob.19.41b. URL: https://doi.org/10.5479/ads/bib/1939licob.19.41b.

[4] E. Corbelli and P. Salucci. "The extended rotation curve and the dark matter halo of M33". In: *Monthly Notices of the Royal Astronomical Society* 311.2 (Jan. 2000), pp. 441–447. ISSN: 1365-2966. DOI: 10.1046/j.1365-8711.2000.03075.x. URL: http://dx.doi.org/10.1046/j.1365-8711.2000.03075.x.

[5] J. P. Ostriker, P. J. E. Peebles, and A. Yahil. "The size and mass of galaxies, and the mass of the universe". In: *The Astrophysical Journal* 193 (Oct. 1974), p. L1. DOI: 10.1086/181617. URL: https://doi.org/10.1086/181617.

[6] NASA/CXC/M.Weiss. *Composite image of the galaxy cluster 1E0657-56 (thebullet-cluster)*. URL: http://chandra.harvard.edu/photo/2006/1e0657/more.html. (accessed: 23.06.2020).

[7] Planck Collaboration I. "*Planck* 2013 results. I. Overview of products and scientific results". In: *Astronomy & Astrophysics* 571 (2014), A1. DOI: 10.1051/0004-6361/201321529. arXiv: 1303.5062.

[8] F. Zwicky. "Nebulae as Gravitational Lenses". In: *Phys. Rev.* 51 (4 Feb. 1937), pp. 290–290. DOI: 10.1103/PhysRev.51.290. URL: https://link.aps.org/doi/10.1103/PhysRev.51.290.

[9] D. Walsh, R. F. Carswell, and R. J. Weymann. "0957 + 561 A, B: twin quasistellar objects or gravitational lens?" In: *Nature* 279.5712 (May 1979), pp. 381–384. DOI: 10.1038/279381a0. URL: https://www.nature.com/articles/279381a0.

[10] A. N. Taylor et al. "Gravitational Lens Magnification and the Mass of Abell 1689". In: *The Astrophysical Journal* 501.2 (July 1998), p. 539. DOI: 10.1086/305827. URL: https://doi.org/10.1086/305827.

[11] Xiang-Ping Wu et al. "A comparison of different cluster mass estimates: consistency or discrepancy?" In: *Monthly Notices of the Royal Astronomical Society* 301.3 (Dec. 1998), pp. 861–871. DOI: 10.1046/j.1365-8711.1998.02055.x. URL: https://doi.org/10.1046/j.1365-8711.1998.02055.x.

[12] Douglas Clowe, Anthony Gonzalez, and Maxim Markevitch. "Weak-Lensing Mass Reconstruction of the Interacting Cluster 1E 0657–558: Direct Evidence for the Existence of Dark Matter*". In: *The Astrophysical Journal* 604.2 (Apr. 2004), p. 596. DOI: 10.1086/381970. URL: https://doi.org/10.1086/381970.

[13] M. Markevitch et al. "Direct Constraints on the Dark Matter Self-Interaction Cross Section from the Merging Galaxy Cluster 1E 0657–56". In: *The Astrophysical Journal* 606.2 (Mar. 2004), p. 819. DOI: 10.1086/383178. URL: https://doi.org/10.1086/383178.

[14] Douglas Clowe et al. "A Direct Empirical Proof of the Existence of Dark Matter*". In: *The Astrophysical Journal* 648.2 (Aug. 2006), p. L109. DOI: 10.1086/508162. URL: https://doi.org/10.1086/508162.

[15] M. Milgrom. "A modification of the Newtonian dynamics as a possible alternative to the hidden mass hypothesis". In: *The Astrophysical Journal* 270 (July 1983), p. 365. DOI: 10.1086/161130. URL: https://doi.org/10.1086/161130.

[16] G. Gamow. "The evolution of the universe". In: *Nature* 162.4122 (Oct. 1948), pp. 680–682. DOI: 10.1038/162680a0. URL: https://doi.org/10.1038/162680a0.

[17] D. J. Fixsen. "THE TEMPERATURE OF THE COSMIC MICROWAVE BACKGROUND". In: *The Astrophysical Journal* 707.2 (Nov. 2009), pp. 916–920. DOI: 10.1088/0004-637x/707/2/916. URL: https://doi.org/10.1088/0004-637x/707/2/916.

[18] P. J. E. Peebles et al. "The case for the relativistic hot Big Bang cosmology". In: *Nature* 352.6338 (Aug. 1991), pp. 769–776. DOI: 10.1038/352769a0. URL: https://doi.org/10.1038/352769a0.

[19] N. Aghanim et al. "Planck2018 results: VI. Cosmological parameters". In: *Astronomy & Astrophysics* 641 (Sept. 2020), A6. ISSN: 1432-0746. DOI: 10.1051/0004-6361/201833910. URL: http://dx.doi.org/10.1051/0004-6361/201833910.

[20] William H. Press and Paul Schechter. "Formation of galaxies and clusters of galaxies by Self-Similar gravitational condensation". In: *The Astrophysical Journal* 187 (Feb. 1974), p. 425. DOI: 10.1086/152650. URL: https://doi.org/10.1086/152650.

[21] P. J. E. Peebles. "Primeval adiabatic perturbations - Effect of massive neutrinos". In: *The Astrophysical Journal* 258 (July 1982), p. 415. DOI: 10.1086/160094. URL: https://doi.org/10.1086/160094.

[22] D. N. Schramm and G. Steigman. "Relic neutrinos and the density of the universe". In: *The Astrophysical Journal* 243 (Jan. 1981), p. 1. DOI: 10.1086/158559. URL: https://doi.org/10.1086/158559.

[23] D. J. Hegyi and K. A. Olive. "A case against baryons in galactic halos". In: *The Astrophysical Journal* 303 (Apr. 1986), p. 56. DOI: 10.1086/164051. URL: https://doi.org/10.1086/164051.

[24] C. Alcock et al. "The MACHO Project: Microlensing Results from 5.7 Years of Large Magellanic Cloud Observations". In: *The Astrophysical Journal* 542.1 (Oct. 2000), p. 281. DOI: 10.1086/309512. URL: https://doi.org/10.1086/309512.

[25] B. J. Carr and S. W. Hawking. "Black holes in the early Universe". In: *Monthly Notices of the Royal Astronomical Society* 168.2 (Aug. 1974), pp. 399–415. DOI: 10.1093/mnras/168.2.399. URL: https://doi.org/10.1093/mnras/168.2.399.

[26] Benjamin W. Lee and Steven Weinberg. "Cosmological Lower Bound on Heavy-Neutrino Masses". In: *Phys. Rev. Lett.* 39 (4 July 1977), pp. 165–168. DOI: 10.1103/PhysRevLett.39.165. URL: https://link.aps.org/doi/10.1103/PhysRevLett.39.165.

[27] M. Tanabashi et al. "Review of Particle Physics". In: *Phys. Rev. D* 98 (3 Aug. 2018), p. 030001. DOI: 10.1103/PhysRevD.98.030001. URL: https://link.aps.org/doi/10.1103/PhysRevD.98.030001.

[28] Yong-Hamb Kim, Sang-Jun Lee, and Byeongsu Yang. "Superconducting detectors for rare event searches in experimental astroparticle physics". In: *Superconductor Science and Technology* 35.6 (Apr. 2022), p. 063001. DOI: 10.1088/1361-6668/ac6a1c. URL: https://doi.org/10.1088/1361-6668/ac6a1c.

[29] Heinz Pagels and Joel R. Primack. "Supersymmetry, Cosmology, and New Physics at Teraelectronvolt Energies". In: *Phys. Rev. Lett.* 48 (4 Jan. 1982), pp. 223–226. DOI: 10.1103/PhysRevLett.48.223. URL: https://link.aps.org/doi/10.1103/PhysRevLett.48.223.

[30] John Ellis et al. "Supersymmetric relics from the big bang". In: *Nuclear Physics B* 238.2 (1984), pp. 453–476. ISSN: 0550-3213. DOI: https://doi.org/10.1016/0550-3213(84)90461-9. URL: https://www.sciencedirect.com/science/article/pii/0550321384904619.

[31] Gerard Jungman, Marc Kamionkowski, and Kim Griest. "Supersymmetric dark matter". In: *Physics Reports* 267.5 (1996), pp. 195–373. ISSN: 0370-1573. DOI: https://doi.org/10.1016/0370-1573(95)00058-5. URL: https://www.sciencedirect.com/science/article/pii/0370157395000585.

[32] R. Bernabei et al. *The dark matter: DAMA/LIBRA and its perspectives*. 2021. arXiv: 2110.04734 [hep-ph]. URL: https://arxiv.org/abs/2110.04734.

[33] Q. Arnaud et al. "First Germanium-Based Constraints on Sub-MeV Dark Matter with the EDELWEISS Experiment". In: *Physical Review Letters* 125.14 (Oct. 2020). ISSN: 1079-7114. DOI: 10.1103/physrevlett.125.141301. URL: http://dx.doi.org/10.1103/PhysRevLett.125.141301.

[34] G. Angloher et al. "Detector development for the CRESST experiment". In: *Journal of Low Temperature Physics* 216.1-2 (May 2024), pp. 393–401. DOI: 10.1007/s10909-024-03154-6. URL: https://doi.org/10.1007/s10909-024-03154-6.

[35] CDMS Collaboration et al. *Silicon Detector Dark Matter Results from the Final Exposure of CDMS II*. 2013. arXiv: 1304.4279 [hep-ex]. URL: https://arxiv.org/abs/1304.4279.

[36] David E. Kaplan, Markus A. Luty, and Kathryn M. Zurek. "Asymmetric dark matter". In: *Phys. Rev. D* 79 (11 June 2009), p. 115016. DOI: 10.1103/PhysRevD.79.115016. URL: https://link.aps.org/doi/10.1103/PhysRevD.79.115016.

[37] Graciela B Gelmini. "Light weakly interacting massive particles". In: *Reports on Progress in Physics* 80.8 (June 2017), p. 082201. DOI: 10.1088/1361-6633/aa6e5c. URL: https://doi.org/10.1088/1361-6633/aa6e5c.

[38] Jonathan L. Feng and Jason Kumar. "Dark-Matter Particles without Weak-Scale Masses or Weak Interactions". In: *Phys. Rev. Lett.* 101 (23 Dec. 2008), p. 231301. DOI: 10.1103/PhysRevLett.101.231301. URL: https://link.aps.org/doi/10.1103/PhysRevLett.101.231301.

[39] R. Adhikari et al. "A White Paper on keV sterile neutrino Dark Matter". In: *Journal of Cosmology and Astroparticle Physics* 2017.01 (Jan. 2017), p. 025. DOI: 10.1088/1475-7516/2017/01/025. URL: https://doi.org/10.1088/1475-7516/2017/01/025.

[40] A. Aguilar et al. "Evidence for neutrino oscillations from the observation of $\overline{\nu}_e$ appearance in a $\overline{\nu}_\mu$ beam". In: *Phys. Rev. D* 64 (11 Nov. 2001), p. 112007. DOI: 10.1103/PhysRevD.64.112007. URL: https://link.aps.org/doi/10.1103/PhysRevD.64.112007.

[41] Alexander Merle, Viviana Niro, and Daniel Schmidt. "New production mechanism for keV sterile neutrino Dark Matter by decays of frozen-in scalars". In: *Journal of Cosmology and Astroparticle Physics* 2014.03 (Mar. 2014), p. 028. DOI: 10.1088/1475-7516/2014/03/028. URL: https://doi.org/10.1088/1475-7516/2014/03/028.

[42] J. H. Christenson et al. "Evidence for the 2π Decay of the K_2^0 Meson". In: *Phys. Rev. Lett.* 13 (4 July 1964), pp. 138–140. DOI: 10.1103/PhysRevLett.13.138. URL: https://link.aps.org/doi/10.1103/PhysRevLett.13.138.

[43] A. Alavi-Harati et al. "Observation of Direct CP Violation in $K_{S,L} \to \pi\pi$ Decays". In: *Phys. Rev. Lett.* 83 (1 July 1999), pp. 22–27. DOI: 10.1103/PhysRevLett.83.22. URL: https://link.aps.org/doi/10.1103/PhysRevLett.83.22.

[44] Steve Lamoreaux. "The first axion?" In: *Nature* 441.7089 (May 2006), pp. 31–32. DOI: 10.1038/441031a. URL: https://doi.org/10.1038/441031a.

[45] Paolo Gondolo and Graciela Gelmini. "Cosmic abundances of stable particles: Improved analysis". In: *Nuclear Physics B* 360.1 (1991), pp. 145–179. ISSN: 0550-3213. DOI: https://doi.org/10.1016/0550-3213(91)90438-4. URL: https://www.sciencedirect.com/science/article/pii/0550321391904384.

[46] Mark Srednicki, Richard Watkins, and Keith A. Olive. "Calculations of relic densities in the early universe". In: *Nuclear Physics B* 310.3 (1988), pp. 693–713. ISSN: 0550-3213. DOI: https://doi.org/10.1016/0550-3213(88)90099-5. URL: https://www.sciencedirect.com/science/article/pii/0550321388900995.

[47] Gary Steigman, Basudeb Dasgupta, and John F. Beacom. "Precise relic WIMP abundance and its impact on searches for dark matter annihilation". In: *Phys. Rev. D* 86 (2 July 2012), p. 023506. DOI: 10.1103/PhysRevD.86.023506. URL: https://link.aps.org/doi/10.1103/PhysRevD.86.023506.

[48] Rodrigo Capucha et al. *Freeze-in as a Complementary Process to Freeze-Out*. 2024. arXiv: 2407.04809 [hep-ph]. URL: https://arxiv.org/abs/2407.04809.

[49] Patrick J. Fox et al. "Missing energy signatures of dark matter at the LHC". In: *Phys. Rev. D* 85 (5 Mar. 2012), p. 056011. DOI: 10.1103/PhysRevD.85.056011. URL: https://link.aps.org/doi/10.1103/PhysRevD.85.056011.

[50] S. Chatrchyan et al. "Search for dark matter and large extra dimensions in monojet events in pp collisions at $\sqrt{s} = 7$ TeV". In: *Journal of High Energy Physics* 2012.9 (Sept. 2012). DOI: 10.1007/jhep09(2012)094. URL: https://doi.org/10.1007/jhep09(2012)094.

[51] Gordon Kane and Scott Watson. "DARK MATTER AND LHC: WHAT IS THE CONNECTION?" In: *Modern Physics Letters A* 23.26 (Aug. 2008), pp. 2103–2123. DOI: 10.1142/s0217732308028314. URL: https://doi.org/10.1142/s0217732308028314.

[52] Jennifer M. Gaskins. "A review of indirect searches for particle dark matter". In: *Contemporary Physics* 57.4 (June 2016), pp. 496–525. DOI: 10.1080/00107514.2016.1175160. URL: https://doi.org/10.1080/00107514.2016.1175160.

[53] F. W. Stecker. "The cosmic gamma-ray background from the annihilation of primordial stable neutral heavy leptons". In: *The Astrophysical Journal* 223 (Aug. 1978), p. 1032. DOI: 10.1086/156336. URL: https://doi.org/10.1086/156336.

[54] Marc Kamionkowski and Michael S. Turner. "Distinctive positron feature from particle dark-matter annihilations in the galatic halo". In: *Phys. Rev. D* 43 (6 Mar. 1991), pp. 1774–1780. DOI: 10.1103/PhysRevD.43.1774. URL: https://link.aps.org/doi/10.1103/PhysRevD.43.1774.

[55] Lars Bergström, Joakim Edsjö, and Paolo Gondolo. "Indirect detection of dark matter in km-size neutrino telescopes". In: *Phys. Rev. D* 58 (10 Oct. 1998), p. 103519. DOI: 10.1103/PhysRevD.58.103519. URL: https://link.aps.org/doi/10.1103/PhysRevD.58.103519.

[56] Joseph Silk, Keith Olive, and Mark Srednicki. "The photino, the sun, and high-energy neutrinos". In: *Phys. Rev. Lett.* 55 (2 July 1985), pp. 257–259. DOI: 10.1103/PhysRevLett.55.257. URL: https://link.aps.org/doi/10.1103/PhysRevLett.55.257.

[57] Gustavo A. Medina Tanco, Elisabete M. De Gouveia Dal Pino, and Jorge E. Horvath. "Deflection of Ultra–High-Energy cosmic rays by the galactic magnetic field: from the sources to the detector". In: *The Astrophysical Journal* 492.1 (Jan. 1998), pp. 200–204. DOI: 10.1086/305044. URL: https://doi.org/10.1086/305044.

[58] Gianfranco Bertone, Dan Hooper, and Joseph Silk. "Particle dark matter: evidence, candidates and constraints". In: *Physics Reports* 405.5 (2005), pp. 279–390. ISSN: 0370-1573. DOI: https://doi.org/10.1016/j.physrep.2004.08.031. URL: https://www.sciencedirect.com/science/article/pii/S0370157304003515.

[59] P.F. Smith and J.D. Lewin. "Dark matter detection". In: *Physics Reports* 187.5 (1990), pp. 203–280. ISSN: 0370-1573. DOI: https://doi.org/10.1016/0370-1573(90)90081-C. URL: https://www.sciencedirect.com/science/article/pii/037015739090081C.

[60] Andriy Kurylov and Marc Kamionkowski. "Generalized analysis of the direct weakly interacting massive particle searches". In: *Phys. Rev. D* 69 (6 Mar. 2004), p. 063503. DOI: 10.1103/PhysRevD.69.063503. URL: https://link.aps.org/doi/10.1103/PhysRevD.69.063503.

[61] Mark W. Goodman and Edward Witten. "Detectability of certain dark-matter candidates". In: *Phys. Rev. D* 31 (12 Jan. 1985), pp. 3059–3063. DOI: 10.1103/PhysRevD.31.3059. URL: https://link.aps.org/doi/10.1103/PhysRevD.31.3059.

[62] Ira Wasserman. "Possibility of detecting heavy neutral fermions in the Galaxy". In: *Phys. Rev. D* 33 (8 Apr. 1986), pp. 2071–2078. DOI: 10.1103/PhysRevD.33.2071. URL: https://link.aps.org/doi/10.1103/PhysRevD.33.2071.

[63] Andrzej K. Drukier, Katherine Freese, and David N. Spergel. "Detecting cold dark-matter candidates". In: *Phys. Rev. D* 33 (12 Jan. 1986), pp. 3495–3508. DOI: 10.1103/PhysRevD.33.3495. URL: https://link.aps.org/doi/10.1103/PhysRevD.33.3495.

[64] R. Bernabei et al. "Final model independent result of DAMA/LIBRA–phase1". In: *The European Physical Journal C* 73.12 (Nov. 2013). DOI: 10.1140/epjc/s10052-013-2648-7. URL: https://doi.org/10.1140/epjc/s10052-013-2648-7.

[65] Walter C. Pettus. *DM-Ice: Current Status and Future Prospects*. 2015. arXiv: 1510.00378 [physics.ins-det]. URL: https://arxiv.org/abs/1510.00378.

[66] Iván Coarasa et al. "ANAIS–112 three years data: a sensitive model independent negative test of the DAMA/LIBRA dark matter signal". In: *Communications Physics* 7.1 (Oct. 2024). DOI: 10.1038/s42005-024-01827-y. URL: https://www.nature.com/articles/s42005-024-01827-y.

[67] G. Adhikari et al. "Initial performance of the COSINE-100 experiment". In: *The European Physical Journal C* 78.2 (Feb. 2018). DOI: 10.1140/epjc/s10052-018-5590-x. URL: https://doi.org/10.1140/epjc/s10052-018-5590-x.

[68] N. Carlin et al. "Combined Annual Modulation Dark Matter Search with COSINE-100 and ANAIS-112". In: *Phys. Rev. Lett.* 135 (12 Sept. 2025), p. 121002. DOI: 10.1103/9j7w-qp1c. URL: https://link.aps.org/doi/10.1103/9j7w-qp1c.

[69] SuperCDMS Collaboration et al. *A Strategy for Low-Mass Dark Matter Searches with Cryogenic Detectors in the SuperCDMS SNOLAB Facility*. 2023. arXiv: 2203.08463 [physics.ins-det]. URL: https://arxiv.org/abs/2203.08463.

[70] XENON1T project-Gran Sasso Underground Laboratory (LNGS). *Comparison between the current experimental limits and the foreseen result from XENON1T*. URL: https://www.lngs.infn.it/en/xenon. (accessed: 09.07.2020).

[71] D.S. Akerib et al. "The Large Underground Xenon (LUX) experiment". In: *Nuclear Instruments and Methods in Physics Research Section A: Accelerators, Spectrometers, Detectors and Associated Equipment* 704 (Mar. 2013), pp. 111–126. ISSN: 0168-9002. DOI: 10.1016/j.nima.2012.11.135. URL: http://dx.doi.org/10.1016/j.nima.2012.11.135.

[72] Abdusalam Abdukerim et al. "PandaX-xT—A deep underground multi-ten-tonne liquid xenon observatory". In: *Science China Physics, Mechanics & Astronomy* 68.2 (Nov. 2024). ISSN: 1869-1927. DOI: 10.1007/s11433-024-2539-y. URL: http://dx.doi.org/10.1007/s11433-024-2539-y.

[73] P. Agnes et al. "Search for dark matter annual modulation with DarkSide-50". In: *Phys. Rev. D* 110 (10 Nov. 2024), p. 102006. DOI: 10.1103/PhysRevD.110.102006. URL: https://link.aps.org/doi/10.1103/PhysRevD.110.102006.

[74] S K Kim (for the KIMS Collaboration). "New results from the KIMS experiment". In: *Journal of Physics: Conference Series* 120.4 (July 2008), p. 042021. DOI: 10.1088/1742-6596/120/4/042021. URL: https://dx.doi.org/10.1088/1742-6596/120/4/042021.

[75] D.S. Akerib et al. "The LUX-ZEPLIN (LZ) experiment". In: *Nuclear Instruments and Methods in Physics Research Section A: Accelerators, Spectrometers, Detectors and Associated Equipment* 953 (Feb. 2020), p. 163047. ISSN: 0168-9002. DOI: 10.1016/j.nima.2019.163047. URL: http://dx.doi.org/10.1016/j.nima.2019.163047.

[76] Bei Cai. *The DEAP-3600 Dark Matter Experiment*. 2015. arXiv: 1511.00949 [astro-ph.IM]. URL: https://arxiv.org/abs/1511.00949.

[77] Spencer Chang et al. "CoGeNT interpretations". In: *Journal of Cosmology and Astroparticle Physics* 2010.08 (Aug. 2010), pp. 018–018. ISSN: 1475-7516. DOI: 10.1088/1475-7516/2010/08/018. URL: http://dx.doi.org/10.1088/1475-7516/2010/08/018.

[78] Rouven Essig, Jeremy Mardon, and Tomer Volansky. "Direct detection of sub-GeV dark matter". In: *Phys. Rev. D* 85 (7 Apr. 2012), p. 076007. DOI: 10.1103/PhysRevD.85.076007. URL: https://link.aps.org/doi/10.1103/PhysRevD.85.076007.

[79] Masahiro Ibe et al. "Migdal effect in dark matter direct detection experiments". In: *Journal of High Energy Physics* 2018.3 (Mar. 2018). DOI: 10.1007/jhep03(2018)194. URL: https://doi.org/10.1007/jhep03(2018)194.

[80] I. Arnquist et al. "First Constraints from DAMIC-M on Sub-GeV Dark-Matter Particles Interacting with Electrons". In: *Phys. Rev. Lett.* 130 (17 Apr. 2023), p. 171003. DOI: 10.1103/PhysRevLett.130.171003. URL: https://link.aps.org/doi/10.1103/PhysRevLett.130.171003.

[81] Yonit Hochberg et al. "Directional detection of dark matter with two-dimensional targets". In: *Physics Letters B* 772 (2017), pp. 239–246. ISSN: 0370-2693. DOI: https://doi.org/10.1016/j.physletb.2017.06.051. URL: https://www.sciencedirect.com/science/article/pii/S0370269317305270.

[82] Katelin Schutz and Kathryn M. Zurek. "Detectability of Light Dark Matter with Superfluid Helium". In: *Phys. Rev. Lett.* 117 (12 Sept. 2016), p. 121302. DOI: 10.1103/PhysRevLett.117.121302. URL: https://link.aps.org/doi/10.1103/PhysRevLett.117.121302.

[83] Yonit Hochberg, Yue Zhao, and Kathryn M. Zurek. "Superconducting Detectors for Superlight Dark Matter". In: *Phys. Rev. Lett.* 116 (1 Jan. 2016), p. 011301. DOI: 10.1103/PhysRevLett.116.011301. URL: https://link.aps.org/doi/10.1103/PhysRevLett.116.011301.

[84] Rouven Essig. "Some progress & challenges for the direct-detection of sub-GeV dark matter". In: *Nuclear Physics B* 1003 (2024). Special Issue of Nobel Symposium 182 on Dark Matter, p. 116484. ISSN: 0550-3213. DOI: https://doi.org/10.1016/j.nuclphysb.2024.116484. URL: https://www.sciencedirect.com/science/article/pii/S0550321324000506.

[85] Yonatan Kahn and Tongyan Lin. "Searches for light dark matter using condensed matter systems". In: *Reports on Progress in Physics* 85.6 (May 2022), p. 066901. DOI: 10.1088/1361-6633/ac5f63. URL: https://doi.org/10.1088/1361-6633/ac5f63.

[86] Tanner Trickle et al. "Multi-channel direct detection of light dark matter: theoretical framework". In: *Journal of High Energy Physics* 2020.3 (Mar. 2020). DOI: 10.1007/jhep03(2020)036. URL: https://doi.org/10.1007/jhep03(2020)036.

[87] D. G. Cerdeño and A. M. Green. "Direct detection of WIMPs". In: *Particle Dark Matter*. Cambridge University Press, Jan. 2010, pp. 347–369. DOI: 10.1017/cbo9780511770739.018. URL: http://dx.doi.org/10.1017/CBO9780511770739.018.

[88] Bob Holdom. "Two U(1)'s and ϵ charge shifts". In: *Physics Letters B* 166.2 (1986), pp. 196–198. ISSN: 0370-2693. DOI: https://doi.org/10.1016/0370-2693(86)91377-8. URL: https://www.sciencedirect.com/science/article/pii/0370269386913778.

[89] Jim Alexander et al. *Dark Sectors 2016 Workshop: Community Report*. 2016. arXiv: 1608.08632 [hep-ph]. URL: https://arxiv.org/abs/1608.08632.

[90] Timon Emken. *Dark Matter in the Earth and the Sun – Simulating Underground Scatterings for the Direct Detection of Low-Mass Dark Matter*. 2019. arXiv: 1906.07541 [hep-ph].

[91] Frederick James. *Statistical Methods in Experimental Physics*. 2nd. WORLD SCIENTIFIC, 2006. DOI: 10.1142/6096. eprint: https://www.worldscientific.com/doi/pdf/10.1142/6096. URL: https://www.worldscientific.com/doi/abs/10.1142/6096.

[92] Gary J. Feldman and Robert D. Cousins. "Unified approach to the classical statistical analysis of small signals". In: *Phys. Rev. D* 57 (7 Apr. 1998), pp. 3873–3889. DOI: 10.1103/PhysRevD.57.3873. URL: https://link.aps.org/doi/10.1103/PhysRevD.57.3873.

[93] Glen Cowan et al. "Asymptotic formulae for likelihood-based tests of new physics". In: *The European Physical Journal C* 71.2 (Feb. 2011). DOI: 10.1140/epjc/s10052-011-1554-0. URL: https://doi.org/10.1140/epjc/s10052-011-1554-0.

[94] R. Bernabei et al. "Recent Results from DAMA/LIBRA and Comparisons". In: *Moscow University Physics Bulletin* 77.2 (Apr. 2022), pp. 291–300. DOI: 10.3103/s0027134922020138. URL: https://doi.org/10.3103/s0027134922020138.

[95] Felix Kahlhoefer et al. "Model-independent comparison of annual modulation and total rate with direct detection experiments". In: *Journal of Cosmology and Astroparticle Physics* 2018.05 (May 2018), p. 074. DOI: 10.1088/1475-7516/2018/05/074. URL: https://dx.doi.org/10.1088/1475-7516/2018/05/074.

[96] G. Angloher et al. "The COSINUS project: perspectives of a NaI scintillating calorimeter for dark matter search". In: *European physical journal. C, Particles and fields* 76.8 (Aug. 2016). DOI: 10.1140/epjc/s10052-016-4278-3. URL: https://doi.org/10.1140/epjc/s10052-016-4278-3.

[97] K. Schäffner et al. "A NaI-Based Cryogenic Scintillating Calorimeter: Results from a COSINUS Prototype Detector". In: *Journal of low temperature physics* 193.5-6 (May 2018), pp. 1174–1181. DOI: 10.1007/s10909-018-1967-3. URL: https://doi.org/10.1007/s10909-018-1967-3.

[98] G. Angloher et al. "COSINUS: Cryogenic Calorimeters for the Direct Dark Matter Search with NaI Crystals". In: *Journal of low temperature physics* 200.5-6 (May 2020), pp. 428–436. DOI: 10.1007/s10909-020-02464-9. URL: https://doi.org/10.1007/s10909-020-02464-9.

[99] Gintaras Dūda, Ann Kemper, and Paolo Gondolo. "Model-independent form factors for spin-independent neutralino–nucleon scattering from elastic electron scattering data". In: *Journal of Cosmology and Astroparticle Physics* 2007.04 (Apr. 2007), p. 012. DOI: 10.1088/1475-7516/2007/04/012. URL: https://dx.doi.org/10.1088/1475-7516/2007/04/012.

[100] F. Mayet et al. "A review of the discovery reach of directional Dark Matter detection". In: *Physics Reports* 627 (2016). A review of the discovery reach of directional Dark Matter detection, pp. 1–49. ISSN: 0370-1573. DOI: https://doi.org/10.1016/j.physrep.2016.02.007. URL: https://www.sciencedirect.com/science/article/pii/S0370157316001022.

[101] Ciaran A. J. O'Hare et al. "Readout strategies for directional dark matter detection beyond the neutrino background". In: *Phys. Rev. D* 92 (6 Oct. 2015), p. 063518. DOI: 10.1103/PhysRevD.92.063518. URL: https://link.aps.org/doi/10.1103/PhysRevD.92.063518.

[102] Timon Emken. *Dark Matter in the Earth and the Sun – Simulating Underground Scatterings for the Direct Detection of Low-Mass Dark Matter*. 2019. arXiv: 1906.07541 [hep-ph]. URL: https://arxiv.org/abs/1906.07541.

[103] J.D. Lewin and P.F. Smith. "Review of mathematics, numerical factors, and corrections for dark matter experiments based on elastic nuclear recoil". In: *Astroparticle Physics* 6.1 (1996), pp. 87–112. ISSN: 0927-6505. DOI: https://doi.org/10.1016/S0927-6505(96)00047-3. URL: https://www.sciencedirect.com/science/article/pii/S0927650596000473.

[104] Giulia D'Imperio (for the SABRE collaboration). "Dark matter search with the SABRE experiment". In: *Journal of Physics: Conference Series* 1342.1 (Jan. 2020), p. 012060. DOI: 10.1088/1742-6596/1342/1/012060. URL: https://dx.doi.org/10.1088/1742-6596/1342/1/012060.

[105] Jingke Xu et al. "Scintillation efficiency measurement of Na recoils in NaI(Tl) below the DAMA/LIBRA energy threshold". In: *Phys. Rev. C* 92 (1 July 2015), p. 015807. DOI: 10.1103/PhysRevC.92.015807. URL: https://link.aps.org/doi/10.1103/PhysRevC.92.015807.

[106] D. Cintas et al. "Measurement of the sodium and iodine scintillation quenching factors across multiple NaI(Tl) detectors to identify systematics". In: *Phys. Rev. C* 110 (1 July 2024), p. 014613. DOI: 10.1103/PhysRevC.110.014613. URL: https://link.aps.org/doi/10.1103/PhysRevC.110.014613.

[107] G. Angloher et al. *COSINUS – a model-independent challenge of the DAMA/LIBRA dark matter claim with cryogenic NaI detectors operated in a new low-background facility*. 2025. arXiv: 2507.02429 [physics.ins-det]. URL: https://arxiv.org/abs/2507.02429.

[108] COSINUS project-Gran Sasso Underground Laboratory (LNGS). *Cosinus*. URL: https://www.lngs.infn.it/it/cosinus. (accessed: 09.07.2020).

[109] G. Angloher et al. "First measurements of remoTES cryogenic calorimeters: Easy-to-fabricate particle detectors for a wide choice of target materials". In: *Nuclear Instruments and Methods in Physics Research Section A: Accelerators, Spectrometers, Detectors and Associated Equipment* 1045 (2023), p. 167532. ISSN: 0168-9002. DOI: https://doi.org/10.1016/j.nima.2022.167532. URL: https://www.sciencedirect.com/science/article/pii/S0168900222008245.

[110] F. Pröbst et al. "Model for cryogenic particle detectors with superconducting phase transition thermometers". In: *Journal of Low Temperature Physics* 100.1-2 (July 1995), pp. 69–104. DOI: 10.1007/bf00753837. URL: https://doi.org/10.1007/bf00753837.

[111] G. Angloher et al. "A likelihood framework for cryogenic scintillating calorimeters used in the CRESST dark matter search". In: *The European Physical Journal C* 84.9 (Sept. 2024). DOI: 10.1140/epjc/s10052-024-13141-6. URL: https://doi.org/10.1140/epjc/s10052-024-13141-6.

[112] Fedja Kadribasic et al. "Directional Sensitivity in Light-Mass Dark Matter Searches with Single-Electron-Resolution Ionization Detectors". In: *Physical Review Letters* 120.11 (Mar. 2018). DOI: 10.1103/physrevlett.120.111301. URL: https://doi.org/10.1103%2Fphysrevlett.120.111301.

[113] Sebastian Sassi et al. "Energy loss in low energy nuclear recoils in dark matter detector materials". In: *Phys. Rev. D* 106 (6 Oct. 2022), p. 063012. DOI: 10.1103/PhysRevD.106.063012. URL: https://link.aps.org/doi/10.1103/PhysRevD.106.063012.

[114] Matti Heikinheimo et al. "Identification of the low-energy excess in dark matter searches with crystal defects". In: *Phys. Rev. D* 106 (8 Oct. 2022), p. 083009. DOI: 10.1103/PhysRevD.106.083009. URL: https://link.aps.org/doi/10.1103/PhysRevD.106.083009.

[115] CRESST Collaboration et al. *Observation of a low energy nuclear recoil peak in the neutron calibration data of an Al_2O_3 crystal in CRESST-III*. 2025. arXiv: 2506.09059 [physics.ins-det]. URL: https://arxiv.org/abs/2506.09059.

[116] A. P. Thompson et al. "LAMMPS - a flexible simulation tool for particle-based materials modeling at the atomic, meso, and continuum scales". In: *Comp. Phys. Comm.* 271 (2022), p. 108171. DOI: 10.1016/j.cpc.2021.108171.

[117] X.W. Zhou, F.P. Doty, and P. Yang. "Atomistic simulation study of atomic size effects on B1 (NaCl), B2 (CsCl), and B3 (zinc-blende) crystal stability of binary ionic compounds". In: *Computational Materials Science* 50.8 (2011), pp. 2470–2481. ISSN: 0927-0256. DOI: https://doi.org/10.1016/j.commatsci.2011.03.028. URL: http://www.sciencedirect.com/science/article/pii/S0927025611001716.

[118] Alexander Stukowski. "Visualization and analysis of atomistic simulation data with OVITO-the Open Visualization Tool". In: *MODELLING AND SIMULATION IN MATERIALS SCIENCE AND ENGINEERING* 18.1 (Jan. 2010). ISSN: 0965-0393. DOI: 10.1088/0965-0393/18/1/015012.

[119] G. Kresse and J. Hafner. "Ab initio molecular dynamics for liquid metals". In: *Phys. Rev. B* 47 (1 Jan. 1993), pp. 558–561. DOI: 10.1103/PhysRevB.47.558. URL: https://link.aps.org/doi/10.1103/PhysRevB.47.558.

[120] G. Kresse and D. Joubert. "From ultrasoft pseudopotentials to the projector augmented-wave method". In: *Phys. Rev. B* 59 (3 Jan. 1999), pp. 1758–1775. DOI: 10.1103/PhysRevB.59.1758. URL: https://link.aps.org/doi/10.1103/PhysRevB.59.1758.

[121] John P. Perdew, Kieron Burke, and Matthias Ernzerhof. "Generalized Gradient Approximation Made Simple". In: *Phys. Rev. Lett.* 77 (18 Oct. 1996), pp. 3865–3868. DOI: 10.1103/PhysRevLett.77.3865. URL: https://link.aps.org/doi/10.1103/PhysRevLett.77.3865.

[122] V. Hizhnyakov, D. Nevedrov, and A.J. Sievers. "Quantum properties of intrinsic localized modes". In: *Physica B: Condensed Matter* 316-317 (2002). Proceedings of the 10th International Conference on Phonon Scatte ring in Condensed Matter, pp. 132–135. ISSN: 0921-4526. DOI: https://doi.org/10.1016/S0921-4526(02)00440-4. URL: https://www.sciencedirect.com/science/article/pii/S0921452602004404.

[123] S. A. Kiselev and A. J. Sievers. "Generation of intrinsic vibrational gap modes in three-dimensional ionic crystals". In: *Phys. Rev. B* 55 (9 Mar. 1997), pp. 5755–5758. DOI: 10.1103/PhysRevB.55.5755. URL: https://link.aps.org/doi/10.1103/PhysRevB.55.5755.

[124] S V Dmitriev et al. "Discrete breathers in crystals". In: *Physics-Uspekhi* 59.5 (May 2016), p. 446. DOI: 10.3367/UFNe.2016.02.037729. URL: https://dx.doi.org/10.3367/UFNe.2016.02.037729.

[125] Liya Z. Khadeeva and Sergey V. Dmitriev. "Discrete breathers in crystals with NaCl structure". In: *Phys. Rev. B* 81 (21 June 2010), p. 214306. DOI: 10.1103/PhysRevB.81.214306. URL: https://link.aps.org/doi/10.1103/PhysRevB.81.214306.

[126] A. A. Kistanov, Yu. A. Baimova, and S. V. Dmitriev. "A molecular dynamics study of [111]-polarized gap discrete breathers in a crystal with NaCl-type structure". In: *Technical Physics Letters* 38.7 (July 2012), pp. 676–679. DOI: 10.1134/s1063785012070206. URL: https://doi.org/10.1134/s1063785012070206.

[127] Paul Lecoq, Alexander Gektin, and Mikhail Korzhik. "Influence of Crystal Structure Defects on Scintillation Properties". In: *Inorganic Scintillators for Detector Systems: Physical Principles and Crystal Engineering*. Cham: Springer International Publishing, 2017, pp. 197–252. ISBN: 978-3-319-45522-8. DOI: 10.1007/978-3-319-45522-8_6. URL: https://doi.org/10.1007/978-3-319-45522-8_6.

[128] Zheng Zhang et al. "Effects of irradiation defects on the electronic structure and optical properties of LiI scintillator". In: *Optical Materials* 112 (2021), p. 110727. ISSN: 0925-3467. DOI: https://doi.org/10.1016/j.optmat.2020.110727. URL: https://www.sciencedirect.com/science/article/pii/S0925346720310661.

[129] Meicong Li et al. "Electronic structure and optical properties of doped γ-CuI scintillator: a first-principles study". In: *RSC Advances* 13.14 (Jan. 2023), pp. 9615–9623. DOI: 10.1039/d2ra07988g. URL: https://pubs.rsc.org/en/content/articlelanding/2023/ra/d2ra07988g.

[130] A. Lim et al. "Electron Elevator: Excitations across the Band Gap via a Dynamical Gap State". In: *Phys. Rev. Lett.* 116 (4 Jan. 2016), p. 043201. DOI: 10.1103/PhysRevLett.116.043201. URL: https://link.aps.org/doi/10.1103/PhysRevLett.116.043201.

[131] Andrew P. Horsfield et al. "Adiabatic perturbation theory of electronic stopping in insulators". In: *Phys. Rev. B* 93 (24 June 2016), p. 245106. DOI: 10.1103/PhysRevB.93.245106. URL: https://link.aps.org/doi/10.1103/PhysRevB.93.245106.

[132] N. Shiran et al. "Luminescence and radiation resistance of undoped NaI crystals". In: *Materials Research Bulletin* 59 (2014), pp. 13–17. ISSN: 0025-5408. DOI: https://doi.org/10.1016/j.materresbull.2014.06.019. URL: https://www.sciencedirect.com/science/article/pii/S0025540814003419.

[133] Reza Ebadi et al. "Directional detection of dark matter using solid-state quantum sensing". In: *AVS Quantum Science* 4.4 (Nov. 2022), p. 044701. ISSN: 2639-0213. DOI: 10.1116/5.0117301. eprint: https://pubs.aip.org/avs/aqs/article-pdf/doi/10.1116/5.0117301/19803671/044701_1_online.pdf. URL: https://doi.org/10.1116/5.0117301.

[134] Sebastian Baum et al. "Mineral detection of neutrinos and dark matter. A whitepaper". In: *Physics of the Dark Universe* 41 (2023), p. 101245. ISSN: 2212-6864. DOI: https://doi.org/10.1016/j.dark.2023.101245. URL: https://www.sciencedirect.com/science/article/pii/S2212686423000791.

[135] Rouven Essig et al. *Direct Detection of sub-GeV Dark Matter with Semiconductor Targets*. 2016. arXiv: 1509.01598 [hep-ph]. URL: https://arxiv.org/abs/1509.01598.

[136] Simon Knapen, Jonathan Kozaczuk, and Tongyan Lin. "Dark matter-electron scattering in dielectrics". In: *Phys. Rev. D* 104 (1 July 2021), p. 015031. DOI: 10.1103/PhysRevD.104.015031. URL: https://link.aps.org/doi/10.1103/PhysRevD.104.015031.

[137] Sinéad M. Griffin et al. "Extended calculation of dark matter-electron scattering in crystal targets". In: *Phys. Rev. D* 104 (9 Nov. 2021), p. 095015. DOI: 10.1103/PhysRevD.104.095015. URL: https://link.aps.org/doi/10.1103/PhysRevD.104.095015.

[138] Michael Crisler et al. "SENSEI: First Direct-Detection Constraints on Sub-GeV Dark Matter from a Surface Run". In: *Physical Review Letters* 121.6 (Aug. 2018). ISSN: 1079-7114. DOI: 10.1103/physrevlett.121.061803. URL: http://dx.doi.org/10.1103/PhysRevLett.121.061803.

[139] A. Aguilar-Arevalo et al. *The DAMIC dark matter experiment*. 2015. arXiv: 1510.02126 [physics.ins-det]. URL: https://arxiv.org/abs/1510.02126.

[140] Brenda A. Cervantes-Vergara et al. "Skipper-CCD sensors for the Oscura experiment: requirements and preliminary tests". In: *Journal of Instrumentation* 18.08 (Aug. 2023), P08016. DOI: 10.1088/1748-0221/18/08/P08016. URL: https://dx.doi.org/10.1088/1748-0221/18/08/P08016.

[141] Stephen L. Adler. "Quantum Theory of the Dielectric Constant in Real Solids". In: *Phys. Rev.* 126 (2 Apr. 1962), pp. 413–420. DOI: 10.1103/PhysRev.126.413. URL: https://link.aps.org/doi/10.1103/PhysRev.126.413.

[142] Nathan Wiser. "Dielectric Constant with Local Field Effects Included". In: *Phys. Rev.* 129 (1 Jan. 1963), pp. 62–69. DOI: 10.1103/PhysRev.129.62. URL: https://link.aps.org/doi/10.1103/PhysRev.129.62.

[143] Mark S. Hybertsen and Steven G. Louie. "Ab initio static dielectric matrices from the density-functional approach. I. Formulation and application to semiconductors and insulators". In: *Phys. Rev. B* 35 (11 Apr. 1987), pp. 5585–5601. DOI: 10.1103/PhysRevB.35.5585. URL: https://link.aps.org/doi/10.1103/PhysRevB.35.5585.

[144] D. Pines, P. Nozieres, and Noel Corngold. "The Theory of Quantum Liquids". In: *American Journal of Physics* 36.3 (Mar. 1968), pp. 279–280. ISSN: 0002-9505. DOI: 10.1119/1.1974502. eprint: https://pubs.aip.org/aapt/ajp/article-pdf/36/3/279/10113617/279_2_online.pdf. URL: https://doi.org/10.1119/1.1974502.

[145] Steven M. Girvin and Kun Yang. *Modern Condensed Matter Physics*. Cambridge University Press, 2019.

[146] Martin Dressel and George Grüner. *Electrodynamics of Solids: Optical Properties of Electrons in Matter*. Cambridge University Press, 2002.

[147] Yang Sun et al. "Calculations of Energy-Loss Function for 26 Materials". In: *Chinese Journal of Chemical Physics* 29 (Dec. 2016), pp. 663–670. DOI: 10.1063/1674-0068/29/cjcp1605110.

[148] Simon Knapen, Jonathan Kozaczuk, and Tongyan Lin. "python package for dark matter scattering in dielectric targets". In: *Phys. Rev. D* 105 (1 Jan. 2022), p. 015014. DOI: 10.1103/PhysRevD.105.015014. URL: https://link.aps.org/doi/10.1103/PhysRevD.105.015014.

[149] R. Tsu. "Landau Damping and Dispersion of Phonon, Plasmon, and Photon Waves in Polar Semiconductors". In: *Phys. Rev.* 164 (2 Dec. 1967), pp. 380–383. DOI: 10.1103/PhysRev.164.380. URL: https://link.aps.org/doi/10.1103/PhysRev.164.380.

[150] N. D. Mermin. "Lindhard Dielectric Function in the Relaxation-Time Approximation". In: *Phys. Rev. B* 1 (5 Mar. 1970), pp. 2362–2363. DOI: 10.1103/PhysRevB.1.2362. URL: https://link.aps.org/doi/10.1103/PhysRevB.1.2362.

[151] P. Hohenberg and W. Kohn. "Inhomogeneous Electron Gas". In: *Phys. Rev.* 136 (3B Nov. 1964), B864–B871. DOI: 10.1103/PhysRev.136.B864. URL: https://link.aps.org/doi/10.1103/PhysRev.136.B864.

[152] W. Kohn and L. J. Sham. "Self-Consistent Equations Including Exchange and Correlation Effects". In: *Phys. Rev.* 140 (4A Nov. 1965), A1133–A1138. DOI: 10.1103/PhysRev.140.A1133. URL: https://link.aps.org/doi/10.1103/PhysRev.140.A1133.

[153] Richard M. Martin. *Electronic Structure: Basic Theory and Practical Methods*. Cambridge University Press, 2004. DOI: 10.1017/CBO9780511805769.

[154] Judith Harl. "The linear response function in density functional theory". en. In: (2008). DOI: 10.25365/THESIS.2622. URL: https://utheses.univie.ac.at/detail/2259.

[155] Mel Levy. "Universal variational functionals of electron densities, first-order density matrices, and natural spin-orbitals and solution of the v-representability problem". In: *Proceedings of the National Academy of Sciences* 76.12 (1979), pp. 6062–6065. DOI: 10.1073/pnas.76.12.6062. eprint: https://www.pnas.org/doi/pdf/10.1073/pnas.76.12.6062. URL: https://www.pnas.org/doi/abs/10.1073/pnas.76.12.6062.

[156] Erich Runge and E. K. U. Gross. "Density-Functional Theory for Time-Dependent Systems". In: *Phys. Rev. Lett.* 52 (12 Mar. 1984), pp. 997–1000. DOI: 10.1103/PhysRevLett.52.997. URL: https://link.aps.org/doi/10.1103/PhysRevLett.52.997.

[157] Silvana Botti et al. "Time-dependent density-functional theory for extended systems". In: *Reports on Progress in Physics* 70.3 (Feb. 2007), p. 357. DOI: 10.1088/0034-4885/70/3/R02. URL: https://doi.org/10.1088/0034-4885/70/3/R02.

[158] Jens Jørgen Mortensen et al. "GPAW: An open Python package for electronic structure calculations". In: *The Journal of Chemical Physics* 160.9 (Mar. 2024). DOI: 10.1063/5.0182685. URL: https://doi.org/10.1063/5.0182685.

[159] Ask Hjorth Larsen et al. "The atomic simulation environment—a Python library for working with atoms". In: *Journal of Physics: Condensed Matter* 29.27 (June 2017), p. 273002. DOI: 10.1088/1361-648X/aa680e. URL: https://dx.doi.org/10.1088/1361-648X/aa680e.

[160] Pauli Virtanen et al. "SciPy 1.0: Fundamental Algorithms for Scientific Computing in Python". In: *Nature Methods* 17 (2020), pp. 261–272. DOI: 10.1038/s41592-019-0686-2.

[161] P. Abbamonte et al. *SPLENDOR: a novel detector platform to search for light dark matter with narrow-gap semiconductors*. 2025. arXiv: 2507.17782 [physics.ins-det]. URL: https://arxiv.org/abs/2507.17782.

[162] Katherine Inzani, Alireza Faghaninia, and Sinéad M. Griffin. "Prediction of tunable spin-orbit gapped materials for dark matter detection". In: *Phys. Rev. Res.* 3 (1 Jan. 2021), p. 013069. DOI: 10.1103/PhysRevResearch.3.013069. URL: https://link.aps.org/doi/10.1103/PhysRevResearch.3.013069.

[163] M-Á Sánchez-Martínez et al. "Spectral and optical properties of Ag3Au(Se2,Te2) and dark matter detection". In: *Journal of Physics: Materials* 3.1 (Oct. 2019), p. 014001. DOI: 10.1088/2515-7639/ab3ea2. URL: https://doi.org/10.1088/2515-7639/ab3ea2.

[164] Peizhi Du et al. "Doped semiconductor devices for sub-MeV dark matter detection". In: *Phys. Rev. D* 109 (5 Mar. 2024), p. 055009. DOI: 10.1103/PhysRevD.109.055009. URL: https://link.aps.org/doi/10.1103/PhysRevD.109.055009.

[165] A. Migdal. In: *Sov. Phys. JETP 9, 1163* (1939).

[166] A. Migdal. In: *J. Phys. Acad. Sci. USSR 4(1-6), 449* (1941).

[167] R. BERNABEI et al. "ON ELECTROMAGNETIC CONTRIBUTIONS IN WIMP QUESTS". In: *International Journal of Modern Physics A* 22.19 (2007), pp. 3155–3168. DOI: 10.1142/S0217751X07037093. URL: https://doi.org/10.1142/S0217751X07037093.

[168] Masahiro Ibe et al. "Migdal effect in dark matter direct detection experiments". In: *Journal of High Energy Physics* 2018.3 (Mar. 2018). DOI: 10.1007/jhep03(2018)194. URL: https://doi.org/10.1007/jhep03(2018)194.

[169] Matthew J. Dolan, Felix Kahlhoefer, and Christopher McCabe. "Directly Detecting Sub-GeV Dark Matter with Electrons from Nuclear Scattering". In: *Phys. Rev. Lett.* 121 (10 Sept. 2018), p. 101801. DOI: 10.1103/PhysRevLett.121.101801. URL: https://link.aps.org/doi/10.1103/PhysRevLett.121.101801.

[170] Nicole F. Bell et al. "Low-mass inelastic dark matter direct detection via the Migdal effect". In: *Phys. Rev. D* 104 (7 Oct. 2021), p. 076013. DOI: 10.1103/PhysRevD.104.076013. URL: https://link.aps.org/doi/10.1103/PhysRevD.104.076013.

[171] Peter Cox et al. "Precise predictions and new insights for atomic ionization from the Migdal effect". In: *Phys. Rev. D* 107 (3 Feb. 2023), p. 035032. DOI: 10.1103/PhysRevD.107.035032. URL: https://link.aps.org/doi/10.1103/PhysRevD.107.035032.

[172] Simon Knapen, Jonathan Kozaczuk, and Tongyan Lin. "Migdal Effect in Semiconductors". In: *Phys. Rev. Lett.* 127 (8 Aug. 2021), p. 081805. DOI: 10.1103/PhysRevLett.127.081805. URL: https://link.aps.org/doi/10.1103/PhysRevLett.127.081805.

[173] Zheng-Liang Liang et al. "Describing the Migdal effect with a bremsstrahlung-like process and many-body effects". In: *Phys. Rev. D* 104 (5 Sept. 2021), p. 056009. DOI: 10.1103/PhysRevD.104.056009. URL: https://link.aps.org/doi/10.1103/PhysRevD.104.056009.

[174] Jonathan Kozaczuk and Tongyan Lin. "Plasmon production from dark matter scattering". In: *Phys. Rev. D* 101 (12 June 2020), p. 123012. DOI: 10.1103/PhysRevD.101.123012. URL: https://link.aps.org/doi/10.1103/PhysRevD.101.123012.

[175] Kim V. Berghaus et al. "The Migdal effect in semiconductors for dark matter with masses below $\sim$ 100 MeV". In: *Journal of High Energy Physics* 2023.1 (Jan. 2023). ISSN: 1029-8479. DOI: 10.1007/jhep01(2023)023. URL: http://dx.doi.org/10.1007/JHEP01(2023)023.

[176] Rouven Essig et al. "Relation between the Migdal Effect and Dark Matter-Electron Scattering in Isolated Atoms and Semiconductors". In: *Phys. Rev. Lett.* 124 (2 Jan. 2020), p. 021801. DOI: 10.1103/PhysRevLett.124.021801. URL: https://link.aps.org/doi/10.1103/PhysRevLett.124.021801.

[177] Ming Feng Gu. "The Flexible Atomic Code". In: *AIP Conference Proceedings* 730.1 (Oct. 2004), pp. 127–136. ISSN: 0094-243X. DOI: 10.1063/1.1824864. eprint: https://pubs.aip.org/aip/acp/article-pdf/730/1/127/12102653/127_1_online.pdf. URL: https://doi.org/10.1063/1.1824864.

[178] Liron Barak et al. "SENSEI: Direct-Detection Results on sub-GeV Dark Matter from a New Skipper CCD". In: *Phys. Rev. Lett.* 125 (17 Oct. 2020), p. 171802. DOI: 10.1103/PhysRevLett.125.171802. URL: https://link.aps.org/doi/10.1103/PhysRevLett.125.171802.

[179] M. F. Albakry et al. "Search for low-mass dark matter via bremsstrahlung radiation and the Migdal effect in SuperCDMS". In: *Phys. Rev. D* 107 (11 June 2023), p. 112013. DOI: 10.1103/PhysRevD.107.112013. URL: https://link.aps.org/doi/10.1103/PhysRevD.107.112013.

[180] E. Aprile et al. "Search for Light Dark Matter Interactions Enhanced by the Migdal Effect or Bremsstrahlung in XENON1T". In: *Phys. Rev. Lett.* 123 (24 Dec. 2019), p. 241803. DOI: 10.1103/PhysRevLett.123.241803. URL: https://link.aps.org/doi/10.1103/PhysRevLett.123.241803.

[181] P. Agnes et al. "Search for Dark-Matter–Nucleon Interactions via Migdal Effect with DarkSide-50". In: *Phys. Rev. Lett.* 130 (10 Mar. 2023), p. 101001. DOI: 10.1103/PhysRevLett.130.101001. URL: https://link.aps.org/doi/10.1103/PhysRevLett.130.101001.

[182] Duncan Adams et al. "Measuring the Migdal effect in semiconductors for dark matter detection". In: *Phys. Rev. D* 107 (4 Feb. 2023), p. L041303. DOI: 10.1103/PhysRevD.107.L041303. URL: https://link.aps.org/doi/10.1103/PhysRevD.107.L041303.

[183] H.M. Araújo et al. "The MIGDAL experiment: Measuring a rare atomic process to aid the search for dark matter". In: *Astroparticle Physics* 151 (2023), p. 102853. ISSN: 0927-6505. DOI: https://doi.org/10.1016/j.astropartphys.2023.102853. URL: https://www.sciencedirect.com/science/article/pii/S0927650523000397.

[184] P. J. Brown et al. *Intensity of diffracted intensities*. Sept. 2006, pp. 554–595. DOI: 10.1107/97809553602060000600. URL: https://doi.org/10.1107/97809553602060000600.

[185] EasySpin. *Rotations and Euler angles*. 2014.

[186] J. J. Sakurai and Jim Napolitano. *Modern Quantum Mechanics*. 2nd ed. Cambridge University Press, 2017.

[187] Nassim Bozorgnia, Graciela B. Gelmini, and Paolo Gondolo. "Daily modulation due to channeling in direct dark matter crystalline detectors". In: *Phys. Rev. D* 84 (2 July 2011), p. 023516. DOI: 10.1103/PhysRevD.84.023516. URL: https://link.aps.org/doi/10.1103/PhysRevD.84.023516.

[188] Sebastian Sassi. *Dark matter in next generation detectors*. 2025.

[189] An-Wen Deng and Chih-Ying Gwo. "A Stable Algorithm computing high-order 3D Zernike Moments and Shape Reconstructions". In: *Association for Computing Machinery* (2020). DOI: 10.1145/3408127.3408130. URL: https://doi.org/10.1145/3408127.3408130.

[190] Sebastian Sassi et al. "Fast numerical evaluation of dark matter direct detection event rates". In: *Phys. Rev. D* 112 (4 Aug. 2025), p. 043003. DOI: 10.1103/jzmc-r2k6. URL: https://link.aps.org/doi/10.1103/jzmc-r2k6.

[191] NIST: Digital library of mathemathical functions. URL: https://dlmf.nist.gov/18.17#iv.

[192] Yonit Hochberg et al. "Detection of sub-MeV dark matter with three-dimensional Dirac materials". In: *Phys. Rev. D* 97 (1 Jan. 2018), p. 015004. DOI: 10.1103/PhysRevD.97.015004. URL: https://link.aps.org/doi/10.1103/PhysRevD.97.015004.

[193] Ahmet Coskuner et al. "Directional dark matter detection in anisotropic Dirac materials". In: *Phys. Rev. D* 103 (1 Jan. 2021), p. 016006. DOI: 10.1103/PhysRevD.103.016006. URL: https://link.aps.org/doi/10.1103/PhysRevD.103.016006.

[194] Yonit Hochberg et al. "Directional detection of dark matter with two-dimensional targets". In: *Physics Letters B* 772 (2017), pp. 239–246. ISSN: 0370-2693. DOI: https://doi.org/10.1016/j.physletb.2017.06.051. URL: https://www.sciencedirect.com/science/article/pii/S0370269317305270.

[195] Yonit Hochberg, Yue Zhao, and Kathryn M. Zurek. "Superconducting Detectors for Superlight Dark Matter". In: *Phys. Rev. Lett.* 116 (1 Jan. 2016), p. 011301. DOI: 10.1103/PhysRevLett.116.011301. URL: https://link.aps.org/doi/10.1103/PhysRevLett.116.011301.

[196] Yonit Hochberg et al. "Detecting Sub-GeV Dark Matter with Superconducting Nanowires". In: *Phys. Rev. Lett.* 123 (15 Oct. 2019), p. 151802. DOI: 10.1103/PhysRevLett.123.151802. URL: https://link.aps.org/doi/10.1103/PhysRevLett.123.151802.

[197] Yonit Hochberg et al. "Directional detection of light dark matter in superconductors". In: *Phys. Rev. D* 107 (7 Apr. 2023), p. 076015. DOI: 10.1103/PhysRevD.107.076015. URL: https://link.aps.org/doi/10.1103/PhysRevD.107.076015.

[198] J. Bardeen, L. N. Cooper, and J. R. Schrieffer. "Theory of Superconductivity". In: *Phys. Rev.* 108 (5 Dec. 1957), pp. 1175–1204. DOI: 10.1103/PhysRev.108.1175. URL: https://link.aps.org/doi/10.1103/PhysRev.108.1175.

[199] Xiaolong Xu et al. "Investigation of TI/AU Transition-Edge sensors for Single-Photon detection". In: *Journal of Low Temperature Physics* 209.3-4 (Aug. 2022), pp. 372–378. DOI: 10.1007/s10909-022-02818-5. URL: https://doi.org/10.1007/s10909-022-02818-5.

[200] Dylan J. Temples et al. "Performance of a phonon-mediated kinetic inductance detector at the NEXUS cryogenic facility". In: *Phys. Rev. Appl.* 22 (4 Oct. 2024), p. 044045. DOI: 10.1103/PhysRevApplied.22.044045. URL: https://link.aps.org/doi/10.1103/PhysRevApplied.22.044045.

[201] Klaus Pretzl. "Cryogenic Detectors". In: *Particle Physics Reference Library: Volume 2: Detectors for Particles and Radiation*. Ed. by Christian W. Fabjan and Herwig Schopper. Cham: Springer International Publishing, 2020, pp. 871–912. ISBN: 978-3-030-35318-6. DOI: 10.1007/978-3-030-35318-6_19. URL: https://doi.org/10.1007/978-3-030-35318-6_19.

[202] Alan J. Bennett. "Theory of the Anisotropic Energy Gap in Superconducting Lead". In: *Phys. Rev.* 140 (6A Dec. 1965), A1902–A1920. DOI: 10.1103/PhysRev.140.A1902. URL: https://link.aps.org/doi/10.1103/PhysRev.140.A1902.

[203] S. Souma et al. "The origin of multiple superconducting gaps in MgB2". In: *Nature* 423.6935 (Apr. 2003), pp. 65–67. DOI: 10.1038/nature01619. URL: https://doi.org/10.1038/nature01619.

[204] P. G. De Gennes. *Superconductivity Of Metals And Alloys*. CRC Press, 1999. ISBN: 9780429497032. URL: https://doi.org/10.1201/9780429497032.

[205] L. N. Oliveira, E. K. U. Gross, and W. Kohn. "Density-Functional Theory for Superconductors". In: *Phys. Rev. Lett.* 60 (23 June 1988), pp. 2430–2433. DOI: 10.1103/PhysRevLett.60.2430. URL: https://link.aps.org/doi/10.1103/PhysRevLett.60.2430.

[206] M. Lüders et al. "Ab initio theory of superconductivity. I. Density functional formalism and approximate functionals". In: *Phys. Rev. B* 72 (2 July 2005), p. 024545. DOI: 10.1103/PhysRevB.72.024545. URL: https://link.aps.org/doi/10.1103/PhysRevB.72.024545.

[207] M. A. L. Marques et al. "Ab initio theory of superconductivity. II. Application to elemental metals". In: *Phys. Rev. B* 72 (2 July 2005), p. 024546. DOI: 10.1103/PhysRevB.72.024546. URL: https://link.aps.org/doi/10.1103/PhysRevB.72.024546.

[208] T. Kreibich and E. K. U. Gross. "Multicomponent Density-Functional Theory for Electrons and Nuclei". In: *Phys. Rev. Lett.* 86 (14 Apr. 2001), pp. 2984–2987. DOI: 10.1103/PhysRevLett.86.2984. URL: https://link.aps.org/doi/10.1103/PhysRevLett.86.2984.

[209] E.H. Brandt et al. *Superconductivity of Transition Metals: Their Alloys and Compounds*. Springer Series in Solid-State Sciences. Springer Berlin Heidelberg, 1982. ISBN: 9783642618192. URL: https://books.google.it/books?id=2A9uzwEACAAJ.

[210] Philip B. Allen and Božidar Mitrović. "Theory of Superconducting Tc". In: ed. by Henry Ehrenreich, Frederick Seitz, and David Turnbull. Vol. 37. Solid State Physics. Academic Press, 1983, pp. 1–92. DOI: https://doi.org/10.1016/S0081-1947(08)60665-7. URL: https://www.sciencedirect.com/science/article/pii/S0081194708606657.

[211] Antonio Sanna et al. *Introduction to Superconducting Density Functional Theory*. Forschungszentrum Jülich, Jan. 2017. URL: https://www.cond-mat.de/events/correl17/manuscripts/.

[212] D.D Koelling and J.H Wood. "On the interpolation of eigenvalues and a resultant integration scheme". In: *Journal of Computational Physics* 67.2 (1986), pp. 253–262. ISSN: 0021-9991. DOI: https://doi.org/10.1016/0021-9991(86)90261-5. URL: https://www.sciencedirect.com/science/article/pii/0021999186902615.

[213] *The Elk Code*. http://elk.sourceforge.net/.

[214] M.A. Hapgood. "Space physics coordinate transformations: A user guide". In: *Planetary and Space Science* 40.5 (1992), pp. 711–717. ISSN: 0032-0633. DOI: https://doi.org/10.1016/0032-0633(92)90012-D. URL: https://www.sciencedirect.com/science/article/pii/003206339290012D.

[215] U.S. Naval Observatory. https://aa.usno.navy.mil/data/siderealtime.

[216] P. Duffett-Smith. *Practical Astronomy with Your Calculator*. Cambridge University Press, Cambridge, England, 1992.

[217] Anne M Green. "Dependence of direct detection signals on the WIMP velocity distribution". In: *Journal of Cosmology and Astroparticle Physics* 2010.10 (Oct. 2010), p. 034. DOI: 10.1088/1475-7516/2010/10/034. URL: https://doi.org/10.1088/1475-7516/2010/10/034.

[218] Ralph Schönrich, James Binney, and Walter Dehnen. "Local kinematics and the local standard of rest". In: *Monthly Notices of the Royal Astronomical Society* 403.4 (Apr. 2010), pp. 1829–1833. ISSN: 0035-8711. DOI: 10.1111/j.1365-2966.2010.16253.x. eprint: https://academic.oup.com/mnras/article-pdf/403/4/1829/18575828/mnras0403-1829.pdf. URL: https://doi.org/10.1111/j.1365-2966.2010.16253.x.

[219] K. R. Lang. *Astrophysical formulae*. Springer, 1999.

[220] Chris Savage, Katherine Freese, and Paolo Gondolo. "Annual modulation of dark matter in the presence of streams". In: *Phys. Rev. D* 74 (4 Aug. 2006), p. 043531. DOI: 10.1103/PhysRevD.74.043531. URL: https://link.aps.org/doi/10.1103/PhysRevD.74.043531.

[221] G. Kresse and D. Joubert. "From ultrasoft pseudopotentials to the projector augmented-wave method". In: *Phys. Rev. B* 59 (3 Jan. 1999), pp. 1758–1775. DOI: 10.1103/PhysRevB.59.1758. URL: https://link.aps.org/doi/10.1103/PhysRevB.59.1758.